A Journey
from Partition Coefficients in Melt Inclusions of Lunar Samples to the Prediction of Vibrational Modes Under High P/T Conditions and the Thermodynamics of Sulfide-mediated Redox Reactions in Sediments

by

Sha Chen

A dissertation submitted in partial fulfillment
of the requirements for the degree of
Doctor of Philosophy
(Earth and Environmental Sciences)
in the University of Michigan
2022

Doctoral Committee:

Professor Udo Becker, Chair
Professor Ted Bergin
Professor Rose Cory
Professor Rebecca A. Lange
Professor Jie Li
Professor Adam C. Simon

Sha Chen

chensha@umich.edu

ORCID iD: 0000-0002-0816-1752

DEDICATION

To my family (my parents, brother, and nephew) for their love

To myself for never giving up

ACKNOWLEDGEMENTS

First of all, I would like to thank my advisor, Dr. Udo Becker, for lending me a hand at the most difficult time of my graduate school by allowing me to join his research group. Transferring an advisor at the end of the fourth year is stressful for the academic advisor and me alike. I will always be grateful for this kind gesture, without which I would have never come this far. A big thank you to other members of my dissertation committee, Jie Li, Adam Simon, Becky Lange, Ted Bergin, and Rose Cory, for their support and valuable feedback for this dissertation. I am also extremely grateful to the department, graduate chairs Naomi Levin and Jeroen Ritsema, and academic program managers Anne Hudon and Chrissy Zigulis, for funding and constantly checking on me.

Without any prior background in quantum computation or much time to learn, I am constantly anxious because I know I have to grasp the knowledge fast. My new research group members, Sooyeon Kim, Jerry (Zhongrui) Li, Ben Gebarski, YoungJae Kim, and Yingwei Wang, helped a lot, saving me much time and easing my stress. I would also thank the group members in the old research group, Peng Ni, Chenghuan Guo, and Zhengjiu Xu, who taught me a lot in academia and life when I first arrived in Ann Arbor and have been caring about me.

Special thanks to people in the department who have been nice to me and helped a lot: Juliana Mesa, Owen Neill, Natalie Packard, Jamie Gleason, Bian Wang, James Jolles, María Alejandra Rodríguez Mustafa, Justin Casaus, Prithvi Thakur, Allison Pease, Mack Taylor,

Madelyn Cook, Colleen Yancey, Xue Su, YoungJae Kim, Xiaojing Du, Tristan Childress, Becca Dzomba, Sophia Macarewich, Sharon Grim, Sarah Katz, Bekah Stein, etc.

Nobody knows how much I have learned and grown during the last six years. There are many people I would like to thank along the journey that kept me company, broadened my mind, and inspired me. The list is non-exhaustive: people I met in Ann Arbor, Pamela Bogart, Will Salisbury, Michael Shen, Jingwei Zhang, Kang Peng, Fan Xia, Sicen Du, Guanglong Huang; and my close friends in China, Lifan Zhou, Xiaofeng Ye, Yongchao Shen, Kaizhang Yu, etc.

TABLE OF CONTENTS

DEDICATION ii
ACKNOWLEDGEMENTS iii
LIST OF TABLES viii
LIST OF FIGURES x
LIST OF APPENDICES xiii
ABSTRACT xiv
CHAPTER 1 Introduction 1
1.1 Olivine and planetary science 1
1.2 Computational simulations of crystalline and non-crystalline systems 7
1.2.1 Applications of DFT on vibrational properties under high *T*/*P* conditions 9
1.2.2 Applications of DFT to molecular chemical reactions 11
1.3 References 13
CHAPTER 2 Trace Element Partitioning Between Olivine and Melt in Lunar Basalts 17
2.1 Abstract 17
2.2 Introduction 18
2.3 Samples and Methods 20
2.3.1 General considerations 20
2.3.2 Sample description and preparation 22
2.3.3 Major and trace element concentration measurement 24
2.4 Results 30
2.4.1 Comparison of melt inclusion and whole rock composition 30
2.4.2 Partition coefficients between olivine and melt 30
2.5 Discussion 36
2.5.1 Comparison with literature data 36
2.5.2 Implications 43
2.6 Acknowledgments 50

2.7 References 50
CHAPTER 3 Temperature and Pressure Effect on the Structural and Vibrational Properties of Forsterite From DFT Studies 59
3.1 Abstract 59
3.2 Introduction 60
3.3 Background of olivine 62
3.4 Methods 65
3.4.1 Pressure and temperature effect on vibrational frequencies and QHA 65
3.4.2 Calculation of vibrational frequencies under changing T and P conditions 67
3.5 Results 69
3.5.1 Crystal structure changes with increasing temperature and pressure 69
3.5.2 IR and Raman spectra and mode assignments 77
3.5.3 Pressure dependence of the vibrational frequencies for forsterite 83
3.5.4 Temperature dependence of the vibrational frequencies for forsterite 87
3.5.5 Vibrational frequencies of forsterite under simultaneous high T and P conditions. 89
3.5.6 Compositional and isotope effect on vibrational frequencies 89
3.6 Discussions and implications 95
3.7 Conclusions 97
3.8 References 98
CHAPTER 4 Reduction of Aqueous Fe(III) and Mn(III) by Hydroquinone in the Presence and Absence of Mackinawite Nanoparticles From DFT Calculations 105
4.1 Abstract 105
4.2 Introduction 107
4.3 Computational details 110
4.3.1 DFT calculations and initial structures 110
4.3.2 Pourbaix (pK_a, E^o) diagram construction 113
4.4 Results 115
4.4.1 Reaction of (hydro-/semi-)quinone and Fe/Mn in aqueous solution 119
4.4.2 Adsorption to the Fe_8S_8 cluster 123
4.4.3 Derivation of Pourbaix diagrams for adsorbed species 130
4.5 Discussions and implications 134
4.5.1 Implications on Fe and Mn cycle for natural systems 134
4.5.2 Mackinawite oxidation 136

4.6 Conclusions 136
4.7 References 137
CHAPTER 5 Conclusions 143
Appendix A Supplemental Figures for Chapter 2 149
Appendix B Supplemental Tables for Chapter 3 158
Appendix C Thermodynamics of Forsterite-Fayalite Solid Solution 161
C.1 Abstract 161
C.2 Introduction 161
C.3 Computational methods 163
C.4 Thermodynamics 165
C.5 Results 167
C.6 References 172
Appendix D Spin State of Iron in Mackinawite 174
D.1 Introduction 174
D.2 Spin configuration of mackinawite cluster Fe_8S_8 175
D.3 Conclusion 178
D.4 References 179

LIST OF TABLES

Table 1.1 Comparison of the two types of molecular simulation: quantum mechanics and classical mechanics. 9

Table 2.1 Major element concentrations for olivine and melt inclusions (MIs) measured by EMPA.. 25

Table 2.2 Trace element composition for olivine and MI with 1σ error. Concentration data and associated errors in melt inclusion for 74235,12040, 12040, 15016, and 15647 are from Ni et al. (2019). 29

Table 2.3 Partition coefficients for major and trace elements between olivine and melt. 35

Table 3.1 Classification of normal modes (81) of olivine for Pbnm. The three acoustic modes are excluded. 64

Table 3.2 Calculated unit-cell parameters for forsterite under temperature (in the unit of K) and pressure (in the unit of GPa). 71

Table 3.3 Bulk modulus calculated in this study and the literature. Fo = Mg_2SiO_4. Fa = Fe_2SiO_4. Compo. = composition. 73

Table 3.4 Thermal expansion coefficient equation from this study and the literature. The α_0, α_1, and α_2 are coefficients of the equation $\alpha = a_0 + a_1 \cdot T + a_2/T^2$. 75

Table 3.5 IR vibrational frequencies compared with the literature and their mode assignment... 81

Table 3.6 Raman vibrational frequencies compared with the literature and their mode assignment.. 82

Table 3.7 Cell parameters and energetics calculation of olivine. All calculations started from the same structure with cell parameters of 4.749, 10.1985, and 5.9792 Å from Bostroem (1987) for forsterite. The ΔME is for per formula unit mole, not the unit cell mole. 91

Table 3.8 Cell parameters for Fo, $Fo_{50}Fa_{50}$, and Fa in natural or synthetic olivine grains. 91

Table 4.1 The electronic energy ΔEL, enthalpy ΔH, and Gibbs free energy ΔG (all in kJ/mol) for all processes 117

Table 4.2 Bader charge (char) and spin (S, #n of unpaired spins) distribution for each species. 118

Table 4.3 Electron transfer between the M-aqua, quinone, and mackinawite cluster. 129

Table 4.4 Thermodynamic data from the literature for dissolved Fe species. 132

Table 4.5 Pourbaix diagram construction for Fe in solution from literature thermodynamic data in Table 4.4. 132

Table 4.6 Pourbaix diagram construction for Fe adsorbed on a mackinawite cluster. The unit for Gibbs free energy: kJ/mol. The unit for potentials: V. 133

Table B0.1 Adsorption IR vibrational frequencies at different temperature and pressure by CRYSTAL17. 159

Table B0.2. Raman vibrational frequencies at different temperature and pressure by CRYSTAL17. For some low frequency data (Ag), it is replaced by — because of inaccurate data. 160

Table C0.1 The number of configurations for each solid solution composition in the olivine unit cell. Symmetry is considered. For each composition, the multiplicity may be more than 1. The total multiplicity of all configurations gives 2^8=256. 164

Table C0.2 The Gibbs free energy of mixing for each configuration at 273 K. X_{Fa}: the mole fraction of fayalite in olivine. It has nine possible values: 0, 0.125, 0.25, 0.375, 0.5, 0.625, 0.75, 0.875, and 1. XFeM1: mole fraction of Fe in M1 site. It has five possible values: 0, 0.25, 0.5, 0.75, and 1. $\mathrm{XMgM1} + \mathrm{XFeM1} = 1$. XFeM2: mole fraction of Fe in M2 site. It has five possible values: 0, 0.25, 0.5, 0.75, and 1. $\mathrm{XMgM2} + \mathrm{XFeM2} = 1$. 168

Table C0.3 The weighted Gibbs free energy of mixing with X_{Fo} and X_{Fa} at various temperatures, including both vibrational and configurational parts. X_{Fo}: the mole fraction of forsterite in the forsterite-fayalite solid solution. . f.u.: formula unit. The energy calculated for a unit cell is divided by four to obtain the mixing energy for one formula unit. 171

Table C0.4 The weighted Gibbs free energy of mixing with X_{Mg}^{M1} and X_{Mg}^{M2} at various temperatures, including both vibrational and configurational parts. X_{Fo}: the mole fraction of forsterite in the forsterite-fayalite solid solution. $XMgM1$: the mole fraction of Mg in M1 site of the unit cell. The possible values are 0, 0.25, 0.5, 0.75, and 1 given four positions in M1. The same for M2. $XMgM2$: the mole fraction of Mg in M2 site of the unit cell. f.u.: formula unit. The energy calculated for a unit cell is divided by four to obtain the mixing energy for one formula unit. 171

Table D0.1 Gaussian calculation results for the mackinawite cluster. E: the calculated total energy. E_rela: the total energy relative to FM. Low spin: all eight Fe atoms have no unpaired electrons; AFM: four Fe atoms spin up and the rest four Fe atoms spin down to a total spin of 0. S=16: six Fe atoms spin up and two Fe atoms spin down. FM: all 8 Fe atoms spin up with a total spin of 32. The atom number position can be found in Figure D0.1. 176

Table D0.2 Crystal17 computational results for the spin of mackinawite cluster. The atom number position can be found in Figure D0.1. 176

Table D0.3 CASTEP computational results for the spin of mackinawite cluster. 177

LIST OF FIGURES

Figure 1.1 Olivine and its trapped melt inclusion from lunar sample 12009. a is a natural crystalline melt inclusion, while b is a glassy melt inclusion after re-homogenization. 4

Figure 1.2a The MMX rover performing in site surface investigations on Phobos.. 6

Figure 1.3 Visualization of a vibrational mode of forsterite. It was computed at 15 gigapascal (GPa) and 0 kelvin (K). The mode is Raman active but not IR active. The frequency is at 890 cm^{-1} with the symmetry B1g. The arrows show the directions of atomic movements..... 11

Figure 2.1 Microscope images of olivine grains with homogenized melt inclusions in 12009. Images were taken under reflected light. The target melt inclusions are marked by red circles. 24

Figure 2.2 Correlations between partition coefficients of selected elements between olivine and melt in lunar basalts. Data are from this study. Error bars are at 1σ level. 32

Figure 2.3 Partition coefficient dependence on major element composition in the melt. 34

Figure 2.4 Partition coefficients between olivine and melt in lunar basalt from this study (colored symbols) compared with literature data at terrestrial conditions (gray vertical bars)..... 37

Figure 2.5 a. Correlation between $\ln D_{Li}$ and square root of Fa# in olivine. b. Comparison of calculated $\ln D_{Li}$ using Equation 2.1 (vertical axis) with experimental values (horizontal axis). 38

Figure 2.6 Fit of Cr partition coefficient data using Equation 2.2 with parameters given in Equations 2.3a-c. 41

Figure 2.7 Li concentration versus Yb concentration in terrestrial MORB and OIB and lunar basalts. Li and Yb have similar compatibility in terrestrial basalts (Salters and Stracke 2004). Lunar basalt data are from Mare Basalt Database (https://www3.nd.edu/~cneal/lunar-l/), MORB data are from the compilation by Gale et al. (2013) and OIB data are from GeoRoc. 44

Figure 2.8 Cr concentration versus MgO and Cr versus FeOt in lunar basalts and terrestrial MORB and OIB ($SiO_2 \leq 55$ wt%). Data sources are the same as in Figure 2.7. 46

Figure 2.9 Vanadium concentration versus MgO and FeO in lunar and terrestrial basalts. Data sources are the same as Figure 2.7. 47

Figure 2.10 Vanadium concentration versus Cr concentration in lunar and terrestrial basalts. Data sources are the same as Figure 2.7. 49

Figure 3.1 Character table for point group of D2h from http://symmetry.jacobs-university.de/.. 63

Figure 3.2 The vibrational motion of v_1, v_2, v_3, through v_4 for an isolated SiO_4 tetrahedron. From Figure 3 of Lam et al. (1990). 64

Figure 3.3 Lattice parameter changes (*a, b, c,* and volume V divided by their respective values at ambient conditions P ~ 0 GPa or T ~ 300 K) with pressure (left panel) and temperature (right) in this study compared with the literature..... 72

Figure 3.4a Bulk modulus at different pressures at 0 K. A linear fitting equation is shown. b. Isothermal and adiabatic bulk modulus at different temperatures. The second-order polynomial equation is shown. 74

Figure 3.5 Thermal expansion α and linear thermal expansion coefficient α_a, α_b, and α_c. 75

Figure 3.6a Bond lengths ratios (bond length at given *T* / bond length at 0 K) change with temperature for calculated structures in this study for forsterite; b. bond lengths ratios (bond length at given *P* / bond length at 0 GPa) with pressure..... 77

Figure 3.7 IR and Raman spectra (relative intensity versus wavenumber) at static conditions. .. 78

Figure 3.8 The first peak of the Raman doublet. Frequency 837.8 cm^{-1}. Symmetry Ag. 80

Figure 3.9 IR and Raman spectra under different pressures up to 15 GPa. 85

Figure 3.10 Linear frequency fitting with pressure. 86

Figure 3.11 IR and Raman frequencies shift with pressures.. 86

Figure 3.12 Linear frequency fitting with temperature..... 88

Figure 3.13 IR and Raman frequencies shift with temperature.. 88

Figure 3.14 IR and Raman spectra at simultaneous high temperatures and pressures. 89

Figure 3.15 IR and Raman vibrational frequencies for Fo-Fa solid solutions. 92

Figure 3.16 Vibrational spectra with different isotopes..... 93

Figure 3.17 Vibration frequencies ratio for each mode due to the isotope effect.. 94

Figure 3.18 Mode frequency shift percentages caused by differences in mass of the cations (total change = change due to Δmass vs Δcomposition). 95

Figure 4.1a The mackinawite cluster from the crystal structure is free from relaxation. b. Relaxed mackinawite cluster in the vacuum. Atoms are color-coded by element and labeled. ... 112

Figure 4.2 Dissolved Fe/Mn-aqua complexation with quinone species. 122

Figure 4.3 Geometry-optimized structure of $[Fe(OH)_3(H_2O)]^0$ adsorption on a mackinawite cluster using a monodentate model (a) and bidentate model (b). 125

Figure 4.4a-d. Fe(III) adsorption on mackinawite at different pH. e-g. Fe(II) adsorption on mackinawite at different pH..... 126

Figure 4.5a Adsorption of $[MnIII(OH)_3(H_2O)_3]^0$ on a mackinawite cluster. b. Adsorption of $[MnII(OH)_2(H_2O)_2]^0$ on a mackinawite cluster..... 127

Figure 4.6 Optimized quinone species with all three oxidation states adsorbed on the mackinawite cluster. 128

Figure 4.7 Optimized structures of co-adsorption. 130

Figure 4.8 Grey lines represent the Pourbaix diagram of Fe with all dissolved species. The green line illustrates the Pourbaix diagram when dissolved Fe species are adsorbed on a mackinawite cluster. It is constructed manually using data in Tables 4.5 and 4.6. 133

Figure 4.9 Speciation of Fe(III) in seawater (Millero et al., 1995; Millero, 1998)..... 135

Figure A.0.1 Calibration curves for LA-ICP-MS analyses with 65-μm spot size. 152

Figure A.0.2 Calibration curves for LA-ICP-MS analyses with 85-μm spot size. 153

Figure A.0.3 Calibration curves for LA-ICP-MS analyses of San Carlos olivine with spot size of 110 μm.. 154

Figure A.0.4 Comparison of measured concentrations in 8 reference materials 155

Figure A.0.5 SIMS calibration for transition elements for sample 12009. 156

Figure A.0.6 Comparison of measured concentration in 6 reference materials..... 157

Figure C0.1 The Gibbs free energy of mixing for each configuration with the mole fraction of Fe in M1/M2 site at 273 K. 169

Figure C0.2 The weighted Gibbs free energy of mixing with X_{Fa} for temperatures from 273 K to 1273 K..... 169

Figure C0.3 The weighted Gibbs free energy of mixing with X_{Mg}^{M1} and X_{Mg}^{M2} (3D plot) at temperature 273 K and 1273 K. 170

Figure D0.1 Structure of the mackinawite cluster 175

LIST OF APPENDICES

Appendix A Supplemental Figures for Chapter 2 149
Appendix B Supplemental Tables for Chapter 3 158
Appendix C Thermodynamics of Forsterite-Fayalite Solid Solution 161
C.1 Abstract 161
C.2 Introduction 161
C.3 Computational methods 163
C.4 Thermodynamics 165
C.5 Results 167
C.6 References 172
Appendix D Spin State of Iron in Mackinawite 174
D.1 Introduction 174
D.2 Spin configuration of mackinawite cluster Fe_8S_8 175
D.3 Conclusion 178
D.4 References 179

ABSTRACT

The research topics in this dissertation vary from high-temperature, high-pressure processes in planetary science to low-temperature environmental problems on the Earth's surface.

Chapters 2 and 3 focus on olivine, an important mineral not just in the Earth's interior but also on many planetary bodies. Its morphology, chemical composition, element distribution with another mineral/melt phase, and mineral properties provide valuable information about the magma's composition and physical conditions, cooling rates, and even the formation of the solar system. Chapter 2 systematically studies the element partitioning between host mineral olivine and its melt inclusions in lunar basalts. Results show that the partition coefficient of V (D_V) is significantly higher, and D_{Cr} is lower in lunar basalts than in terrestrial basalts. The partitioning difference can better explain the element behavior in the two bodies. The results also show that the V/Cr ratio is constant in lunar basalts, which is essential for constraining concentrations of Cr (slightly volatile and siderophile) and V (slightly siderophile) in the bulk silicates of the Moon.

Chapter 3 uses density functional theory (DFT) to simulate, for the first time, the vibrational properties of forsterite (Mg-end olivine) under high temperature and pressure simultaneously. Vibrational spectra (absorption infrared and Raman) are an essential tool for studying the mineral structure, composition, and thermodynamic properties that are sometimes challenging to obtain experimentally. This work aims to improve and enhance the IR and Raman databases in the entire P/T space to better understand the lattice dynamics of olivine at an atomic level. We show that lattice vibrational frequencies are just a function of lattice structures when

anharmonicity is insignificant. Using the Quasi-Harmonic Approximation (QHA), we obtain the cell parameters under different temperatures and pressure, and from these, the infrared and Raman spectra. Good agreement is achieved between calculations and experiments for forsterite's vibrational frequencies and thermodynamic properties. Results show that the vibrational frequencies change approximately linearly with temperature/pressure. The slope of each mode is different depending on if they are associated with external lattice modes or internal stretching and bending within the SiO_4 tetrahedra.

Computational simulation is also an excellent way to study the thermodynamics, kinetics, and reaction mechanism of geochemical reactions in aqueous solutions. Chapter 4 determines the thermodynamics and electronic interactions of redox reactions between the organic reductant hydroquinone and inorganic oxidants Fe(III)/Mn(III) and their (co-)adsorption on a mackinawite cluster (Fe_8S_8). Iron sulfides can be critical mineral catalysts for electron transfer. The results show that the complexation and adsorption processes are mostly thermodynamically favorable, and whether there is spontaneous electron transfer from the reduced organic molecule or the mackinawite cluster to the metal oxidant is pH-dependent. Using the Gibbs free energy data computed for each species, we calculate the potential reduction shift of Fe^{3+}/Fe^{2+} when adsorbed or complexed and derived the Eh-pH diagram. In short, the complexation and adsorption may induce remarkable changes in the reactivity of the metal and affect Fe and Mn cycling in various water bodies.

CHAPTER 1

Introduction

1.1 Olivine and planetary science

Geology is different from other sciences not only due to the enormous time scale but also because we do not always have direct access to direct samples or can witness the processes that happened millions/billions of years ago. We look for geological records, mostly in minerals and rocks, and other indirect evidence to understand the composition and processes. For example, the mineral olivine, found in many planetary bodies (Earth, Moon, Mars, Mercury, etc.) and often crystallized first in basaltic magma, holds information about the primary magna composition, sometimes even the formation and evolution processes of the solar system.

Geochemical composition is an important aspect we can work on to obtain information from minerals. Naturally occurring olivine minerals have the general formula of $(Mg,Fe)_2SiO_4$ with the major elements Mg and Fe, minor elements Ni, Co, Cr, and Mn, and a large variety of trace elements. The distribution of elements between two phases at equilibrium is usually a function of magma composition and physical conditions (temperature T, pressure P, and oxygen fugacity fO_2). Therefore, partition coefficients can be used to deduce formation conditions. For example, knowing the composition of olivine and partition coefficients between olivine and melt, we can calculate the magma composition when olivine crystallized. The Ni/Mg/Al composition in olivine or the olivine-clinopyroxene/spinel pair can tell us the temperature of the magma. Even

when processes happened fast and no equilibrium was reached, the metal partitioning in the two octahedral olivine sites (Redfern et al., 1996) and diffusivities of elements (Hart, 1984) can be used to constrain the cooling rate of the magma.

The element partitioning between olivine and melt has been studied extensively for terrestrial samples/conditions. Typical methods include analyzing phenocryst-matrix or mineral-melt inclusion pairs in natural samples, or synthesized mineral-melt in experiments. Each method has its own advantages and shortcomings. Although olivine exists mainly in Earth's upper mantle, it is not rare because volcanoes and xenoliths can bring it to the surface resulting in a sufficient number of natural samples for analysis. However, specimen availability is an issue for other planetary bodies. Extraterrestrial samples are rare and precious due to expensive sample-return missions. For instance, six Apollo missions brought back 842 pounds of lunar materials in total, with an average cost of around $50,800 per gram in 1973 dollars. Limited by lunar samples and measuring techniques, far less work has been conducted on Moon samples than on Earth ones.

Why do we have to make a great effort to study the Moon if there is already plenty of research done for Earth? Besides the curiosity to understand our celestial neighbor, the Moon can also help unravel processes that shaped the early Earth, where plenty of evidence on the formation was erased by plate tectonics and weathering processes. The Moon, on the other hand, has not changed much since its formation 4.53 billion years ago. It is generally believed and supported by piling evidence that the formation of the Earth and the Moon are closely connected. The most widely accepted theory is the giant-impact theory (Canup and Asphaug, 2001; Canup, 2004, 2012; Ćuk and Stewart, 2012). It proposes that the Moon formed during a collision between the proto-Earth and another Mars-sized planet by collecting the debris from this impact. However, no definite conclusion has been drawn yet about whether it is mainly from the proto-Earth, the impactor, or

both. It is safe to say that the Moon is a time capsule for the history of Earth and even of our solar system. Despite the fact that the two bodies share a lot of compositional similarities, they are different in some ways, such as the Moon is more reduced and has a higher concentration of Cr in its mantle. Those differences will result in different element partitioning and, thus, different compositions in minerals and rocks.

Most element partitioning for the Moon was examined in the 1900s. It was mainly analyzed using electron microprobes with an accuracy of 0.01%. Trace elements in natural olivine are typically way below the detection limit. To obtain their partition coefficients, aliquots of such trace elements had to be added to synthesize specimens with higher concentrations. With improved analytical techniques, concentrations below the prior detection limits can now be accurately obtained by other in-situ methods. For example, current laser ablation inductively coupled plasma mass spectrometry (LA-ICP-MS) can measure trace element concentrations to as low as μg/kg levels. Secondary ion mass spectrometry (SIMS) may have a significant matrix effect, but it has a higher lateral resolution (smaller beam size compared to LA-ICP-MS) (Pisonero et al., 2006). Small beam size and high accuracy are essential when analyzing small samples. These techniques were used in the sample analysis in Chapter 2.

In this context, **Chapter 2** focuses on a systematic study of element partitioning between olivine and melts on the Moon using the olivine host and its melt inclusions (Figure 1.1). The lunar basalt samples are from the Apollo missions. Melt inclusions in minerals are excellent representatives of the primitive magma if well preserved. They are particularly valuable in retaining volatiles such as H_2O, usually lost as magma degasses when ascending and erupting (Wallace et al., 2021). However, a series of processes may happen and modify both the olivine and melt inclusion compositions after trapping, such as post-entrapment crystallization (PEC) and

diffusive exchange between a melt inclusion and its host. Therefore, careful evaluation of such post-entrapment processes is necessary. Different methods have been developed for PEC: 1) for naturally quenched glassy melt inclusions with olivine crystallized along the host-inclusion phase boundary, corrections can be performed by adding back the crystallized olivine until equilibrium is reached (Danyushevsky et al., 2000; Kress and Ghiorso, 2004; Lloyd et al., 2013; Brahm et al., 2021); 2) heat re-homogenization of the melt inclusion to be glassy (Portnyagin et al., 2007; Jennings et al., 2017; Ni et al., 2019); 3) direct analysis by LA-ICP-MS without prior re-homogenization (Halter et al., 2002; Chang and Audétat, 2021). Here, we adopt the method of heat re-homogenization. Figure 1.1 shows a naturally crystallized melt and a re-homogenized melt inclusion by heating to the appropriate temperature and quenching quickly to form a glass. High accuracy is obtained for the partition coefficients of 26 elements by using LA-ICP-MS and SIMS for trace element measurement. The partition coefficients for lunar olivine melts are then compared with the data for terrestrial samples, and implications are made.

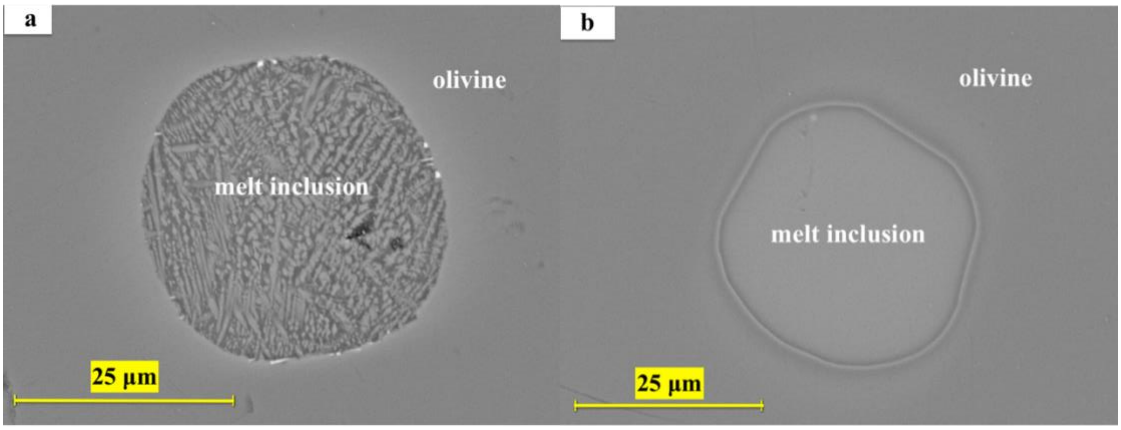

Figure 1.1 Olivine and its trapped melt inclusion from lunar sample 12009. **a** is a natural crystalline melt inclusion, while **b** is a glassy melt inclusion after re-homogenization.

In addition to the geochemical perspective, mineral-physics-related properties are crucial in many deep-Earth processes, such as propagation of seismic waves, phase transition, plate tectonics, and mantle convection. In order to better understand mineral behavior under increased

pressure and temperature conditions, **Chapter 3** works on the vibrational and thermodynamic properties of olivine. Vibrational spectroscopy is widely used to identify mineral phases' structure, composition, concentration, and interatomic forces. Thermodynamic properties are important for phase transition and melting.

This project was originally motivated by space exploration missions that are equipped with spectrometers for mineral identification/composition on planetary surfaces. For instance, the Martian Moons eXploration (MMX) mission by the Japan Aerospace Agency is planned to be launched in 2024 to the surface of Phobos and has a Raman spectrometer (Figure 1.2). The MMX rover will perform site investigations of the mineralogical composition by Raman spectroscopy (Cho et al., 2021). IR and Raman spectra are sensitive to mineral compositions and phases. To interpret the data returned from the space missions and for research on Earth samples, comprehensive spectral databases of common minerals for various factors, such as temperature, pressure, phase transition, isotope composition, and element substitution etc., are required.

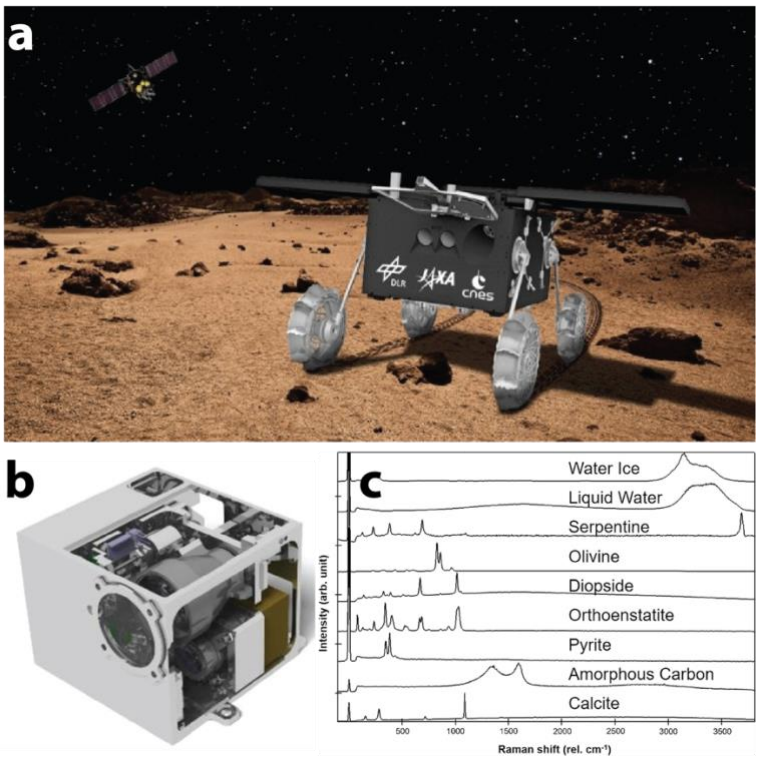

Figure 1.2a The MMX rover performing onsite surface investigations on Phobos. The instruments onboard the Rover are a Raman spectrometer (RAX), an infrared radiometer (miniRad), two forward-looking cameras for navigation and science purposes (NavCams), and two cameras observing the interactions of regolith and the rover wheels (WheelCams); **b.** Raman spectrometer (RAX); **c.** Raman spectra of different minerals.

There are three principal vibrational spectroscopy techniques, infrared, Raman, and neutron scattering. While the first two types of spectroscopy are common, neutron scattering is more rarely performed because it requires a neutron source which is usually a nuclear reactor. Laboratory infrared measurements can be absorption, reflection, and emission. Reflected and emitted IR radiation are usually used in remote sensing in planetary surface exploration, which is not the scope of this thesis. Both infrared (IR) absorption and Raman spectra are widely used for multiple purposes.

Vibrational frequencies of IR and Raman are strongly affected by temperature and pressure due to the change in interatomic distances. However, experimental studies of infrared absorption and Raman spectroscopy for olivine have largely been carried out either under ambient conditions (Paques-Ledent and Tarte, 1973; Iishi, 1978; Hofmeister, 1987, 1997; Kuebler et al., 2006; Dyar

et al., 2009), high pressure at room temperature (Besson et al., 1982; Chopelas, 1990; Durben et al., 1993), or high temperature at ambient pressure (Kolesov and Geiger, 2004). Systematic experimental investigations for simultaneous changes in pressure, temperature, and composition are rare due to the difficulty in the experimental setup. Computational methods then provide a complementary way for high T/P mineral properties. Chapter 3 examines the temperature and pressure effect systematically on vibrational frequencies and thermodynamic properties of forsterite. A close examination of the vibrational spectra with temperature and pressure may be indicative of phase transitions at certain temperatures, pressures, and compositions. Since we only studied olivine in this thesis, it may not be applied to olivine phase transitions but may be interesting for broader application of this methodology.

In addition to temperature and pressure, vibrational spectra are also affected by the mineral's composition, isotopes, cation distribution, and spin if transition elements are involved. In Chapter 3, we also briefly examined the isotope effect of Mg, forsterite (Fo) - fayalite (Fa) compositional effect, and cation ordering on the vibrational frequencies, as well as the thermodynamics of Fo-Fa solid solution. The thermodynamics of solid solution is presented in Appendix B.

1.2 Computational simulations of crystalline and non-crystalline systems

Computational simulations at the molecular level have revolutionized many fields of sciences in the past decades, such as chemistry, biology, material science, and geological and environmental sciences. One can model various systems in different forms, e.g., the gas phase, dissolved species in solution, or solids, such as periodic minerals or non-periodic nanoparticle clusters. Molecular simulations can be divided into two main types, classical mechanics and quantum mechanics. A comparison of the two types is listed in Table 1.1. Molecular modeling

concentrates on the minimization of energy of the system to find the most thermodynamically favorable structure. Classical mechanics is based on the calculation of forces using classical Newtonian physics F=ma and the evaluation of the time evolution of a system at the time scale of pico- and nanoseconds; these calculations are generally fast but highly dependent on typically empirically-derived forcefield potentials of bulk properties. For the derivation of electronic properties, as needed for simulating spin densities or electron transfer of redox reactions, a quantum mechanical approach is necessary. Quantum mechanics examines the behavior of electrons in molecules by using the Schrödinger equation. This approach is orders of magnitude more computationally expensive but not dependent on an empirical forcefield. In this thesis (Chapters 3 and 4), only quantum mechanics, specifically the density functional theory (DFT), one class of quantum-chemistry calculations, is used. Solving a many-body (three or more particles) Schrödinger equation is computationally impossible. Therefore, additional approximations have to be made that require additional computational parameters, such as density functional, pseudopotentials that simplify the role of core electrons, and basis sets from which the final molecular orbitals are composed. When high-level first-principles methods are used, the results are often comparable in quality with experiments, sometimes even providing information in regions of the pressure-temperature space inaccessible to experiments. Most first-principles studies of high-pressure and high-temperature properties of Earth-forming materials are based on the DFT.

Table 1.1 Comparison of the two types of molecular simulation: quantum mechanics and classical mechanics.

	Theory	Static calculation	High-temperature calculation
Quantum mechanics (done in this thesis)	Schrödinger equation $\hat{H}\Psi = E\Psi$	**Application:** geometry optimization, energy minimization, phonons, etc. **Pro:** not dependent on empirical classical force fields. Electronic (including charge transfer), magnetic (spin), orbital information obtainable. **Con:** computationally expensive, depend on the selection of parameters such as DFT functional, basis and pseudopotential set.	Methods: phonon calculations to approximate temperature effects, QHA with DFT, molecular dynamics with DFT (extremely expensive even for small unit cells)
Classical mechanics	Newtonian physics F=ma	**Application:** geometry optimizations, energy minimizations , phonons (forcefields not accurate), etc. **Pro:** fast **Con:** dependent on forcefields	accuracy of force fields may be insufficient

1.2.1 Applications of DFT on vibrational properties under high *T*/*P* conditions

A quantum system is constantly moving with translation, rotation, and vibration. The vibration concept in quantum mechanics is important because many properties are controlled by the lowest Gibbs free energy, which has a part contributed by vibration. The simplest vibration model is a diatomic molecule considered a harmonic oscillator whose wave profile is a sinusoidal function. Hooke's law gives the force $F = -k\Delta r$ where k is the force constant and Δr the displacement of the atoms. The potential energy function for the harmonic oscillator is $1/2\ k\ (\Delta r)^2$. The frequency can be easily calculated as $\nu = \frac{1}{2\pi}\sqrt{k/\mu}$, with μ being the reduced mass. The concept can be extended to polyatomic molecules.

The computational simulation of vibrational spectra has some advantages over experimental methods. The changes in infrared and Raman spectra frequencies of olivine are a combined effect of temperature, pressure, chemical composition (isotope and element), spin status, cation ordering, etc. Separating the factors in studying these effects is difficult. In addition, most experimental data published have been performed under ambient conditions due to the difficulty in setting up simultaneous temperature and pressure. DFT calculations can model high *T*/*P*

conditions that are beyond experiments. It is also much easier to model the isotope effect, solid solution, and spin status than synthesize a comprehensive series of olivine crystals. Furthermore, simulations allow us to understand the macro-properties at the atom level. Using simulations, we can visualize each normal mode (SiO_4 stretching, bending and rotation, Mg1-O and Mg2-O translation and rotation) (Figure 1.3), making it easier to delineate how different the variables affect the vibrational modes the way they do.

The vibration of polyatomic molecules can be considered harmonic at 0 K, although the true interatomic potentials are anharmonic. For solids at not too high a temperature, it is often accurate enough to use the quasi-harmonic approximation (QHA). QHA is similar to a harmonic approach but considers the influence of temperature. This quasi-harmonic potential usually provides an accurate description of the dynamic properties of the system at low to moderate temperatures. It gives easy access to the free energy of the system, which can be calculated analytically as a function of temperature. For highly anharmonic solids and liquids, one must use molecular dynamics (MD) or Monte Carlo techniques to sample the phase space. In the temperature range calculated, QHA is accurate enough (Baroni et al., 2010; Dovesi et al., 2018; Allen, 2020).

Chapter 3 uses DFT to model the IR and Raman vibrational frequencies of forsterite and some of its thermodynamic properties under high *T*/*P*. To simulate materials under pressure is not complicated; all it needs to do is change the volume of the simulation cell. Compression of a mineral has the effect of reducing interatomic distances. By contrast, high-temperature simulations are much more complex. Because free energy plays an essential role at high temperatures, and an accurate calculation of this requires expensive sampling of the phase space. There are two standard techniques for modeling systems at finite temperatures, which are molecular dynamics and Monte

Carlo methods. Both represent numerical integrations of the system properties to determine the ensemble average. Although both can be useful, they are only strictly valid for solids at elevated temperatures as they neglect the effect of vibrational quantum effects such as the zero point energy. QHA simulates the properties of materials as a function of temperature by minimizing the free energy instead of the internal energy. The main restriction is that it relies on the validity of the quasi-harmonic approximation.

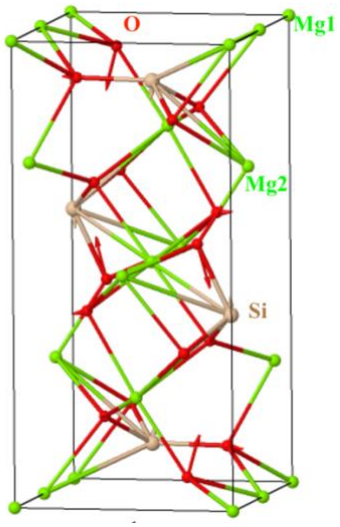

Figure 1.3 Visualization of a vibrational mode of forsterite. It was computed at 15 gigapascals (GPa) and 0 kelvin (K). The mode is Raman active but not IR active. The frequency is at 890 cm^{-1} with the symmetry B1g. The arrows show the directions of atomic movements.

1.2.2 Applications of DFT to molecular chemical reactions

In addition to the application of computations on the properties of minerals and melts in the Earth's interior, the quantum-mechanical approach can also be applied to understand low-temperature processes happening at the Earth's surface, such as mineral solubility, (ad-)sorption, and the thermodynamics and kinetics of geochemical reactions.

The complexation and redox reaction between dissolved metal and natural organic matter are common in natural water solutions. They play an essential role in the reactivities of metals and their cycling. For example, the dissolved Fe binding to organic molecules is the dominant reason

that dissolved Fe concentration in the ocean is higher than its thermodynamic solubility limit. Mn^{3+} is thermodynamically unstable in solution and undergoes disproportionation to form Mn^{2+} and MnO_2. However, it is found abundant (up to 90%) in sediment porewater of the total dissolved Mn (Madison et al., 2013) due to the complexation with organic matters.

In light of the above, **Chapter 4** uses the computational method to simulate the complexation and redox reactions between dissolved Fe and Mn with small organic molecules. Here, we choose hydroquinone/semiquinone/quinone. Quinones at different protonation/redox states are ubiquitous in solution, and they are involved in many biological processes, such as photosynthesis and electron transfer between proteins in membranes. Quinone moieties are also important redox-active constituents of natural organic matter. We use different Fe and Mn species representing various pH conditions.

Sorption to mineral surfaces can affect the thermodynamics and kinetics of reactions. Pyrite (FeS_2) has been considered a redox mediators in many processes, such as in hydrogenation of nitroaromatics (Ma et al., 2016), actinyl immobilization (Sundararajan et al., 2011), oxidation of As (III) (Wiertz et al., 2006). Another iron sulfide mineral, mackinawite (FeS), however, has received much less attention than it should. Mackinawite is widespread in anoxic environmental systems such as deep ocean vents, freshwater, and anoxic ocean and sediments. FeS can catalyze electron transfer in a wide variety of biological processes. Metal sulfide clusters are also ubiquitous (Luther, 2005). Mackinawite may be more important in redox cycling than pyrite but is underestimated because of its long-term metastability against pyrite and its typically small grain size, making it rare to appear in public mineral collections. We use a mackinawite cluster to test if co-adsorption makes the electron transfer more favorable between metal oxidant and organic reductant. Clusters reflect better the character of suspended nanoparticulates and their edge and

corner sites. For computations, clusters have the advantages of being small, allowing the use of charged particles, and it is easier to calculate how an adsorbed spin-carrying species such as Fe(III)/Fe(II) or Mn(III)/Mn(II) induces a spin on the mackinawite cluster or even the co-adsorbate HQ species.

In Chapter 4, we first worked on the complexation and oxidation process of hydroquinone by aqueous metal oxidants in the absence of the mackinawite cluster, then studied the adsorption and redox processes of quinones and metal ions on mackinawite cluster to test the catalytic role of mackinawite nanoparticles. The acquired thermodynamic data for each species/equation are then used to derive the standard reduction potential of Fe(III)/Fe(II) adsorbing on the mackinawite cluster and an Eh-pH diagram of Fe when adsorbed to the mackinawite cluster.

1.3 References

Allen P. B. (2020) Theory of thermal expansion: Quasi-harmonic approximation and corrections from quasi-particle renormalization. *Mod. Phys. Lett. B* **34**, 2050025.

Baroni S., Giannozzi P. and Isaev E. (2010) Density-functional perturbation theory for quasi-harmonic calculations. *Reviews in Mineralogy and Geochemistry* **71**, 39–57.

Besson J. M., Pinceaux J. P., Anastopoulos C. and Velde B. (1982) Raman spectra of olivine up to 65 kilobars. *Journal of Geophysical Research: Solid Earth* **87**, 10773–10775.

Brahm R., Zellmer G. F., Kuritani T., Coulthard D., Nakagawa M., Sakamoto N., Yurimoto H. and Sato E. (2021) MushPEC: Correcting post-entrapment processes affecting melt inclusions hosted in olivine antecrysts. *Frontiers in Earth Science* **8**.

Chang J. and Audétat A. (2021) LA-ICP-MS analysis of crystallized melt inclusions in olivine, plagioclase, apatite and pyroxene: Quantification strategies and effects of post-entrapment modifications. *Journal of Petrology* **62**.

Cho Y., Böttger U., Rull F., Hübers H.-W., Belenguer T., Börner A., Buder M., Bunduki Y., Dietz E., Hagelschuer T., Kameda S., Kopp E., Lieder M., Lopez-Reyes G., Moral Inza A. G., Mori S., Ogura J. A., Paproth C., Perez Canora C., Pertenais M., Peter G., Prieto-Ballesteros O., Rockstein S., Rodd-Routley S., Rodriguez Perez P., Ryan C., Santamaria P., Säuberlich T., Schrandt F., Schröder S., Stangarone C., Ulamec S., Usui T., Weber I., Westerdorff K. and Yumoto K. (2021) In situ science on Phobos with the Raman

spectrometer for MMX (RAX): preliminary design and feasibility of Raman measurements. *Earth, Planets and Space* **73**, 232.

Chopelas A. (1990) Thermal properties of forsterite at mantle pressures derived from vibrational spectroscopy. *Phys Chem Minerals* **17**, 149–156.

Canup R. M. (2004) Dynamics of lunar formation. *Annual Review of Astronomy and Astrophysics* **42**, 441–475.

Canup R. M. (2012) Forming a moon with an Earth-like composition via a giant impact. *Science* **338**, 1052–1055.

Canup R. M. and Asphaug E. (2001) Origin of the Moon in a giant impact near the end of the Earth's formation. *Nature* **412**, 708–712.

Ćuk M. and Stewart S. T. (2012) Making the Moon from a fast-spinning Earth: A giant impact followed by resonant despinning. *Science* **338**, 1047–1052.

Danyushevsky L. V., Della-Pasqua F. N. and Sokolov S. (2000) Re-equilibration of melt inclusions trapped by magnesian olivine phenocrysts from subduction-related magmas: petrological implications. *Contrib Mineral Petrol* **138**, 68–83.

Dovesi R., Erba A., Orlando R., Zicovich-Wilson C. M., Civalleri B., Maschio L., Rérat M., Casassa S., Baima J., Salustro S. and Kirtman B. (2018) Quantum-mechanical condensed matter simulations with CRYSTAL. *WIREs Computational Molecular Science* **8**, e1360.

Durben D. J., McMillan P. F. and Wolf G. H. (1993) Raman study of the high-pressure behavior of forsterite (Mg2SiO4) crystal and glass. *American Mineralogist* **78**, 1143–1148.

Dyar M. D., Sklute E. C., Menzies O. N., Bland P. A., Lindsley D., Glotch T., Lane M. D., Schaefer M. W., Wopenka B., Klima R., Bishop J. L., Hiroi T., Pieters C. and Sunshine J. (2009) Spectroscopic characteristics of synthetic olivine: An integrated multi-wavelength and multi-technique approach. *American Mineralogist* **94**, 883–898.

Halter W. E., Pettke T., Heinrich C. A. and Rothen-Rutishauser B. (2002) Major to trace element analysis of melt inclusions by laser-ablation ICP-MS: methods of quantification. *Chemical Geology* **183**, 63–86.

Hart S. R. (1984) He diffusion in olivine. *Earth and Planetary Science Letters* **70**, 297–302.

Hofmeister A. M. (1997) Infrared reflectance spectra of fayalite, and absorption datafrom assorted olivines, including pressure and isotope effects. *Phys Chem Min* **24**, 535–546.

Hofmeister A. M. (1987) Single-crystal absorption and reflection infrared spectroscopy of forsterite and fayalite. *Phys Chem Minerals* **14**, 499–513.

Iishi K. (1978) Lattice dynamics of forsterite. *American Mineralogist* **63**, 1198–1208.

Jennings E. S., Gibson S. A., Maclennan J. and Heinonen J. S. (2017) Deep mixing of mantle melts beneath continental flood basalt provinces: Constraints from olivine-hosted melt inclusions in primitive magmas. *Geochimica et Cosmochimica Acta* **196**, 36–57.

Kolesov B. A. and Geiger C. A. (2004) A Raman spectroscopic study of Fe–Mg olivines. *Phys Chem Minerals* **31**, 142–154.

Kress V. C. and Ghiorso M. S. (2004) Thermodynamic modeling of post-entrapment crystallization in igneous phases. *Journal of Volcanology and Geothermal Research* **137**, 247–260.

Kuebler K. E., Jolliff B. L., Wang A. and Haskin L. A. (2006) Extracting olivine (Fo–Fa) compositions from Raman spectral peak positions. *Geochimica et Cosmochimica Acta* **70**, 6201–6222.

Lloyd A. S., Plank T., Ruprecht P., Hauri E. H. and Rose W. (2013) Volatile loss from melt inclusions in pyroclasts of differing sizes. *Contrib Mineral Petrol* **165**, 129–153.

Luther G. W. (2005) Manganese(II) Oxidation and Mn(IV) Reduction in the environment—two one-electron transfer steps versus a single two-electron step. *Geomicrobiology Journal* **22**, 195–203.

Ma B., Tong X., Guo C., Guo Xiaoning, Guo Xiangyun and Keil F. J. (2016) Pyrite nanoparticles: an Earth-abundant mineral catalyst for activation of molecular hydrogen and hydrogenation of nitroaromatics. *RSC Adv.* **6**, 55220–55224.

Madison A. S., Tebo B. M., Mucci A., Sundby B. and George W. Luther I. I. I. (2013) Abundant porewater Mn(III) is a major component of the sedimentary redox system. *Science*.

Ni P., Zhang Y., Chen S. and Gagnon J. (2019) A melt inclusion study on volatile abundances in the lunar mantle. *Geochimica et Cosmochimica Acta* **249**, 17–41.

Paques-Ledent M. Th. and Tarte P. (1973) Vibrational studies of olivine-type compounds—I. The i.r. and Raman spectra of the isotopic species of Mg_2SiO_4. *Spectrochimica Acta Part A: Molecular Spectroscopy* **29**, 1007–1016.

Pisonero J., Kroslakova I., Guenther D. and Latkoczy C. (2006) Laser ablation inductively coupled plasma mass spectrometry for direct analysis of the spatial distribution of trace elements in metallurgical-grade silicon. *Anal. Bioanal. Chem.* **386**, 12–20.

Portnyagin M., Hoernle K., Plechov P., Mironov N. and Khubunaya S. (2007) Constraints on mantle melting and composition and nature of slab components in volcanic arcs from volatiles (H_2O, S, Cl, F) and trace elements in melt inclusions from the Kamchatka Arc. *Earth and Planetary Science Letters* **255**, 53–69.

Redfern S. a. T., Henderson C. M. B., Wood B. J., Harrison R. J. and Knight K. S. (1996) Determination of olivine cooling rates from metal-cation ordering. *Nature* **381**, 407–409.

Sundararajan M., S. Assary R., H. Hillier I. and J. Vaughan D. (2011) The mechanism of the reduction of $[AnO_2]^{2+}$ (An = U, Np, Pu) in aqueous solution, and by Fe(II) containing proteins and mineral surfaces, probed by DFT calculations. *Dalton Transactions* **40**, 11156–11163.

Wallace P. J., Plank T., Bodnar R. J., Gaetani G. A. and Shea T. (2021) Olivine-hosted melt inclusions: A microscopic perspective on a complex magmatic world. *Annual Review of Earth and Planetary Sciences* **49**, 465–494.

Wiertz J. V., Mateo M. and Escobar B. (2006) Mechanism of pyrite catalysis of As(III) oxidation in bioleaching solutions at 30 °C and 70 °C. *Hydrometallurgy* **83**, 35–39.

CHAPTER 2

Trace Element Partitioning Between Olivine and Melt in Lunar Basalts

Citation: Chen, S., Ni, P., Zhang Y., Gagnon, J., Trace element partitioning between olivine and melt in lunar basalts. American Mineralogist, **2021**.

Co-authors: Sha Chen, Peng Ni, Youxue Zhang, Joel Gagnon

2.1 Abstract

Mineral/melt partition coefficients have been widely used in providing insights into magmatic processes. Olivine is one of the most abundant and important minerals in the lunar mantle and mare basalts. Yet, no systematic olivine/melt partitioning data are available tailored to lunar conditions. We report trace element partition data between host mineral olivine and its melt inclusions in lunar basalts. Equilibrium is evaluated using the Fe-Mg exchange coefficient, leading to the choice of melt inclusion-host olivine pairs in lunar basalts 12040, 12009, 15016, 15647, and 74235. Partition coefficients of 22 elements (Li, Mg, Al, Ca, Ti, V, Cr, Mn, Fe, Co, Ni, Y, Zr, Nb, Gd, Tb, Dy, Ho, Er, Tm, Yb, and Lu) were measured. Except for Li, V, and Cr, other elements show no significant difference in olivine-melt partitioning compared to the data for terrestrial samples. The partition coefficient of Li between olivine and melt in some lunar basalts with low Mg# (Mg# < 0.75 in olivine, or < ~0.5 in the melt) is higher than in literature terrestrial samples, attributed to the dependence of D_{Li} on Mg# and the lack of literature D_{Li} data with low Mg#. The

partition coefficient of V in lunar basalts is measured to be 0.17 to 0.74, significantly higher than that in terrestrial basalts (0.003 to 0.21), which can be explained by the lower oxygen fugacity in lunar basalts. The significantly higher V partition coefficient in olivine can explain why V is less enriched in evolved lunar basalts than terrestrial basalts. The partition coefficient of Cr between olivine and basalt melt in the Moon is from 0.11 to 0.62, lower than those in terrestrial settings by a factor of approximately 2. This is surprising because previous authors showed that Cr partition coefficient is independent of fO_2. A quasi-thermodynamically-

based model is developed to roughly relate Cr partition coefficient to olivine and melt composition and fO_2. The lower Cr partition coefficient between olivine and basalt in the Moon can lead to more Cr enrichment in the lunar magma ocean, as well as more Cr enrichment in mantle-derived basalts in the Moon. Hence, even though Cr is a typical compatible element in terrestrial basalts, it is incompatible in primitive lunar basalts, with a similar degree of incompatibility as V, as evidenced by the roughly constant V/Cr ratio of 0.039 ± 0.011 in lunar basalts. The confirmation of constant V/Cr ratio is important for constraining concentrations of Cr (slightly volatile and siderophile) and V (slightly siderophile) in the bulk silicate Moon.

2.2 Introduction

Mineral/melt partition coefficients have been widely used to provide insights into magmatic processes. Olivine is one of the most abundant and important minerals in the lunar mantle and mare basalts. Olivine fractionation in the lunar magma ocean (LMO) (Wood et al. 1970; Longhi 1977; Solomon and Longhi 1977; Snyder et al. 1992; Elardo et al. 2011; Charlier et al. 2018) and during lunar basalt differentiation plays a significant role in the evolution of the magma. Olivine-melt partitioning also plays a role in controlling the composition of mantle-

derived basalts. Hence, quantifying olivine-melt partitioning is critical to understanding and modeling magma evolution of the LMO and lunar basalts.

Although numerous partitioning studies have been published for olivine and basaltic melt, they show significant variability for most elements due to the wide range of compositions, conditions, and methods involved. For example, the Ti partition coefficient between olivine and melt varies by more than two orders of magnitude, ranging from 0.0019 to 0.43 (Duke 1976; Rollinson 1993; McDade et al. 2003; Spandler and O'Neill 2010; Papike et al. 2013; Laubier et al. 2014; Burnham and O'Neill 2016; Leitzke et al. 2016). In addition, these studies often focus on terrestrial samples and conditions. Though lunar and terrestrial basalts share many similarities in terms of their chemical composition, they are distinct in several aspects. Compared to typical terrestrial basalts, lunar basalts have highly variable TiO_2, lower Al_2O_3 and alkalis, and often higher FeO and Cr_2O_3 concentrations. For example, terrestrial basalts rarely have TiO_2 over 5 wt% in the melt due to Fe-Ti oxide saturation at ~1100 °C (Toplis and Carroll 1995), whereas lunar basalts may contain up to 14 wt% TiO_2. Such compositional differences have been shown to affect the physical properties of the melt, metal solubility in silicate melts (Borisov et al. 2004), and partition coefficients of multiple elements (Xirouchakis et al. 2001; Dygert et al. 2013; Leitzke et al. 2016). Another important difference between lunar and terrestrial conditions that might affect elemental partitioning behavior is the oxygen fugacity (fO_2). The fO_2 has been estimated to be approximately IW - 1 (Sato et al. 1973; Wadhwa 2008) for lunar mantle and basalts and ~ QFM for the terrestrial upper mantle (O'Neill et al. 2018), representing a difference of over four orders of magnitude. Therefore, partitioning coefficients for multivalent elements, such as V, Cr, Fe and Ti, could be significantly different under lunar conditions. Previous work on olivine-melt partitioning of lunar basalts is not systematic, though many elements (Mg, Al, P, Ca, Ti, V, Cr,

Mn, Fe, Ga, Sr, Zr, Nb, Mo, Ru, Hf, Ta, W, Au, Th, U) have been investigated (e.g. Longhi et al. 1978; Seifert and Ringwood 1988; Xirouchakis et al. 2001; Papike et al. 2013; Fonseca et al. 2014; Sharp et al. 2015; Leitzke et al. 2016). Chen et al. (2015) and Ni et al. (2017, 2019) have accumulated a dataset of major element concentrations in melt inclusions and their olivine hosts as well as trace element data in melt inclusions in a number of lunar basalts. In this study, we supplement the data of Ni et al. (2019) with trace element measurements in olivine to estimate their partition coefficients. We also examine new olivine-melt inclusion pairs in lunar basalt 12009 for this partitioning study. Here we report partition coefficients of 22 major and trace elements between olivine and melt in lunar basalts and compare the obtained partition coefficients with published data in the literature for terrestrial conditions.

2.3 Samples and Methods

2.3.1 General considerations

The compositions of a melt inclusion (MI) and its host olivine can be used to estimate melt/mineral partition coefficients. A melt inclusion is a droplet of melt trapped during mineral crystallization. At the time of entrapment, a melt inclusion can be considered to be in equilibrium with the host mineral. If well preserved, coexisting host minerals and melt inclusions are a good way to estimate partition coefficients (e.g., Nikogosian and Sobolev 1997; Thomas et al. 2002; Zajacz and Halter 2007) and may have advantages over experimental methods. For example, host/melt inclusion reflects natural composition and conditions and can be better applied to geological processes. This method, however, also has its disadvantages. The compositions of melt inclusions can be affected during natural cooling, including post-entrapment crystallization (PEC) and diffusive exchange between the melt inclusion and the magma outside the host crystal. PEC

of the host mineral into the melt inclusion as well as crystallization of the melt inclusion during cooling is supposed to be reversed (corrected for) by laboratory homogenization, which was carried out for all melt inclusions in this study. Whether homogenization reverses PEC is evaluated by the equilibrium between a given melt inclusion and its host olivine. Diffusive exchange happens during cooling between melt inclusions and magma outside of the host crystal or between melt inclusion and olivine. The extent of exchange depends on the cooling rate, diffusivity and compatibility of the element, size of the olivine crystal and melt inclusion, and residence time of the crystal in the magma. Significant diffusive exchange between a melt inclusion and melt surrounding the host olivine will occur when the cooling rate is 1 to 2°C/year or lower (Gaetani and Watson 2000, 2002). All lunar samples investigated in this work cooled at >10°C/hour, much more rapidly than 1 to 2°C/year (see section 2.3.2). Furthermore, most of the samples reported here (except 12009) have been examined for volatile concentrations (Ni et al. 2019), which showed preservation of rapidly diffusing components, such as F, Cl, and S, except for H_2O. Such observations indicate negligible diffusive exchange for the elements examined here, which diffuse more slowly than F except for Li (e.g., Zhang et al. 2010).

All melt inclusions studied here were crystalline. Naturally glassy melt inclusions did not pass our selection criterion based on Fe/Mg exchange coefficient, as described below. Therefore, homogenization was needed. Homogenization experiments were conducted at 1 bar with temperature slightly higher than the liquidus of the corresponding lunar rock.

It is difficult to completely restore the MI composition to that at the time of entrapment (i.e., equilibrium). Therefore, a criterion is needed to assess whether there is approximate equilibrium between the melt inclusion and the host olivine. The Fe/Mg exchange coefficient K_D (= $(FeO/MgO)_{olivine}/(FeO/MgO)_{melt}$) between olivine and basaltic melt was used to evaluate

whether there is approximate olivine-melt equilibrium. Roeder and Emslie (1970) first showed that Fe^{2+}-Mg exchange coefficient between olivine and melt is independent of temperature and equals 0.30 ± 0.03 at equilibrium. This ratio has been widely used in equilibrium calculations ever since (e.g., Langmuir and Hanson 1980). Longhi et al. (1978), using lunar samples, reached a similar conclusion but noted decreasing K_D with increasing TiO_2. Xirouchakis et al. (2001) further studied the effect of Ti concentration in melt and found that K_D can vary from 0.36 to 0.22 with a TiO_2 increase from <1 wt % to 20 wt %. From the data summarized in Xirouchakis et al. (2001), an equation showing this dependence was fitted ($K_D = -0.006668 \cdot TiO_2 + 0.35$). We allowed a variation of ± 0.06 (~20 % relative) in K_D from the calculated value in choosing olivine-inclusion pairs thought to be in equilibrium. Using this criterion, we have chosen previously investigated lunar samples 12040, 15016, 15647, and 74235 (Ni et al., 2019) for trace element measurement in olivine. In addition, a new lunar sample that we are investigating (12009) also satisfies the criterion.

2.3.2 Sample description and preparation

Five lunar samples, 12009, 12040, 15016, 15647, and 74235, satisfying the criterion for equilibrium based on KD between the host olivine and melt inclusion, were analyzed for olivine-melt partitioning. Among the five lunar samples, four (all except 12009) were examined for volatiles in olivine-hosted melt inclusions by Ni et al. (2019). One sample (74235) is a high-Ti basalt, and the other four samples are low-Ti basalts. A brief description of each sample is presented here. Sample 12040 is a coarse-grained olivine basalt with ~ 2.6 % TiO_2 and accumulation of olivine was inferred for the sample. 15016 is an olivine-normative basalt with ~2.3 wt% TiO_2 and ~50 vol.% of vesicularity. Ca- or Fe-rich zonation in pyroxene indicates rapid

crystallization. 15647 is a relatively coarse-grained olivine basalt with ~2.4 wt% TiO_2. 74235 is a fine-grained high-Ti basalt (~12.3 wt% TiO_2) containing skeletal phenocrysts of olivine, pyroxene and ilmenite. 12009 is a rapidly cooled low-Ti (3.3 wt % TiO_2) olivine vitrophyre basalt with large vesicles. More detailed descriptions of these samples can be found in The Lunar Sample Compendium (https://curator.jsc.nasa.gov/lunar/lsc/) and Ni et al. (2019).

Cooling rates of 74235, 12009, and 12040 have been estimated and are all >10 °C/hour (Donaldson et al. 1975; Usselman et al. 1975; Walker et al. 1976). For 15016 and 15647, no cooling rate data are available. Based on the H_2O/Ce ratio versus cooling rate relation in Ni et al. (2019), they should have quenched faster than 12040, and hence at a cooling rate faster than 10 °C/hour. Hence, all lunar samples we studied cooled much more rapidly than 2°C/year, but 12040 cooled the slowest, and 15647 a close second.

The olivine-hosted melt inclusions in 12040, 15016, 15647, and 74235 were homogenized by Ni et al. (2019), and those in sample 12009 were homogenized in this study following the procedures in Chen et al. (2015) and Ni et al. (2017, 2019). The homogenization temperature was chosen to be slightly higher than the liquidus temperature of the host rock. An olivine grain from 12009 was placed in a graphite crucible under continuous high purity N_2 flow to maintain a reducing environment, heated to 1240–1250 ºC at one bar for 2 minutes, and quickly quenched by immersing the crucible in water. The fO_2 in the crucible was measured to be between IW-1.9 and IW-2.6 (Ni et al. 2017). The reducing condition prevented olivine oxidation, but did not establish a new fO_2 for the olivine-inclusion equilibrium due to the short duration of the experiments. More detailed description of the homogenization experiments may be found in Chen et al. (2015) and Ni et al. (2017, 2019). After homogenization, the olivine crystals were polished to reveal the enclosed melt inclusions (Figure 2.1). The diameter of each melt inclusion was measured and reported in

Table 2.2. Major and trace element concentrations in both melt inclusions and host mineral grains were analyzed.

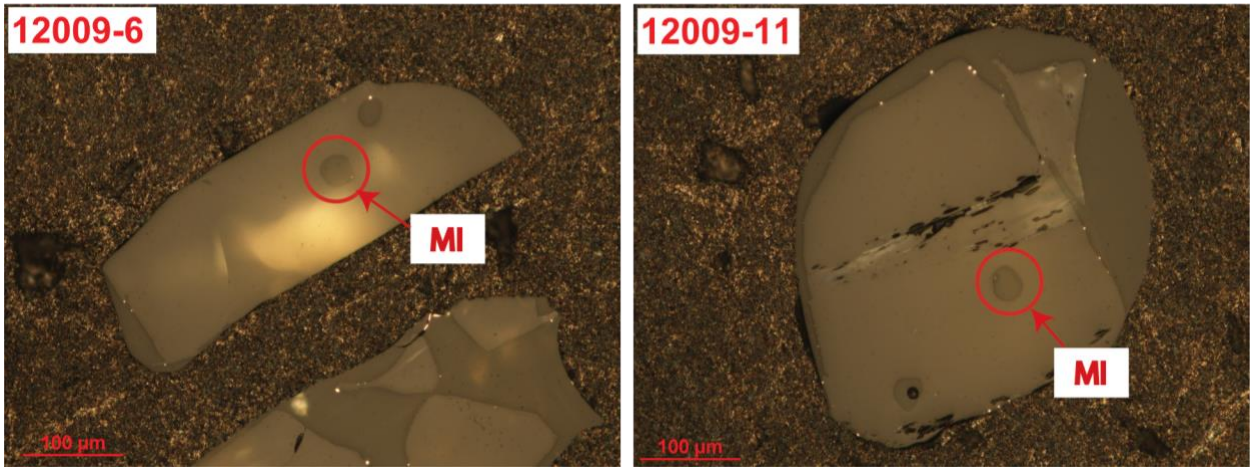

Figure 2.1 Microscope images of olivine grains with homogenized melt inclusions in 12009. Images were taken under reflected light. The target melt inclusions are marked by red circles.

2.3.3 Major and trace element concentration measurement

2.3.3.1 Major element analysis

Major element concentrations of melt inclusions and host olivine grains were analyzed using a CAMECA SX-100 electron microprobe (EMPA) at the University of Michigan. Analyses were carried out using a 15 kV, 10 nA and 5 µm defocused beam in wavelength-dispersive spectrometry (WDS) mode. At least five data points were measured on the host olivine at locations adjacent to each melt inclusion. Fewer data points were obtained for some melt inclusions due to the limitation of their small sizes. Data are reported in Table 2.1. We only report olivine-melt inclusion pairs that were considered to be approximately in equilibrium based on their Fe^{2+}-Mg K_D values.

Table 2.1 Major element concentrations of olivine and melt inclusions (MIs) measured by EMPA. The major element concentrations in melt inclusion for 74235-4, 12040-36, 12040-41, 15016-10, and 15647-6 are from Ni et al. (2019). Ol, MI, and WR represent the concentration in olivine crystal, melt inclusion and whole rock. Whole rock composition from The Lunar Sample Compendium is listed for comparison. Errors (1σ) are reported based on the standard deviation of multiple measurements.

		SiO_2	TiO_2	Al_2O_3	Cr_2O_3	FeO	MnO	MgO	CaO	Na_2O	K_2O	Total	Mg#	K_D
74235-4	Ol	38.6±0.19	0.14±0.04	0.06±0.04	0.24±0.05	25.3±0.10	0.29±0.01	35.6±0.30	0.28±0.01	--	--	100.5	71.5	0.21
	MI	38.04	12.45	8.18	--	22.16	0.31	6.53	9.95	0.32	0.06	--	34.4	--
	WR	38.6-39.4	12.2-12.4	8.61-9.21	0.42-0.51	18.6-19.3	0.27-0.28	8.35-8.67	10.7-10.9	0.37-0.4	0.07-0.08	--	--	--
12040-36	Ol	33.2±0.19	0.07±0.04	0.02±0.02	0.05±0.03	44.4±0.37	0.40±0.02	20.3±0.49	0.37±0.03	--	--	98.8	44.9	0.38
	MI	46.28	3.08	8.42	--	25.34	0.27	4.34	9.42	0.36	0.09	--	23.4	--
	WR	43.4-44.9	2.27-2.78	6.67-7.8	0.52-0.71	19.7-23	0.24-0.28	16.1-17.1	6.9-8.1	0.16-1.99	0.04-0.05	--	--	--
12040-41	Ol	35.6±0.47	0.06±0.03	0.02±0.01	0.11±0.05	36.7±0.34	0.35±0.02	27.7±0.36	0.32±0.02	--	--	100.8	57.4	0.39
	MI	46.49	3.68	10.6	--	20.33	0.23	5.94	11.1	0.46	0.10		34.2	--
	WR	43.4-44.9	2.27-2.78	6.67-7.8	0.52-0.71	19.7-23	0.24-0.28	16.1-17.1	6.9-8.1	0.16-1.99	0.04-0.05	--	--	--
12009-6	Ol	38.7±0.15	0.04±0.01	0.03±0.02	0.46±0.02	24.0±0.37	0.22±0.02	37.0±0.29	0.29±0.01	--	--	100.8	73.3	0.29
	MI	45.8±0.22	3.37±0.10	10.4±0.18	--	17.3±0.34	--	7.66±0.40	11.7±0.16	0.24±0.02	0.05±0.01	--	44.1	--
	WR	41-45.0	2.9-3.3	8.59-11	--	20-21.0	0.19-0.28	11.6-12.5	9.42-10	0.23-0.51	0.05-0.06	--	--	--
12009-11	Ol	38.3±0.09	0.03±0.03	0.04±0.02	0.46±0.04	23.7±0.06	0.24±0.01	36.9±0.14	0.28±0.01	--	--	100.0	73.5	0.27
	MI	47.4±0.48	3.46±0.20	10.3±0.36	0.65±0.05	17.4±0.43	0.24±0.02	7.20±0.57	11.5±0.16	0.27±0.02	0.06±0.004	98.5	42.5	--
	WR	41-45.0	2.9-3.3	8.59-11	--	20-21.0	0.19-0.28	11.6-12.5	9.42-10	0.23-0.51	0.05-0.06	--	--	--
15016-10	Ol	37.9±0.21	0.04±0.01	0.03±0.01	0.32±0.14	26.7±0.40	0.27±0.02	35.4±0.34	0.31±0.02	--	--	100.9	70.3	0.34
	MI	48.3	1.94	9.12	--	19.04	0.24	8.6	10.4	0.24	0.03	--	44.6	--
	WR	43.8-44.3	2.1-3	8.17-8.8	--	16.5-23.0	0.26-0.33	11-11.7	9.06-10.9	0.21-0.32	0.03-0.05	--	--	--
15647-6	Ol	34.3±0.43	0.07±0.01	0.01±0.01	0.11±0.04	44.0±0.98	0.43±0.03	20.6±0.92	0.41±0.04	--	--	100.0	45.5	0.29
	MI	42.12	3.24	6.71	--	32.82	0.35	4.53	8.16	0.24	0.08	--	19.7	--
	WR	44.4-46.2	2.35-3	7.86-9	--	22.2-23.9	0.26-0.29	10.0-10.5	8.8-9.67	0.22-0.33	0.04-0.047	--	--	--

2.3.3.2 Trace element concentrations in melt inclusions

Trace element concentrations in melt inclusions were analyzed using secondary ion mass spectrometry (SIMS) at the California Institute of Technology using a Cameca IMS 7f- GEO. Trace element measurements for sample 12009 were conducted in this study, while those for lunar samples 12040, 15016, 15647, and 74235 are from Ni et al. (2019). The analytical procedures are very similar and briefly described below.

Twenty-two trace elements (Li, Na, K, Sr, Y, Zr, Nb, Ba, La, Ce, Pr, Nd, Sm, Eu, Gd, Tb, Dy, Ho, Er, Tm, Yb, Lu) and five transition metal elements (V, Cr, Mn, Co, Ni) were analyzed in two separate sessions. For the analyses of the trace elements, a 10 to 13 nA O^- primary ion beam was used to generate secondary ion signals for measurement. Sensitivity factors were calculated using the internal standard of ^{30}Si based on reported concentrations in NIST glass standard SRM 610 (Pearce et al. 1997). The accuracy of the analyses was verified by measuring two additional NIST standards (NIST 612 and NIST 614) and two MPI-DING glass standards (GOR128-G and KL2-G). For the analyses of transition metal elements, an 11 to 17 nA O^- primary ion beam was used and a mass resolution power (MRP) of 5500 was applied to the mass spectrometer to separate interferences from the target masses. For Ni concentrations, two isotopes of Ni (^{60}Ni, ^{62}Ni) were analyzed simultaneously to assess whether mass interferences were present in our analyses. The results of $^{62}Ni/^{60}Ni$ in our analyses are consistent with their natural ratio, indicating negligible mass interferences. Calibration curves for the transition metal elements for 12009 can be found in Supplementary Figure A0.4.

2.3.3.3 Trace element concentrations in olivine

Trace element analyses for all olivine crystals reported in this study were carried out using a laser ablation inductively coupled plasma mass spectrometry (LA-ICP-MS) in the Element and

Heavy Isotope Analytical Laboratories at the University of Windsor. The instrumentation comprises a Photon Machines Analyte Excite 193 nm, short (sub 4 ns) pulse width Ar-F Excimer laser ablation system coupled with an Agilent 7900, fast scanning quadrupole ICP-MS. For each LA-ICP-MS analysis, 30 s of gas and instrument background were acquired with the laser off, followed by 40 s ablation signal with the laser on. The laser was operated at pulse energy of 120 mJ and repetition rate of 5 Hz, and 60 % output. Three spot sizes, 50 µm, 85 µm, and 110 µm, were applied depending on olivine crystal size.

Most trace elements are highly incompatible in olivine relative to the coexisting silicate melt, leading to their extremely low concentrations. The concentrations of Na, K, La, Ce, Pr, Nd, Sm, Eu, Nb, Mo, and Sn in olivine were found to be below detection limit. Nonetheless, twenty-two trace elements (using isotopes of ^{7}Li, ^{27}Al, ^{45}Sc, ^{49}Ti, ^{51}V, ^{52}Cr, ^{55}Mn, ^{59}Co, ^{60}Ni, ^{66}Zn, ^{89}Y, ^{90}Zr, ^{93}Nb, ^{118}Sn,^{157}Gd, ^{159}Tb, ^{163}Dy, ^{165}Ho, ^{166}Er, ^{169}Tm, ^{172}Yb and ^{175}Lu) were successfully measured and their concentrations with 1σ errors are reported in Table 2.2. When possible, two isotopes per element (^{6}Li and ^{7}Li, ^{47}Ti and ^{49}Ti, ^{52}Cr and ^{53}Cr, ^{60}Ni and ^{62}Ni, ^{66}Zn and ^{68}Zn, ^{90}Zr and ^{91}Zr, ^{95}Mo and ^{98}Mo, ^{116}Sn and ^{118}Sn) were measured to check for reproducibility and mass interferences. NIST standards 610, 612, 614, and 616 plus three MPI-DING standards (GOR128-G, GOR132-G, St-Hs-G) were used as external calibration standards. The NIST standards are soda lime silicate glasses doped with various concentration levels of trace elements. NIST 610, 612, 614 and 616 are nominally doped with approximately 500, 50, 1, and 0.01 ppm, respectively, of most trace elements. Since all the aforementioned standards contain more than 1 wt% Al, a SRM 1830 glass with a more comparable Al concentration (635 ppm, certified) to the olivine samples was used for LA-ICP-MS calibration. ^{29}Si was used as the internal calibration standard to correct for differences in the rate of ablation between the standards and olivine crystals. Inclusions were

avoided during LA-ICP-MS measurement both by positioning the laser spot away from visible inclusions, and by assessing each spectrum for evidence of compositional change in olivine. Calibration curves are shown in Supplementary Figures A0.1 and A0.2 for beam diameters of 65 μm and 85 μm, respectively.

Table 2.2 Trace element composition of olivine and MI with 1σ error. Concentration data and associated errors in melt inclusion for 74235,12040, 12040, 15016, and 15647 are from Ni et al. (2019).

	74235		12040		12040		12009		12009		15016		15647	
	Olivine ppm	MI ppm	Olivine ppm	MI ppm	Olivine ppm	Olivi ppm	Melt ppm	MI ppm	Olivine ppm	MI ppm	Olivine ppm	MI ppm	Olivine ppm	MI ppm
Li	4.28±0.31	7.7	7.97±0.54	5.1	8.91±0.61	2.37	2.7	--	2.69±0.14	--	2.37±0.13	2.7	7.19±0.36	6.2
Na	--	3667	--	3065	--	--	2092	--	--	--	--	2092	--	1996
Al	312±9	--	81.7±3.2	--	84.4±3.5	222±	--	--	254±4	--	222±4	--	83.6±2.0	--
K	--	614	--	635	--	--	209	--	--	--	--	209	--	580
Sc	14.5±1.2	--	13.0±1.1	--	11.8±1.0	8.95	--	--	10.8±0.7	--	8.95±0.57	--	12.3±0.7	--
Ti	809±46	--	329±20	--	321±20	145±	--	--	203±8	--	145±6	--	383±15	--
V	33.1±1.0	141	10.2±0.3	30	34.5±1.1	93.9	142	123±8	91.2±1.7	123±19	93.9±1.8	142	18.9±0.5	111
Cr	1318±74	5169	344±21	1735	753±45	2654	8835	4629±205	2851±113	4730±4820	2654±107	8835	460±21	4308
Mn	2220±56	3223	3159±80	2129	2676±75	2059	2860	2132±72	1975±34	2251±173	2059±37	2860	3977±85	3891
Co	52.4±2.5	23	87.5±3.9	22	105±5	113±	28	70.3±8.1	115±4	64.6±17.0	113±4	28	113±4	129
Ni	5.71±0.21	0.3	27.2±0.9	2.1	78.3±2.5	288±	--	48.4±7.0	243±5	39.3±15.7	288±6	--	44.0±1.1	18
Zn	3.47±0.45	--	3.13±0.41	--	2.81±0.37	2.60	--	--	2.49±0.23	--	2.60±0.24	--	3.38±0.31	--
Sr	--	177	--	128	--	--	93	--	--	--	--	93	--	105
Y	0.53±0.02	102	10.5±0.3	501	1.92±0.08	0.18	29.3	--	0.278±0.009	--	0.18±0.01	29.3	0.89±0.03	43.6
Zr	0.13±0.006	254	0.17±0.01	161	0.080±0.004	0.04	101	--	0.0766±0.0027	--	0.049±0.002	101	0.085±0.0034	183
Nb	0.0039±0.0004	28.1	--	9.9	0.0026±0.0003	0.00	7.2	--	0.0046±0.0003	--	0.005±0.0004	7.2	0.0040±0.0004	10.9
Sn	0.182±0.022		0.13±0.02	--	0.16±0.02	0.09		--	0.104±0.0094	--	0.096±0.009		0.11±0.010	
Ba	--	65	--	85	--	--	42	--	--	--	--	42	--	80
La	--	6.5	--	9.4	--	--	5.3	--	--	--	--	5.3	--	9.8
Ce	--	25.9	--	28.6	--	--	15.7	--	--	--	--	15.7	--	25.7
Pr	--	4.4	--	5.5	--	--	2.0	--	--	--	--	2.0	--	3.8
Nd	--	23.6	--	40.1	--	--	12.2	--	--	--	--	12.2	--	19.7
Sm	--	8.4	--	27.3	--	--	4.1	--	--	--	--	4.1	--	6.5
Eu	--	3.0	--	1.9	--	--	0.7	--	--	--	--	0.7	--	0.6
Gd	0.015±0.0011	12.0	0.29±0.016	53.9	0.044±0.003	0.00	4.8	--	0.0078±0.00045	--	0.006±0.0004	4.8	0.044±0.003	7.6
Tb	0.0064±0.0003	2.7	0.12±0.005	12.9	0.023±0.001	0.00	0.9	--	0.0028±0.00012	--	0.00097±0.00006	0.9	0.011±0.0005	1.4
Dy	0.065±0.0035	19.6	1.28±0.054	95.6	0.223±0.011	0.02	6.4	--	0.033±0.0013	--	0.020±0.0009	6.4	0.105±0.0044	8.4
Ho	0.020±0.001	3.9	0.38±0.014	20.0	0.074±0.003	0.00	1.2	--	0.0097±0.00035	--	0.0057±0.00023	1.2	0.036±0.0013	1.6
Er	0.079±0.004	10.8	1.46±0.06	52.0	0.260±0.013	0.03	3.4	--	0.049±0.0019	--	0.032±0.0013	3.4	0.142±0.0056	4.8
Tm	0.021±0.0009	1.8	0.29±0.01	5.8	0.046±0.002	0.00	0.4	--	0.010±0.0003	--	0.0077±0.0003	0.4	0.025±0.0009	0.60
Yb	0.16±0.0076	11.2	2.18±0.082	36.8	0.404±0.018	0.05	2.8	--	0.095±0.003	--	0.055±0.0020	2.8	0.220±0.0079	3.7
Lu	0.038±0.002	1.4	0.36±0.012	4.8	0.075±0.003	0.00	0.6	--	0.020±0.0006	--	0.0086±0.0003	0.6	0.047±0.0015	0.44

2.4 Results

2.4.1 Comparison of melt inclusion and whole rock composition

Melt inclusions in olivine crystals studied here have a range of SiO_2 concentrations from 38.0 wt% to 48.3 wt%, and the Mg# range of the host olivine is from 44.1 to 73.9. Three samples (15016, 74235, and 12009) have olivine Mg# higher than 70, while samples 12040 and 15647 with slower cooling rates have low olivine Mg# ranging from 44.9 to 57.4.

Major oxide concentrations in melt inclusions for 74235, 15016 and 12009 are generally consistent with the whole rock. On the other hand, melt inclusions in 12040 are considerably different in composition from the whole rock, especially in MgO (4 to 6 wt% in MIs vs. ~16 wt% in whole rock, The Lunar Sample Compendium), which is consistent with the accumulation of olivine in 12040 whole rock (e.g., Newton et al. 1971). The high FeO in olivine (36.7 wt% and 44.4 wt%) indicates late crystallization or re-equilibration during the relatively slow cooling process (The Lunar Sample Compendium).

Another slowly cooled basalt, 15647, also contains high FeO (43.9 wt%) in olivine. The melt inclusion investigated here is enriched in FeO by ~10 wt%, depleted in MgO by ~5 wt%, and SiO_2 by ~3 wt% compared with the whole rock. The high FeO in both olivine host and melt inclusion from sample 15647 indicates a more evolved composition than the whole rock.

2.4.2 Partition coefficients between olivine and melt

Partition coefficients and associated errors (1σ) between the two phases are reported in Table 2.3. Errors are calculated using the equation: $\sigma_D = D * \sqrt{(\frac{\sigma_X}{X})^2 + (\frac{\sigma_Y}{Y})^2}$ (X and Y are the concentrations in the mineral and melt inclusion, respectively). In general, Ni, Mg, and Co behave compatibly in olivine. Iron, manganese, and lithium exhibit close to neutral compatibility.

Vanadium and chromium are moderately incompatible in olivine, while most other elements (Al, Ca, Ti, Y, Zr, Nb, and REEs) are highly incompatible.

Among all the elements investigated, Ni partition coefficient varies the most by 1.5 orders of magnitude (2.4 ~ 72.5). The large variation might be due to the high compatibility of Ni in olivine, metal (e.g., Sharp et al. 2015), and sulfide (e.g., Li and Audetat 2012), indicating that a small amount of addition or removal of these phases could significantly modify Ni concentration in the melt and hence the obtained D_{Ni} value. Therefore, these apparent D_{Ni} values are listed in Table 2.3 but not further discussed. The partition coefficients for other elements may vary by up to a factor of 5, which may be due to data scatter and/or compositional dependence.

To examine whether the variation of partition coefficients is mainly due to data scatter such as measurement uncertainty or disequilibrium, partition coefficients of different elements are plotted versus each other, and good correlations are found between element pairs such as REE-Y, Y-Ti, Ca-Ti, Cr-Ca, and Li-Al (Figure 2.2). As a dominant major element in olivine, Mg partition coefficient has a narrow range (4.12 to 5.45). Hence, no obvious correlation was found between DMg and the partition coefficients of any other element. There is excellent correlation among REE and Y partition coefficients (Figure 2.2a). Furthermore, the partition coefficients of REE are positively correlated with D_{Ca} and D_{Ti} (Figures 2.2b and 2.2c), and the partition coefficients of V and Cr are negatively correlated with D_{Ca} and D_{Ti} (Figures 2.2d and 2.2e). The partition coefficient of Al is negatively related to that of Li (Figure 2.2f).

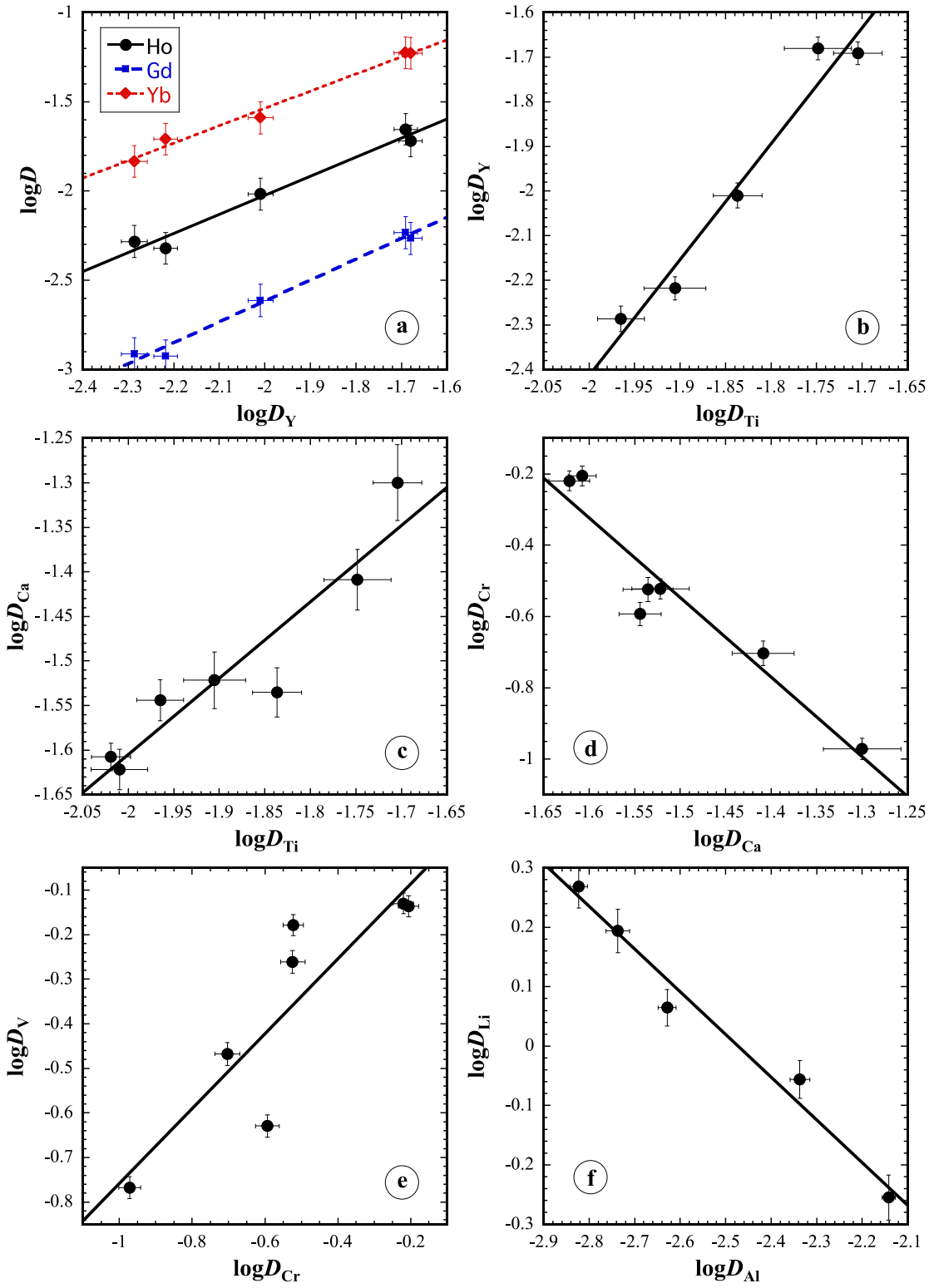

Figure 2.2 Correlations between partition coefficients of selected elements between olivine and melt in lunar basalts. Data are from this study. Error bars are at 1σ level.

The correlations in Figure 2.2 indicate that, at least for the elements shown, the variation of the partition coefficients is not due to measurement uncertainty or disequilibrium. Specifically, the good correlation between D_{Li} and D_{Al} indicates that D_{Li} is not significantly affected by disequilibrium due to post-entrapment diffusion. The most likely cause for the variation is compositional dependence. Hence, we examined the dependence of the partition coefficients on melt composition by plotting D against various oxide concentrations in the melt. The dependence of partition coefficients on TiO_2 in the melt is not obvious, partially because there is only one high-Ti basalt in our study. Some consistent trends between the partition coefficients and concentrations of oxides are observed and shown in Figure 2.3. For example, D_{Ca} and D_{Ti} increase with FeO content of the melt (Figures 2.3a and 2.3b), whereas D_V and D_{Cr} decrease with FeO content of the melt (Figures 2.3c and 2.3d). Because oxide concentrations in the limited number of melt inclusions investigated in this work are not independent of each other, it is not possible to assess whether or not the partition coefficients depend only on FeO. For example, D_{Ca} appears to also decrease with CaO or Al_2O_3 concentration in the melt (Figures 2.3e and 2.3f), which might be an artifact due to the correlation between CaO and FeO and between Al_2O_3 and FeO in the melt.

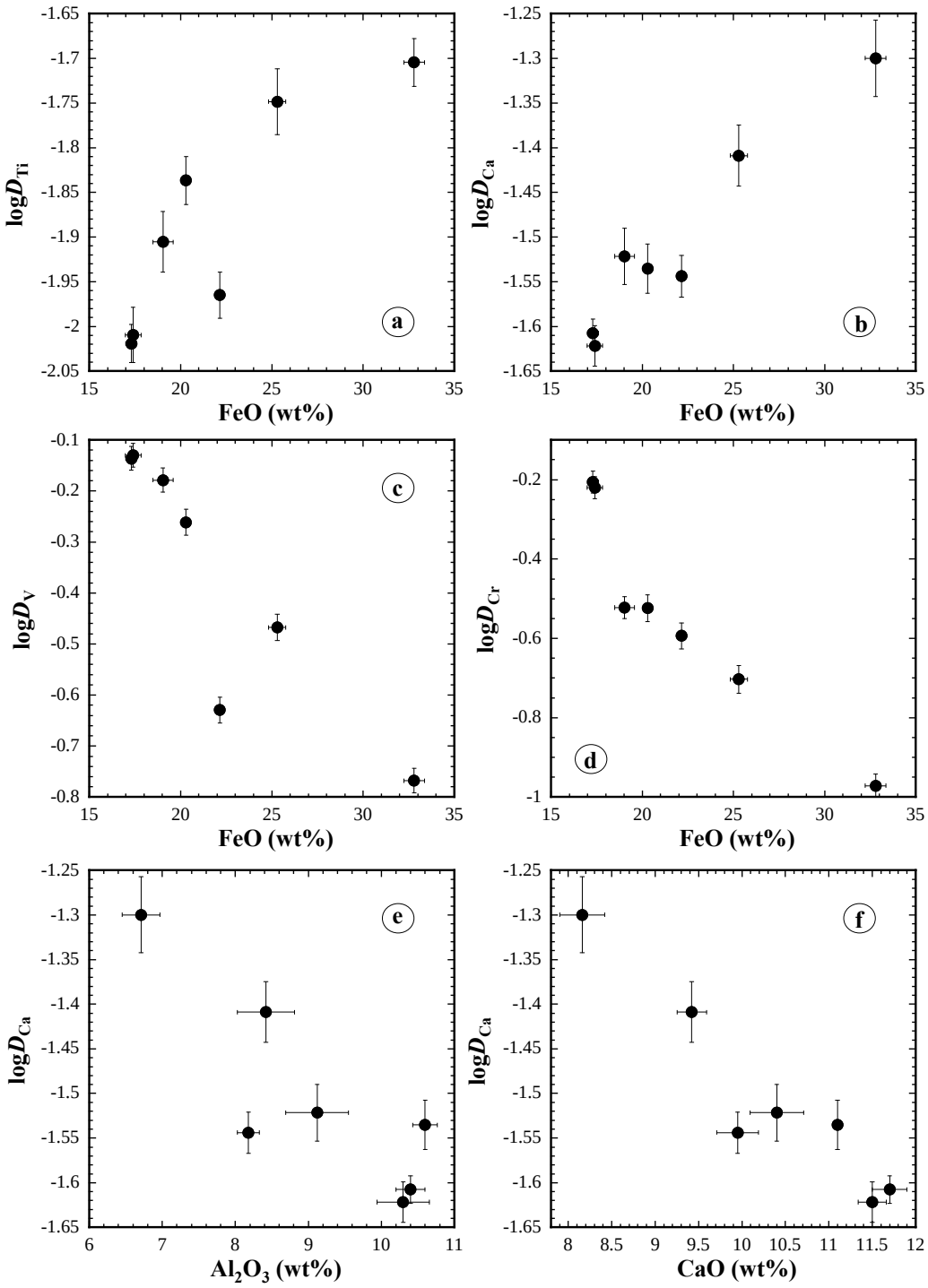

Figure 2.3 Partition coefficient dependence on major element composition in the melt. Black dots are partition data between olivine and melt in lunar basalt from this study. Error bars are at 1σ level.

Table 2.3 Partition coefficients of major and trace elements between olivine and melt.

	74235	12040	12040	12009	12009	15016	15647	Literature	Reference
Li	0.556 ± 0.049	1.56 ± 0.13	1.86 ± 0.16	--	--	0.879 ± 0.064	1.16 ± 0.082	0.1-1.3	[1, 2, 3, 4]
Mg*	5.45 ± 0.29	4.67 ± 0.12	4.66 ± 0.22	4.83 ± 0.25	5.12 ± 0.40	4.12 ± 0.43	4.55 ± 0.44	1.64-7.46	[5, 6, 7]
Al	0.0072 ± 0.00024	0.0018 ± 0.00011	0.0015 ± 0.00007	0.0046 ± 0.00011	0.0046 ± 0.00018	0.0046 ± 0.00023	0.0024 ± 0.00011	0.002-0.022	[4, 6, 8, 9]
Ca*	0.029 ± 0.0015	0.039 ± 0.0031	0.029 ± 0.0018	0.025 ± 0.00088	0.024 ± 0.0012	0.030 ± 0.0022	0.050 ± 0.0049	0.0116-0.0676	[3, 4, 5, 6, 7, 9]
Ti	0.011 ± 0.0006	0.018 ± 0.0015	0.015 ± 0.0009	0.010 ± 0.00048	0.010 ± 0.0007	0.012 ± 0.00097	0.020 ± 0.0012	0.0019-0.43	[2, 3, 4, 8, 9, 10, 11]
V	0.235 ± 0.014	0.341 ± 0.020	0.548 ± 0.032	0.733 ± 0.039	0.741 ± 0.040	0.663 ± 0.036	0.171 ± 0.0095	0.013-0.19	[3, 7, 9, 10, 11]
Cr	0.255 ± 0.019	0.198 ± 0.016	0.299 ± 0.023	0.624 ± 0.040	0.603 ± 0.039	0.300 ± 0.019	0.107 ± 0.007	0.35-5.2	[3, 5, 6, 7, 10, 11]
Mn	0.689 ± 0.039	1.48 ± 0.083	1.24 ± 0.071	0.929 ± 0.049	0.877 ± 0.046	0.720 ± 0.038	1.02 ± 0.056	0.5-1.67	[3, 5, 6, 9, 10, 11]
Fe*	1.14 ± 0.014	1.75 ± 0.036	1.80 ± 0.017	1.38 ± 0.035	1.37 ± 0.034	1.40 ± 0.045	1.34 ± 0.038	0.49-1.87	[5, 6, 7, 9]
Co	2.28 ± 0.16	3.98 ± 0.27	5.00 ± 0.34	1.64 ± 0.10	1.78 ± 0.10	4.03 ± 0.24	0.877 ± 0.05	1.1-6.6	[3, 5, 6, 9, 10, 11]
Ni†	*~19.0*	*~12.9*	*~71.2*	*~5.1*	*~6.2*	--	*~2.4*	1.83-48	[3, 5, 7, 9, 10, 11]
Y	0.0052 ± 0.0003	0.0209 ± 0.0012	0.0098 ± 0.0006	--	--	0.0061 ± 0.00036	0.020 ± 0.0012	0.001-0.0997	[1, 2, 3, 6, 7, 8, 9, 11,12, 13]
Zr	0.00051 ± 0.00004	0.0010 ± 0.00007	0.00044 ± 0.00003	--	--	0.00049 ± 0.00003	0.0010 ± 0.00007	0.00015-0.012	[2, 3, 8, 11]
Nb	0.00014 ± 0.00003	--	0.00022 ± 0.00005	--	--	0.00076 ± 0.00016	0.00037 ± 0.00008	0.0001-0.01	[1, 2, 11]
Gd	0.0012 ± 0.00026	0.0054 ± 0.00113	0.0024 ± 0.00051	--	--	0.0012 ± 0.00025	0.0058 ± 0.00122	0.00059-0.0341	[1, 3, 7, 8, 9, 11, 12, 13]
Tb	0.0024 ± 0.00049	0.0091 ± 0.0019	0.0052 ± 0.0011	--	--	0.0011 ± 0.00022	0.0080 ± 0.00086	0.00163-0.035	[1, 6, 7]
Dy	0.0033 ± 0.00043	0.0134 ± 0.0013	0.0066 ± 0.0007	--	--	0.0032 ± 0.00031	0.0125 ± 0.0011	0.005-0.0997	[1, 7, 11, 13]
Ho	0.0052 ± 0.0011	0.019 ± 0.0039	0.0096 ± 0.0020	--	--	0.0048 ± 0.00010	0.0222 ± 0.0026	0.004-0.037	[1, 6, 7, 8, 12]
Er	0.0073 ± 0.0015	0.028 ± 0.0057	0.0124 ± 0.0026	--	--	0.0095 ± 0.00019	0.0297 ± 0.0060	0.0023-0.1775	[1, 2, 6, 7, 8, 11, 13]
Tm	0.0116 ± 0.0029	0.0502 ± 0.013	0.0178 ± 0.0045	--	--	0.0193 ± 0.0049	0.0410 ± 0.010	0.007-0.071	[1,7, 8]
Yb	0.0146 ± 0.003	0.0592 ± 0.012	0.0257 ± 0.0053	--	--	0.0196 ± 0.0040	0.0595 ± 0.012	0.006-0.301	[1, 2, 6, 7, 8, 9, 11, 13]
Lu	0.0272 ± 0.0069	0.0753 ± 0.019	0.0311 ± 0.0079	--	--	0.0143 ± 0.0036	0.106 ± 0.027	0.0089-0.33	[1, 2, 3, 7, 8, 11, 12, 13]

[1] Dunn and Sen, 1994. [2] McDade et al., 2003. [3] Spandler and O'Neill, 2010. [4] Burnham and O'Neill, 2016. [5] Leeman and Scheidegger, 1977. [6] Beattie, 1994. [7] Imai et al., 2012. [8] Evans et al., 2008. [9] Laubier et al., 2014. [10] Duke, 1976. [11] Rollinson, 1993. [12] Nielsen et al., 1992. [13] Stead et al., 2017.

* data from EMPA.

† Ni partition data might have been affected by the homogenization process.

2.5 Discussion

2.5.1 Comparison with literature data

All elemental partition coefficients between olivine and melt obtained for lunar basalts in this study are shown in Table 2.3 and plotted in Figure 2.4. Literature data for terrestrial conditions are also shown in Figure 2.4 for comparison. The literature data for the partition coefficient of each element between olivine and mafic melt typically span a large range, 0.7 to 2 orders of magnitude. For most elements, partition coefficients between lunar olivine and basalt determined in this study fall within the range of terrestrial values reported in the literature. However, the partition coefficients of Li, V, Cr, Co, Dy and Tm show difference between our data for lunar basalts and literature data for terrestrial conditions (Figure 2.4). The difference in D_{Dy} and D_{Tm} between lunar and terrestrial basalts is because only one paper reported experimental Dy and Tm partition data for terrestrial conditions. For example, if interpolated D_{Dy} and D_{Tm} in Nielsen et al. (1992) (as listed in Geochemical Earth Reference Model website, https://earthref.org/KDD/) were included, the terrestrial range would cover all the lunar Dy and Tm data. For Co, one lunar sample (15647) has a lower Co partition coefficient than in other lunar samples and in literature terrestrial data. This is probably due to the fact that Co is compatible in olivine, sulfide and metal, leading to easy disturbance of Co partition coefficient. For example, we earlier excluded Ni partition data because they vary widely, which is attributed to the high compatibility of Ni in olivine, sulfide and metal. Cobalt is similar to Ni but less compatible and hence less affected. Below, we examine the difference in D_{Li}, D_{Cr} and D_{V} in lunar and terrestrial basalts.

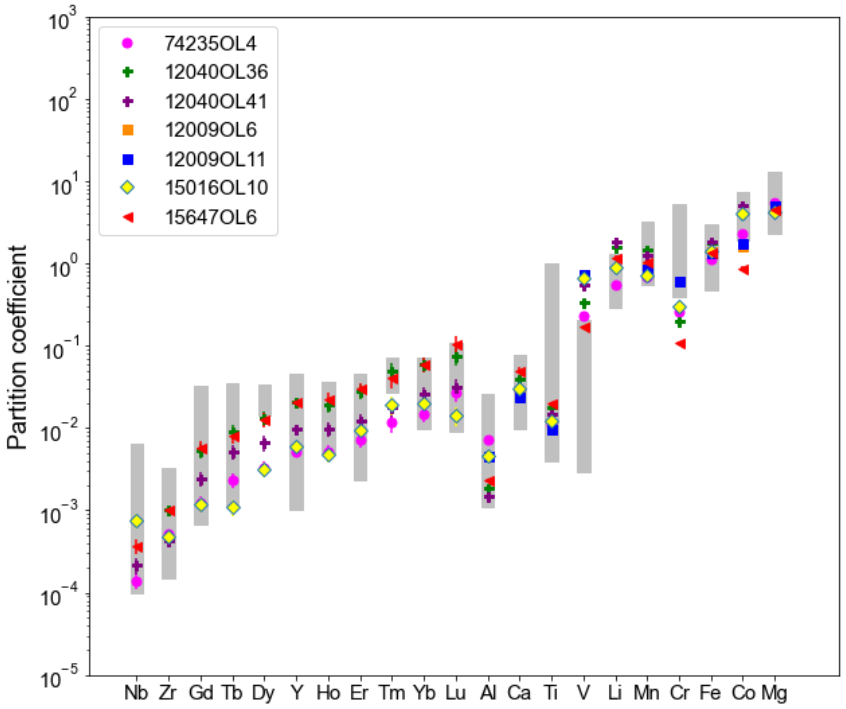

Figure 2.4 Partition coefficients between olivine and melt in lunar basalt from this study (colored symbols) compared with literature data at terrestrial conditions (gray vertical bars). Data and references can be found in Table 2.3. The partition coefficients for terrestrial basalts are selected from literature data based on the following: experimental data only, oxygen fugacity higher than QFM-2, and melt composition with 2 to 20 wt% FeO_t, >10 wt% Al_2O_3, and < 5 wt% TiO_2.

Lithium partition coefficient between olivine and basalt is higher in some lunar samples than in terrestrial samples. The partition coefficient of Li appears to increase with the Fa# (= Fe/(Fe+Mg) of olivine) (Figure 2.5a). Literature Li partition data are limited (Dunn and Sen 1994; Brenan et al. 1998; Taura et al. 1998; McDade et al. 2003; Ottolini et al. 2009; Dalou et al. 2012; Nielsen and Ustunisik 2019): Only 25 data points satisfy the following conditions: nominally dry, < 20% relative error on Li concentrations, containing > 30 wt% SiO_2, and having olivine and melt composition reported. All these literature data are for low-Fa# olivine (Fa# ≤ 0.22, that is, Fo# ≥ 0.78), whereas D_{Li} values in this work are for samples with Fa# as high as 0.55, leading to higher D_{Li} values in the Fe-rich samples (Figure 2.5a). One explanation for the increase of D_{Li} with Fa# is that the ionic radius of Li^+ (0.76 Å in octahedral site, Shannon 1976) is more similar to that of

high-spin Fe^{2+} (0.78 Å) than to Mg^{2+} (0.72 Å). We modeled the dependence of D_{Li} on temperature, pressure, and composition. It turns out that the pressure effect is insignificant. A rough fit is as follows:

$$lnD_{Li} = 3.33 + [-13457 + 8216\sqrt{Fa\#} + 51.9(SiO_2 + 2Al_2O_3)]/T \quad (2.1)$$

where T is in kelvin, and SiO_2 and Al_2O_3 are in wt% in the melt (i.e., 50 wt% SiO_2 means SiO_2 = 50 in the above equation, not 0.5). The above equation can reproduce lnD_{Li} data with a standard deviation of 0.19 after excluding two outlier points (Figure 2.5b). Based on the above equation, D_{Li} between olivine and melt increases with Fa# in olivine and SiO_2+2Al_2O_3 in the melt.

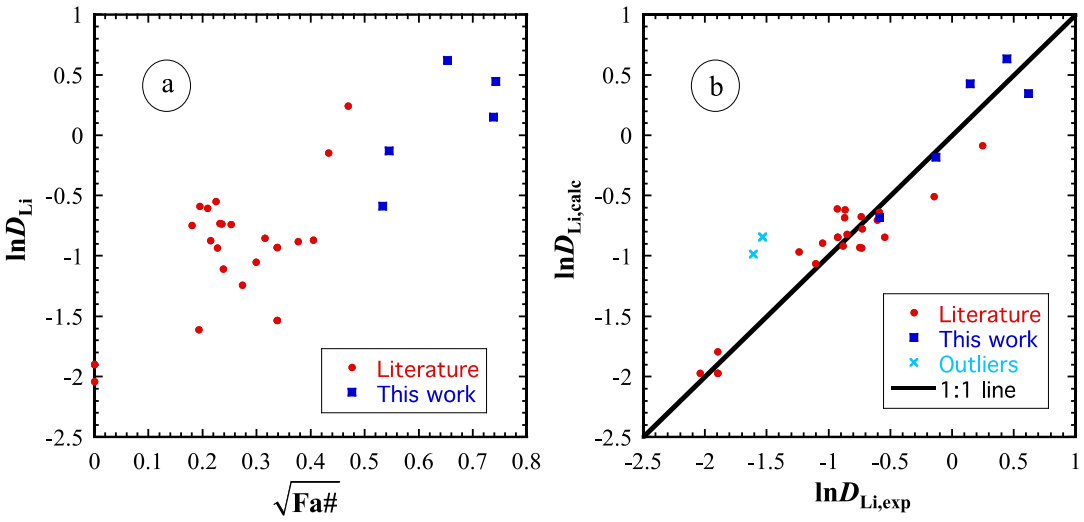

Figure 2.5 a. Correlation between lnD_{Li} and square root of Fa# in olivine. **b.** Comparison of calculated lnD_{Li} using Equation 2.1 (vertical axis) with experimental values (horizontal axis). Data sources include: Dunn and Sen 1994; Brenan et al. 1998; Taura et al. 1998; McDade et al. 2003; Ottolini et al. 2009; Dalou et al. 2012; Nielsen and Ustunisik 2019. Data with >20% relative error in Li concentration or with less than 10 wt% SiO_2 are excluded. Two outlier points are from Taura et al. (1998) and Dalou et al. (2012).

Chromium exists mainly in the form of Cr^{3+} in terrestrial basalts, but a significant fraction of Cr is Cr^{2+} under the reducing conditions in lunar glass and minerals (Schreiber and Haskin 1976; Sutton et al. 1993; Papike et al. 2005; Berry et al. 2006; Bell et al. 2014; Simon and Sutton 2017).

Considerable research has been devoted to Cr partitioning under terrestrial and lunar conditions, showing complicated Cr partitioning behavior between olivine and melt. Schreiber and Haskin (1976) determined Cr partition coefficients in forsterite-anorthite-diopside and forsterite-anorthite-silica systems with an fO_2 range of about 10 orders of magnitude and showed that D_{Cr} between forsterite and melt depends on temperature, composition, and fO_2. D_{Cr} data by Milkouchi et al. (1994) and Gaetani and Grove (1996) in FeO-bearing systems and a narrower fO_2 range showed no dependence on fO_2. Hanson and Jones (1998) reconciled these results by proposing that Cr^{3+} partitioning is sensitive to composition and Cr^{2+} partitioning is highly sensitive to temperature, so that for some composition and temperature, Cr^{3+} partition coefficient is similar to that of Cr^{2+}, leading to approximately constant D_{Cr} with fO_2. Mallmann and O'Neill (2009) reported that for some melts that contains < 1.7 wt% FeO at 1300°C, Cr partition coefficient between olivine and melt is roughly constant between QFM-10 and QFM+4. Yet, our data show that Cr partition coefficient between olivine and melt in lunar basalts is significantly lower than that in terrestrial rocks. The significantly lower D_{Cr} in lunar basalts than in terrestrial basalts must be due to differences in some combination of composition, fO_2 and temperature (Hanson and Jones 1998).

We modeled D_{Cr} as a function of temperature, olivine and melt composition and fO_2. The following criteria were used in filtering D_{Cr} data: 1) fO_2 values must be reported for each D_{Cr} value, 2) if Cr_2O_3 concentration is measured by electron microprobe, the Cr_2O_3 concentration must be > 0.10 wt% so that Cr_2O_3 concentration does not have too large an uncertainty, 3) the 1σ uncertainty must be < 20% of the measured concentration, 4) the chemical composition must contain < 5 wt% other oxides relative to the typical major oxides. Data sources are listed in Figure 2.6.

We first tried an empirical linear model in which $\ln D_{Cr}$ is assumed to be linearly dependent on $1000/T$, P, $\log fO_2$, $(1\text{-}Mg\#_{oliv})^2/T$, X_i/T (where X_i is the cation mole fraction of, e.g., Si, Ti, Al),

plus various multiplications of these terms. The model is similar to the model of Mallmann and O'Neill (2013) for V partitioning, but it includes more complicated terms than that. Unfortunately, the effort did not lead to satisfactory fits (e.g., mean error in reproducing $\ln D_{Cr}$ being ≤ 0.2) even with ≥ 14 parameters unless some coefficients were large positive and negative values, leading to wide swings in the calculated $\ln D_{Cr}$, which are an indication of overfitting.

We then tried to model D_{Cr} as a function of temperature, pressure, melt composition, and fO_2 using a quasi-thermodynamically based formulation. In this formulation, D_{Cr} is related to D_{CrO}, $D_{CrO_{1.5}}$ (CrO_3 is not included for simplicity), and the equilibrium constant K_{hom} for the homogeneous reaction of CrO(melt) +(1/4)O_2 □ $CrO_{1.5}$(melt) as follows (e.g., Mallmann and O'Neill, 2009):

$$lnD_{Cr} = ln\frac{D_{CrO}+D_{CrO_{1.5}}K_{hom}fO_2^{1/4}}{1+K_{hom}fO_2^{1/4}} \quad (2.2)$$

Each of $\ln D_{CrO}$, $\ln D_{CrO_{1.5}}$, and $\ln K_{hom}$ is expressed as a linear function of $1/T$, P/T, Fo#/T, X_i/T in the melt, and X_iX_j/T (e.g., regular solution model would have X_iX_j/T terms in the activity coefficients). Such a model requires nonlinear minimization involving numerous terms, which was performed using MATLAB. The terms are added or removed based on the examination of fitting results. However, by increasing the number of fitting parameters to improve fitting precision, some fitting parameters would take large positive and negative values, leading to wide swings in the calculated D_{Cr} values. After much effort, we decided to adopt the following less complicated model to avoid overfitting:

$$\ln D_{CrO} = -2.92 + 41698\cdot Si\cdot Mg/T, \quad (2.3a)$$

$$\ln D_{CrO_{1.5}} = -4.52 + [5395 + 1338Fo\# + 35299Mg\cdot(Na+K)]/T, \quad (2.3b)$$

$$\ln K_{hom} = -79.00 + [104330+126061(Mg+Ca+Na+K)]/T, \quad (2.3c)$$

where T is temperature in K, Si, Mg, Ca, Na, and K are the cation mole fractions of the melt, and Fo# = Mg/(Mg+Fe) in olivine. Using D_{CrO}, $D_{CrO_{1.5}}$ and K_{hom} in Equations 2.3a-c to calculate lnD_{Cr} in Equation 2.2, lnD_{Cr} can reproduce experimental data with a standard deviation of 0.20 ln$D$ units (Figure 2.6) after excluding 15 points. However, K_{hom} values based on the parameters of the fitting results vary by 11 orders of magnitude, which may be unrealistic. Hence, even though lnD_{Cr} values can be roughly reproduced using the fit, the physical interpretation of the fitted D_{CrO}, $D_{CrO_{1.5}}$ and especially K_{hom} may not be meaningful. Based on Equations 3a-c, the lower D_{Cr} values between olivine and melt in lunar basalts may be attributed to lower Si·Mg, lower Fo#, and lower Mg·(Na+K) than terrestrial basalts. In addition to the above quasi-thermodynamically-based modeling, we also made an effort to examine different substitution mechanisms to explain the variation in Cr partition coefficients but did not arrive at satisfactory answers.

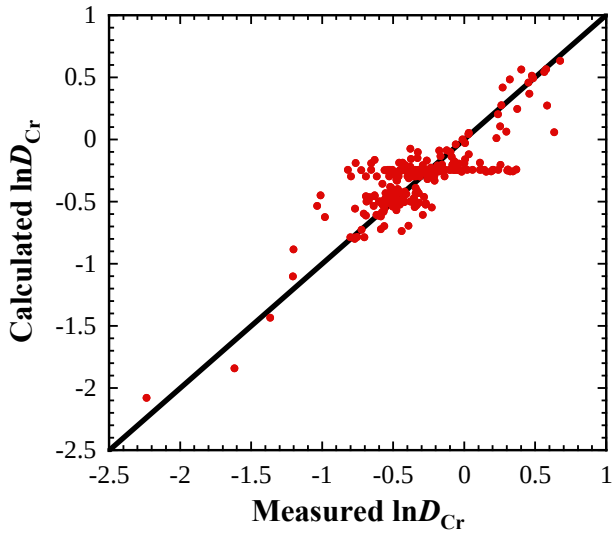

Figure 2.6 Calculated ln$D$Cr using the model in this study versus measured ln$D$Cr (data reported in the literature). Fit of Cr partition coefficient data using Equation 2.2 with parameters given in Equations 2.3a-c. Literature Cr partition data are from EarthChem (Nielsen and Ustunisik 2019), Beattie (1994), Canil (1998, 1999), Hanson and Jones (1998), Righter et al. (2004), Mallmann and O'Neill (2009, 2013), Tuff and O'Neill (2010), Fellows and Canil (2012), Davis et al. (2013), Bell et al. (2014), Fonseca et al. (2014), Liu et al. (2014), and Leizke et al. (2016). Fifteen data points

are excluded, including 7 points in Mallmann and O'Neill (2009), 3 in Fonseca et al. (2014), 3 in Leitzke et al. (2016), and 2 points in Liu et al. (2014).

Vanadium partitioning has been evaluated systematically in numerous studies and is insensitive to temperature or composition but increases strongly with decreasing fO_2 (e.g., Canil 1997; Mallmann and O'Neill 2009, 2013; Papike et al. 2013). Therefore, partitioning of V has been used as an important redox indicator (e.g., Canil and Fedortchouk 2001; Shearer et al. 2006; Wood et al. 2008; Mallmann and O'Neill 2013). The V partition coefficient data for lunar samples range from 0.17 to 0.74, with an average of ~0.43, and are systematically higher than the values of 0.003 to 0.21 reported for terrestrial basalts (Table 2.3), which is expected for more reduced lunar rocks. For example, XANES measurements of lunar samples show that V in lunar basalts is predominantly in the form of V^{3+}, with up to 20% of V^{2+} (Sutton and Newville 2005; Karner et al. 2006). The dominant valence state in terrestrial basalts, however, is V^{4+} (Papike et al. 2005), which explains the difference in V partition coefficients between lunar samples and terrestrial samples. The observed variation of V partition coefficient from 0.17 to 0.74 in lunar basalts can be explained by variations of $\log fO_2$, from NNO - 3.17 to NNO - 5.86 (IW + 1.5 to IW – 1.2) according to the Canil's relationship between D_V and $\log fO_2$ (Canil 1997), or from IW + 1.5 to IW – 1.8 using the model of Mallmann and O'Neill (2009), which are approximately consistent with estimated oxygen fugacity for lunar basalts (IW-2 to IW, Sato et al. 1973; Wadhwa 2008). There may also be significant dependence of V partition coefficient on melt composition, as recently modeled empirically by Mallmann and O'Neill (2013). However, although the model by Mallmann and O'Neill (2013) attempted to improve the model of Mallmann and O'Neill (2009) by incorporating the compositional dependence of D_V, it fails to reproduce the measured values of D_V in this study by assuming a reasonable fO_2 for lunar basalts (from IW to IW-2): the predicted D_V values would be too high by up to 1.5 orders of magnitude. This points to the limitations of empirical modeling

of the partition coefficient of V, which has multiple oxidation states. Due to the difficulty in our modeling of Cr partition coefficient, and because there are more potential oxidation states for V, we did not attempt to model V partition coefficient using a thermodynamically-based formulation. Nonetheless, our data on V partitioning are as expected.

2.5.2 Implications

The set of olivine-melt partition coefficients for lunar mare basalts obtained in this study may be applied to investigate the effect of olivine fractionation during lunar basaltic magma evolution and shallow-level (low pressure) lunar magma ocean evolution. In addition, our data for olivine-melt partitioning can be combined with partition data between other mantle minerals and melt to quantify trace element behavior during lunar mantle partial melting and trace element concentration in primary mare basalts and the lunar mantle.

Data for most elements in this study for lunar olivine-melt partitioning are similar to those in terrestrial basalts. Hence, no reconsideration is needed for relevant modeling for those elements. However, Li, V, and Cr partition coefficients between olivine and melt in lunar basalts are significantly different from those in terrestrial basalts. There are several consequences of this.

As shown in Figure 2.5a, Li becomes a compatible element in olivine when the Fa# in olivine is greater than 0.25, roughly corresponding to a low Mg# $\leq$ 0.47 using a K_D value of 0.3. That is, in evolved basalt, Li is compatible in olivine. However, because Li partition coefficient in pyroxenes is smaller than that in olivine (Ottolini et al. 2009), the effect of the increased compatibility of Li in olivine in evolved basalt does not appear to result in a clear shift in Li behavior. For example, Figure 2.7 shows Li versus Yb in terrestrial and lunar basalts. Terrestrial MORB and OIB show a positive correlation between Li and Yb to at least 17 ppm Yb. The lunar data show a similar trend as the MORB trend for A14, A15, and A16, but a slower increase of Li

with Yb for most of A11 and A17. It is not clear how much of the difference for the A11 and A17 should be attributed to data scatter and how much to the higher compatibility of Li in more fayalitic olivine.

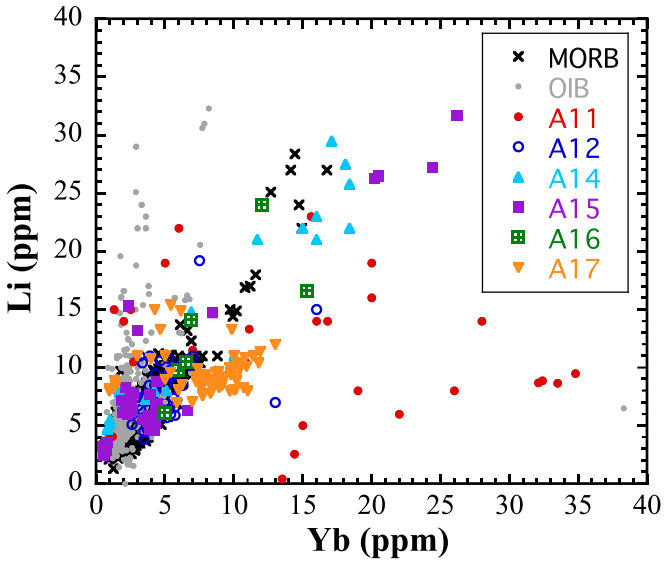

Figure 2.7 Li concentration versus Yb concentration in terrestrial MORB and OIB and lunar basalts. Li and Yb have similar compatibility in terrestrial basalts (Salters and Stracke 2004). Lunar basalt data are from Mare Basalt Database (https://www3.nd.edu/~cneal/lunar-l/), MORB data are from the compilation by Gale et al. (2013), and OIB data are from GeoRoc.

The Cr partition coefficient between olivine and melt is smaller in lunar basalts than in terrestrial basalts. Combined with the observation that Cr partition coefficients between clinopyroxene and melt and between orthopyroxene and melt decreases with decreasing fO_2 (Canil, 1999; Mallmann and O'Neill, 2009), Cr is an incompatible element during lunar mantle partial melting and early basalt evolution, opposite to being strongly compatible during terrestrial mantle partial melting and basalt evolution. Therefore, Cr concentration in mantle-derived basalts is expected to be high and to become higher in evolved melts before oxide minerals crystallize. That is, the higher Cr concentration in lunar olivine than in terrestrial olivine (e.g., Steele and Smith, 1975) is not due to the larger Cr partition coefficient but to higher Cr concentration in the melt

(Schreiber and Haskin, 1976). Figure 2.8 displays Cr versus MgO and Cr versus FeO in terrestrial and lunar basalts. MgO is a compatible element, and a lower MgO concentration means more evolved basalts. Cr concentrations in lunar basalts are much higher than in terrestrial MORB and OIB, as expected from its incompatibility in the lunar mantle and its compatibility in the terrestrial mantle. Furthermore, in terrestrial MORB and OIB, Cr shows a relatively simple positive (roughly linearly) relation to MgO, meaning that Cr is a compatible element during terrestrial basalt evolution. On the other hand, the Cr versus MgO trend in lunar basalts is more complicated: Cr concentration increases with decreasing MgO for MgO from 25 to approximately 11 wt%, and then decreases with further decreasing MgO. Hence, Cr is incompatible when MgO concentration is above 11 wt% (primitive basalt), and then becomes compatible when the MgO concentration is below 11 wt%. The trend of first increasing and then decreasing Cr concentration as MgO decreases in lunar basalts is similar to the FeO versus MgO trend in terrestrial basalts (Grove and Baker 1984) and might be controlled by chromite or other oxide mineral crystallization. In Cr versus FeO (Figure 2.8b), Cr is crudely positively correlated with FeO in lunar basalts (Seifert and Ringwood 1988), with Cr being more incompatible than FeO, indicating that Cr and Fe are both incompatible during mafic silicate mineral fractionation and compatible in Fe-Ti oxides. On the other hand, in terrestrial basalts, Cr concentration has an apparent maximum at approximately 9 wt% FeO in MORB and 12 wt% FeO in OIB because tholeiitic FeO enrichment is accompanied by Cr depletion (Cr is compatible), and subsequent FeO depletion due to oxide crystallization is also accompanied by Cr depletion.

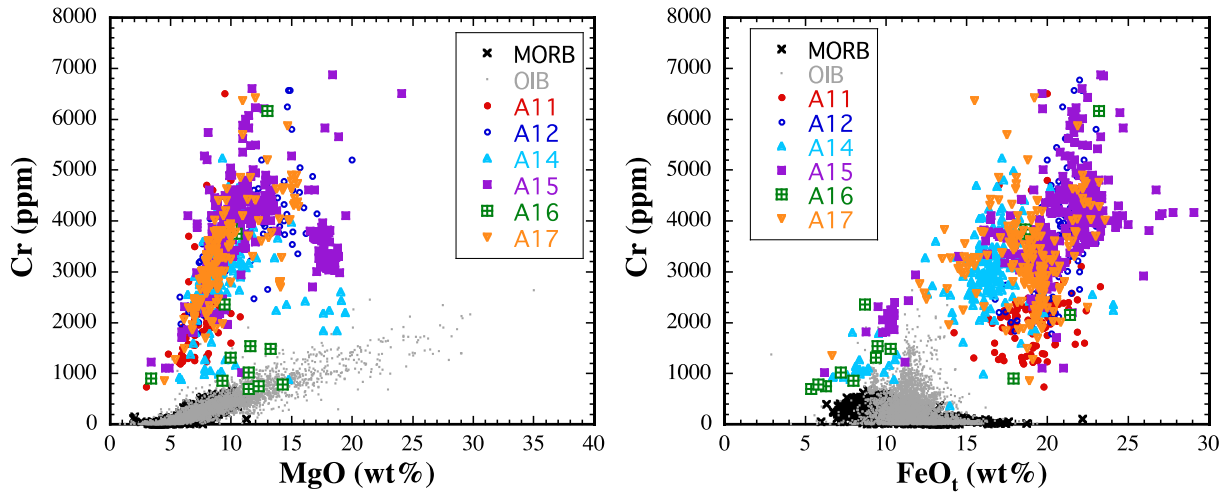

Figure 2.8 Cr concentration versus MgO and FeO total (FeO_t) in lunar basalts and terrestrial MORB and OIB ($SiO_2 \leq 55$ wt%). Data sources are the same as in Figure 2.7.

Vanadium partition coefficient between olivine and melt is higher in lunar settings than in terrestrial settings because of the more reduced lunar conditions. Combined with increasing V partition coefficients between other mafic minerals and melts as fO_2 decreases (Mallmann and O'Neill 2009), V is less incompatible during lunar basalt evolution than in terrestrial basalt evolution. Figure 2.9 confirms this expectation. In terrestrial basalts, V is highly incompatible in primitive basalts, whereas Mg is compatible. Hence, V concentration increases steeply as MgO concentration decreases (Figure 2.9a, MORB and OIB trends). At lunar conditions, however, V is incompatible when MgO is greater than approximately 11 wt% (meaning that V concentration increases as MgO concentration decreases), but less so than in terrestrial basalts. At lower MgO, V in lunar basalts becomes compatible and decreases as MgO decreases. Vanadium concentration in lunar basalts, when plotted against MgO, also has a maximum at approximately 10 to 12 wt% MgO, which is similar to Cr. The positive trends of V-FeO_t for both terrestrial and lunar samples but with a smaller slope for lunar samples also indicate that V in terrestrial basalts is much more incompatible than in lunar basalts.

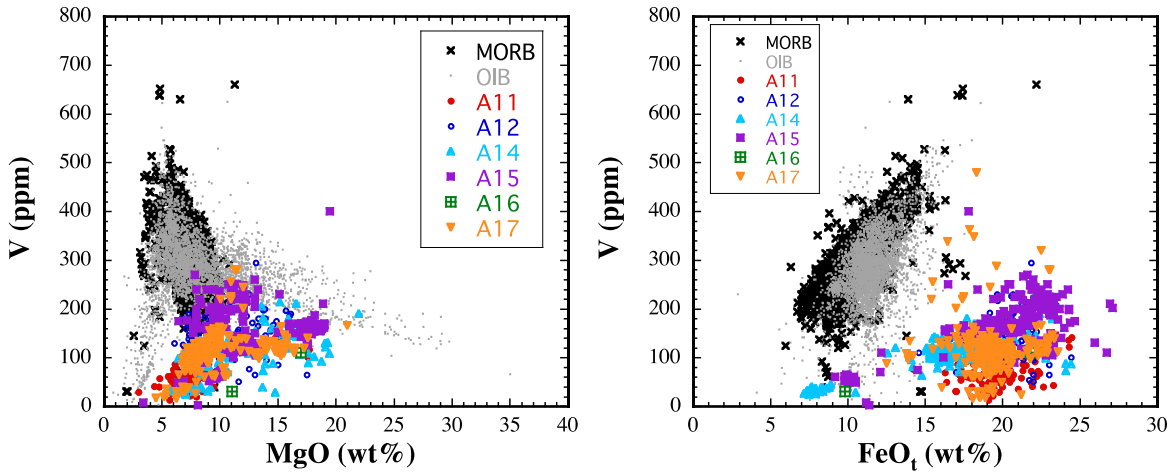

Figure 2.9 Vanadium concentration versus MgO and FeO in lunar and terrestrial basalts. Data sources are the same as Figure 2.7.

The partition coefficients of V and Cr between olivine and melt are similar in lunar basalts (0.17 to 0.74 for V versus 0.11 to 0.62 for Cr). However, in terrestrial basalts, the partition coefficient for V is much smaller than that of Cr. Hence, olivine fractionation would not significantly change the V/Cr ratio in the lunar magma ocean or lunar basalts, but the V/Cr ratio in terrestrial basalts would increase significantly with olivine fractionation. The similarity of V and Cr partition coefficients between olivine and melt in lunar basalts apparently also applies to other mafic minerals in lunar settings, which leads to a nearly constant V/Cr ratio in lunar basalts (Seifert and Ringwood 1988). Figure 2.10 shows V versus Cr concentrations in lunar basalts and terrestrial MORB and OIB, and indicates that V and Cr are positively correlated in lunar basalts (Figure 2.10a) with nearly constant V/Cr ratio. Because some authors argue that the constancy of an elemental ratio is best examined by using a log-log concentration plot (Sims and DePaolo, 1997; Hofmann et al. 2020), we do so in Figure 2.10b. A slope of 1 in the log-log plot means a constant V/Cr ratio. In Figure 2.10b, even though there is much scatter (most of the very low V/Cr ratios are from A11 samples, and most of the high V/Cr ratios are from A17 samples), the slope from

simple linear fitting of log(V) versus log(Cr) is 0.956±0.037 (1σ error), which is approximately 1. After removing the outliers (outside 3σ), the average V/Cr slope in lunar basalts is 0.039±0.011, which is in excellent agreement with the ratio of 0.038 obtained by Seifert and Ringwood (1988). The V/Cr ratio in lunar basalts is not much different from the ratio in the bulk silicate Earth (0.031, McDonough and Sun 1995). The depletion of Cr (50% condensation temperature is 1296K by Lodders 2003, 1291 K by Wood et al. 2019) in the Moon relative to V (condensation temperature is 1429 K by Lodders 2003, 1370 K by Wood et al. 2019) is slight, about 20% based on the ratios, but the large errors in the ratios allow no relative depletion. Because the data in Figure 2.10 reflect the involvement of not only olivine but also other minerals, Figure 2.10 shows that V and Cr have similar degrees of incompatibility not only in olivine as shown in this study, but also in other minerals in lunar basalts. Because element pairs with nearly constant ratios are often used to estimate the mantle composition (e.g., McDonough and Sun 1995; Salters and Stracke 2003; Hofmann et al. 2020) as well as particular processes that might affect a given ratio (e.g., Cooper et al. 2012), the similar degree of incompatibility for V and Cr provides a useful tool for examining lunar basalt evolution as well as the lunar mantle composition.

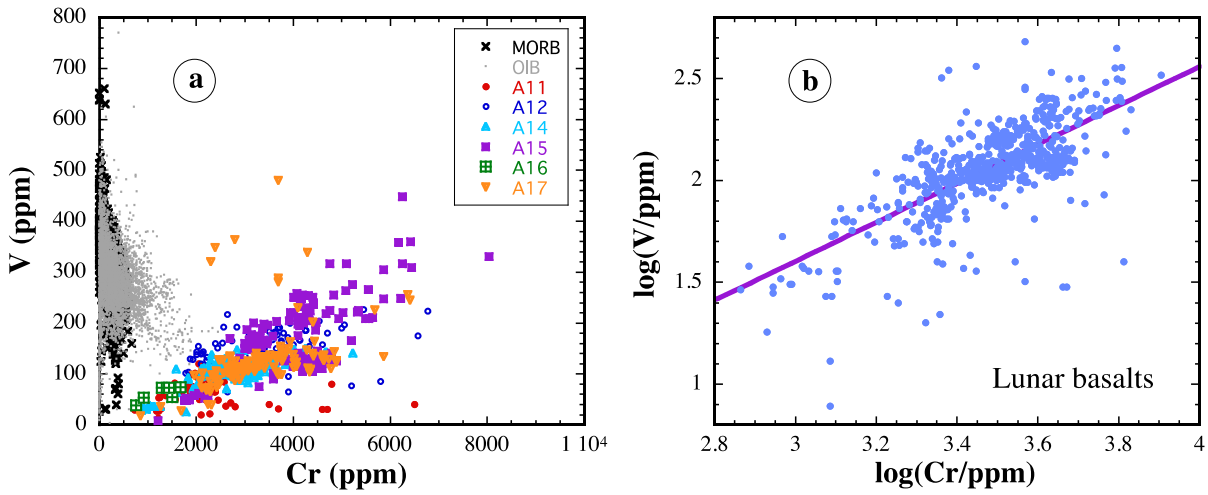

Figure 2.10 Vanadium concentration versus Cr concentration in lunar and terrestrial basalts. Data sources are the same as Figure 2.7.

To conclude, partition coefficients between olivine and melt in lunar basalts are measured for 22 elements. Most of the data are in good agreement with those in terrestrial basalts despite the large differences in basalt composition and oxygen fugacity, except for the partition coefficients of Li, V, and Cr. The slightly higher Li partition coefficient between olivine and melt in lunar basalts than in terrestrial basalts is largely due to the higher Fa# in olivine in typical lunar basalts and does not seem to lead to clear and consistent consequences in Li behavior during lunar basalt evolution. The higher V partition coefficients in lunar basalts can be readily explained by the lower oxidation state of lunar basalts compared to terrestrial basalts. On the other hand, the smaller partition coefficients of Cr in lunar basalts than in terrestrial basalts seem to be due to compositional effects. Chromium behaves as an incompatible element during crystal fractionation of lunar basalt when MgO is ≥ 11 wt%, which is opposite to its compatibility during terrestrial basalt evolution. Vanadium is less incompatible during lunar basalt evolution than terrestrial basalt evolution. In addition, V and Cr have similar partition coefficients between mafic minerals and basalt in the Moon. Our new partition data can explain: 1) the much higher Cr concentration in

high-FeO lunar basalts than in terrestrial basalts, 2) the much lower V concentration in evolved lunar basalts than in evolved terrestrial basalts, and 3) the roughly constant V/Cr ratio of about 0.039 in lunar basalts. The partition coefficients determined in this study can be applied to model lunar magma evolution, infer melt composition from olivine composition, and model partial melting of the lunar mantle.

2.6 Acknowledgments

This work was supported by NASA grants NNX15AH37G and 80NSSC19K0782. We would like to thank NASA CAPTEM for providing the lunar samples, K.P. Jochum for providing the MPI-DING glass standards, J.C. Barrette for assistance in LA-ICP-MS analyses, and Yunbin Guan for assistance in SIMS analyses.

2.7 References

Agee C. B. and Walker D. (1990) Aluminum partitioning between olivine and ultrabasic silicate liquid to 6 GPa. *Contrib. Mineral. Petrol.* **105**, 243–254.

Beattie P. (1994) Systematics and energetics of trace-element partitioning between olivine and silicate melts: Implications for the nature of mineral/melt partitioning. *Chem. Geol.* **117**, 57–71.

Bell A. S., Burger P. V., Le L., Shearer C. K., Papike J. J., Sutton S. R., Newville M. and Jones J. (2014) XANES measurements of Cr valence in olivine and their applications to planetary basalts. *Am. Mineral.* **99**, 1404–1412.

Berry A. J., O'Neill H. St. C., Scott D. R., Foran G. J. and Shelley J. M. G. (2006) The effect of composition on Cr^{2+}/Cr^{3+} in silicate melts. *Am. Mineral.* **91**, 1901–1908.

Blundy J. and Wood B. (1994) Prediction of crystal–melt partition coefficients from elastic moduli. *Nature* **372**, 452–454.

Borisov A., Lahaye Y. and Palme H. (2004) The effect of TiO_2 on Pd, Ni, and Fe solubilities in silicate melts. *Am. Mineral.* **89**, 564–571.

Brenan J. M., Neroda E., Lundstrom C. C., Shaw H. F., Ryerson F. J. and Phinney D. L. (1998) Behaviour of boron, beryllium, and lithium during melting and crystallization: constraints

from mineral-melt partitioning experiments. *Geochimica et Cosmochimica Acta* **62**, 2129–2141.

Bucholz, C.E., Gaetani, G.A., Behn, M.D. and Shimizu, N. (2013) Post-entrapment modification of volatiles and oxygen fugacity in olivine-hosted melt inclusions. *Earth Planet. Sci. Lett.* **374**, 145-155.

Canil D. (1997) Vanadium partitioning and the oxidation state of Archaean komatiite magmas. *Nature* **389**, 842–845.

Canil, D. (2002) Vanadium in peridotites, mantle redox and tectonic environments: Archean to present. *Earth Planet. Sci. Lett.* **195**, 75-90.

Canil D. and Fedortchouk Y. (2001) Olivine-liquid partitioning of vanadium and other trace elements, with applications to modern and ancient picrites. *Can. Mineral.* **39**, 319–330.

Charlier B., Grove T. L., Namur O. and Holtz F. (2018) Crystallization of the lunar magma ocean and the primordial mantle-crust differentiation of the Moon. *Geochim. Cosmochim. Acta* **234**, 50–69.

Chen, Y., Provost, A., Schiano, P. and Cluzel, N. (2011) The rate of water loss from olivine-hosted melt inclusions. *Contrib. Mineral. Petrol.* **162**, 625-636.

Chen, Y., Provost, A., Schiano, P. and Cluzel, N. (2013) Magma ascent rate and initial water concentration inferred from diffusive water loss from olivine-hosted melt inclusions. *Contrib. Mineral. Petrol.* **165**, 525-541.

Chen Y., Zhang Y., Liu Y., Guan Y., Eiler J. and Stolper E. M. (2015) Water, fluorine, and sulfur concentrations in the lunar mantle. *Earth Planet. Sci. Lett.* **427**, 37–46.

Cottrell E. and Kelley K. A. (2011) The oxidation state of Fe in MORB glasses and the oxygen fugacity of the upper mantle. *Earth Planet. Sci. Lett.* **305**, 270–282.

Dalou C., Koga K. T., Shimizu N., Boulon J. and Devidal J.-L. (2012) Experimental determination of F and Cl partitioning between lherzolite and basaltic melt. *Contrib Mineral Petrol* **163**, 591–609.

Donaldson CH, Usselman TM, Wiliams RJ, Lofgren GE (1975) Experimental modeling of the cooling history of Apollo 12 olivine basalts. *P. Lunar Planet Sci. C.* **6**, 843–869.

Duke J. M. (1976) Distribution of the period four transition elements among olivine, calcic clinopyroxene and mafic silicate liquid: experimental results. *J. Petrol.* **17**, 499–521.

Dunn T. and Sen C. (1994) Mineral/matrix partition coefficients for orthopyroxene, plagioclase, and olivine in basaltic to andesitic systems: A combined analytical and experimental study. *Geochim. Cosmochim. Acta* **58**, 717–733.

Dygert N., Liang Y. and Hess P. (2013) The importance of melt TiO_2 in affecting major and trace element partitioning between Fe–Ti oxides and lunar picritic glass melts. *Geochim. Cosmochim. Acta* **106**, 134–151.

Elardo S. M., Draper D. S. and Shearer C. K. (2011) Lunar magma ocean crystallization revisited: bulk composition, early cumulate mineralogy, and the source regions of the highlands Mg-suite. *Geochim. Cosmochim. Acta* **75**, 3024–3045.

Evans T. M., C. O'Neill H. St. and Tuff J. (2008) The influence of melt composition on the partitioning of REEs, Y, Sc, Zr and Al between forsterite and melt in the system CMAS. *Geochim. Cosmochim. Acta* **72**, 5708–5721.

Fonseca, R.O.C., Mallmann, G., Sprung, P., Sommer, J.E., Heuser, A., Speelmanns, I.M. and Blanchard, H. (2014) Redox controls on tungsten and uranium crystal/silicate melt partitioning and implications for the U/W and Th/W ratio of the lunar mantle. *Earth Planet. Sci. Lett.* **404**, 1-13.

Gaetani G. A. and Grove T. L. (1997) Partitioning of moderately siderophile elements among olivine, silicate melt, and sulfide melt: Constraints on core formation in the Earth and Mars. *Geochimica et Cosmochimica Acta* **61**, 1829–1846.

Gaetani G. A. and Watson E. B. (2000) Open system behavior of olivine-hosted melt inclusions. *Earth Planet. Sci. Lett.* **183**, 27–41.

Gaetani, G.A. and Watson, E.B. (2002) Modeling the major-element evolution of olivine-hosted melt inclusions. *Chem. Geol.* **183**, 25-41.

Gaetani, G.A., O'Leary, J.A., Shimizu, N., Bucholz, C.E. and Newville, M. (2012) Rapid reequilibration of H2O and oxygen fugacity in olivine-hosted melt inclusions. *Geology* **40**, 915-918.

Gale A., Dalton C. A., Langmuir C. H., Su Y. and Schilling J.-G. (2013) The mean composition of ocean ridge basalts. *Geochem. Geophys. Geosystems* **14**, 489–518.

Grant K. J. and Wood B. J. (2010) Experimental study of the incorporation of Li, Sc, Al and other trace elements into olivine. *Geochimica et Cosmochimica Acta* **74**, 2412–2428.

Grove T. L. and Baker M. B. (1984) Phase equilibrium controls on the tholeiitic versus calc-alkaline differentiation trends. *Journal of Geophysical Research: Solid Earth* **89**, 3253–3274.

Hanson B. and Jones J. H. (1998) The systematics of Cr^{3+} and Cr^{2+} partitioning between olivine and liquid in the presence of spinel. *Am. Mineral.* **83**, 669–684.

Hart S. R. and Davis K. E. (1978) Nickel partitioning between olivine and silicate melt. *Earth Planet. Sci. Lett.* **40**, 203–219.

Hofmann, A.W., Class, C. and Goldstein, S.L. (2020) Size and composition of the residual and depleted mantle reservoir. Preprint.

Huebner, J.S., Lipin, B.R., and Wiggens, L.B. (1976) Partitioning of chromium between silicate crystals and melts. *Proceedings of the 7th Lunar Science Conference*, 1195–1220.

Jones, J.H. (1995) Trace element partitioning. Rock physics and phase relations, A handbook of physical constants, *AGU Reference Shelf*, **3**, 73–104.

Karner J. M., Sutton S. R., Papike J. J., Shearer C. K., Jones J. H. and Newville M. (2006) Application of a new vanadium valence oxybarometer to basaltic glasses from the Earth, Moon, and Mars. *Am. Mineral.* **91**, 270–277.

Kennedy A. K., Lofgren G. E. and Wasserburg G. J. (1993) An experimental study of trace element partitioning between olivine, orthopyroxene and melt in chondrules: equilibrium values and kinetic effects. *Earth Planet. Sci. Lett.* **115**, 177–195.

Langmuir C. H., Hanson G. N., O'Hara M. J., Bailey D. K., Tarney J. and Dunham K. C. (1980) An evaluation of major element heterogeneity in the mantle sources of basalts. *Philosophical Transactions of the Royal Society of London. Series A, Mathematical and Physical Sciences* **297**, 383–407.

Laubier M., Grove T. L. and Langmuir C. H. (2014) Trace element mineral/melt partitioning for basaltic and basaltic andesitic melts: An experimental and laser ICP-MS study with application to the oxidation state of mantle source regions. *Earth Planet. Sci. Lett.* **392**, 265–278.

Leeman W. P. and Scheidegger K. F. (1977) Olivine/liquid distribution coefficients and a test for crystal-liquid equilibrium. *Earth Planet. Sci. Lett.* **35**, 247–257.

Leitzke, F.P., Fonseca, R.O.C., Michely, L.T., Sprung, P., Munker, C., Heuser, A. and Blanchard, H. (2016) The effect of titanium on the partitioning behavior of high-field strength elements between silicates, oxides and lunar basaltic melts with applications to the origin of mare basalts. *Chem. Geol.* **440**, 219-238.

Li, Y. and Audetat, A. (2012) Partitioning of V, Mn, Co, Ni, Cu, Zn, As, Mo, Ag, Sn, Sb, W, Au, Pb, and Bi between sulfide phases and hydrous basanite melt at upper mantle conditions. *Earth Planet. Sci. Lett.* **355-356**, 327-340.

Libourel G. (1999) Systematics of calcium partitioning between olivine and silicate melt: implications for melt structure and calcium content of magmatic olivines. *Contrib. Mineral. Petrol.* **136**, 63–80.

Lodders K. (2003) Solar system abundances and condensation temperatures of the elements. *ApJ* **591**, 1220.

Longhi, J. (1977) Magma oceanography 2: chemical evolution and crustal formation. *Proc. Lunar Sci. Conf.* **8**, 601-621.

Longhi J., Walker D. and Hays J. F. (1978) The distribution of Fe and Mg between olivine and lunar basaltic liquids. *Geochim. Cosmochim. Acta* **42**, 1545–1558.

Mallmann G. and O'Neill H. S. C. (2009) The crystal/melt partitioning of V during mantle melting as a function of oxygen fugacity compared with some other elements (Al, P, Ca, Sc, Ti, Cr, Fe, Ga, Y, Zr and Nb). *J. Petrol.* **50**, 1765–1794.

Mallmann, G. and O'Neill, H.S.C. (2013) Calibration of an empirical thermometer and oxybarometer based on the partitioning of Sc, Y and V between olivine and silicate melt. *J. Petrol.* **54**, 933-949.

McDade P., Blundy J. D. and Wood B. J. (2003) Trace element partitioning on the Tinaquillo Lherzolite solidus at 1.5GPa. *Phys. Earth Planet. Inter.* **139**, 129–147.

Mikouchi, T., McKay, G., and Le, L. (1994) Cr, Mn, and Ca distributions for olivine in angritic systems: Constraints on the origins of Cr-rich and Ca-poor core olivine in angrite LEW87051. *Lunar and Planetary Science*, **25**, 907–908.

Newton R. C., Anderson A. T. and Smith J. V. (1971) Accumulation of olivine in rock 12040 and other basaltic fragments in the light of analysis and syntheses. *P. Lunar Planet. Sci. C.* **1**, 575-582.

Ni P., Zhang Y., Chen S. and Gagnon J. (2019) A melt inclusion study on volatile abundances in the lunar mantle. *Geochim. Cosmochim. Acta* **249**, 17–41.

Ni P., Zhang Y. and Guan Y. (2017) Volatile loss during homogenization of lunar melt inclusions. *Earth Planet. Sci. Lett.* **478**, 214–224.

Nielsen R. L., Gallahan W. E. and Newberger F. (1992) Experimentally determined mineral-melt partition coefficients for Sc, Y and REE for olivine, orthopyroxene, pigeonite, magnetite and ilmenite. *Contrib. Mineral. Petrol.* **110**, 488–499.

Nielsen, R.L., and Ustunisik, G.K. (2019) EarthChem Data. Olivine/melt partition coefficient experiments, version 1.0. Interdisciplinary Earth Data Alliance (IEDA). https://doi.org/10.1594/IEDA/111285.

Nikogosian I. and Sobolev A. (1997) Ion-microprobe analysis of melt Inclusions in olivine: experience in estimating the olivine-melt partition coefficients of trace elements. *Geochem. Int.* **35**, 119–126.

O'Neill H. St. C., Berry A. J. and Mallmann G. (2018) The oxidation state of iron in Mid-Ocean Ridge Basaltic (MORB) glasses: Implications for their petrogenesis and oxygen fugacities. *Earth Planet. Sci. Lett.* **504**, 152–162.

Onuma N., Higuchi H., Wakita H. and Nagasawa H. (1968) Trace element partition between two pyroxenes and the host lava. *Earth Planet. Sci. Lett.* **5**, 47–51.

Ottolini L., Laporte D., Raffone N., Devidal J.-L. and Le Fèvre B. (2009) New experimental determination of Li and B partition coefficients during upper mantle partial melting. *Contrib Mineral Petrol* **157**, 313–325.

Papike J. J., Karner J. M. and Shearer C. K. (2005) Comparative planetary mineralogy: Valence state partitioning of Cr, Fe, Ti, and V among crystallographic sites in olivine, pyroxene, and spinel from planetary basalts. *Am. Mineral.* **90**, 277–290.

Papike J. J., Burger P. V., Bell A. S., Le L., Shearer C. K., Sutton S. R., Jones J. and Newville M. (2013) Developing vanadium valence state oxybarometers (spinel-melt, olivine-melt, spinel-olivine) and V/(Cr+Al) partitioning (spinel-melt) for martian olivine-phyric basalts. *American Mineralogist* **98**, 2193–2196.

Paster T. P., Schauwecker D. S. and Haskin L. A. (1974) The behavior of some trace elements during solidification of the Skaergaard layered series. *Geochim. Cosmochim. Acta* **38**, 1549–1577.

Pearce N. J. G., Perkins W. T., Westgate J. A., Gorton M. P., Jackson S. E., Neal C. R. and Chenery S. P. (1997) A compilation of new and published major and trace element data for NIST SRM 610 and NIST SRM 612 glass reference materials. *Geostand. Geoanal. Res.* **21**, 115–144.

Roeder P. L. and Emslie R. F. (1970) Olivine-liquid equilibrium. *Contrib. Mineral. Petrol.* **29**, 275–289.

Rollinson H. R. (1993) Using geochemical data: Evaluation, presentation, interpretation. Harlow, UK, Longman, 352 p.

Salters V. J. M. and Stracke A. (2004) Composition of the depleted mantle. *Geochemistry, Geophysics, Geosystems* **5**.

Sato, M., Hickling, N.L., and McLane, J.E. (1973) Oxygen fugacity values of Apollo 12, 14, and 15 lunar samples and reduced state of lunar magmas. *Proc. 4th Lunar Sci. Conf.* (Suppl. Geochim. Cosmochim. Acta), **1**, 1061-1079.

Schreiber, H.D., and Haskin, L.A. (1976) Chromium in basalts: Experimental determination of redox states and partitioning among synthetic silicate phases. *Proceedings of Lunar Science Conference*, **7**, 1221–1259.

Seifert S. and Ringwood A. . E. (1988) The lunar geochemistry of chromium and vanadium. *Earth Moon Planets* **40**, 45–70.

Shannon R. D. (1976) Revised effective ionic radii and systematic studies of interatomic distances in halides and chalcogenides. *Acta Cryst. A.* **32**, 751–767.

Sharp, M., Righter, K. and Walker, R.J. (2015) Estimation of trace element concentrations in the lunar magma ocean using mineral- and metal-silicate melt partition coefficients. *Meteor. Planet. Sci.* **50**, 733-758.

Shearer C. K., McKay G., Papike J. J. and Karner J. M. (2006) Valence state partitioning of vanadium between olivine-liquid: Estimates of the oxygen fugacity of Y980459 and application to other olivine-phyric martian basalts. *American Mineralogist* **91**, 1657–1663.

Simon S. B. and Sutton S. R. (2017) Valence of Ti, V, and Cr in Apollo 14 aluminous basalts 14053 and 14072. *Meteorit. Planet. Sci.* **52**, 2051–2066.

Snyder G. A., Taylor L. A. and Neal C. R. (1992) A chemical model for generating the sources of mare basalts: Combined equilibrium and fractional crystallization of the lunar magmasphere. *Geochim. Cosmochim. Acta* **56**, 3809–3823.

Spandler C. and O'Neill H. S. C. (2010) Diffusion and partition coefficients of minor and trace elements in San Carlos olivine at 1,300°C with some geochemical implications. *Contrib. Mineral. Petrol.* **159**, 791–818.

Solomon, S.C. and Longhi, J. (1977) Magma oceanography: 1. thermal evolution. *Proc. Lunar Sci. Conf.* **8**, 583-599.

Stead C. V., Tomlinson E. L., Kamber B. S., Babechuk M. G. and McKenna C. A. (2017) Rare earth element determination in olivine by laser ablation-quadrupole-ICP-MS: an analytical strategy and applications. *Geostand. Geoanalytical Res.* **41**, 197–212.

Steele, I.M., and Smith, J.V. (1975) Minor elements in lunar olivine as a petrologic indicator. *Proceedings of Lunar Science Conference*, **6**, 451-467.

Sun C. and Liang Y. (2012) Distribution of REE between clinopyroxene and basaltic melt along a mantle adiabat: effects of major element composition, water, and temperature. *Contrib. Mineral. Petrol.* **163**, 807–823.

Sun C. and Liang Y. (2013) The importance of crystal chemistry on REE partitioning between mantle minerals (garnet, clinopyroxene, orthopyroxene, and olivine) and basaltic melts. *Chem. Geol.* **358**, 23–36.

Sutton S. R., Jones K. W., Gordon B., Rivers M. L., Bajt S. and Smith J. V. (1993) Reduced chromium in olivine grains from lunar basalt 15555: X-ray Absorption Near Edge Structure (XANES). *Geochim. Cosmochim. Acta* **57**, 461–468.

Sutton S. R., Karner J., Papike J., Delaney J. S., Shearer C., Newville M., Eng P., Rivers M. and Dyar M. D. (2005) Vanadium K edge XANES of synthetic and natural basaltic glasses and application to microscale oxygen barometry. *Geochim. Cosmochim. Acta* **69**, 2333–2348.

Suzuki T. and Akaogi M. (1995) Element partitioning between olivine and silicate melt under high pressure. *Phys Chem Minerals* **22**, 411–418.

Taura H., Yurimoto H., Kurita K. and Sueno S. (1998) Pressure dependence on partition coefficients for trace elements between olivine and the coexisting melts. *Phys. Chem. Miner.* **25**, 469–484.

Taylor, S.R. and Jakes, P. (1974) The geochemical evolution of the moon. *Proc. 5th Lunar Conf.*, 1287-1305.

Thomas J. B., Bodnar R. J., Shimizu N. and Sinha A. K. (2002) Determination of zircon/melt trace element partition coefficients from SIMS analysis of melt inclusions in zircon. *Geochim. Cosmochim. Acta* **66**, 2887–2901.

Toplis M. J. and Carroll M. R. (1995) An experimental study of the influence of oxygen fugacity on Fe-Ti oxide stability, phase relations, and mineral-melt equilibria in ferro-basaltic systems. *J. Petrol.* **36**, 1137–1170.

Usselman T. M., Lofgren G. E., Donaldson C. H. and Williams R. J. (1975) Experimentally reproduced textures and mineral chemistries of high-titanium mare basalts. In pp. 997–1020.

Wadhwa M. (2008) Redox conditions on small bodies, the Moon and Mars. *Rev. Mineral. Geochem.* **68**, 493–510.

Walker, D., kirkpatrick, R.J., Longhi, J., and Hays, J.F. (1976) Crystallization history of lunar picritic basalt sample 12002: Phase-equilibria and cooling-rate studies. *GSA Bulletin* **87**, 646–656.

Watson E. B. (1979) Calcium content of forsterite coexisting with silicate liquid in the system Na_2O-CaO-MgO-Al_2O_3-SiO_2. *Am. Mineral.* **64**, 824–829.

Wood B. J., Smythe D. J. and Harrison T. (2019) The condensation temperatures of the elements: A reappraisal. *American Mineralogist* **104**, 844–856.

Wood B. J., Wade J. and Kilburn M. R. (2008) Core formation and the oxidation state of the Earth: Additional constraints from Nb, V and Cr partitioning. *Geochim. Cosmochim. Acta* **72**, 1415–1426.

Wood, J.A., Dickey Jr., J.S., Marvin, U.B. and Powell, B.N. (1970) Lunar anorthosites and a geophysical model of the Moon. *Proc. Apollo 11 Lunar Sci. Conf.* **1**, 965-988.

Xirouchakis D., Hirschmann M. M. and Simpson J. A. (2001) The effect of titanium on the silica content and on mineral-liquid partitioning of mantle-equilibrated melts. *Geochim. Cosmochim. Acta* **65**, 2201–2217.

York D. (1968) Least squares fitting of a straight line with correlated errors. *Earth Planet. Sci. Lett.* **5**, 320–324.

Zajacz Z. and Halter W. (2007) LA-ICPMS analyses of silicate melt inclusions in co-precipitated minerals: Quantification, data analysis and mineral/melt partitioning. *Geochim. Cosmochim. Acta* **71**, 1021–1040.

Zanetti A., Tiepolo M., Oberti R. and Vannucci R. (2004) Trace-element partitioning in olivine: modelling of a complete data set from a synthetic hydrous basanite melt. *Lithos* **75**, 39–54.

Zhang, Y., Ni, H., and Chen, Y. (2010) Diffusion data in silicate melts. *Reviews in Mineralogy and Geochemistry*, **72**, 311-408.

CHAPTER 3

Temperature and Pressure Effect on the Structural and Vibrational Properties of Forsterite From DFT Studies

Co-authors: Sha Chen and Udo Becker

3.1 Abstract

Vibrational spectroscopy is widely used to identify the composition and structure of minerals. The conditions, such as temperature (T) and pressure (P), affect the lattice parameters of the mineral, thus the frequency and amplitude of vibrational modes. However, studies at high temperatures, especially simultaneous high temperatures and pressure, are rare due to the experimental challenges in the instrumental setup and the difficulty of modeling temperature for computational work. This study applies the quasi-harmonic approximation (QHA) in combination with density functional theory (DFT) to evaluate the temperature and pressure effects on the structure and infrared (IR) and Raman vibrational modes of forsterite. We show that temperature and pressure affect vibrational frequencies merely by changing cell parameters and atomic positions before the temperature is too high that anharmonicity becomes significant. We first obtain lattice parameters under each temperature and pressure pair, then optimize the internal crystal structure, and finally calculate the IR and Raman spectra. The influence of T (up to 1000 K) and P (up to 15 GPa) were investigated separately before a simultaneous change in T and P. The results show strong anisotropy for forsterite, with axis b being the most sensitive to temperature and

pressure, *c* the next, and axis *a* the stiffest. Generally, mode positions shift to higher frequencies by 2.70 ± 1.30 cm^{-1}/GPa with increasing pressure and by -0.017 ± 0.018 cm^{-1}/K with increasing temperature. The modes associated with stretching and bending of SiO_4 are relatively less affected by *T* or *P* than translational and rotational ones. In addition, we studied the isotope and chemical substitution and cation distribution effect on the vibrational modes for solid solution $(Mg, Fe)_2SiO_4$. All modes of fayalite (Fa) are smaller in wavenumber than of forsterite (Fo) as a combined effect of the heavier mass of Fe and larger cell parameters in fayalite. Intermediate species, $fo_{50}fa_{50}$, have the normal modes in between in general. However, different configurations of intermediate species show a significant difference in vibrational modes ($\Delta\nu_i$ = 28 to - 41.5 cm^{-1}). This study provides a methodology to compute vibrational frequencies under simultaneous temperature and pressure, and evaluates the effect of various factors on the vibration modes. Results show that multiple factors (*T*, *P*, isotope, chemical composition, cation distribution) can significantly affect IR and Raman modes. Therefore, caution should be taken when using the modes to identify solid solution compositions.

3.2 Introduction

Vibrational spectroscopy is a powerful tool for understanding lattice dynamics, mineral structures and compositions, and the thermodynamic behavior of minerals. It is not only applicable to the conditions of the Earth's interior but also widely used in extraterrestrial exploration. Space exploration missions are usually equipped with spectrometers for mineral identification and composition on planetary surfaces. For example, the Martian Moons eXploration (MMX) mission by the Japan Aerospace Agency is planned to be launched in 2024 to the surface of Phobos and is equipped with a Raman spectrometer. The MMX rover will perform site investigations of the mineralogical composition using Raman spectroscopy (Cho et al., 2021). Vibrational spectra are

sensitive to various factors, such as temperature, pressure, chemical composition, isotopic substitution, cation distribution, and spin states. A thorough examination of the effect of each on vibrational modes is essential before any applications.

This study focuses on olivine, a common rock-forming mineral found in many planetary bodies (Earth, Moon, Mars, Mercury, etc.). The structural and vibrational properties of olivine have been widely studied by using both experimental and physical-mechanical computations (Iishi, 1978; Akaogi et al., 1984; Hofmeister, 1987; Rao et al., 1988; Chopelas, 1990; Gillet et al., 1991; Chopelas, 1991; Ghose et al., 1992; Wang et al., 1993; Gillet, 1996; Noel et al., 2006; Li et al., 2007; McKeown et al., 2010; Stangarone et al., 2017). However, many, if not all, studies of infrared absorption and Raman spectroscopy for olivine have primarily been carried out either under ambient conditions (Paques-Ledent and Tarte, 1973; Iishi, 1978; Hofmeister, 1987, 1997; Kuebler et al., 2006; Dyar et al., 2009), high pressure at room temperature (Besson et al., 1982; Chopelas, 1990; Durben et al., 1993), or high temperature at ambient pressure (Kolesov and Geiger, 2004). To our knowledge, there are no published studies for simultaneous changes in temperature and pressure for olivine due to the difficulties in experimental setup and computational modeling.

Here, we focus on the temperature and pressure effect on the crystal structure and vibrational modes of forsterite (Mg_2SiO_4), the Mg-rich endmember of olivine, using DFT. While the simulation of high pressures is fairly straightforward, it is not for high temperatures. Before the temperature gets very high such that anharmonicity is significant, QHA is accurate enough to model the temperature effect. In addition, T and P changes affect the vibrational frequencies of a crystal mainly by changing the cell parameters and internal coordinates when anharmonicity is insignificant. Details on the pros and cons of this approach can be found in Section 3.4.1 in

Methods. Therefore, three steps are taken to compute the vibrational modes: using QHA to obtain cell parameters under *T* and *P*, performing geometry optimizations under fixed cell parameters to optimize the internal coordinates of atoms, and lastly, computing the vibrational frequencies of IR and Raman. In addition, we briefly examine the isotope and chemical compositional effect and cation ordering on the vibrational frequencies. The thermodynamics of the Fo-Fa solid solution is examined and presented in Appendix C.

3.3 Background of olivine

Olivine belongs to the orthorhombic crystal system with the point group mmm in Hermann-Mauguin notation or D2h in the Schönflies notation. The space group is Pbnm, a non-conventional setting of Pnma with its space group number 62. The formula of olivine can be written as $M1M2SiO_4$, with the two types of octahedral sites, $M1O_6$ and $M2O_6$, being non-equivalent. There are four formula units in the unit cell. Therefore, both octahedral sites have multiplicities of 4. The M1 octahedron is distorted and smaller in size than M2. The most common metal cations in the octahedral sites are Fe and Mg. Because of the similar ionic radii of Fe and Mg, they form a complete solid solution, and the two end members are forsterite Mg_2SiO_4 and fayalite Fe_2SiO_4. There are 28 atoms in a unit cell, resulting in 84 vibrational modes corresponding to the total degree of freedom.

The theoretically derived symmetry decomposition of the 84 normal modes at the center of the Brillouin zone Γ is

$$\Gamma_{\text{total}} = 11A_g + 11B_{1g} + 7B_{2g} + 7B_{3g} + 10A_u + 10B_{1u} + 14B_{2u} + 14B_{3u} \qquad (3.1)$$

A Brillouin zone is a primitive cell of a crystal in its reciprocal space. A_g, $B_{1g,}$ and such are Mulliken symbols representing different symmetry types (irreducible representations).

The character table of a point group can tell us which irreducible representations are IR

active and Raman active (Figure 3.1). The irreducible representations corresponding to linear functions are IR active (B_{1u}, B_{2u}, and B_{3u}), and quadratic functions are Raman active (A_g, B_{1g}, B_{2g}, and B_{3g}). Symmetry A_u modes are silent. There are 35 IR-active and 36 Raman-active vibrational modes in total. Three (acoustic) modes are translations of the entire system ($B_{1u} + B_{2u} + B_{3u}$).

$$\Gamma_{IR} = 9B_{1u} + 13B_{2u} + 13B_{3u} \tag{3.2}$$

$$\Gamma_{Raman} = 11A_g + 11B_{1g} + 7B_{2g} + 7B_{3g} \tag{3.3}$$

Character table for point group D_{2h}

D_{2h}	E	C_2 (z)	C_2 (y)	C_2 (x)	i	σ (xy)	σ (xz)	σ (yz)	linear functions, rotations	quadratic functions	cubic functions
A_g	+1	+1	+1	+1	+1	+1	+1	+1	-	x^2, y^2, z^2	-
B_{1g}	+1	+1	-1	-1	+1	+1	-1	-1	R_z	xy	-
B_{2g}	+1	-1	+1	-1	+1	-1	+1	-1	R_y	xz	-
B_{3g}	+1	-1	-1	+1	+1	-1	-1	+1	R_x	yz	-
A_u	+1	+1	+1	+1	-1	-1	-1	-1	-	-	xyz
B_{1u}	+1	+1	-1	-1	-1	-1	+1	+1	z	-	z^3, y^2z, x^2z
B_{2u}	+1	-1	+1	-1	-1	+1	-1	+1	y	-	yz^2, y^3, x^2y
B_{3u}	+1	-1	-1	+1	-1	+1	+1	-1	x	-	xz^2, xy^2, x^3

Figure 3.1 Character table for point group of D2h from http://symmetry.jacobs-university.de/.

The olivine structure consists of isolated SiO_4 tetrahedra and two different MgO_6 octahedra. The tetrahedra have three different Si-O distances. The skewing of the tetrahedra is caused by the Coulomb force from Mg on Si and O atoms (Lam et al., 1990). Each of the two different Mg-octahedra has three distinct Mg1-O distances and four distinct Mg2-O distances.

Aside from the three acoustic modes, the remaining vibrational modes can be attributed to the translations of M1, M2, and SiO_4, and the rotation and internal movement of SiO_4. The internal movements of SiO_4, bending and stretching, can be divided into four types based on their symmetries ν_1, ν_2, ν_3, and ν_4 (Figure 3.2) (Lam et al., 1990). The ν_1 and ν_2 modes are symmetric stretching and bending of the Si-O bond, respectively, with the Si atom being stationary. The ν_3 and ν_4 modes are antisymmetric stretching and bending modes, respectively, with the Si atom not

stationary. The type of vibration is connected to the symmetry derived from the correlation method and summarized in Table 3.1 (Paques-Ledent and Tarte, 1973; Hofmeister, 1987).

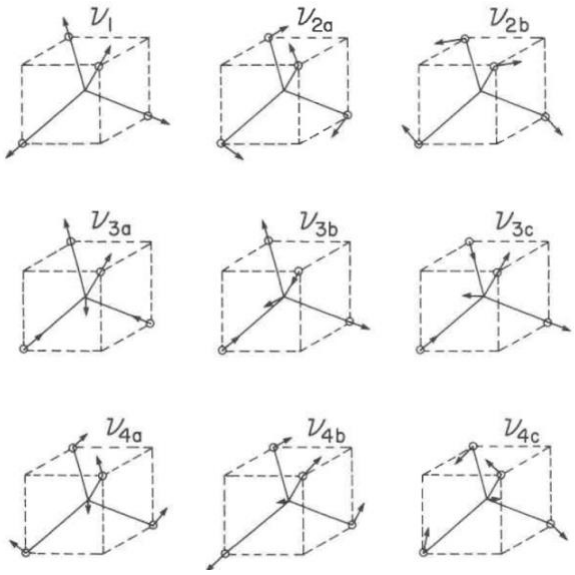

Figure 3.2 The vibrational motion of v_1, v_2, v_3, through v_4 for an isolated SiO_4 tetrahedron. From Figure 3 of Lam et al. (1990).

Table 3.1 Classification of normal modes (81) of olivine for Pbnm. The three acoustic modes are excluded.

		Raman				infrared			silent
		A_g	B_{1g}	B_{2g}	B_{3g}	B_{1u}	B_{2u}	B_{3u}	A_u
SiO_4 internal (N = 36)	ν1	1	1	0	0	0	1	1	0
	ν2	1	1	1	1	1	1	1	1
	ν3	2	2	1	1	1	2	2	1
	ν4	2	2	1	1	1	2	2	1
	total	**6**	**6**	**3**	**3**	**3**	**6**	**6**	**3**
Rotation (N = 12)	SiO_4 rotation	**1**	**1**	**2**	**2**	**2**	**1**	**1**	**2**
Translation (N = 33)	SiO_4 translation	2	2	1	1	0	1	1	1
	M1 translations	0	0	0	0	3	3	3	3
	M2 translations	2	2	1	1	1	2	2	1
	total	**4**	**2**	**4**	**2**	**4**	**6**	**6**	**5**

3.4 Methods

3.4.1 Pressure and temperature effect on vibrational frequencies and QHA

The temperature and pressure dependence of a given frequency includes contributions from two aspects: 1) volume change due to compressibility (*P*) and thermal expansion (*T*); 2) a volume independent contribution from lattice anharmonicity (*T*) (Gillet et al., 1989; Dai et al., 2013; Deshpande et al., 2014). When the temperature is not very high such that anharmonicity can be ignored, vibrational frequencies with fixed composition are a function of volume (Liu, 1993; Gillet, 1996). When the temperature is very high, the interaction between phonons must be considered. Other ways such as molecular dynamics and Monte Carlo have to be used. Although both can be useful, they are only strictly valid for solids at elevated temperatures as they neglect the effect of vibrational quantum effects such as the zero point energy. Therefore, anharmonicity has to be evaluated to use QHA. Gillet et al. (1989) stated that the anharmonic effect for mantle minerals became noticeable above 1000 K. The anharmonic correction at 1000 K led to a difference of 2% in heat capacity C_v, and it became 7% at 2000 K. However, their experiments were conducted at room pressure. The higher the pressure, the valid domain of QHA in temperature is also larger (Carrier et al., 2007). Several studies (Baroni et al., 2010; Dovesi et al., 2018; Allen, 2020) show that simulation with QHA is remarkably accurate in a wide temperature range up to close to the melting line. The temperature and pressure range of olivine in the upper mantle is about 1800 °C and 14 GPa. Our simulations never go beyond that. Therefore, the temperature and pressure range simulated in this study should be accurate enough using QHA.

Another way to evaluate the anharmonicity is to use the parameter mode anharmonicity a_i, which is defined as $a_i = \left(\frac{\partial ln\nu_i}{\partial T}\right)_V = \alpha(\gamma_{iT} - \gamma_{iP})$ (Gillet et al., 1989). If a_i is not equal to 0, then it is anharmonic. Gillet (1996) concluded that the parameter a_i in different silicates and different

high-temperature and high-pressure measurements typically ranges from $-1\cdot10^{-5}$ to $-1\cdot10^{-4}$ K^{-1}. The absolute value is larger for low wavenumber modes (typically lattice modes). To estimate the effect of anharmonicity on vibrational frequencies, we can do the following calculation. Suppose a_i is near the maximum of measured experimental data, i.e., -10^{-4} K^{-1}. When the volume is constant (i.e., the pressure and temperature effect cancel each other out, leaving the volume unchanged), the frequency change increases with temperature change. If the temperature change is 1000 K, then the relative change of ν_i would be ~10%. When the temperature is below 1000 K, this offset caused by anharmonicity is acceptable (which may be smaller than the computational error).

The QHA is a good approximation at low temperature before the temperature is high enough to be anharmonic. It is widely used for thermal properties and temperature effect on vibrational frequencies (Reynard et al., 1992; Li et al., 2007; Wu and Wentzcovitch, 2007; Deringer et al., 2014; Wen et al., 2017) and is expected to be a good approximation for most of the mantle and only becomes a problem near the core-mantle boundary based on the measured melting temperature and expected mantle temperature (Wentzcovitch et al., 2010). QHA assumes all the bonds in a given crystal volume behave harmonically, but their equilibrium length can change. Temperature and pressure affect the vibrational frequencies only through volume changes. However, this is only strictly true for cubic structures. Literature has reported significant anisotropy in compressibility and thermal expansion for olivine (Andrault et al., 1995; Trots et al., 2012). Except for the cell parameters, correct fractional coordinates of atoms in the unit cell are equally important. If we keep the exact fractional coordinates as static, all bond lengths will change proportionally with cell parameters, which is incorrect based on experimental data. SiO_4 tetrahedra are more rigid than MgO_6 octahedra. Hazen (1976) concluded that the thermal expansion and compressibility of Mg octahedra are comparable to those of bulk forsterite. The stronger Si-O bond

neither expands nor compresses much. Therefore, optimization of both cell parameters and fractional coordinates are considered in this study at the equilibrium cell volume.

3.4.2 Calculation of vibrational frequencies under changing T and P conditions

The Crystal17 program is used for the DFT + QHA computations (Erba, 2014; Erba et al., 2015c, a, b). As discussed in the section above, vibrational frequencies under changing *T* and *P* are merely a function of equilibrium geometry. Therefore, geometry optimizations under certain pressures or temperatures are conducted first, followed by respective frequency computations. The initial forsterite structure is from Bostroem (1987), with cell parameters of 4.749, 10.1985, and 5.9792 Å. The functional B3LYP is used, which is a hybrid between a Hartree-Fock approach for the exchange term, and a BLYP functional for correlation. The basis sets used are: 8-511d1G_valenzano_2006 for Mg (Valenzano et al., 2007), 86-311G for Si (Pascale et al., 2005; Noel et al., 2006), and 8-411d11G for O (Valenzano et al., 2006). Isotopes can also affect frequencies. The default isotopes used in the frequency calculations are 23.9850 for Mg, 27.9769 for Si, and 15.9949 for O.

In this study, we conducted three series of calculations to examine the temperature and pressure effect: 1) pressure up to 15 GPa at static temperature (0 K); 2) temperature up to 900 K at static pressure (no hydrostatic pressure) to avoid anharmonicity; 3) simultaneous temperature and pressure. The computation is relatively easy for the sole pressure effect at 0 K. The optimized structure under external hydrostatic pressure can be easily obtained; then, the vibrational frequencies can be computed. When temperature changes, QHA has to be used to obtain volume (only cell parameters *a*, *b*, *c*, no internal coordinates) under *T* and *P* first, then followed by geometry optimization of the internal atomic positions while fixing the cell parameters, and finally IR and Raman frequencies computation for the optimized structure. The pressure at a given volume

V and temperature T has two parts: $P(V,T) = P(V_0 \rightarrow V)_{T=T_0} + P_{th}(T_0 \rightarrow T)_V$. The first term is the pressure needed to change the volume at a reference temperature. The second term is thermal pressure, defined as the pressure change at constant volume V due to the temperature change.

Our ultimate goal is to compute IR and Raman spectra under simultaneous T and P, where there is a lack of relevant data from both experiments and computations. Olivine is one of the dominant mineral phases in Earth's upper mantle down to the 410-km seismic discontinuity, where the phase transition of α-$(Mg,Fe)_2SiO_4$ (olivine) to β-$(Mg,Fe)_2SiO_4$ (wadsleyite) occurs. The pressure at 410 km is approximately 14 GPa, while the temperature is harder to determine. Different methods give different temperatures, but approximate 1800 K (Akimoto et al., 1976; Ito and Katsura, 1989; Trubitsyn and Trubitsyn, 2020). For forsterite, the phase transition at 1600 °C (1873 K) is 15 GPa, and 1200 °C (1473 K) is 14 GPa (Katsura and Ito, 1989). Considering the stability range of forsterite, the temperature/pressure pairs we selected are (1000K, 1GPa), (1000K, 5GPa), (1500K, 1GPa), (1500K, 5GPa), (1500K, 10GPa), and (2000K, 10GPa).

In Crystal17, vibrational frequencies are calculated at the Γ point of the reciprocal unit cell within the harmonic approximation at static temperature and pressure. The Hessian matrix, H_{ij}, is the second derivative matrix of energy due to the displacement of any atom from its equilibrium position. The mass-weighted Hessian matrix is calculated from the dynamic matrix divided by the square root of the mass of any given atom pair. The eigenvalues of the mass-weighted dynamic matrix are the frequencies, and the eigenvectors are the normal modes. Transverse optical (TO) modes are computed by default. Both IR and Raman frequencies and intensities are calculated. Harmonic vibrational frequencies are calculated and fitted for different volumes. Four volumes were used by default. Once the equations of frequencies with volume are determined, all other thermodynamic properties can be analytically derived by minimizing free energy. For example,

the Helmholtz free energy F of the system in QHA can be written as a function of crystal structure X and temperature T:

$$F(X,T) = U(X) + \sum_i \frac{1}{2} h\nu_i(X) + k_B T \sum_i ln\left(1 - e^{-\frac{h\nu_i(X)}{k_B T}}\right), \quad (3.4)$$

where the three terms are the internal energy of the system ($U(X)$), zero-point vibrational energy ($\sum_i \frac{1}{2} h\nu_i(X)$), and the temperature effect of the vibration part ($k_B T \sum_i ln(1 - e^{-\frac{h\nu_i(X)}{k_B T}})$). The minimization of the free energy is also used to compute other mineral properties. For example, the isothermal bulk modulus K_T can be written this way and be computed:

$$K_T = V\left(\frac{\partial^2 F}{\partial V^2}\right)_T. \quad (3.5)$$

The pressure P is a function of both T and V. $P(V, T)$ are fitted by an appropriate equation of state (EoS) to obtain bulk the modulus K_T and its derivative K' at different temperatures. The EoS is the third-order Birch-Murnaghan equation. The third-order Birch-Murnaghan isothermal equation of state is used for the volume change in response to pressure:

$$P(V) = \frac{3B_0}{2}\left[\left(\frac{V_0}{V}\right)^{\frac{7}{3}} - \left(\frac{V_0}{V}\right)^{\frac{5}{3}}\right]\left\{1 + \frac{3}{4}(B_0' - 4)\left[\left(\frac{V_0}{V}\right)^{\frac{2}{3}} - 1\right]\right\}. \quad (3.6)$$

3.5 Results

3.5.1 Crystal structure changes with increasing temperature and pressure

The crystal structure (cell parameters and bond lengths) of forsterite was examined under high temperature and pressure to study its compressibility and thermal expansion. The calculated cell parameters and volume data for each temperature and pressure pair are presented in Table 3.2. Cell parameters and volume with a single parameter changed (P or T) are plotted and compared to the literature data in Figure 3.3. The ratio of the cell parameters at a given temperature and pressure

divided by that under the ambient conditions (~300 K, ~0 GPa) are plotted to remove any slight difference in the initial cell parameters and because we are mainly interested in unit cell changes due to changes in the *P/T* conditions. Good agreement is achieved between our calculated data and the literature data.

To evaluate the volume and cell parameters change as a function of temperature and pressure, two parameters are essential: bulk modulus and thermal expansion coefficient. Bulk modulus is a measure of volume change in resistance to pressure. The thermal expansion coefficient represents the volume change due to temperature. For bulk modulus, the isothermal bulk modulus K_T is defined as

$$K_T = -V\left(\frac{\partial P}{\partial V}\right)_T = -\left(\frac{\partial P}{\partial lnV}\right)_T. \quad (3\text{-}7)$$

The adiabatic bulk modulus K_S is defined analogously through an adiabatic process (no heat exchange). The compressibility is the reverse of the bulk modulus. The bulk thermal expansivity α is defined as

$$\alpha = \frac{1}{V}\left(\frac{\partial V}{\partial T}\right)_P = \left(\frac{\partial lnV}{\partial T}\right)_P. \quad (3\text{-}8)$$

And linear thermal expansivity

$$\alpha_i = \frac{1}{x}\left(\frac{\partial x}{\partial T}\right)_P = \left(\frac{\partial lnx}{\partial T}\right)_P. \quad (3\text{-}9)$$

Table 3.2 Calculated unit-cell parameters for forsterite under temperature (in K) and pressure (in GPa).

temperature (K)	pressure (GPa)	cell parameters			Volume Å^3
		a (Å)	*b* (Å)	*c* (Å)	
0	0	4.791	10.295	6.016	296.7
0	1	4.782	10.259	6.000	294.4
0	5	4.750	10.129	5.942	285.9
0	10	4.715	9.984	5.877	276.7
0	15	4.685	9.858	5.818	268.7
300	0	4.806	10.359	6.045	300.9
500	0	4.813	10.386	6.057	302.8
700	0	4.818	10.409	6.066	304.2
900	0	4.825	10.437	6.078	306.1
1000	0	4.828	10.448	6.083	306.8
1000	5	4.791	10.297	6.018	296.9
1500	10	4.772	10.219	5.984	291.8
1500	5	4.809	10.369	6.050	301.6
2000	10	4.789	10.288	6.014	296.3
2000	20	4.726	10.024	5.894	279.2

There is a connection between the logarithm of volume and cell parameters. Therefore, logarithmic fitting for data computed in this study is conducted and shown in Figure 3.3. A second-order polynomial rather than a linear function is used for the large *P*, *T* range. Because of the significantly smaller (four orders lower) coefficient in the T^2 and P^2 terms, the coefficient for *T* and *P* can be used to compare the compressibility and linear thermal expansivity along different axes of olivine.

Compression and thermal expansion work in an opposite way on cell parameters, in such that increasing pressure decreases the cell volume, and increasing temperature does the opposite. The dln/d*P* for the *a*, *b*, and *c* axis are -0.0018, -0.0034, and -0.0026 GPa^{-1} at 0 GPa. The slope indicates that the compressibility is the highest along the *b* axis, followed by *c* and *a*. This agrees with the literature (Andrault et al., 1995; Finkelstein et al., 2014). The dln/d*T* for the *a*, *b*, and *c* axis are $1.04\cdot10^{-5}$, $2.02\cdot10^{-5}$, $1.54\cdot10^{-5}$ K^{-1} at 0 K. They also represent the linear thermal expansion at 0 K. Axis *b* is the most sensitive to temperature, then *c*, and *a*, the same order as compressibility.

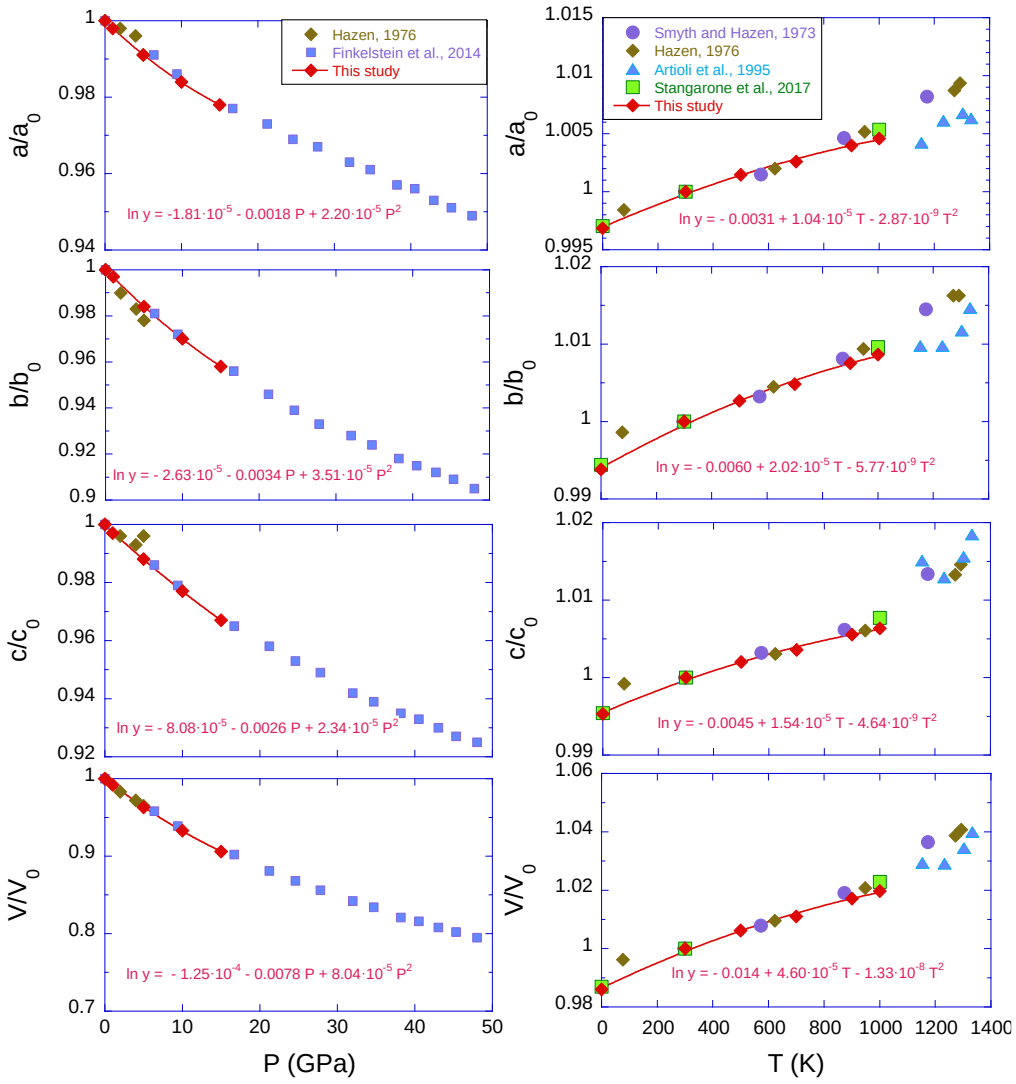

Figure 3.3 Lattice parameter changes (*a*, *b*, *c*, and volume V divided by their respective values at ambient conditions P ~ 0 GPa or T ~ 300 K) with pressure (left panel) and temperature (right) in this study compared with the literature. A second-order polynomial equation is used to fit the logarithm of (cell parameter or volume)/(respective value at zero *P*/*T*) ratio with either a function of P or T. Only data in this study is used for the fitting.

The two bulk moduli, K_S and K_T, of the system are also computed in this study at different *P* and *T* by minimizing the second derivative of energy to the volume. The data are shown in Table 3.3 and Figure 3.4. The values of K_S and K_T are equal to each other at zero temperature only. The K_S is always larger than K_T at any finite temperature. The bulk modulus and its derivative to pressure computed by fitting the third-order Birch-Murnaghan equation at 0 K and 0 GPa are 123.5 GPa and 4.35, respectively, comparable to the literature (Table 3.3). The bulk modulus at 0 K is

reported at different pressures. A linear fit of the bulk modulus with P is $K = 123.3 + 4.30\ P$ (in GPa). This value falls within the range of literature values, although a large range is reported. The K_T and K_S data at different temperatures are also reported. To quantify the bulk modulus as a function of temperature, we use a second-order polynomial to fit K_S and K_T with T and obtain the Equations 3.10 and 3.11 (also shown in Figure 3.4):

$$K_T = 121.1 - 0.015\ T - 1.03 \cdot 10^{-5}\ T^2, \quad (3.10)$$

$$K_S = 121.5 - 0.012\ T - 8.36 \cdot 10^{-6}\ T^2. \quad (3.11)$$

Table 3.3 Bulk modulus calculated in this study and the literature. Fo = Mg_2SiO_4. Fa = Fe_2SiO_4. Compo. = composition.

	compo.	$K_{T=298K}$	K_S	$K_{T=298K}$'	$K_{T=0K}$	$K_{T=0K}$'	methods
This study	Fo	115.7		4.35	123.5	4.35	DFT + QHA simulation
(Fabrizio Nestola et al., 2011)	$Fo_{92}Fa_8$	123.2		5.6			measure the P-V curve
(F. Nestola et al., 2011)	Fo-Fa	124.7 ± 0.9		5.3 ± 0.3			experiment
(Poe et al., 2010)	Fo	124.4		4.9			single-crystal XRD
(Couvy et al., 2010)	Fo	129.6 ± 3.2					macro-powder forsterite
(Couvy et al., 2010)	Fo	123.3 ± 3.4					nanocrystalline forsterite
(Abramson et al., 1997)	Fo	126.3	129.4	4.28			
(Zha et al., 1996)	Fo	128.8		4.2			
(Downs et al., 1996)	Fo	125		4			
(Andrault et al., 1995)	Fo-Fa	131		4			sound velocity measurements
(Kudoh and Takéuchi, 1985)	Fo	123		4.3			
(Suzuki et al., 1983)	Fo	127.6	128.9				
(Hazen, 1977)	Fo	113		4			
(Hazen, 1976)	Fo	132		4			

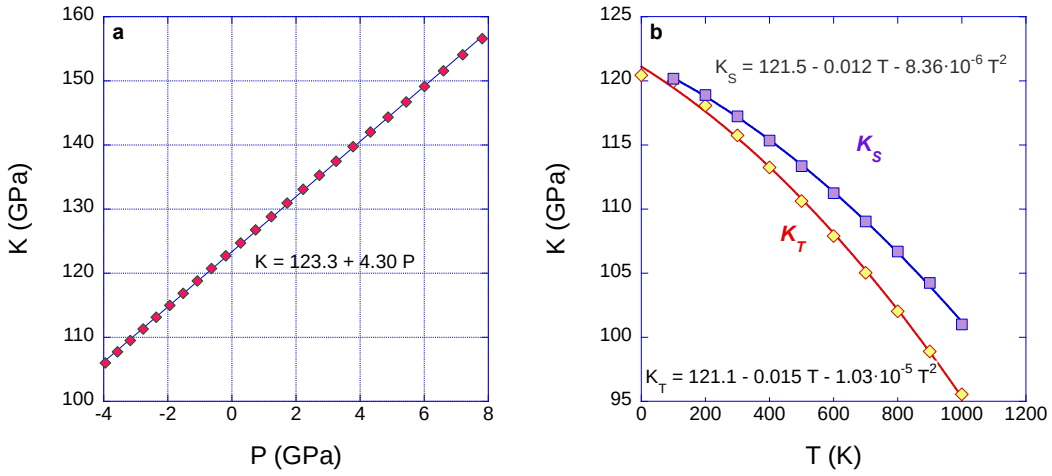

Figure 3.4a Bulk modulus at different pressures at 0 K. A linear fitting equation is shown. **b.** Isothermal and adiabatic bulk modulus at different temperatures. The second-order polynomial equation is shown.

Both volumetric and linear thermal expansion coefficients are calculated in this study up to 1000 K. Thermal expansivity increases with T while $\frac{\partial \alpha}{\partial T}$ decreases with T (Figure 3.5). Forsterite shows a strong anisotropy with $\alpha_b > \alpha_c > \alpha_a$. Axis a is the stiffest among the three axes. Various equations about the thermal expansion coefficient with temperature have been proposed. We fit our data using the equation $\alpha = a_0 + a_1 \cdot T + a_2/T^2$ and compare them with the literature (Table 3.4). Some papers use a linear relation (without the $1/T^2$ term).

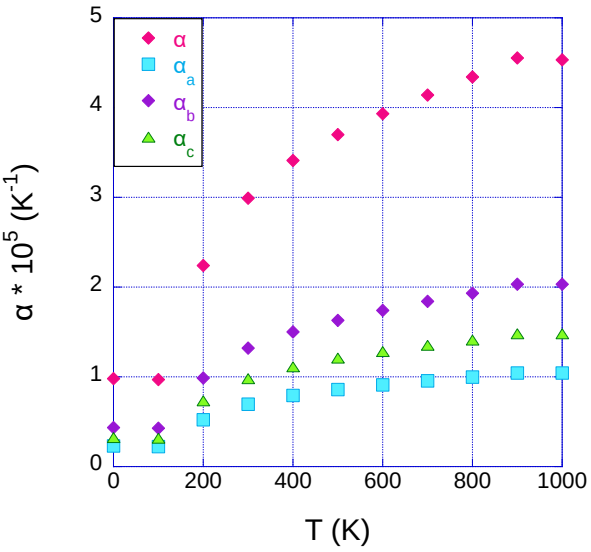

Figure 3.5 Thermal expansion α and linear thermal expansion coefficient α_a, α_b, and α_c. The connection between the bulk and linear thermal expansion coefficients is $\boldsymbol{\alpha_V = \alpha_a + \alpha_b + \alpha_c}$.

Table 3.4 Thermal expansion coefficient equation from this study and the literature. The α_0, α_1, and α_2 are coefficients of the equation $\alpha = a_0 + a_1 \cdot T + a_2/T^2$.

	T (K)	$10^5\ a_0$	$10^8\ a_1$	a_2
This study (including $1/T^2$ term)	0 - 1000	1.96	2.28	1.81
(Kumazawa and Anderson, 1969)		2.47	4.7	
(Hazen, 1976)	298 - 1293	2.56		
(Suzuki et al., 1983)	298 - 1213	2.48		
(Gillet et al., 1991)	300 - 2000	2.77	0.97	-0.32
(Bouhifd et al., 1996)	300 - 2150	2.832	0.758	
(Trots et al., 2012)	297 - 1313	3.23	0.63	

The bond lengths in the crystal structures calculated at different *T*/*P* are plotted in Figure 3.6. The ratio is used in reference to the 0 K or 0 GPa conditions. Generally, Mg2-O bonds are more sensitive to *P*/*T* than Mg1-O bonds, and Si-O bonds are the least.

For thermal expansion, different Mg-O expansions with temperature vary from $(1.7\pm0.2)\cdot10^{-5}$ to $(5.1 \pm 0.5)\cdot10^{-5}$ Å/K with the average $2.9\cdot10^{-5}$ Å/K, which agrees well with 2-5 10^{-5} Å/K in Hazen (1976). The temperature effect on Si-O is less significant. The bond lengths first increase with temperature up to 700 K and then drop for T = 1000 K. The variations are small.

A linear fitting gives the expansion rate of Si-O from $(2.3 \pm 4.8)\cdot10^{-6}$ to $(6.1 \pm 2.5)\cdot10^{-6}$ Å/K with the average $4.1\cdot10^{-6}$ Å/K. The expansion of Mg-O is approximately seven times higher than the one of Si-O. Hazen (1976) concludes that the Si-O neither expands nor compresses with temperature, and the change of Mg-O is comparable to the volume change. The insignificant change of Si-O bonds with temperature can be explained by isolated tetrahedra in olivine. For silicates, the bond lengths and volumes for tetrahedra with four bridging O atoms seem to increase with temperature faster than those with four non-bridging O atoms.

The Mg-O compression with pressure varies from $(-7.7 \pm 0.4)\cdot10^{-3}$ to $(-3.5 \pm 0.06)\cdot10^{-3}$ Å/GPa with an average of $-5.4\cdot10^{-3}$ Å/GPa. The compression rate for Si-O varies from $(-1.5 \pm 0.02)\cdot10^{-3}$ to $(-1.0 \pm 0.02)\cdot10^{-3}$ Å/GPa with the average of $-1.29\cdot10^{-3}$ Å/GPa. The compression of Mg-O is approximately four times higher than Si-O on average.

Under Earth interior conditions, compression under pressure affects olivine cell parameters and bond lengths more than thermal expansion. If we take the pressure at the 410 km discontinuity to be 14 GPa and the temperature being ~ 1800 K, the average Mg-O changes by -0.0756 Å due to pressure and 0.0522 due to temperature. The same is true for the Si-O bond and volume. That explains a generally smaller volume and bond length with depth.

Considering the bond length change to the volume, from 0 to 900 K, the volume change is 3.2%. Si-O is 0.21%, and Mg1-O 0.9%. Mg2-O 1.54%. With pressure from 0 to 15 GPa, the volume change is -9.4%. Si-O is -1.2%. Mg1-O -3.1%. Mg2-O -4.2%.

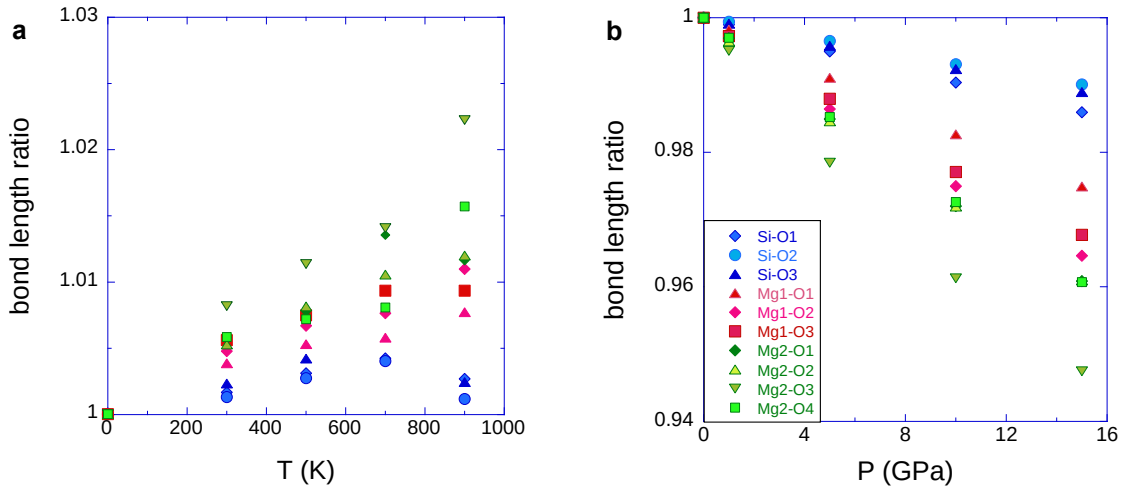

Figure 3.6a Bond lengths ratios (bond length at given *T* / bond length at 0 K) change with temperature for calculated structures in this study for forsterite; **b.** bond lengths ratios (bond length at given *P* / bond length at 0 GPa) with pressure. Blue symbols: Si-O. Green symbols: Mg2-O. Red symbols: Mg1-O.

3.5.2 IR and Raman spectra and mode assignments

Under different temperatures and pressures, the IR and Raman spectra are similar in peak intensities with some shifts in peak positions. Here, we start with the mode assignments of IR and Raman spectra at 0 external pressure and a temperature of 0 K (static). Then, spectra with varying temperature and pressure results are presented in the following two sections.

For the Raman spectra, there is a typical doublet consisting of two high-intensity modes in the Raman spectra between 800 and 880 cm^{-1}, with their peak positions being a function of composition. Therefore, many studies have used the peak positions of this doublet to derive olivine composition (Wang et al., 2004; Kuebler et al., 2006; Breitburg et al., 2018). For forsterite at static conditions (0 K, 0 GPa), the highest-intensity peak (DB1) is calculated to be 837.8 cm^{-1}, and the second peak (DB2) is 855.8 cm^{-1} for static calculations (Figure 3.7). A visualization of the DB1 is shown in Figure 3.8. Both modes have Ag symmetry, in agreement with the literature.

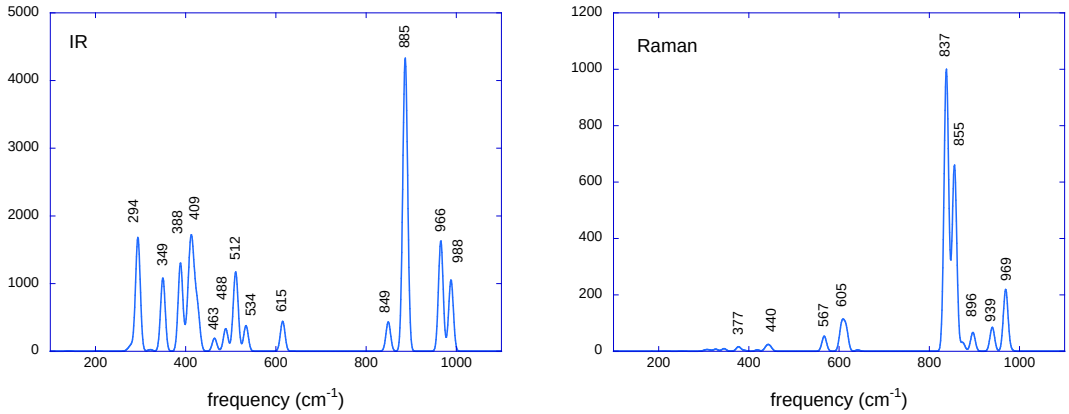

Figure 3.7 IR and Raman spectra (relative intensity versus wavenumber) at static conditions.

IR and Raman spectra have been intensely investigated by FTIR and Raman spectroscopy and computations. However, most of them were obtained at ambient T and P by experiment and static (0 K, 0 GPa) conditions by calculations. The IR and Raman frequencies calculated at 300 K and 0 GPa is used to compare with the experimental data from different sources; the frequencies calculated at static are compared with computational data in the literature (Tables 3.5 and 3.6). The lowest frequencies of Ag were calculated to be negative, thus not presented. There is a lack of good consistency in the reported data, probably due to errors in both experiments and computations. In the IR and Raman measurements, polarization mixing could induce errors in the peak positions. In calculations, different computational parameters can introduce systematic errors.

The energy required to excite a phonon is the greatest for stretching, followed by bending, rotation, and translation. Bending movement changes the bond angle between two neighboring O atoms and a cation in the center while stretching changes the bond length. Stretching modes are typically higher energy (i.e., higher wave number) than bending modes. The stretching vibration frequency depends on the mass of the atoms and the stiffness of the bond. Heavier atoms vibrate more slowly than lighter ones, thus vibrating at a lower frequency. Stretching modes can have symmetric and asymmetric stretching. The asymmetric stretching is usually of higher energy.

Kuebler et al. (2006) have divided them into ranges of wave numbers < 400, 400 - 700, 700 - 900 cm^{-1} for Raman. Others use 500 (Breitburg et al., 2018) and 800 cm^{-1} as the separating wavenumber. Generally speaking, Raman-active phonons below 500 cm^{-1} are lattice modes, where the SiO_4 tetrahedra act as rigid units, and Mg2 translations are mixed with SiO_4 rotations and translations. The Raman modes above 500 cm^{-1} have atomic displacements dominated by motions internal to the SiO_4 tetrahedra. Paques-Ledent and Tarte (1973) summarized that the IR region of 800-1050 cm^{-1} corresponds to stretching vibrations of the SiO_4 tetrahedron, 650 - 475 cm^{-1} to the bending of SiO_4, and below 475 cm^{-1} are external modes mainly due to the vibrations of the MgO_6 octahedra.

For static calculation in this work, the mode assignment for IR and Raman are summarized in Tables 3.5 and 3.6. Types of vibration predicted from symmetry (Table 3.1) are used as a constraint, although the visualization of each mode shows extensive mode mixing, especially between translation and rotation. As the literature stated, the lower modes are attributed to the translation of Mg cations and the rotation of SiO_4. The boundary is between 400 – 500 cm^{-1}. Many modes are a mixture of two or more movements; therefore, they are hard to distinguish clearly. This is understandable because the Mg-O bond and SiO_4 share the O atoms. Thus, the movement of Mg atoms may perturb SiO_4 tetrahedra.

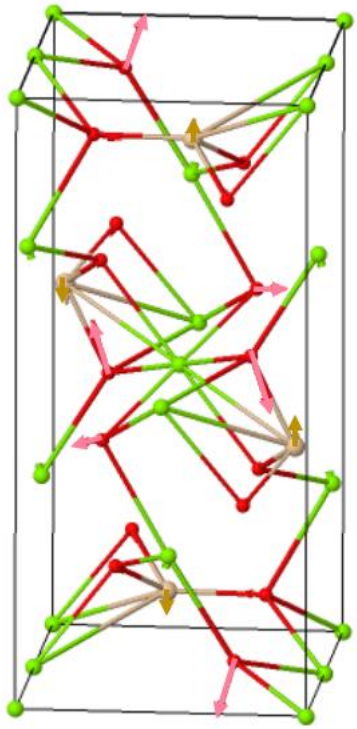

Figure 3.8 The first peak of the Raman doublet. Frequency 837.8 cm^{-1}. Symmetry Ag. Green balls represent Mg atoms; red is O; pink is Si. The arrows, if any, represent the movement of each atom This mode is attributed to the symmetric stretching of SiO_4 with the Si atom being approximately stationary (ν_1).

Table 3.5 IR vibrational frequencies compared with the literature and their mode assignment. Noel2006: Noel et al. (2006); Hofmeister 1987: Hofmeister (1987); Iishi1978: Iishi (1978).

	This study			Noel2006		Hofmeister1987			Iishi1978		
	TO 0 K	TO 300 K	mode	TO	LO	TO	LO	mode	TO	LO	mode
B1u											
1	210	205	T(Mg1)	207	207	276	276	T(M2)	201		T(M1)
2	279	268	T(Mg1, Mg2)	278	279	293	299	T(M1)	224		T(M1)
3	293	276	T(Mg1, Mg2)	290	313	309	313	T(M1)	274	278	T(M1, M2)
4	310	291	R(SiO_4), T(Mg)	313	320	365	371	T(M1)	296	318	T(M1)
5	416	395	R(SiO_4)	420	426	412	450	R?	365	371	R(SiO_4)
6	424	409	R(SiO_4),T(Mg1)	428	461	463	482	R	423	459	R(SiO4)
7	489	476	ν2	490	499	502	538	ν2	483	489	ν2
8	512	502	ν4	514	592	543	573	ν4	502	585	ν4
9	886	867	ν3	874	1005	865	957	ν3	885	994	ν3
B2u											
1	206	192	T(Mg,SiO_4)	143	144	142	144	T(SiO_4)	144		T(M1,
2	271	265	T(Mg)	277	277	268	276	T(M2)	224		T(M2)
3	296	281	T(Mg2)	292	312	290	298	T(M1)	280	283	T(M1)
4	322	317	T(Mg, SiO_4)	350	387	300	308	T(M1)	294	313	T(M1, M2)
5	388	367	T(Mg), R(SiO_4)	403	417	345	375	T(M2)	352	376	T(M2)
6	410	398	T(Mg), R(SiO_4)	432	453	398	408	T(M1)	400	412	T(M1)
7	476	460	T(Mg), R(SiO_4)	465	495	418	438	R	421	446	R(SiO_4)
8	509	496	T(Mg), ν2	517	520	452	488	ν2	465	493	ν2
9	539	527	T(Mg), ν4	535	588	504	511	ν4	510	516	ν4
10	615	605	ν4	638	638	520	572	ν4	537	597	ν4
11	850	829	ν1	835	843	828	844	ν1	838	843	ν1
12	966	950	ν3	870	966	865	961	ν3	882	979	ν3
13	988	973	ν3	989	999	984	996	ν3	987	993	ν3
B3u											
1	141	135	T(Mg,SiO_4)	206	207	201	201	T(SiO_4)	201		T(M1,SiO_4)
2	279	265	T(Mg2)	275	276	275	276	T(M2)	224		T(M2)
3	294	278	T(Mg1)	294	300	294	298	T(M1)	274	276	T(M1,M2)
4	349	333	T(Mg2)	322	323	309	313	T(M1)	293	298	T(M1)
5	403	392	T(Mg1)	388	398	319	321	T(M2)	320	323	T(M1)
6	428	414	T(Mg1)	412	473	377	388	R?	378	386	T(M1)
7	464	448	T(Mg1), R(SiO_4)	476	482	405	430	T(M1)	403	469	R(SiO_4)
8	515	501	T(Mg), ν2	513	539	434	463	ν2	498	544	ν2
9	534	523	ν4	540	563	505	511	ν4	562	566	ν4
10	639	626	ν4	614	660	601	644	ν4	601	645	ν4
11	849	828	ν1	838	838	841	842	ν1	838	845	ν1
12	889	865	ν3	962	971	950	961	ν3	957	963	ν3
13	991	972	ν3	982	1086	988	991	ν3	980	1086	ν3

Table 3.6 Raman vibrational frequencies compared with the literature and their mode assignment. Iishi1978: Iishi (1978); Chopelas1991: Chopelas (1991); Noel: Noel et al. (2006); McKeown: McKeown et al. (2010); S2017: Stangarone et al. (2017).

	This study, calc			Iishi 1978		Chopelas1991		Noel	McKeo	S2017
	0 K	300 K	mode	Exp.	mode	Exp.	mode	Calc.	Exp.	Calc.
Ag										
1	66	109	T(Mg2,SiO_4)	183	T(M2, SiO_4)	183	T(SiO_4)	188	183	191
2	211	259	T(Mg2,SiO_4)	227	T(M2, SiO_4)	226	T(SiO_4)	234	227	234
3	306	296	T(Mg2,SiO_4)	305	T(M2, SiO_4)	304	T(M2)	307	305	315
4	327	314	T(Mg2)	329	T(M2)	329	R(SiO_4)	329	329	335
5	345	333	R(SiO_4)	340	R(SiO_4)	339	R(M2)	345	340	351
6	440	411	ν2	424	ν2	422	ν2	425	423	432
7	567	510	ν4	546	ν4	545	ν4	560	546	556
8	606	611	ν4	609	ν4	608	ν4	618	609	616
9	838	812	ν1	826	ν1	824	ν1 + ν3	819	826	819
10	856	858	ν3	856	ν3	856	ν1 + ν3	856	856	857
11	969	948	ν3	966	ν3	965	ν3	967	966	974
B1g										
1	222	216	T(Mg2,SiO_4)	192	T(M2, SiO_4)	220	T(SiO_4)	225	227	228
2	259	249	T(Mg2,SiO_4)	224	T(M2, SiO_4)	274	T(SiO_4)	260	275	263
3	313	301	T(Mg2,SiO_4)	260	T(M2, SiO_4)	318	R(SiO_4)	317	318	323
4	361	347	T(Mg2)	318	T(M2)	351	T(M2)	367	374	372
5	390	383	R(SiO_4)	418	R(SiO_4)	383	T(M2)	391	384	393
6	440	426	ν2	434	ν2	434	ν2	442	434	447
7	608	584	ν4	583	ν4	582	ν4	596	583	593
8	641	629	ν4	632	ν4	632	ν4	645	632	644
9	854	830	ν1	839	ν1	838	ν1 (+ν3)	835	839	834
10	874	857	ν3	866	ν3	866	ν3(+ ν1)	866	866	867
11	981	963	ν3	976	ν3	975	ν3	979	976	985
B2g										
1	188	171	M2, R(SiO4)	142	T(Mg2)	175	T(SiO_4)	183	175	195
2	298	288	R(SiO_4), M2	244	T(SiO_4)	242	R(SiO_4)	253	244	304
3	323	310	T(SiO_4), M2	324	R(SiO_4)	323	T(M2)	324	324	327
4	377	364	R(SiO_4)	368	R(SiO_4)	365	R(SiO_4)	373	368	388
5	419	406	ν2	441	ν2	439	ν2	451	441	424
6	615	596	ν4	588	ν4	586	ν4	608	588	605
7	940	920	ν4	884	ν3	881	ν3	883	882	929
B3g										
1	183	177	M2, R(SiO_4)	226	T(SiO_4)	286	T(SiO_4)	190	203	183
2	250	232	M2, R(SiO_4)	272	T(M2)	315	R(SiO_4)	303	272	257
3	325	309	M2, T(SiO_4)	318	R(SiO_4)	374	T(M2)	322	318	331
4	375	360	R(SiO_4)	376	R(SiO_4)	410	ν2	381	376	378
5	447	430	ν2	412	ν2	435	R(SiO_4)	421	411	455
6	615	594	ν4	595	ν4	592	ν4	609	595	603
7	897	876	ν3	922	ν3	920	ν3	927	922	886

3.5.3 Pressure dependence of the vibrational frequencies for forsterite

The pressure dependence of the vibrational frequencies is calculated up to 15 GPa at 0 K. The peak positions for IR and Raman active modes are presented in Tables 3.5 and 3.6. The spectra are provided in Figure 3.9. The IR spectra are similar for different pressures, just shift to higher frequencies with pressure (Figure 3.9 and 3.10) and show a good roughly linear trend except for one B_{1u} mode at 209.7 cm^{-1} for 0 GPa (Figure 3.10). This mode barely changes its peak position with pressure. The linear fitting gives a slightly negative slope (-0.18 ± 0.29). For Raman, a similar trend is observed with some deviations. For example, the frequencies at 5 GPa are higher than at 10 GPa, and four modes do not show a good linear trend (Figure 3.10). All the four Raman modes that deviate from linear trends have the symmetry of A_g. This rough linear trend agrees well with the literature studies. Wang et al. (1993) and Chopelas (1990) showed that all of the Raman bands move to higher frequencies with increasing pressure, and the frequency shift displays a linear relation for pressure up to ~7 – 9 GPa. Then there is a decrease in the pressure derivative of some Raman modes. They attributed the change in slope to the compression mechanism change of forsterite with pressure. It may explain the deviation of some Raman modes in our study.

Except for the B_{1u} mode being invariant with pressure, the dv_i/dP for IR varies from 1.5 to 4.7 with an average of 3.0 ± 1.0 (σ) cm^{-1}/GPa. For Raman, except for the mode with a frequency of 211 cm^{-1} at 0 GPa, the dv_i/dP varies from 0.6 to 4.8 with an average of 2.6 cm^{-1}/GPa. Although the dv_i/dP shows no significant difference for low-frequency and high-frequency modes (Figure 3.11), the relative frequency change shows a much higher value for low-frequency modes than for high-frequency modes. The isothermal mode Grüneisen parameter can be used to quantify the relative frequency change with pressure.

The Grüneisen parameter connects the volume and vibrational frequencies directly. The *i*th

vibrational mode of a crystal has a mode Grüneisen parameter γ_i

$$\Gamma_i = -\frac{d\ ln\nu_i}{d\ lnV}. \tag{3.12}$$

If we combine Equation 3.4 (the definition of the bulk modulus) and 3.9, the Grüneisen parameter of *i*th mode at a specific temperature (isothermal mode Grüneisen parameter) γ_{iT} can be written as

$$\gamma_{iT} = K_T\left(\frac{\partial \ln \nu_i}{\partial P}\right)_T. \tag{3.13}$$

Similarly, if we combine Equation 3.5 (the definition of thermal expansion coefficient) and (9), the Grüneisen parameter of the *i*th mode at a given pressure *P* (isobaric mode Grüneisen parameter) can be written as

$$\gamma_{iP} = \frac{1}{\alpha}\left(\frac{\partial \ln \nu_i}{\partial T}\right)_P. \tag{3.14}$$

In the QHA, pressure and temperature affect the vibrational frequencies only through the volume changes and then $\gamma_{iT} = \gamma_{iP}$ (Gillet, 1996).

The isothermal mode Grüneisen parameter, γ_{iT}, is much smaller for modes > 600 cm^{-1} which are associated with the internal stretching and bending within the SiO_4 tetrahedra. Therefore, we can conclude that the internal movement of SiO_4 is less affected than the external lattice modes. This is consistent with Chopelas (1990). They attributed this to more volume change of the MgO_6 octahedra than SiO_4 tetrahedra (Hazen 1976).

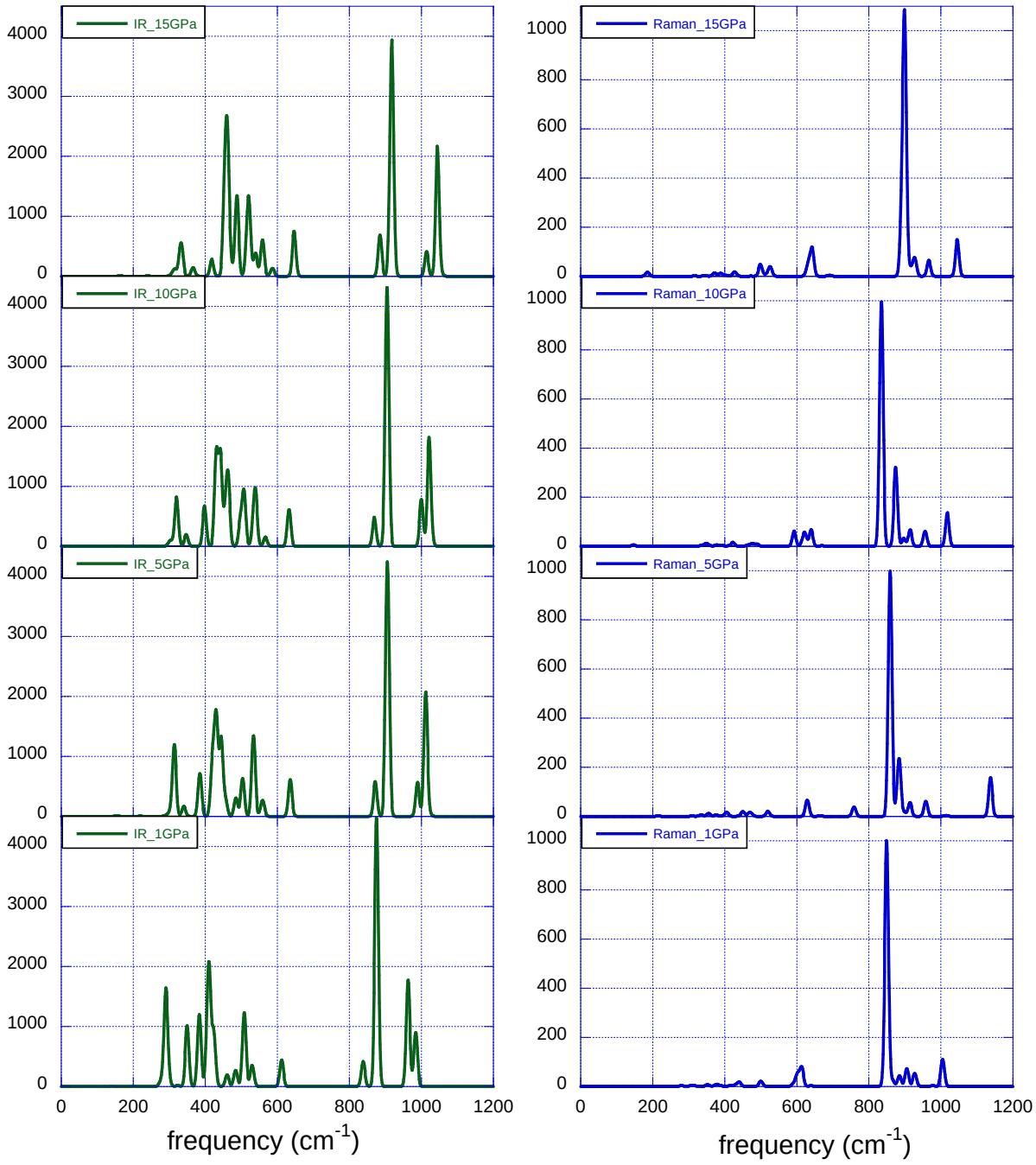

Figure 3.9 IR and Raman spectra under different pressures up to 15 GPa. All temperatures are at 0 K.

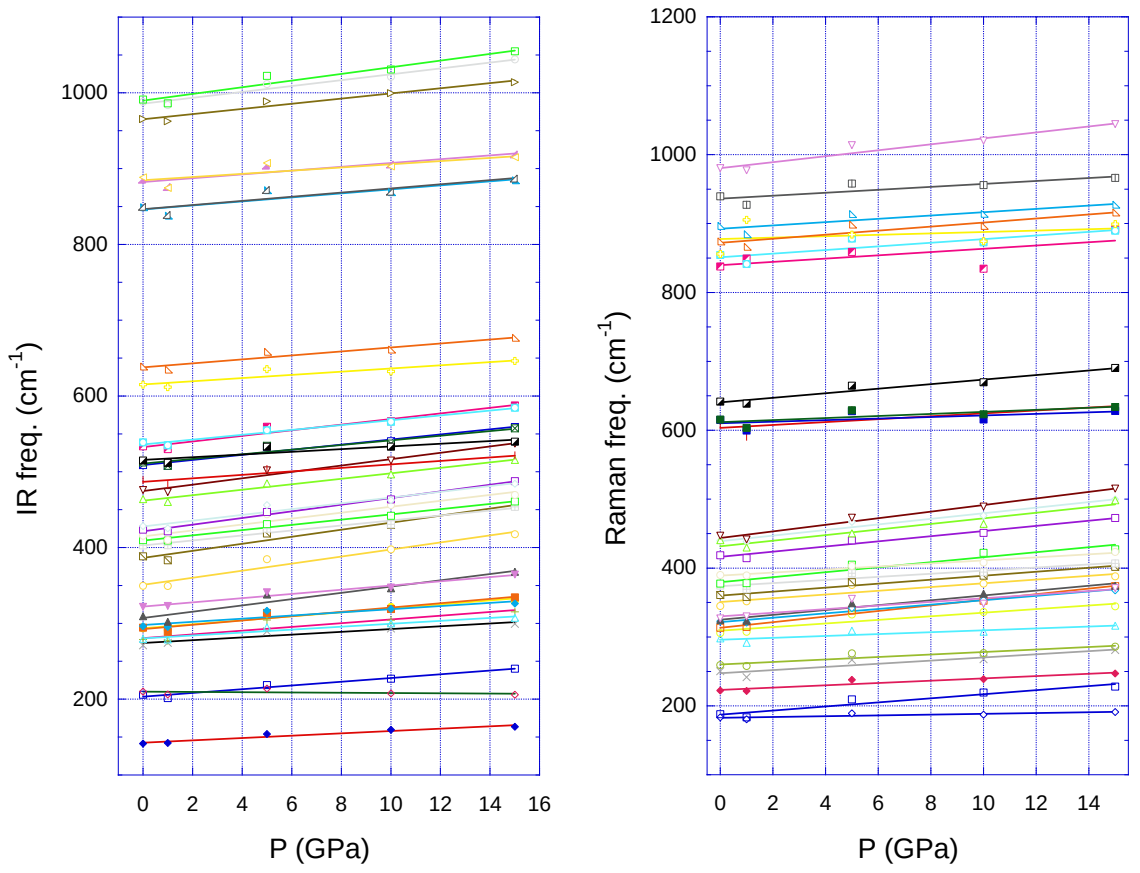

Figure 3.10 Linear frequency fitting with pressure. Four Raman modes (#4, 23, 24, and 35) are removed from the figure because of a high scattering with pressure. All four modes have the symmetry of Ag.

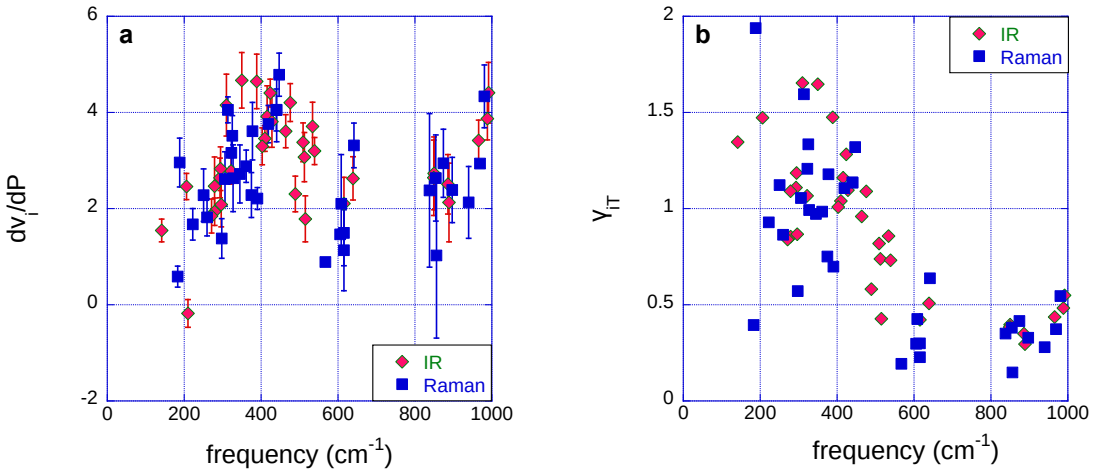

Figure 3.11a IR and Raman frequencies shift (dv_i/dP) with pressures. All temperatures are at 0 K. The lowest frequency data for Raman is excluded. The frequency data in the plot is from 0 GPa. **b.** The isothermal mode mode Grüneisen parameter (γ_{iT}) at 0 K. The bulk modulus is used 123.3 GPa in this study. The frequency data in the figure is from 0 GPa. The two negative modes (one IR, one Raman) are not shown.

3.5.4 Temperature dependence of the vibrational frequencies for forsterite

The IR and Raman vibrational modes for different temperatures are grouped based on the irreducible representation (symmetry) mode. With increasing temperature, the frequency at each mode shifts to a lower wavenumber and shows a roughly linear relationship (Figure 3.12), consistent with the literature on Raman studies (Gillet et al., 1991; Stangarone et al., 2017; Liu et al., 2021). No IR spectra with temperature have been reported, to our knowledge. For each mode, linear fitting was conducted. The slope represents the frequency shift with temperature $\Delta v_i/\Delta T$. The $\Delta v_i/\Delta T$ varies from -0.033 to -0.007 cm^{-1}/K, with an average of -0.020 ± 0.005 cm^{-1}/K for IR (Figure 3.13a). For Raman, a few modes do not show a good linear trend. All the outlier modes have the symmetry of A_g and are associated with the internal movement of SiO_4. The rest of the Raman modes have a $\Delta v_i/\Delta T$ from -0.029 to -0.009, with an average of -0.019 ± 0.005 cm^{-1}/K (Figure 3.13a), which is consistent with the range reported from -0.029 to -0.008 with an average of -0.017 in Gillet et al. (1991) by experiments and -0.024 to -0.005 with an average of -0.016 in Stangarone et al. (2017) by computations.

Similar to the pressure effect, the absolute frequency shift with temperature ($\Delta v_i/\Delta T$) does not show a dependence on frequencies (Figure 3.13a). However, the relative change, $\Delta v_i/(\Delta T \cdot v_i)$, shows that temperature affects lower frequencies that are associated with transition and rotation more strongly than the higher-frequency modes that are associated with the internal stretching and bending of SiO_4 (Figure 3.13b).

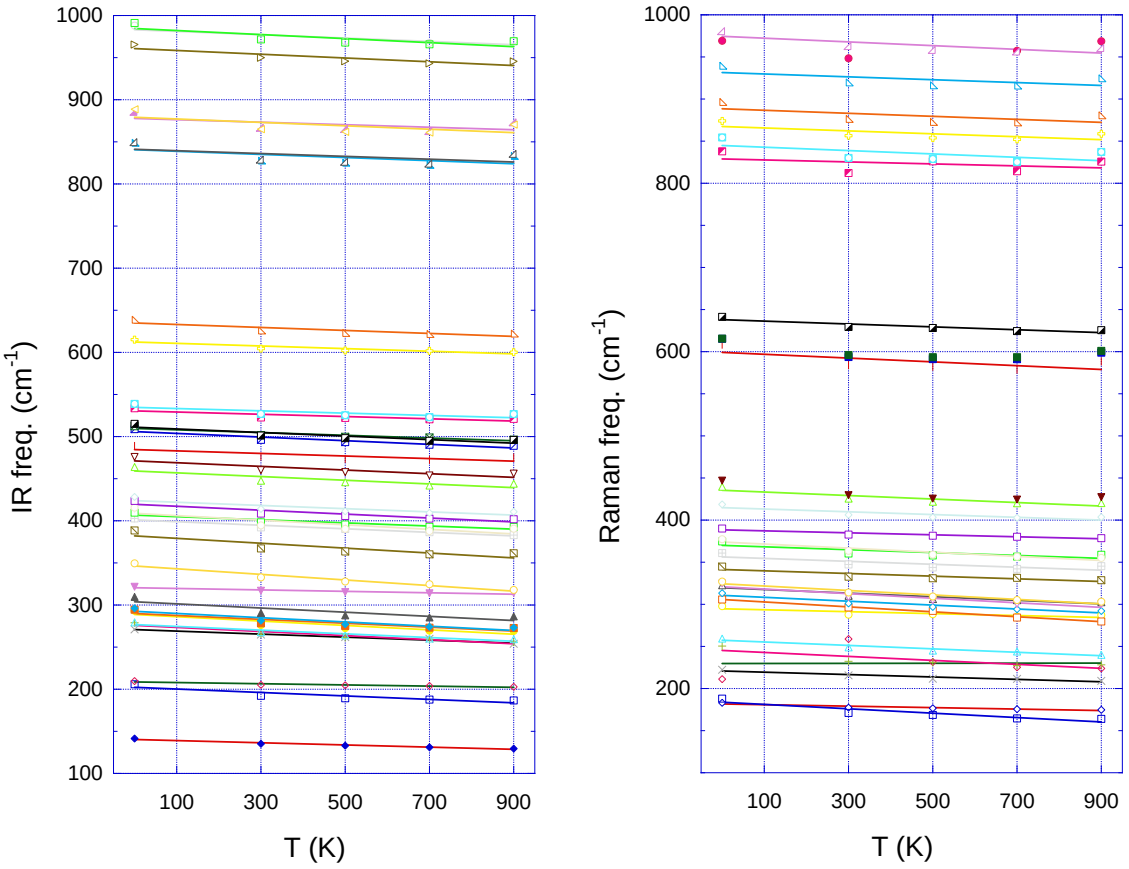

Figure 3.12 Linear frequency fitting with temperature. Four Raman modes (#21, 23, 24, and 31) are removed from the figure because of their non-linear trend with temperature. All four modes have the symmetry of Ag.

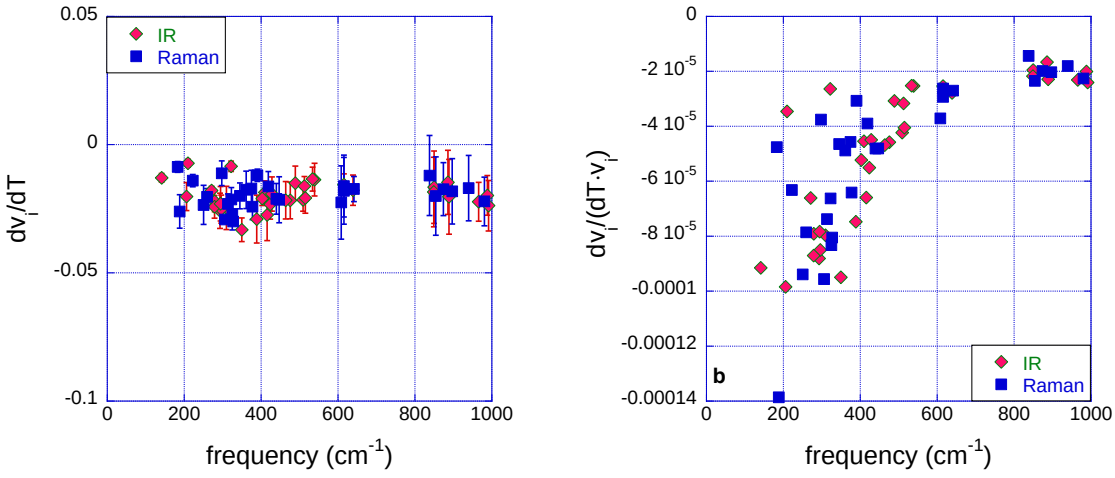

Figure 3.13a IR and Raman frequencies shift (dv_i/dT) with temperature. All pressures are 0 GPa. The lowest frequency data for Raman is excluded. The frequency data in the plot is from static conditions (0 K, 0 GPa). **b.** Relative frequency shifts with temperature ($dlnv_i/dT$). The outliers for Raman in Figure 3.13a are not included.

3.5.5 Vibrational frequencies of forsterite under simultaneous high T and P conditions

Five pairs of *T* and *P*, (1000 K, 5GPa), (1500 K, 10 GPa), (1500 K, 5 GPa), (2000 K, 10 GPa), and (2000 K, 20 GPa), were chosen for simultaneous *T* and *P* effects simulation on vibrational modes (Figure 3.14). The IR and Raman frequencies can be found in Appendix B. IR spectra are similar for different *P* and *T* conditions in peaks and relative intensities, and only the peak frequencies change with T and P. However, it is less so for Raman spectra. Among the five pairs, the spectra of (1000 K, 5GPa) and (2000 K, 10 GPa) are very close, with an average peak difference of 2 cm^{-1}.

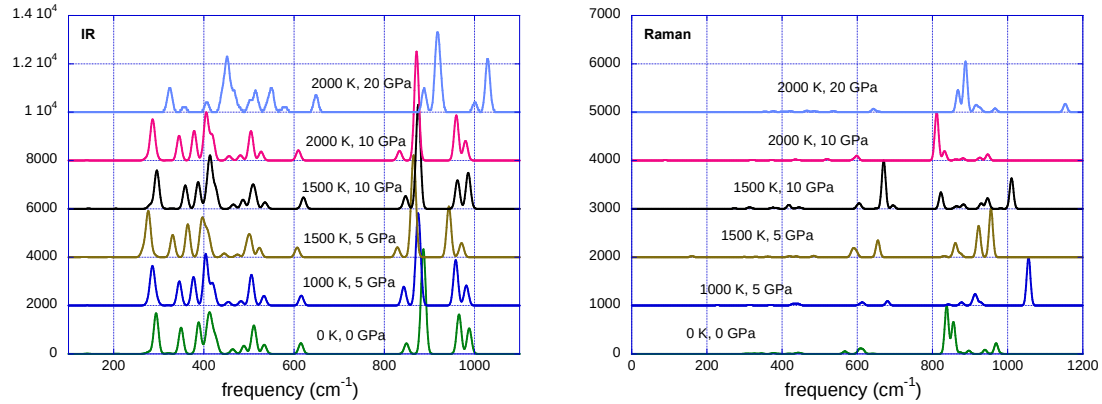

Figure 3.14 IR and Raman spectra at simultaneous high temperatures and pressures.

3.5.6 Compositional and isotope effect on vibrational frequencies

The IR and Raman vibrational frequencies are computed for the endmembers forsterite (Fo) and fayalite (Fa), and the forsterite-fayalite solid solution to examine the compositional effect. There are eight cation positions in the unit cell of olivine. Fe can replace the positions of Mg partially or entirely to form a solid solution. To keep the symmetry of olivine, we only simulated the spectra for $Fo_{50}Fa_{50}$ (four Fe and four Mg atoms in a unit cell) as an intermediate phase and all

four Fe either in the M1 or M2 sites.

One thing to consider is the spin states for Fe. For Fe in fayalite, we considered low-spin and high-spin status, and for the latter, a ferromagnetic (FM) and antiferromagnetic (AFM) configuration. Fayalite has been reported to be a noncollinear antiferromagnetic compound below a Neel temperature of ~65 K with Mossbauer spectroscopy and neutron diffraction studies. T_N decreases to 18.6 K for the composition $Fo_{90}Fa_{10}$. Above the Neel temperature, it is paramagnetic. In our energy computations of different spin states (Table 3.7), fayalite with high-spin Fe is by more than 180 kJ/mol (moles of olivine formula units, not unit cells) more favorable than low-spin fayalite. The Gibbs free energy of the antiferromagnetic spin configuration is 0.8 kJ/(mol Fe) more favorable than its ferromagnetic counterpart. Using $\Delta G=RT_{Neel}$ as an approximation, these calculations result in a calculated Neel temperature of 96 K, which is of a similar order to the experimentally determined value. Therefore, high-spin Fe is more thermodynamically favored in fayalite and, at very low temperatures, with antiferromagnetic spin ordering.

In addition, low-spin fayalite is calculated to have smaller cell parameters than forsterite, while high-spin fayalite shows larger lattice parameters than forsterite. This results from the ionic radius difference. The low-spin Fe^{2+} has an ionic radius of 0.61 Å for VI coordination and 0.78 Å for the high spin, while Mg^{2+} is 0.72 Å (Shannon, 1976). Olivine crystal lattice measurements reported small cell parameters with a higher Fo number in olivine (Jahanbagloo, 1969; Tarantino et al., 2003; F. Nestola et al., 2011; Kroll et al., 2012). Cell parameters data for natural or synthetic olivine from some studies are shown in Table 3.8. Although our calculated cell parameters are relatively larger than natural olivine grains, they can still explain the shift in frequencies due to changes in compositional. Based on the above discussions, high-spin Fe should be used in olivine calculations instead of low spin. Because of the close energy and cell parameters of

antiferromagnetic (AFM) and ferromagnetic (FM) structures and the simplicity of the ferromagnetic setting, we used FM for fayalite and $Fo_{50}Fa_{50}$ computations of the IR and Raman spectra (both FM and AFM configuration are considered for calculations of the thermodynamics of the solid solution, see Appendix C). The energetic comparison between the two $Fo_{50}Fa_{50}$ shows that Fe prefers the M1 site in olivine. A more detailed examination of energy in different configurations shows the same result (details in Appendix C).

Table 3.7 Cell parameters and energetics calculation of olivine. All calculations started from the same structure with cell parameters of 4.749, 10.1985, and 5.9792 Å from Bostroem (1987) for forsterite. The ΔME is for per formula unit mole, not the unit cell mole.

composition	Spin of Fe	a (Å)	b (Å)	c (Å)	ΔME (kJ/mol)
Fa	FM	4.9330	10.4716	6.0469	0
Fa	AFM	4.9219	10.5160	6.0305	-2.5
Fa	LS, unrestricted	4.7159	10.0151	5.8545	184
Fa	LS, restricted	4.6477	9.9543	5.8222	182
$Fo_{50}Fa_{50}$ (Fe in M1)	FM	4.9288	10.4764	5.9402	
$Fo_{50}Fa_{50}$ (Fe in M2)	FM	4.8487	10.4119	6.1459	
Fo	N/A	4.8504	10.3381	6.0581	

Table 3.8 Cell parameters for Fo, $Fo_{50}Fa_{50}$, and Fa in natural or synthetic olivine grains.

composition	a (Å)	b (Å)	c (Å)	reference
Fa	4.818	10.471	6.086	(Smyth, 1975)
Fa	4.8195	10.4788	6.0873	(Fujino et al., 1981)
Fa	4.820	10.476	6.089	Kroll et al., 2012
Fa	4.821	10.474	6.090	Tarantino et al., 2003
$Fo_{50}Fa_{50}$	4.790	10.337	6.037	Tarantino et al., 2003
$Fo_{52.1}Fa_{47.9}$	4.795	10.351	6.045	Kroll et al., 2012
Fo	4.758	10.190	5.982	(Pamato et al., 2019)
Fo	4.7534	10.1902	5.9783	(Fujino et al., 1981)
Fo	4.7554	10.197	5.9822	Kroll et al., 2012
Fo	4.750	10.197	5.980	Tarantino et al., 2003

All modes of fayalite have a lower frequency than the respective ones in forsterite due to larger cell parameters and heavier cation mass (Figure 3.15). The difference varies from -8 to -126 cm^{-1}, with, in general, a slightly more pronounced difference for lower frequency modes. The two solid solutions for $Fo_{50}Fa_{50}$ computations have intermediate frequencies than the two end

members. However, their frequency difference Δv_i varies from 28 to -41.5 cm^{-1}, with the same composition but different Fe-Mg distributions.

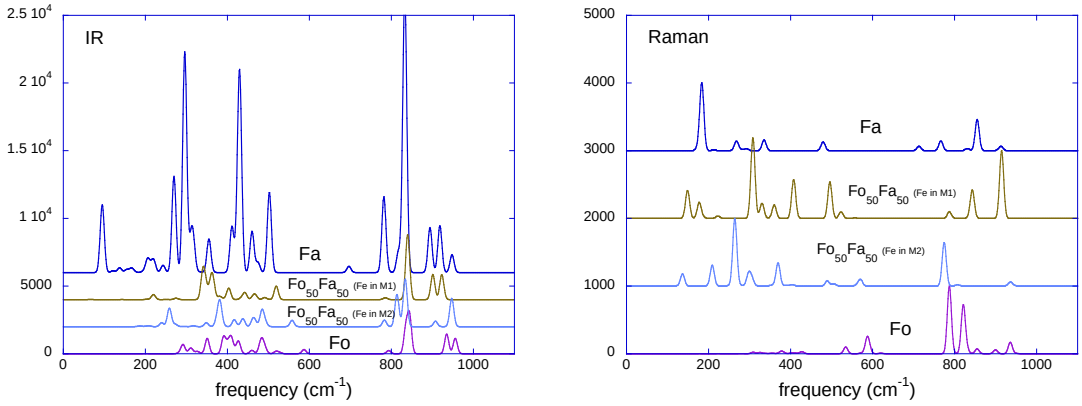

Figure 3.15 IR and Raman vibrational frequencies for Fo-Fa solid solutions.

The lower frequencies in fayalite than forsterite are a combined effect of cell parameters and mass difference. To separate the impact of the two, the isotope effect on vibrational frequencies of olivine alone is examined for metal cations. The default isotope for Mg used is ^{24}Mg. We replace all eight cations in the unit cell of mass 24 with 26 or 56. There is no mass of 56 for Mg (an Mg atom with a mass of 56 behaves chemically as regular Mg but has a mass of Fe, which influences the phonons). This is done to separate the mass and cell parameter effect in fayalite spectra. Both calculations have the same crystal structure with just isotope difference. The results show that ^{26}Mg shifted wavenumbers up to 12 cm^{-1} lighter (Figure 3.16). The high vibrational frequencies (> 800 cm^{-1}) seem to be less impacted (within -1 cm^{-1}) because they are Si-O vibrations. The mass of 56 substitution causes a more significant shift (up to 80 cm^{-1}) than ^{26}Mg because of a larger mass difference.

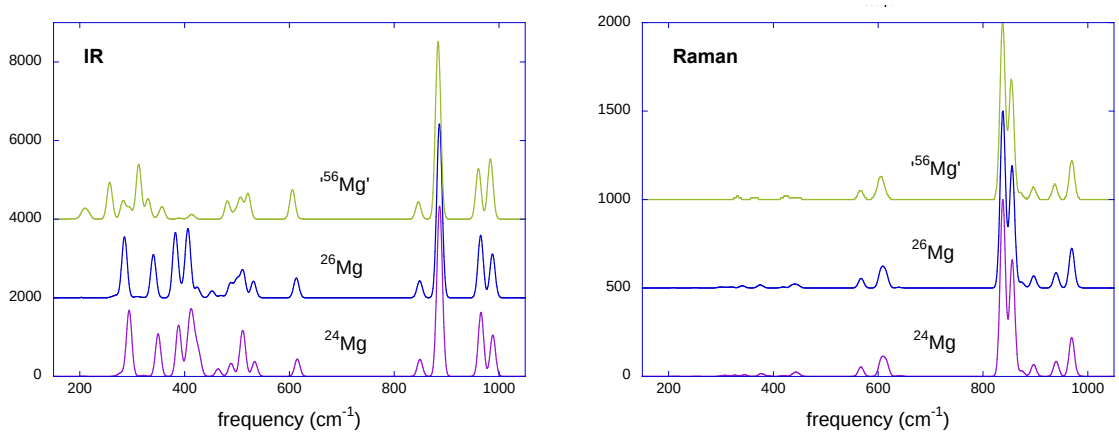

Figure 3.16 Vibrational spectra with different isotopes. All three calculations have the same cell parameters and coordinates but different masses in all eight cations in the unit cell. The intensities of '^{56}Mg' and ^{26}Mg shift up for better visualization (^{26}Mg by 2000 and '^{56}Mg' by 4000 for IR, ^{26}Mg by 500, and '^{56}Mg' by 1000 for Raman).

The vibrational frequencies shift due to mass is not a constant number at different modes, and the shift is not proportional to the mass difference either. For example, the mass difference between ^{24}Mg and ^{26}Mg is 2, and that for '^{56}Mg' is 32. So the shift caused by the '^{56}Mg' mass effect is not simply a factor of 16 for the change caused by ^{26}Mg.

For a simple diatomic molecule harmonic oscillator, the frequency ν can be calculated as $\nu = \frac{1}{2\pi}\sqrt{k/\mu}$ with $\mu = \frac{m_1 m_2}{m_1+m_2}$ being the reduced mass and k the force constant. For the metal cations, they are bonded to O (mass is 16 by default) atoms to form octahedral sites. If we assume that the force constant does not change, then $\nu \sim \sqrt{1/\mu} = \sqrt{\frac{m_1+m_2}{m_1 m_2}} = \sqrt{\frac{m_1+16}{16 m_1}}$. For each mode, the frequency with ^{24}Mg is supposed to be a factor of 1.016 for ^{26}Mg and a factor of 1.139 for '^{56}Mg' (Figure 3.17).

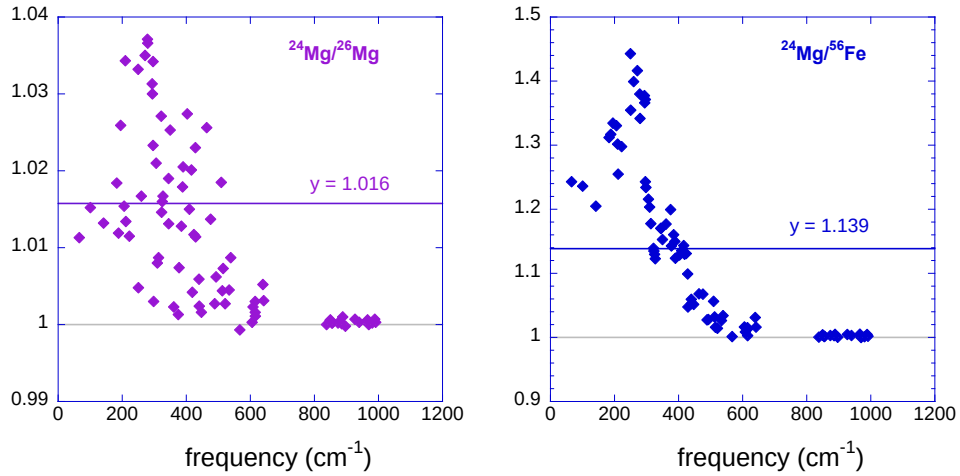

Figure 3.17 Vibration frequencies ratio for each mode due to the isotope effect. All three calculations have the same cell parameters and coordinates but different masses. The isotope substitution applies to all eight cations in the unit cell.

After evaluating the mass effect on vibrational shifts, we can separate the cell parameter and mass effect since the systematic lighter frequencies in fayalite than forsterite are a combined effect of two. Subtracting the shift from the 56 mass effect from a total shift of fayalite should get us the shift caused by cell parameters. The mass effect counts about 50% for the low frequencies and much lower percentages for high frequencies (Figure 3.18), which is plausible. The metal substitution in octahedral sites primarily affects the vibration of MO_6 and less to SiO_4. Because of the shared O atoms, metal ions affect SiO_4 vibrations as well, but to a lesser degree.

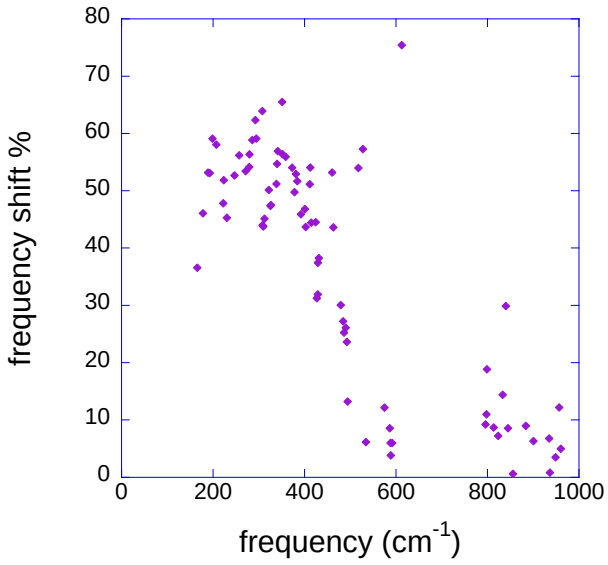

Figure 3.18 Mode frequency shift percentages caused by differences in mass of the cations (total change = change due to Δmass vs Δcomposition).

3.6 Discussions and implications

IR and Raman vibrational properties are a function of composition, temperature, pressure, isotope, spin, etc. In this study, we evaluate the *T*, *P* effect in detail and briefly examine the compositional and cation distribution effect. The results show that all these factors may significantly affect the normal modes. Peak positions of certain vibrational modes, such as the doublet Raman modes, have been used to predict olivine compositions, which is important for geochemists and mineralogists. Forsteritic (higher molar Mg/(Mg+Fe)) olivine is indicative of a primitive magma source, and more fayalitic olivine indicates a more evolved source. However, caution should be taken when there is a relatively large variation in temperature and pressure. The two endmembers of $(Fe,Mg)_2SiO_4$ have approximately a difference of 10 cm^{-1} for the doublet modes. Suppose we take the average of $\Delta v_i/\Delta T$ of – 0.02 cm^{-1} $K^{-1}$and $\Delta v_i/\Delta P$ of 3 cm^{-1} GPa^{-1}. In that case, a 500 K difference in temperature or 3 GPa difference in pressure can entirely supersede the composition indication if failing to consider the temperature and pressure effect. The surface temperature of Mars may vary by 200 K. That temperature difference can lead to a 40% error in

the composition when using Raman to identify mineral compositions/structures on the Martian surface. An alternative option to be tested would be to use lower frequencies controlled by substitution. However, these are typically difficult to measure because of the low relative intensity. This approach may be more widely used with improvements in the experimental technique in the future.

This study helps develop a more comprehensive data set of IR and Raman spectra in *P/T/* compositional space. The data shows that the isotope effect is limited to vibrational frequencies, but factors such as *P*, *T*, composition, and cation ordering, can change peak positions significantly. We can parameterize frequency changes for each mode using a simplified equation as

$$dv_i = a_i dT + b_i dP + c_i X, \tag{3.15}$$

where X is the fractional contribution of fayalite in the olivine. This is a combined effect of temperature-pressure-composition (*P-T-X*). Or, if the specific occupation of iron on the two different cation sites is taken into account, this equation could be expanded to

$$dv_i = a_i dT + b_i dP + c_i X_{Fe}^{M1} + d_i X_{Fe}^{M2}. \tag{3.16}$$

The methodology also allows for a better understanding of under what conditions which phonons or vibrational modes are responsible for certain or abrupt changes in thermal expansion and compression under pressure.

Wide applications can also be found in the reported bulk modulus and thermal expansion data. One important application is in seismic data interpretation. Seismic waves travel at different velocities through any material. The velocity depends on the density and elastic properties of the material. The compressional-wave velocity, $V_p = \sqrt{\frac{K+\frac{4\mu}{3}}{\rho}}$, and shear-wave velocity $V_s = \sqrt{\frac{\mu}{\rho}}$ where *K* is the bulk modulus, μ the shear modulus, and ρ the density. The bulk modulus is important in

the explanation of seismic waves. Although the bulk modulus has been reported in the literature, it is mostly at ambient conditions. However, the bulk modulus of olivine varies significantly with pressure and temperature. We not only report here the data under different *T* and *P*, but also provide a linear/second-order polynomial fitting. It is always better to have the equation of state in an analytical form than just discrete data points at different conditions. Another application of bulk modulus data at high *T*, *P* is on the equation of state, such as the third-order Birch-Murnagham equation. The Birch–Murnaghan isothermal equation of state is usually used at room temperature. With the bulk modulus *K* and its derivative *K'* data at different temperatures, it can then be used for deep Earth conditions.

The methodology introduced in this study provides a way to compute IR absorption and Raman spectra of minerals under simultaneous high temperature and high pressure (not too high that anharmonicity is significant). It can be used not only for olivine but also for other minerals.

3.7 Conclusions

We combine DFT with QHA to simulate the forsterite crystal structure change and vibrational properties under high temperature and pressure. When the temperature is not too high that quasi-harmonic is valid, vibrational frequencies are a sole function of crystal structure (both cell parameters and fractional positions). Using cell parameters obtained by QHA for a certain temperature-pressure pair, we optimized the crystal structure and then computed IR and Raman vibrational frequencies. This is the first time that, to our knowledge, vibrational frequencies under both high temperature and high pressure are reported. A close examination of vibrational frequencies with temperature and pressure reveals that *T* and *P* can significantly affect peak positions. The T- and P- induced frequency shift is different for each mode, but the average is 3 cm^{-1}/GPa and -0.017 cm^{-1}/K. One should take caution when using peak positions to infer olivine

compositions, especially when the environmental conditions (*T*, *P*) change remarkably. In addition to the temperature and pressure effect, we also evaluated the compositional effect (Fe replaces Mg) and isotope effect (^{26}Mg rather than ^{25}Mg) on vibrational frequencies. This study helps develop a more comprehensive data set of IR and Raman spectra in *P/T/* compositional space, which helps predict and interpret olivine data to a wide variety of planetary conditions.

3.8 References

Abramson E. H., Brown J. M., Slutsky L. J. and Zaug J. (1997) The elastic constants of San Carlos olivine to 17 GPa. *Journal of Geophysical Research: Solid Earth* **102**, 12253–12263.

Akaogi M., Ross N. L., McMillan P. and Navrotsky A. (1984) The Mg_2SiO_4 polymorphs (olivine, modified spinel and spinel)–thermodynamic properties from oxide melt solution calorimetry, phase relations, and models of lattice vibrations. *American Mineralogist* **69**, 499–512.

Akimoto S.-I., Akaogi M., Kawada K. and Nishizawa O. (1976) Mineralogic distribution of iron in the upper half of the transition zone in the Earth's mantle. In *The Geophysics of the Pacific Ocean Basin and Its Margin* American Geophysical Union (AGU). pp. 399–405.

Allen P. B. (2020) Theory of thermal expansion: Quasi-harmonic approximation and corrections from quasi-particle renormalization. *Mod. Phys. Lett. B* **34**, 2050025.

Andrault D., Bouhifd M. A., Itié J. P. and Richet P. (1995) Compression and amorphization of $(Mg,Fe)_2SiO_4$ olivines: An X-ray diffraction study up to 70 GPa. *Phys Chem Minerals* **22**, 99–107.

Baroni S., Giannozzi P. and Isaev E. (2010) Density-functional perturbation theory for quasi-harmonic calculations. *Reviews in Mineralogy and Geochemistry* **71**, 39–57.

Besson J. M., Pinceaux J. P., Anastopoulos C. and Velde B. (1982) Raman spectra of olivine up to 65 kilobars. *Journal of Geophysical Research: Solid Earth* **87**, 10773–10775.

Bostroem D. (1987) Single-crystal X-ray diffraction studies of synthetic Ni-Mg olivine solid solutions. *American Mineralogist* **72**, 965–972.

Bouhifd M. A., Andrault D., Fiquet G. and Richet P. (1996) Thermal expansion of forsterite up to the melting point. *Geophysical Research Letters* **23**, 1143–1146.

Breitburg D., Levin L. A., Oschlies A., Grégoire M., Chavez F. P., Conley D. J., Garçon V., Gilbert D., Gutiérrez D., Isensee K., Jacinto G. S., Limburg K. E., Montes I., Naqvi S. W. A.,

Pitcher G. C., Rabalais N. N., Roman M. R., Rose K. A., Seibel B. A., Telszewski M., Yasuhara M. and Zhang J. (2018) Declining oxygen in the global ocean and coastal waters. *Science* **359**, eaam7240.

Carrier P., Wentzcovitch R. and Tsuchiya J. (2007) First-principles prediction of crystal structures at high temperatures using the quasiharmonic approximation. *Phys. Rev. B* **76**, 064116.

Chopelas A. (1991) Single crystal Raman spectra of forsterite, fayalite, and monticellite. *American Mineralogist* **76**, 1101–1109.

Chopelas A. (1990) Thermal properties of forsterite at mantle pressures derived from vibrational spectroscopy. *Phys Chem Minerals* **17**, 149–156.

Couvy H., Chen J. and Drozd V. (2010) Compressibility of nanocrystalline forsterite. *Phys Chem Minerals* **37**, 343–351.

Dai R. C., Ding X., Wang Z. P. and Zhang Z. M. (2013) Pressure and temperature dependence of Raman scattering of MnWO4. *Chemical Physics Letters* **586**, 76–80.

Deringer V. L., Stoffel R. P. and Dronskowski R. (2014) Vibrational and thermodynamic properties of GeSe in the quasiharmonic approximation. *Phys. Rev. B* **89**, 094303.

Deshpande M. P., Bhatt S. V., Sathe V., Rao R. and Chaki S. H. (2014) Pressure and temperature dependence of Raman spectra and their anharmonic effects in Bi2Se3 single crystal. *Physica B: Condensed Matter* **433**, 72–78.

Dovesi R., Erba A., Orlando R., Zicovich-Wilson C. M., Civalleri B., Maschio L., Rérat M., Casassa S., Baima J., Salustro S. and Kirtman B. (2018) Quantum-mechanical condensed matter simulations with CRYSTAL. *WIREs Computational Molecular Science* **8**, e1360.

Downs R. T., Zha C.-S., Duffy T. S. and Finger L. W. (1996) The equation of state of forsterite to 17.2 GPa and effects of pressure media. *American Mineralogist* **81**, 51–55.

Durben D. J., McMillan P. F. and Wolf G. H. (1993) Raman study of the high-pressure behavior of forsterite (Mg_2SiO_4) crystal and glass. *American Mineralogist* **78**, 1143–1148.

Dyar M. D., Sklute E. C., Menzies O. N., Bland P. A., Lindsley D., Glotch T., Lane M. D., Schaefer M. W., Wopenka B., Klima R., Bishop J. L., Hiroi T., Pieters C. and Sunshine J. (2009) Spectroscopic characteristics of synthetic olivine: An integrated multi-wavelength and multi-technique approach. *American Mineralogist* **94**, 883–898.

Erba A. (2014) On combining temperature and pressure effects on structural properties of crystals with standard ab initio techniques. *J. Chem. Phys.* **141**, 124115.

Erba A., Maul J., De La Pierre M. and Dovesi R. (2015a) Structural and elastic anisotropy of crystals at high pressures and temperatures from quantum mechanical methods: The case of Mg_2SiO_4 forsterite. *J. Chem. Phys.* **142**, 204502.

Erba A., Maul J., Itou M., Dovesi R. and Sakurai Y. (2015b) Anharmonic thermal oscillations of the electron momentum distribution in lithium fluoride. *Phys. Rev. Lett.* **115**, 117402.

Erba A., Shahrokhi M., Moradian R. and Dovesi R. (2015c) On how differently the quasi-harmonic approximation works for two isostructural crystals: Thermal properties of periclase and lime. *J. Chem. Phys.* **142**, 044114.

Finkelstein G. J., Dera P. K., Jahn S., Oganov A. R., Holl C. M., Meng Y. and Duffy T. S. (2014) Phase transitions and equation of state of forsterite to 90 GPa from single-crystal X-ray diffraction and molecular modeling. *American Mineralogist* **99**, 35–43.

Fujino K., Sasaki S., Takéuchi Y. and Sadanaga R. (1981) X-ray determination of electron distributions in forsterite, fayalite and tephroite. *Acta Cryst B* **37**, 513–518.

Ghose S., Choudhury N., Chaplot S. L. and Rao K. R. (1992) Phonon density of states and thermodynamic properties of minerals. In *Thermodynamic Data: Systematics and Estimation* (ed. S. K. Saxena). Advances in Physical Geochemistry. Springer, New York, NY. pp. 283–314.

Gillet P. (1996) Raman spectroscopy at high pressure and high temperature. Phase transitions and thermodynamic properties of minerals. *Phys Chem Minerals* **23**, 263–275.

Gillet P., Guyot F. and Malezieux J.-M. (1989) High-pressure, high-temperature Raman spectroscopy of Ca_2GeO_4 (olivine form): Some insights on anharmonicity. *Physics of the Earth and Planetary Interiors* **58**, 141–154.

Gillet P., Richet P., Guyot F. and Fiquet G. (1991) High-temperature thermodynamic properties of forsterite. *Journal of Geophysical Research: Solid Earth* **96**, 11805–11816.

Hazen R. M. (1977) Effects of temperature and pressure on the crystal structure of ferromagnesian olivine. *American Mineralogist* **62**, 286–295.

Hazen R. M. (1976) Effects of temperature and pressure on the crystal structure of forsterite. *American Mineralogist* **61**, 1280–1293.

Hofmeister A. M. (1997) Infrared reflectance spectra of fayalite, and absorption datafrom assorted olivines, including pressure and isotope effects. *Phys Chem Min* **24**, 535–546.

Hofmeister A. M. (1987) Single-crystal absorption and reflection infrared spectroscopy of forsterite and fayalite. *Phys Chem Minerals* **14**, 499–513.

Iishi K. (1978) Lattice dynamics of forsterite. *American Mineralogist* **63**, 1198–1208.

Ito E. and Katsura T. (1989) A temperature profile of the mantle transition zone. *Geophysical Research Letters* **16**, 425–428.

Jahanbagloo I. C. (1969) X-ray diffraction study of olivine solid solution series. *American Mineralogist* **54**, 246–250.

Katsura T. and Ito E. (1989) The system Mg_2SiO_4-Fe_2SiO_4 at high pressures and temperatures: Precise determination of stabilities of olivine, modified spinel, and spinel. *Journal of Geophysical Research: Solid Earth* **94**, 15663–15670.

Kolesov B. A. and Geiger C. A. (2004) A Raman spectroscopic study of Fe–Mg olivines. *Phys Chem Minerals* **31**, 142–154.

Kroll H., Kirfel A., Heinemann R. and Barbier B. (2012) Volume thermal expansion and related thermophysical parameters in the Mg,Fe olivine solid-solution series. *European Journal of Mineralogy* **24**, 935–956.

Kudoh Y. and Takéuchi Y. (1985) The crystal structure of forsterite Mg_2SiO_4 under high pressure up to 149 kb. *Zeitschrift für Kristallographie - Crystalline Materials* **171**, 291–302.

Kuebler K. E., Jolliff B. L., Wang A. and Haskin L. A. (2006) Extracting olivine (Fo–Fa) compositions from Raman spectral peak positions. *Geochimica et Cosmochimica Acta* **70**, 6201–6222.

Kumazawa M. and Anderson O. L. (1969) Elastic moduli, pressure derivatives, and temperature derivatives of single-crystal olivine and single-crystal forsterite. *Journal of Geophysical Research (1896-1977)* **74**, 5961–5972.

Lam P. K., Yu R., Lee M. W. and Sharma S. K. (1990) Structural distortions and vibrational modes in Mg_2SiO_4. *American Mineralogist* **75**, 109–119.

Li L., Wentzcovitch R. M., Weidner D. J. and Da Silva C. R. S. (2007) Vibrational and thermodynamic properties of forsterite at mantle conditions. *Journal of Geophysical Research: Solid Earth* **112**.

Liu D., Guo X., Smyth J. R., Wang X., Zhu X., Miao Y., Bai J. and Ye Y. (2021) High-temperature and high-pressure Raman spectra of $Fo_{89}Fa_{11}$ and $Fo_{58}Fa_{42}$ olivines: Iron effect on thermodynamic properties. *American Mineralogist* **106**, 1668–1678.

Liu L. (1993) Volume, pressure and temperature dependences of vibrational frequencies. *Physics Letters A* **176**, 448–453.

McKeown D. A., Bell M. I. and Caracas R. (2010) Theoretical determination of the Raman spectra of single-crystal forsterite (Mg_2SiO_4). *American Mineralogist* **95**, 980–986.

Nestola Fabrizio, Nimis P., Ziberna L., Longo M., Marzoli A., Harris J. W., Manghnani M. H. and Fedortchouk Y. (2011) First crystal-structure determination of olivine in diamond: Composition and implications for provenance in the Earth's mantle. *Earth and Planetary Science Letters* **305**, 249–255.

Nestola F., Pasqual D., Smyth J. R., Novella D., Secco L., Manghnani M. H. and Dal Negro A. (2011) New accurate elastic parameters for the forsterite-fayalite solid solution. *American Mineralogist* **96**, 1742–1747.

Noel Y., Catti M., D'Arco Ph. and Dovesi R. (2006) The vibrational frequencies of forsterite Mg_2SiO_4: an all-electron ab initio study with the CRYSTAL code. *Phys Chem Minerals* **33**, 383–393.

Pamato M. G., Nestola F., Novella D., Smyth J. R., Pasqual D., Gatta G. D., Alvaro M. and Secco L. (2019) The high-pressure structural evolution of olivine along the forsterite–fayalite join. *Minerals* **9**, 790.

Paques-Ledent M. Th. and Tarte P. (1973) Vibrational studies of olivine-type compounds—I. The i.r. and Raman spectra of the isotopic species of Mg_2SiO_4. *Spectrochimica Acta Part A: Molecular Spectroscopy* **29**, 1007–1016.

Pascale F., Zicovich-Wilson C. M., Orlando R., Roetti C., Ugliengo P. and Dovesi R. (2005) Vibration frequencies of $Mg_3Al_2Si_3O_{12}$ pyrope. An ab initio study with the CRYSTAL Code. *J. Phys. Chem. B* **109**, 6146–6152.

Poe B. T., Romano C., Nestola F. and Smyth J. R. (2010) Electrical conductivity anisotropy of dry and hydrous olivine at 8GPa. *Physics of the Earth and Planetary Interiors* **181**, 103–111.

Rao K. R., Chaplot S. L., Choudhury N., Ghose S., Hastings J. M., Corliss L. M. and Price D. L. (1988) Lattice dynamics and inelastic neutron scattering from forsterite, Mg_2SiO_4: Phonon dispersion relation, density of states and specific heat. *Phys Chem Minerals* **16**, 83–97.

Reynard B., Price G. D. and Gillet P. (1992) Thermodynamic and anharmonic properties of forsterite, α-Mg2SiO4: Computer modelling versus high-pressure and high-temperature measurements. *Journal of Geophysical Research: Solid Earth* **97**, 19791–19801.

Servoin J. L. and Piriou B. (1973) Infrared reflectivity and Raman scattering of Mg_2SiO_4 single crystal. *physica status solidi (b)* **55**, 677–686.

Shannon R. D. (1976) Revised effective ionic radii and systematic studies of interatomic distances in halides and chalcogenides. *Acta Crystallogr A* **32**, 751–767.

Smyth J. R. (1975) High temperature crystal chemistry of fayalite. *American Mineralogist* **60**, 1092–1097.

Stangarone C., Böttger U., Bersani D., Tribaudino M. and Prencipe M. (2017) Ab initio simulations and experimental Raman spectra of Mg_2SiO_4 forsterite to simulate Mars surface environmental conditions. *Journal of Raman Spectroscopy* **48**, 1528–1535.

Suzuki I., Anderson O. L. and Sumino Y. (1983) Elastic properties of a single-crystal forsterite Mg_2SiO_4, up to 1,200 K. *Phys Chem Minerals* **10**, 38–46.

Tarantino S. C., Carpenter M. A. and Domeneghetti M. C. (2003) Strain and local heterogeneity in the forsterite–fayalite solid solution. *Phys Chem Minerals* **30**, 495–502.

Trots D. M., Kurnosov A., Ballaran T. B. and Frost D. J. (2012) High-temperature structural behaviors of anhydrous wadsleyite and forsterite. *American Mineralogist* **97**, 1582–1590.

Trubitsyn A. P. and Trubitsyn V. P. (2020) Temperature distribution in the Earth's mantle. *Dokl. Earth Sc.* **495**, 905–909.

Valenzano L., Noël Y., Orlando R., Zicovich-Wilson C. M., Ferrero M. and Dovesi R. (2007) Ab initio vibrational spectra and dielectric properties of carbonates: magnesite, calcite and dolomite. *Theor Chem Account* **117**, 991–1000.

Valenzano L., Torres F. J., Doll K., Pascale F., Zicovich-Wilson C. M. and Dovesi R. (2006) Ab initio study of the vibrational spectrum and related properties of crystalline compounds; the case of $CaCO_3$ calcite. **220**, 893–912.

Wang A., Kuebler K., Jolliff B. and Haskin L. A. (2004) Mineralogy of a Martian meteorite as determined by Raman spectroscopy. *Journal of Raman Spectroscopy* **35**, 504–514.

Wang S. Y., Sharma S. K. and Cooney T. F. (1993) Micro-Raman and infrared spectral study of forsterite under high pressure. *American Mineralogist* **78**, 469–476.

Wen X., Liang Y., Bai P., Luo B., Fang T., Yue L., An T., Song W. and Zheng S. (2017) First-principles calculations of the structural, elastic and thermodynamic properties of mackinawite (FeS) and pyrite (FeS_2). *Physica B: Condensed Matter* **525**, 119–126.

Wentzcovitch R. M., Yu Y. G. and Wu Z. (2010) Thermodynamic properties and phase pelations in mantle minerals investigated by first principles quasiharmonic theory. *Reviews in Mineralogy and Geochemistry* **71**, 59–98.

Wood B. J. and Nicholls J. (1978) The thermodynamic properties of reciprocal solid solutions. *Contr. Mineral. and Petrol.* **66**, 389–400.

Wu Z. and Wentzcovitch R. M. (2007) Vibrational and thermodynamic properties of wadsleyite: A density functional study. *Journal of Geophysical Research: Solid Earth* **112**.

Zha C.-S., Duffy T. S., Downs R. T., Mao H.-K. and Hemley R. J. (1996) Sound velocity and elasticity of single-crystal forsterite to 16 GPa. *Journal of Geophysical Research: Solid Earth* **101**, 17535–17545.

CHAPTER 4

Reduction of Aqueous Fe(III) and Mn(III) by Hydroquinone in the Presence and Absence of Mackinawite Nanoparticles From DFT Calculations

Co-authors: Sha Chen and Udo Becker

4.1 Abstract

Many redox reactions in the environment are catalyzed by dissolved iron or iron on mineral surfaces. However, little is known about the mechanisms by which iron catalyzes redox reactions in the environment. For example, iron's catalytic effects may be in the dehydration process, electron or spin density transfer, or angular (spin) momentum balance. One important iron mineral that may be particularly important as a catalyst in low-oxygen environments is mackinawite, a layered iron sulfide with an approximate stoichiometry of FeS. It is thought (or known) that nanoparticles of mackinawite are ubiquitous in low-oxygen subsurface environments (e.g., lake sediments), which are also rich in organic matter. Thus, the objective of this study is to investigate a substrate catalyzing electron transfer between a redox-active organic material, which we chose to be (hydro-) quinone, nanoparticulate mackinawite, and manganese or iron as an electron acceptor.

This study determines the thermodynamics and electronic interactions taking place in the reactions between hydroquinone and metal oxidants Fe(III)/Mn(III) and their (co-)adsorption on a mackinawite nanoparticle (Fe_8S_8 molecule). Density functional theory (DFT) is used for theoretical computations. Different metal species are used to simulate the state under various pH conditions. In addition to the traditional stoichiometry and charge balance, spin balance (number

and direction of unpaired electrons) was assessed for each chemical reaction. This is because the spin imbalance may be one major reason for kinetic hindrance. The results show that the interaction between Fe(III)/Mn(III)-aqua and hydroquinone depends on pH (metal species). There is spontaneous electron transfer from hydroquinone to Fe(III)/Mn(III) under acidic conditions ($Fe^{3+} \cdot 6H_2O/Mn^{3+} \cdot 6H_2O$) but not at basic pH values (dissolved $Fe(OH)_3^0 \cdot 3H_2O$ or $Mn(OH)_3^0 \cdot 3H_2O$). When the Fe_8S_8 cluster is present, adsorption of both hydroquinone and the metal-aqua species on mackinawite is energetically favorable. The mackinawite nanoparticle can be oxidized by Fe(III)/Mn(III) in acidic solutions as well as hydroquinone. Using the Gibbs free energy data computed for each species, we calculate the standard reduction potential (SRP, E^0) shift of Fe(III)/Fe(II) and Mn(III)/Mn(II) when adsorbed on mackinawite or complexed to hydroquinone. We also compute the intermediate species for Fe to construct the Pourbaix diagram when dissolved Fe is adsorbed on a mackinawite nanoparticle. This may be one of the first studies that use a combination of experimental literature values for redox and acid-base transitions, and an extensive set of quantum-mechanically derived Gibbs free energies to derive Pourbaix diagrams for redox transitions at different pH values for species that are adsorbed, complexed, or a combination of the two.

It is known that dissolved iron binding to organic ligands is essential for dissolved iron to be present in natural waters above its thermodynamic inorganic solubility limit. For example, concentrations of dissolved iron are several orders above its aqueous solubility in many waters, which is attributed to complexation with organic ligands. The ubiquity and broad application of iron sulfide nanoparticles make them relevant potential catalysts in biological and geological systems. Therefore, our study of the interaction of dissolved Fe/Mn-hydroquinone-mackinawite nanoparticles has significant implications for understanding the reactivity and transport of Fe and

Mn in the environments.

4.2 Introduction

The complexation and redox reactions between metal ions and natural organic matter (NOM) play an essential role in the stability, reactivity, and cycling of metals and organic matter (Strathmann, 2011; Klüpfel et al., 2014; Sander et al., 2015; Poggenburg et al., 2016; Daugherty et al., 2017; C. Wallace et al., 2017. Natural electron acceptors in water/sediments include O_2, NO_3^-, Mn^{4+}, Fe^{3+}, SO_4^{2-}, and CO_2 in the order of their standard reduction potential. Out of these, this study focuses on dissolved Fe(III) and Mn(III) as oxidants. Roman numbers are used in this study to represent the oxidation of the metal ion, not the entire aqueous complex. For example, Fe(III) represents any ferric Fe species such as Fe^{3+} (aquo-complexed Fe(III)) and $Fe(OH)_2^+$. Fe^{3+} is a common electron acceptor in various environments. Although dissolved Mn(III) is known to be a strong oxidant, not many studies have been done because dissolved Mn^{3+} is thermodynamically unstable in solution and undergoes disproportionation to form Mn^{2+} and MnO_2. Recent studies show that Mn(III) is a common transient intermediate species in various reactions such as one-electron transfer processes of Mn(II) or Mn(IV) (Webb et al., 2005). Many reactions involving two-electron transfer are known to proceed in two one-electron steps. Madison et al. (2013) found that soluble Mn(III) accounts for up to 90% of total dissolved Mn, probably stabilized by organic or inorganic ligands.

All environments contain natural organic matter derived from the decomposition of plant and microbial matter. Quinone/hydroquinone moieties are generally considered to be a dominant redox-active functional group within the NOM pool (Yang et al., 2016). Quinone/HQ moieties have been found to account for many of the observed redox properties of NOM (Klüpfel et al., 2014; Sander et al., 2015; Poggenburg et al., 2016; Wallace et al., 2017). For example, NOM serve

as electron shuttles to facilitate redox reactions between physically separated Fe(III) minerals and Fe-reducing bacteria (Bai et al., 2020). Most studies focus on redox reactions between NOM and solid phases of Fe and Mn, such as MnO_2, ferrihydrite, and goethite. Comparatively, few studies investigate the interaction of NOM with dissolved Fe or Mn species.

To address this knowledge gap, this study computes the interactions of hydroquinone/semiquinone/quinone and dissolved Fe/Mn species at various pH conditions. Hydroquinone is a naturally occurring organic compound and can also be a surrogate for more complex reductants. One-electron oxidation of hydroquinone yields the semiquinone radical, and two-electron transfer results in quinone. The transition between these quinone species is formally the release of a neutral hydrogen atom. However, it may be better described by the combination of electron and proton transfer, which may happen along different pathways (proton-coupled electron transfer, Mayer, 2004; Huynh and Meyer, 2007; Hammes-Schiffer, 2010; Weinberg et al., 2012).

Iron sulfide is an important group of minerals that have attracted much attention in the realm of redox processes and redox catalysis mainly because of their small bandgap. The most widely studied iron sulfide mineral is pyrite, FeS_2. Nanoparticulate pyrite has been considered a redox mediator in many studies, such as in hydrogenation of nitroaromatics (Ma et al., 2016), actinyl immobilization (Sundararajan et al., 2011; Hyun et al., 2012), oxidation of As (III) (Wiertz et al., 2006; Renock et al., 2009), etc. Another iron sulfide mineral, mackinawite (FeS), however, received much less attention than it may deserve due to its importance in many subsurface redox processes. While typically understudied because it is not forming museum-worthy specimens and its metastability, its ubiquity in anoxic subsurface environments and reactivity make it a vital reductant and redox catalyst in these environments. Mackinawite, a tetragonal iron sulfide mineral, is widespread in anoxic environmental systems such as deep ocean vents, freshwater sediments,

anoxic ocean and sediments.

Herein, we use Density Functional Theory (DFT) to examine the thermodynamics and electron transfer processes of such organic-metal reactions and the role of mackinawite clusters in these reactions, such as individual adsorption of hydroquinone and metallic aqueous oxidant species on mackinawite, their co-adsorption, and related redox process. Mackinawite clusters can reflect the nanoparticulate character of this mineral in nature with the available surface, step, and corner sites. In addition to the classically balanced parameters in a chemical equation, stoichiometry and charge, we also balance the number and orientation of unpaired spins to preserve the angular momentum of the equations. Spin balance is essential except for molecule systems with a strong spin-orbit coupling where electron angular momentum transfers to the orbital motion (Buchachenko, 1995; Buchachenko and Berdinsky, 2002).

The redox potential of a half-reaction is used to estimate the thermodynamic stability of metal ions in different oxidation states. Although redox potential is a thermodynamic parameter, it is relevant to kinetics because the difference between an actual electrochemical potential from the standard redox potential is one of the major driving forces of the reaction rate (Meyer et al., 1983; Levar et al., 2017). A larger decrease in free energy correlates with a higher reaction rate. For many common dissolved species, the standard reduction potentials are known. However, in addition to the standard reduction potential of the free aqueous species, the ligands and coordination environment of the central transition metal cation can have a significant influence on this standard reduction potential. For example, organic ligands can shift the standard reduction potential of a metal cation significantly (Strathmann and Stone, 2002; Santana-Casiano et al., 2010), and the same is true for a metal ion embedded in a mineral. However, few studies have quantified the standard reduction potential of an adsorbate species. Here, we use the quantum-mechanically

derived difference in the Gibbs free energy between a redox process in the adsorbed state and the respective redox process in the aqueous state and add this difference to the experimental aqueous standard reduction potential to calculate the expected thermodynamic entity in the adsorbed state. The acquired thermodynamic data for each species/equation are then used to derive the reduction potential of Fe(III)/Fe(II) or Mn(III)/Mn(II) adsorbed on the mackinawite cluster, complexed to quinone moieties, or co-adsorbed with quinone on the mackinawite cluster. In addition, we construct the Pourbaix (potential-pH) diagram of dissolved Fe species when adsorbed on a mackinawite nanoparticle.

4.3 Computational details

4.3.1 DFT calculations and initial structures

All density functional theory (DFT) computations were performed using the Gaussian 09 software. The B3LYP density functional, a Hartree-Fock-DFT functional, widely used for systems with a molecular character with a small bandgap that allows for electron transfer, was adopted as the exchange-correlation functional. A triple-zeta basis set 6-311+G* (+ denotes a diffuse function and * a polarization function) was used for the light elements C, H, O, and S, and LANL2DZ was used for heavy metals Fe and Mn. Effective core potentials (ECP, also called pseudopotential) from LANL2DZ were applied to Fe and Mn to reduce computational effort. The B3LYP/triple-zeta basis set pair usually gives better accuracy than the commonly used B3LYP/6-31G.

The mackinawite cluster Fe_8S_8 was obtained by cleaving the periodic mineral structure to get a Fe_8S_8 molecule. The cluster has a symmetry of C2h (2/m) (Figure 4.1a). As for the electron configuration of Fe in mackinawite, literature has conflicting conclusions based on both Mossbauer spectroscopy analysis and DFT calculations. Some studies support low-spin Fe^{2+} while others conclude high spin. Details of the literature background can be found in Appendix D.1. Our

calculations in Appendix D over the Fe_8S_8 cluster, 2D periodic slab, and 3D crystal give consistent conclusions: the Gibbs free energy of Fe in mackinawite thermodynamically favors the high-spin state, especially in antiferromagnetic configurations. The energy differences between ferromagnetic and antiferromagnetic states are minor. To simplify the calculations, ferromagnetic spins (32 unpaired electrons for 8 Fe atoms) for the cluster were used in all the calculations of Fe_8S_8.

Considering the difficulty of having many transition metal atoms in the system and approximating the steric hindrance of surrounding induced by the atoms in typically larger clusters in the environments, the Fe_8S_8 structure is fixed in all calculations presented in this study. To test the stability of the mackinawite cluster and see if the "plane" structure will fold to form a cubic FeS structure, a geometry optimization is conducted in a separate test run for the cluster. The structure after geometry optimization is presented in Figure 4.1b. The original structure cleaved from mackinawite mineral has angles of Fe-S-Fe 70.305° and S-Fe-S 109.695°. The molecular energy of the relaxed structure is lower in energy by 488 kJ/mol than its unrelaxed counterpart. The structural distortion is Fe-S-Fe ranges from 69.522° to 79.662° and S-Fe-S from 98.861° to 115.655°. Although the structure distorted somewhat and lost part of its symmetry, it did not fold, and the optimized structure is not significantly different from the original one.

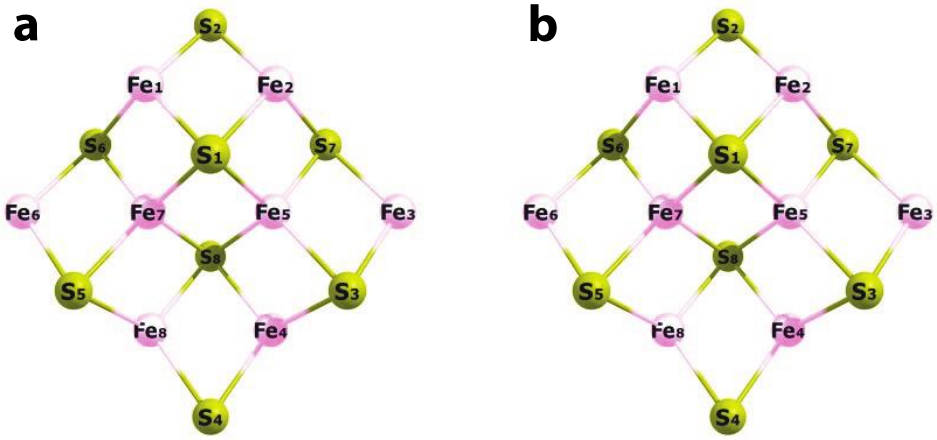

Figure 4.1a The mackinawite cluster from the crystal structure is free from relaxation. **b.** Relaxed mackinawite cluster in the vacuum. Atoms are color-coded by element and labeled.

Aqueous third-row transition metal ions adopt the typical six-coordinated structure as the initial structure. Six water molecules surround the metal ion to form an octahedral shape, corresponding to the first hydration shell. However, a Fe^{3+} hydrolysis study using DFT (De Abreu et al., 2006) shows that the hexaquo-complex of the iron complex is not the most stable one. According to that study, the $Fe(OH)_3$ (aq) complex prefers fivefold coordination with a trigonal bipyramid geometry. However, coordination with predominant water molecules surrounding the transition metal complex exhibits larger Fe-O water bonds with 0.3-0.4 Å longer distances that allow for the space required for sixfold coordination.

For some species, calculations in both vacuum and a dielectric fluid mimicking the surrounding water (Conductor-like Polarization Continuum Model, CPCM) were performed. However, in most calculations presented in this study, one hydration sphere of explicit water or hydroxide was applied in combination with a dielectric fluid surrounding the explicitly hydrated transition metal line and the rest of the system (the mackinawite cluster and the quinone species where applicable). The reaction energy in solution ($\Delta G_{reac,cpcm}$) is the sum of the reaction energy under vacuum ($\Delta G_{reac,vac}$) and the solvation energy ($\Delta G_{reac,solv}$):

$$\Delta G_{reac,cpcm} = \Delta G_{reac,vac} + \Delta G_{reac,solv}. \quad (4.1)$$

In all the equations we tested, the reactant and product side of the equation are not only stoichiometric and charge balanced, but also spin-balanced on each side of the equation. High spin is used for all species. Fe(II) has the electron configuration of $[Ar]3d^6$ and thus has four unpaired electrons for the high-spin state, while Fe(III) has five unpaired spins. Mn(II) and Mn(III) have five and four unpaired spins, respectively.

4.3.2 Pourbaix (pK_a, E^o) diagram construction

The Pourbaix diagram (Eh-pH) is constructed manually for Fe adsorbed on a mackinawite cluster in an aqueous environment. The Pourbaix diagram of aqueous, dissolved Fe in pure water is well defined. However, when the dissolved Fe is complexed by a ligand or adsorbed on a nanoparticle, the potential of each species changes. Therefore, it is necessary to calculate these shifts to represent them in a Pourbaix diagram. The separating lines in the diagram show the domains where the various chemical forms of a dissolved element are predominant. The separating lines in a Pourbaix diagram are constructed by assuming the two separated dissolved species have the same activity at the Eh/pH conditions indicated by the line. Analogously, a line for adsorbed or complexed species indicates where two species with different oxidation or protonation state are in equilibrium in the adsorbed or complexed state.

There are three different types of lines in a Pourbaix diagram: a) vertical lines represent pure acid-base reactions; b) horizontal lines are simple oxidation-reduction processes; c) other lines represent pH-dependent oxidation-reduction processes. Two parameters, acid association constant pK_a and reduction potential E are calculated.

For vertical lines, the pK_a values of dissolved Fe/Mn species adsorbed on mackinawite need to be calculated:

$$\mathrm{HA(aq) \rightarrow A^-(aq) + H^+} \qquad \Delta G_1,\ pK_{a(aq)}$$

$$\mathrm{HA(aq) - L \rightarrow A^-(aq) - L + H^+} \qquad \Delta G_2,\ pK_{a(ads)}$$

$$\Delta\Delta G_1 = \Delta G_2 - \Delta G_1 = G(HA) + G(A^-_{ads}) - G(A^-) + G(HA_{ads}) = 2.3RT(pK_{a(ads)} - pK_{a(aq)})$$

$$pK_{a(ads)} = \frac{\Delta\Delta G_1}{2.3RT} + pK_{a(aq,exp)}. \qquad (4.2)$$

For horizontal lines, the standard reduction potential (SRP, E^o) of different oxidant/reductant pair pairs on mackinawite are calculated using the following half-reactions:

$$M_{ox}(aq) + n\ e^- \rightarrow M_{red}(aq) \qquad \Delta G_3$$

$$M_{ox}(aq) - L + ne^- \rightarrow M_{red}(aq) - L \qquad \Delta G_4$$

$$\Delta\Delta G_2 = \Delta G_4 - \Delta G_2 = G(M_{red} - L) - G(M_{ox} - L) - G(M_{red}) + G(M_{ox}).$$

The change of SRP (ΔE^o) due to adsorption can be calculated as:

$$\Delta E^\circ = \frac{\Delta\Delta G_2}{-nF},$$

where *n* is the number of electrons transferred in the half-reaction, *F* is the Faraday constant. The absolute SRP (E^o) for adsorption can be obtained using the equation

$$E^o_{ads} = E^o_{aq,exp} + \Delta E^\circ = E^o_{aq,exp} - \frac{\Delta\Delta G_2}{nF}. \qquad (4.3)$$

If protons are involved in the reaction, then the reduction potential varies with pH. However, the standard potential does not vary with pH, since it is defined as the potential referred to the hydrogen standard when each species in the reaction, including H^+ if present, is at unit activity.

$$M_{ox}(aq) + n\ e^- + m\ H^+ \rightarrow M_{red}(aq)$$

$$M_{ox}(aq) - L + n\ e^- + m\ H^+ \rightarrow M_{red}(aq) - L$$

$$E_{ads} = E^o_{ads} - \frac{RT}{nF}\ln\frac{1}{[H^+]^m} = E^o - 2.3m \cdot \frac{RT}{nF} \cdot pH \qquad (4.4)$$

If H^+ is in the product as:

$$\mathrm{M}_{ox}(\mathrm{aq}) + \mathrm{n\ e^-} \rightarrow \mathrm{M}_{red}(\mathrm{aq}) + \mathrm{m\ H^+}$$

$$\mathrm{M}_{ox}(\mathrm{aq}) - \mathrm{L} + \mathrm{n\ e^-} \rightarrow \mathrm{M}_{red}(\mathrm{aq}) - \mathrm{L} + \mathrm{m\ H^+}$$

$$\mathrm{E}_{ads} = \mathrm{E}^{o}_{ads} - \frac{\mathrm{RT}}{\mathrm{nF}} \ln[\mathrm{H^+}]^m = \mathrm{E^o} + 2.3\mathrm{m} \cdot \frac{\mathrm{RT}}{\mathrm{nF}} \cdot \mathrm{pH}. \quad (4.5)$$

4.4 Results

To examine the interaction between (hydro-/semi-)quinone and metal ions and the catalytic role of mackinawite clusters, geometry optimizations and thermochemistry calculations were conducted to obtain the Gibbs free energies and electron distributions (charge and spin) for the different species. The energy data are presented in Table 4.1 for each equation, and charge and spin data are listed in Table 4.2 for each species. Both equations and species are numbered in the tables for reference purposes. In the following subsections, we will first present the results of a) the complexation and redox reaction between dissolved Fe/Mn and quinones with various oxidation and protonation states (hydroquinone/semiquinone/quinone) (Section 4.4.1), b) adsorption and co-adsorption of metal species and quinone species on the mackinawite cluster (Section 4.4.2), and c) derivation of the standard reduction potentials of aqueous Fe/Mn complexes adsorbed on mackinawite in an aqueous environment (Section 4.4.3). We also attempt to evaluate what influence adsorption and complexation might have on quantum-mechanically derived Pourbaix (Eh/pH) diagrams.

Some of the processes examined (with $[\mathrm{FeIII(OH)_3(H_2O)_3}]^0$ as the metal oxidant) were computed in both gas and solution medium to obtain the solvation energy (Table 4.1a).

For the neutral Fe complexation with hydroquinone/semiquinone (Equations 4.6 - 4.7), all reaction energies are lower in the solvated medium than in the gas medium. When $[\mathrm{FeIII(OH)_3(H_2O)_3}]^0$ and/or hydroquinone adsorb on the mackinawite cluster (Equations 4.8 - 4.10), all adsorption energies are higher in the aqueous phase than in the gas phase. The energy

difference for vacuum and CPCM is similar for the electronic energy ΔEL, enthalpy ΔH, and Gibbs free energy ΔG. For example, the hydroquinone adsorption on mackinawite (Equation 4.9) in CPCM is 76 kJ/mol less negative than in vacuum for the electronic energy, 81 kJ/mol for the enthalpy, and 70 kJ/mol for the Gibbs free energy. Given that the enthalpy $H = EL + ZPE + C_P T$, and Gibbs free energy $G = H - TS$, the difference is due mainly to the electronic energy (EL) difference. The zero-point vibrational energy (ZPE) and heat capacity (C_P) do not affect the solvation energy of the reactions significantly.

Table 4.1a The electronic energy ΔEL, enthalpy ΔH, and Gibbs free energy ΔG (all in kJ/mol) for Equations 4.6 - 4.10. The $[FeIII(OH)_3(H_2O)_3]^0$ is the oxidant. They were calculated in both the gas and solution medium, the latter using the CPCM model. Roman numbers II and III represent the charge of 2+ and 3+, respectively. Eqn.: Equation number. The same applies to other tables.

Eqn.	Reactions	Fe, vacuum			Fe, CPCM		
		ΔEL	ΔH	ΔG	ΔEL	ΔH	ΔG
	Complexation of Fe with hydro-/semi-quinone						
(4.6)	$H_2Q + [FeIII(OH)_3(H_2O)_3]^0 \rightarrow H_2Q–[FeIII(OH)_3(H_2O)_3]^0$	-53	-45	4	-70.6	-64	-14
(4.7)	$HQ + [FeII(OH)_2(H_2O)_4]^0 \rightarrow HQ–[FeII(OH)_2(H_2O)_4]^0$	-72	-65	-11.0	-128	-118	-60
	Fe and/or hydroquinone adsorbed on mackinawite						
(4.8)	$[FeIII(OH)_3(H_2O)_3]^0 + Fe_8S_8 \rightarrow [FeIII(OH)_3(H_2O)_3]^0–Fe_8S_8$	-256	-348	-208	-168	-253	-109
(4.9)	$H_2Q + Fe_8S_8 \rightarrow H_2Q–Fe_8S_8$	-145	-236	-98	-69	-155	-28
(4.10)	$[FeIII(OH)_3(H_2O)_3]^0 + Fe_8S_8 + H_2Q \rightarrow [FeIII(OH)_3(H_2O)_3]^0–Fe_8S_8–H_2Q$	-357	-442	-251	-276	-355	-166

Table 4.1b The Gibbs free energy (ΔG in kJ/mol) for complexation and (co-) adsorption processes using CPCM model. M represents metal, either Fe or Mn. Energy cells left blank were not computed.

Process	Eqn.	Reactions	ΔG_{Fe}	ΔG_{Mn}
Reaction of Fe/Mn with quinone species				
Hydroquinone and metal(III)	(4.11)	$H_2Q + [MIII(H_2O)_6]^{3+} \rightarrow H_2Q–[MIII(H_2O)_6]^{3+}$	-137	-206
	(4.12)	$H_2Q + [MIII(OH)_3(H_2O)_3]^0 \rightarrow H_2Q–[MIII(OH)_3(H_2O)_3]^0$	-14	4
semiquinone and metal(II)	(4.13)	$HQ + [MII(H_2O)_6]^{2+} \rightarrow HQ–[MII(H_2O)_6]^{2+}$	13	10
	(4.14)	$HQ + [MII(OH)_2(H_2O)_4]^0 \rightarrow HQ–[MII(OH)_2(H_2O)_4]^0$	-60	1
Adsorption of H_2Q/HQ on mackinawite cluster				
	(4.15)	$H_2Q + Fe_8S_8 \rightarrow H_2Q–Fe_8S_8$	-28	
	(4.16)	$HQ + Fe_8S_8 \rightarrow HQ–Fe_8S_8$	-85	
Aqueous Fe/Mn adsorbed on mackinawite at various protonation states (≡ various pH regions)				
Adsorption of metal(III) on mackinawite	(4.17)	$[MIII(H_2O)_6]^{3+} + Fe_8S_8 \rightarrow [MIII(H_2O)_6]^{3+}–Fe_8S_8$	-550	-363
	(4.18)	$[MIII(OH)(H_2O)_5]^{2+} + Fe_8S_8 \rightarrow [MIII(OH)(H_2O)_5]^{2+}–Fe_8S_8$	-225	
	(4.19)	$[MIII(OH)_2(H_2O)_4]^{+} + Fe_8S_8 \rightarrow [MIII(OH)_2(H_2O)_4]^{+}–Fe_8S_8$	-205	
	(4.20)	$[MIII(OH)_3(H_2O)_3]^0 + Fe_8S_8 \rightarrow [MIII(OH)_3(H_2O)_3]^0–Fe_8S_8$	-109	-50
Adsorption of metal(II) on mackinawite	(4.21)	$[MII(H_2O)_6]^{2+} + Fe_8S_8 \rightarrow [MII(H_2O)_6]^{2+}–Fe_8S_8$	14	-326
	(4.22)	$[MII(OH)(H_2O)_5]^{+} + Fe_8S_8 \rightarrow [MII(OH)(H_2O)_5]^{+}–Fe_8S_8$	-95	
	(4.23)	$[MII(OH)_2(H_2O)_4]^0 + Fe_8S_8 \rightarrow [MII(OH)_2(H_2O)_4]^0–Fe_8S_8$	-166	-178
Fe/Mn and hydroquinone co-adsorption on a mackinawite cluster				
	(4.24)	$[MIII(OH)_3(H_2O)_3]^0 + Fe_8S_8 + H_2Q \rightarrow [MIII(OH)_3(H_2O)_3]^0–Fe_8S_8 –H_2Q$	-166	-87
	(4.25)	$[MIII(OH)_3(H_2O)_3]^0 + Fe_8S_8 + H_2Q \rightarrow HQ\cdot –Fe_8S_8–\mathit{MIII}(OH)_3\cdot H\cdot 3H_2O$	-197	-149
	(4.26)	$MIII(H_2O)_6^{3+} + Fe_8S_8 + H_2Q \rightarrow MIII(H_2O)_6^{3+}–Fe_8S_8–H_2Q$	-313	-344
	(4.27)	$MIII(H_2O)_6^{3+}–Fe_8S_8 + Fe_8S_8–H_2Q \rightarrow MIII(H_2O)_6^{3+}–Fe_8S_8–H_2Q + Fe_8S_8$	277	53

Table 4.2a Bader charge (char) and spin (S, #n of unpaired spins, equivalent to the angular momentum of as #n·$\frac{\hbar}{2}$) distribution for each species: hydroquinone (H_2Q), semiquinone (HQ), p-benzoquinone (Q), Fe-aqua, and their interaction with a mackinawite cluster. All species were calculated with the solvation model. For some calculations with multiple structures, only the structures with the lowest energies are listed here.

N†	Species	H_2Q		HQ		Q		Fe_8S_8		Fe-aqua		Fe‡	
		char	S	char	S	char	S	char	S	char	S	char	S
	Dissolved Species for Fe												
1	$[FeIII(H_2O)_6]^{3+}$									3.01	5.00	1.96	4.27
2	$[FeIII(OH)(H_2O)_5]^{2+}$									1.98	5.00	1.89	4.14
3	$[FeIII(OH)_2(H_2O)_4]^{+}$									1.00	5.00	1.81	4.10
4	$[FeIII(OH)_3(H_2O)_3]^{0}$									0.024	5.00	1.79	4.10
5	$[FeII(H_2O)_6]^{2+}$									2.00	4.00	1.60	3.74
6	$[FeII(OH)(H_2O)_5]^{+}$									1.01	4.00	1.54	3.69
7	$[FeII(OH)_2(H_2O)_4]^{0}$									0.015	4.00	1.48	3.70
	Quinone species												
8	H_2Q	-0.01	0										
9	HQ			-0.01	1.00								
10	Q					0.00	0						
	Fe complexation with quinone												
11	$[FeIII(H_2O)_6]^{3+}$–H_2Q	0.98	1.00							1.99	4.00	1.61	3.74
12	$[FeIII(OH)_3(H_2O)_3]^{0}$–$H_2Q$	-0.03	0.00							0.02	4.99	1.80	4.10
13	$[FeII(H_2O)_6]^{2+}$–H_2Q	0.04	0.00							1.93	4.00	1.61	3.73
14	$[FeII(H_2O)_6]^{2+}$–HQ			0.105	1.00					1.92	4.00	1.60	3.73
15	$[FeII(OH)_2(H_2O)_4]^{0}$–HQ			-0.47	0.47					0.45	4.53	1.74	4.02
	Fe adsorb on mackinawite												
16	$[FeIII(H_2O)_6]^{3+}$–Fe_8S_8							1.17	32.9	1.85	4.10	1.57	3.75
17	$[FeIII(OH)(H_2O)_5]^{2+}$–Fe_8S_8							0.89	32.8	1.12	4.17	1.58	3.72
18	$[FeIII(OH)_2(H_2O)_4]^{+}$–$Fe_8S_8$							0.71	32.7	0.30	4.27	1.55	3.71
19	$[FeIII(OH)_3(H_2O)_3]^{0}$–$Fe_8S_8$							-0.17	31.8	0.16	5.19	1.85	4.16
20	$[FeII(H_2O)_6]^{2+}$–Fe_8S_8							0.23	32.0	1.80	4.02	1.53	3.74
21	$[FeII(OH)(H_2O)_5]^{+}$–Fe_8S_8							-0.13	31.8	1.08	4.16	1.57	3.72
22	$[FeII(OH)_2(H_2O)_4]^{0}$–Fe_8S_8							-0.21	31.7	0.247	4.24	1.54	3.71
	Quinone species on mackinawite												
23	H_2Q–Fe_8S_8	0.013	0.07					-0.04	31.9				
24	HQ–Fe_8S_8			-0.76	0.21			0.75	32.8				
25	Q–Fe_8S_8					-0.81	-0.81	0.85	32.8				
	Fe and quinone co-adsorbed												
26	$[FeIII(H_2O)_6]^{3+}$–Fe_8S_8–H_2Q	0.04	0.08					1.07	32.8	1.87	4.09	1.564	3.76
27	$[FeIII(OH)_3(H_2O)_3]^{0}$–$Fe_8S_8$ –H_2Q	0.05	0.08					0.67	32.6	-0.68	4.28	1.480	3.69
28	$[FeII(OH)_2(H_2O)_4]^{0}$– Fe_8S_8 –HQ			-0.74	0.23			0.51	32.5	0.254	4.25	1.540	3.71

†: species number. The same applies to Table 4.2b.

‡: the Fe atom in Fe-aqua.

Table 4.2b. Bader charge (char) and spin (S, #n of unpaired spins, equivalent to the angular momentum of as #n·$\frac{\hbar}{2}$) distribution for Mn aqua and their interaction with quinone species and mackinawite cluster. All the data were calculated with the solvation model. For some calculations with multiple structures, only the structures with the lowest energies are listed here.

N	Species	H_2Q		HQ		Q		Fe_8S_8		Mn- aqua		Mn[§]	
		char	S	char	S	char	S	char	S	char	S	char	S
	Dissolved Species for Fe												
29	$[MnIII(H_2O)_6]^{3+}$									2.98	4.00	1.92	3.72
30	$[MnIII(OH)_3(H_2O)_3]^0$									-0.03	4.00	1.76	3.78
31	$[MnII(H_2O)_6]^{2+}$									1.99	5.00	1.66	4.71
32	$[MnII(OH)_2(H_2O)_4]^0$									0.02	5.00	1.58	4.68
	Mn complexation with quinone												
33	$[MnIII(H_2O)_6]^{3+}$–H_2Q	1.00	-1.00							2.01	5.00	1.67	4.69
34	$[MnIII(OH)_3(H_2O)_3]^0$–H_2Q	-0.03	0.00							0.04	4.00	1.78	3.79
35	$[MnII(H_2O)_6]^{2+}$–H_2Q	0.04	0.00							1.91	5.00	1.68	4.71
36	$MnII(OH)_2^0 \cdot 4H_2O$–HQ			-0.67	0.00					0.67	4.00	1.79	3.77
	Mn adsorb on mackinawite												
37	$[MnIII(H_2O)_6]^{3+}$–Fe_8S_8							1.13	30.9	1.91	5.09	1.65	4.74
38	$[MnIII(OH)_3(H_2O)_3]^0$–Fe_8S_8							-0.14	31.8	0.18	4.22	1.79	3.80
39	$[MnII(H_2O)_6]^{2+}$–Fe_8S_8							0.17	31.9	1.86	5.05	1.63	4.74
40	$[MnII(OH)_2(H_2O)_4]^0$–Fe_8S_8							-0.21	31.8	0.20	5.23	1.62	4.709
	Mn and quinone co-adsorbed												
41	$[MnIII(OH)_3(H_2O)_3]^0$–H_2Q–Fe_8S_8	0.03	0.07					-0.19	31.8	0.14	4.14	1.82	3.82
42	$[MnII(OH)_2(H_2O)_4]^0$–HQ · –Fe_8S_8			-0.69	0.21			0.47	30.5	0.28	5.24	4.72	1.64

[§]: the Mn atom in Mn-aqua.

4.4.1 Reaction of (hydro-/semi-)quinone and Fe/Mn in aqueous solution

Dissolved Fe(III) species depend strongly on the pH, from Fe^{3+} dominating Fe(III) speciation in acidic solutions to $Fe(OH)^{2+}$, $Fe(OH)_2^+$, and $Fe(OH)_3^0$ increasingly dominant with increasing pH. For aqueous Fe(III) complexation with quinone species, we used $[Fe(H_2O)_6]^{3+}$ for pH below 3 and $[Fe(OH)_3(H_2O)_3]^0$ (aq) for pH values from 3- 12. The processes we modeled are the complexation of hydroquinone with Fe(III)-aqua and the following redox reaction. Similar calculations were done for Mn (Equations 4.11 – 4.14).

The initial structures of both Fe/Mn aqua are hexaquo complexes before geometry optimization. The optimized structures for each species are shown in Figure 4.2. The optimized structures for Mn and Fe are similar. When the solution is acidic ($[Fe(H_2O)_6]^{3+}$ or $[Mn(H_2O)_6]^{3+}$ as the oxidant), the aqueous Fe(III)/Mn(III) complexes stay as the hexaquo structure (Figure 4.2a and e). The complexation energies (Gibbs free energy) are negative, -137 and -206 kJ/mol, using the

solvation model for Fe and Mn, respectively (Equation 4.11).

In this study, we use Bader charges and spins. This approach defines a volume around each atom characterized by points where the second derivative (the "Laplacian") of the charge density is 0, i.e., the "bottleneck" of the electron density. Then integration over the charge density minus the number of electrons of the neutral atom results in the negative of the atomic charge. The integral over the spin density (spin up electrons minus spin down ones) results in the atomic spin. Throughout this manuscript, we report the number (#) of unpaired spins such that an atom with # unpaired spins has an angular spin momentum of #·ħ/2, equivalent to S#/2. The Fe atom in $[Fe(H_2O)_6]^{3+}$ has the formal charge of 3 and 5 unpaired spins. Its Bader charge is analyzed to be 1.96 and Bader spin to be 4.27 (Table 4.2a, species 1), which we use as a reference point, later on, to determine if there has been a charge transfer. The Fe^{2+} in $[Fe(H_2O)_6]^{2+}$ has the formal charge of 2 and 4 unpaired spins. Its Bader charge is 1.60 and Bader spin is 3.74 (species 5). The difference in Bader charge between Fe^{3+}/Fe^{2+} is 0.36; the difference in Bader spin is 0.54, indicating that spin density is typically more sensitive to oxidation state changes than charge density. After geometry optimization, $[Fe(H_2O)_6]^{3+}$ in $[Fe(H_2O)_6]^{3+}$–H_2Q has a spin of 4.00 and charge of 1.99, while the hydroquinone part obtains a spin of 1 and charge of 0.98 (species 11), indicating electron transfer from hydroquinone to $[Fe(H_2O)_6]^{3+}$. The charge and spin of the Fe atom are 1.61 and 3.74, respectively, which are about the same as Fe^{2+} in $[Fe(H_2O)_6]^{2+}$ (species 5). Therefore, when the $[Fe(H_2O)_6]^{3+}$ complex approaches the reductant hydroquinone, an electron is transferred from the hydroquinone to Fe^{3+} to form semiquinone and Fe^{2+}. The same redox reaction occurs between $[Mn(H_2O)_6]^{3+}$and hydroquinone. In contrast to Fe(III), Mn(III) has four unpaired electrons, and Mn(II) has five. The Bader spin of Mn^{2+} in $[Mn(H_2O)_6]^{2+}$ (Table 4.2b, species 31) is 0.99 more than Mn^{3+} in $[Mn(H_2O)_6]^{3+}$ (species 29), while the Bader charge is 0.26 less. In the

$[Mn(H_2O)_6]^{3+}$–H_2Q (species 33), the Mn atom has a similar Bader charge and spin as Mn(II), indicating that $[Mn(H_2O)_6]^{3+}$ oxidizes hydroquinone. When hydroquinone donates an electron and becomes the hydroquinone radical or loses an electron and proton and becomes semiquinone, it can either be an electron donor or acceptor. For the complexation of $[Fe(H_2O)_6]^{2+}$ and $[Mn(H_2O)_6]^{2+}$ to semiquinone (Species 14 for Fe and 35 for Mn), no electron transfer occurs.

When the neutral species $[Fe(OH)_3(H_2O)_3]^0$ and $[Mn(OH)_3(H_2O)_3]^0$ complex with H_2Q, one water molecule is pushed away from the aquo-complexed metal, and the Fe/Mn-aqua becomes five-coordinated by OH/H_2O (Figure 4.2c and 4.2g). One hydroxyl group of the hydroquinone molecule is connected to a metal -OH or H_2O group by a hydrogen bond instead of the metal atom, which is outer-sphere complexation. The hydroquinone is not directly bonded to the metal atom. The Gibbs free energy of complexation energy for $[Fe(OH)_3(H_2O)_3]^0$ with hydroquinone is -14 kJ/mol, and for $[Mn(OH)_3(H_2O)_3]^0$, it is 4 kJ/mol using the CPCM solvation model (Equation 4.12). The optimized structure for $[Fe(OH)_2(H_2O)_4]^0$ with semiquinone (Figure 4.2d) is different from H_2Q–$[Fe(OH)_3(H_2O)_3]^0$ (Figure 4.2c). Two water molecules are pushed away from the Fe(II) atom and bonded with other -OH and H_2O groups via a hydrogen bond, making Fe four-coordinated with OH or water. Now, the oxygen atom from the semiquinone is directly bonded to Fe^{2+}. The complexation process for Fe is also thermodynamically favorable with a Gibbs free energy of -60 kJ/mol (Equation 4.14). The complexation of $[Mn(OH)_2(H_2O)_4]^0$ with semiquinone (Figure 4.2h) is different from that of $[Fe(OH)_2(H_2O)_4]^0$ with semiquinone. The semiquinone species accepts one H atom from a water molecule surrounding Mn(III) to become hydroquinone. The complexation energy is 1 kJ/mol (Equation 4.14). Although the structures for $[Mn(OH)_2(H_2O)_4]^0$–HQ and $[Fe(OH)_2(H_2O)_4]^0$–HQ are different, their electron distribution is similar. The Bader charge and spin calculations indicate no spontaneous electron transfer between

H_2Q and $[Fe(OH)_3(H_2O)_3]^0$ or $[Mn(OH)_3(H_2O)_3]^0$ in contrast to the reaction of H_2Q with the charged complexes ($[Fe(H_2O)_6]^{3+}$ and $[Mn(H_2O)_6]^{3+}$) at low pH. During geometry optimization, the Bader charge and spin values in $[Fe(OH)_3(H_2O)_3]^0$/$[Mn(OH)_3(H_2O)_3]^0$ and hydroquinone hardly change and are close to their initial formal numbers. Instead, electron transfer occurs from $[Fe(OH)_2(H_2O)_4]^0$ or $[Mn(OH)_2(H_2O)_4]^0$ to semiquinone to form $[Fe(OH)_3(H_2O)_3]^0$ and $[Mn(OH)_3(H_2O)_3]^0$.

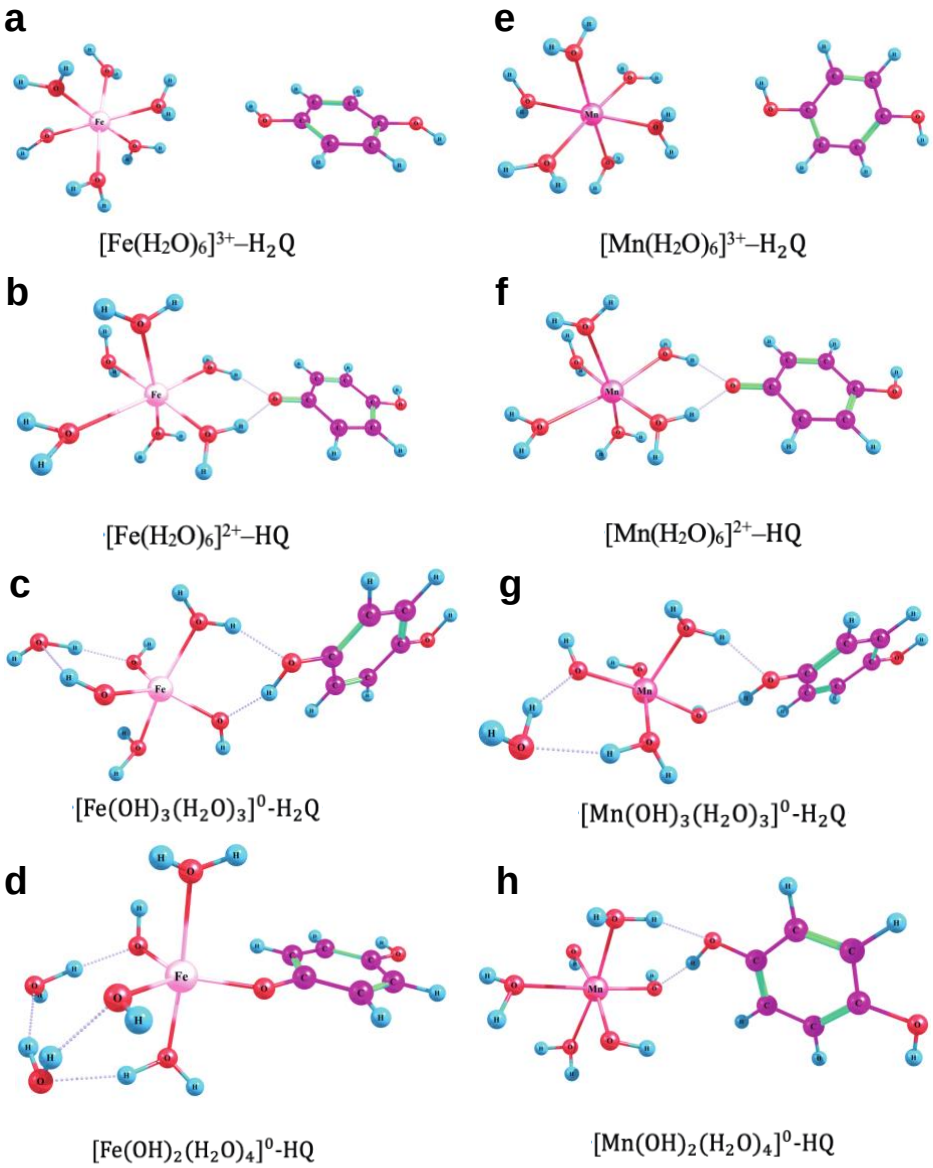

Figure 4.2 Dissolved Fe/Mn-aqua complexation with quinone species.

4.4.2 Adsorption to the Fe_8S_8 cluster

4.4.2.1. Adsorption of Fe/Mn-aqua to the Fe_8S_8 cluster

For Fe-aqua adsorption on the mackinawite cluster, we modeled all seven common species of Fe, which are $[Fe(H_2O)_6]^{3+}$, $[Fe(OH)(H_2O)_5]^{2+}$, $[Fe(OH)_2(H_2O)_4]^{+}$, and $[Fe(OH)_3(H_2O)_3]^{0}$ for ferric iron, and $[Fe(H_2O)_6]^{2+}$, $[Fe(OH)(H_2O)_5]^{+}$, and $[Fe(OH)_2(H_2O)_4]^{0}$ for ferrous iron to understand the deprotonation and redox thermodynamics. We use these data in Section 4.4.3 to approximate changes in the Pourbaix diagram of Fe adsorbed on a mackinawite cluster. There are various ways to adsorb Fe-aqua on the mackinawite cluster. To make the energies comparable, all aqueous Fe species are adsorbed in a similar orientation with the OH^- or H_2O from the Fe-aqua and bonded to a corner Fe of the mackinawite cluster.

We first compare monodentate and bidentate adsorption models for $[Fe(OH)_3(H_2O)_3]^{0}$ on Fe_8S_8 to evaluate which adsorption model is most thermodynamically favorable. The optimized complex structures are shown in Figure 4.3. The Gibbs free energy of monodentate adsorption is -88 kJ/mol, and the bidentate model is -109 kJ/mol (Equation 4.20). The bidentate model has a relatively lower energy by 21 kJ/mol. Fe^{2+} from the mackinawite prefers bonding with a bridging OH^-. Because of their thermodynamic favorability, bidentate models are used for all dissolved Fe species adsorption on the mackinawite cluster. The optimized structures are shown in Figure 4.4. Except for $[Fe(H_2O)_6]^{2+}$ adsorption that shows slightly positive energy, all other six Fe species have exothermic adsorption energies (Table 4.1b, Equation 4.17 – 4.23).

The magnetic/spin status of the mackinawite cluster is set to be ferromagnetic with a total of 32 unpaired electrons (see Appendix D for the spin discussion of mackinawite). The adsorption of all three ferrous Fe species ($[Fe(H_2O)_6]^{2+}$, $[Fe(OH)(H_2O)_5]^{+}$, and $[Fe(OH)_2(H_2O)_4]^{0}$) (species 20 - 22) and the neutral ferric Fe species ($[Fe(OH)_3(H_2O)_3]^{0}$) (species 19) keep the spin

of the iron sulfide cluster and the original spin of Fe, which indicates no electron transfer. However, there is electron transfer from the mackinawite cluster to ferric iron of for the Fe-aqua species $[Fe(H_2O)_6]^{3+}$, $[Fe(OH)(H_2O)_5]^{2+}$, and $[Fe(OH)_2(H_2O)_4]^{+}$ (Species 16 - 18) according to the charge and spin distribution (Table 4.2). The charge and unpaired spin increase by ~1.17 and 0.9, respectively, for mackinawite when $[Fe(H_2O)_6]^{3+}$ is adsorbed. The charge and spin change become smaller for $[Fe(OH)(H_2O)_5]^{2+}$ and $[Fe(OH)(H_2O)_5]^{2+}$. There is less electron transfer for ferric iron with the increasing number of OH groups in the hydration sphere, i.e., at higher pH. For the neutral ferric iron complex with three OH, no electron transfer occurs automatically between the mackinawite cluster and ferric iron.

This result consistent with the literature (Sanden et al., 2021) that mackinawite can be oxidized by Fe^{3+} in acidic solutions according to the Equation 4.28:

$$FeS + 8Fe^{3+} + 4H_2O \rightarrow 9Fe^{2+} + SO_4^{2-} + 8H^{+}. \quad (4.28)$$

However, oxidation may not go all the way to sulfate but rather form elemental sulfur (Equation 4.29):

$$FeS + 2Fe^{3+} \rightarrow 3Fe^{2+} + S. \quad (4.29)$$

In Equations 4.17 – 4.19 and 4.24, electrons from S^{2-} in FeS are transferred to Fe^{3+}.

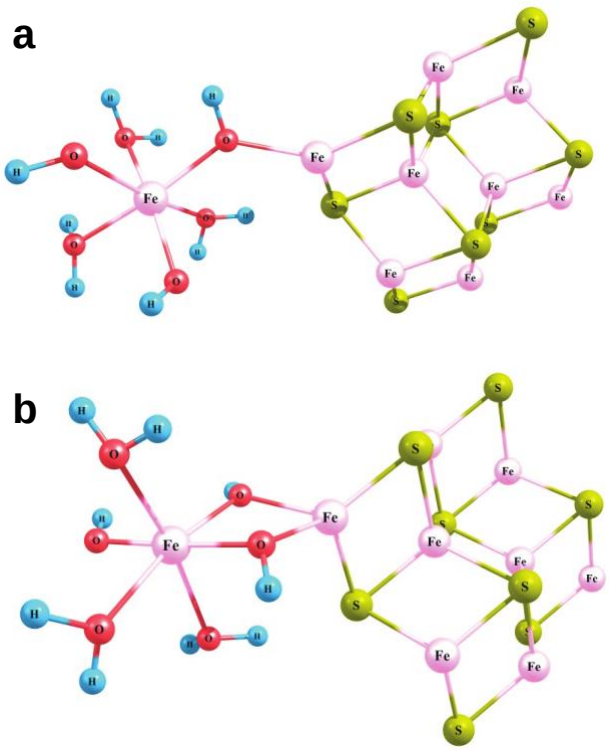

Figure 4.3 Geometry-optimized structure of $[Fe(OH)_3(H_2O)]^0$ adsorption on a mackinawite cluster using a monodentate model (**a**) and bidentate model **(b)**.

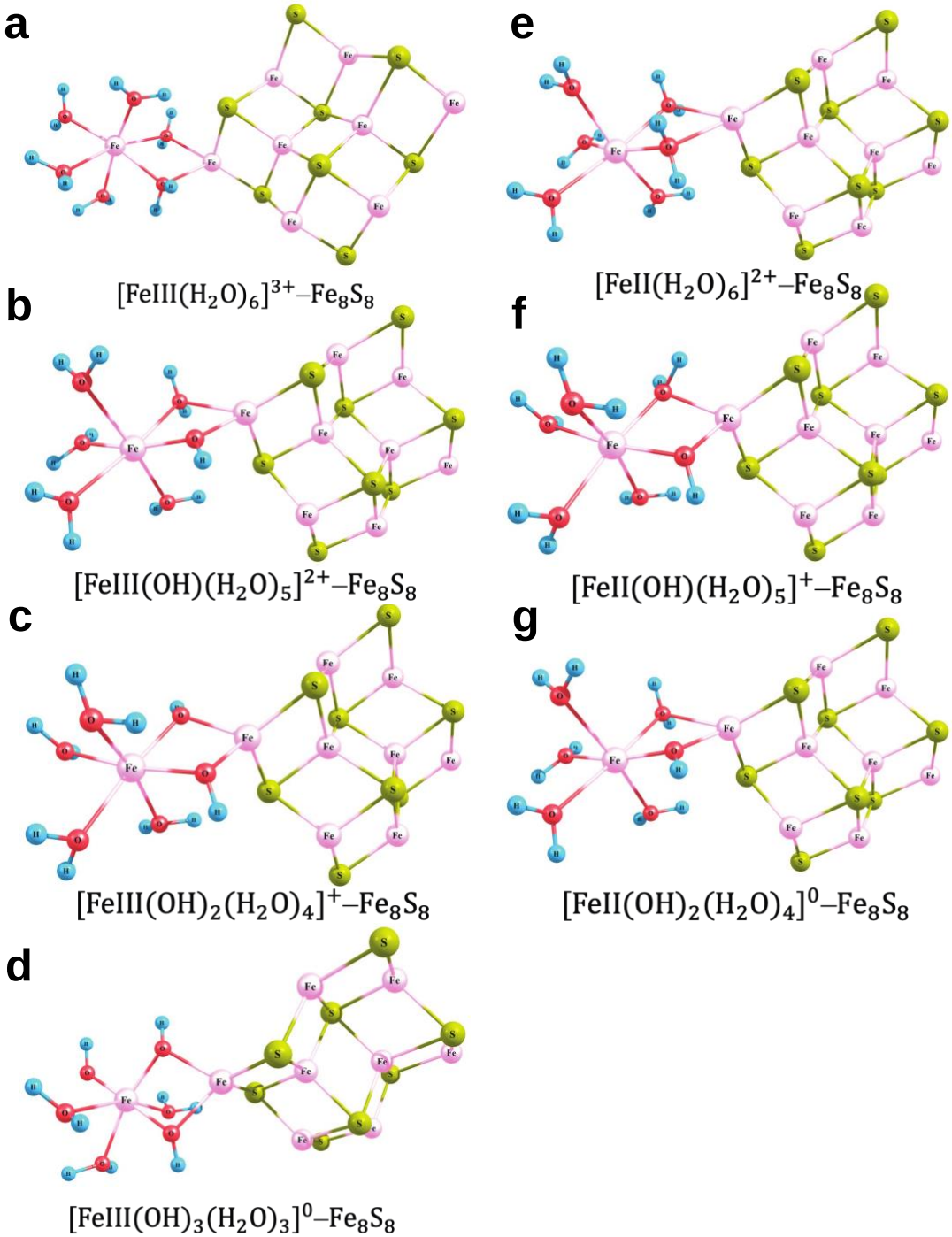

Figure 4.4a-d. Fe(III) adsorption on mackinawite at different pH. **e-g**. Fe(II) adsorption on mackinawite at different pH.

For Mn adsorption, we only modeled unhydroxylated species representing acidic pH values ($[MnIII(H_2O)_6]^{3+}$, Species 37 and $[MnII(H_2O)_6]^{2+}$, Species 39) and neutral species

($[MnIII(OH)_3(H_2O)_3]^0$, Species 38, and $[MnII(OH)_2(H_2O)_4]^0$, Species 40) that would be present at higher pH. The optimized structures are shown in Figure 4.5. Similar to Fe species, there is no electron transfer when Mn(II) or $[Mn(OH)_3(H_2O)_3]^0$ is adsorbed. When $[Mn(H_2O)_6]^{3+}$ is adsorbed on the mackinawite cluster, the charge of Fe_8S_8 increases by 1.1, and the spin decreases by 1.1, indicating one electron from Fe_8S_8 moves to the Mn. The adsorption energies to the mackinawite cluster are all energetically favorable.

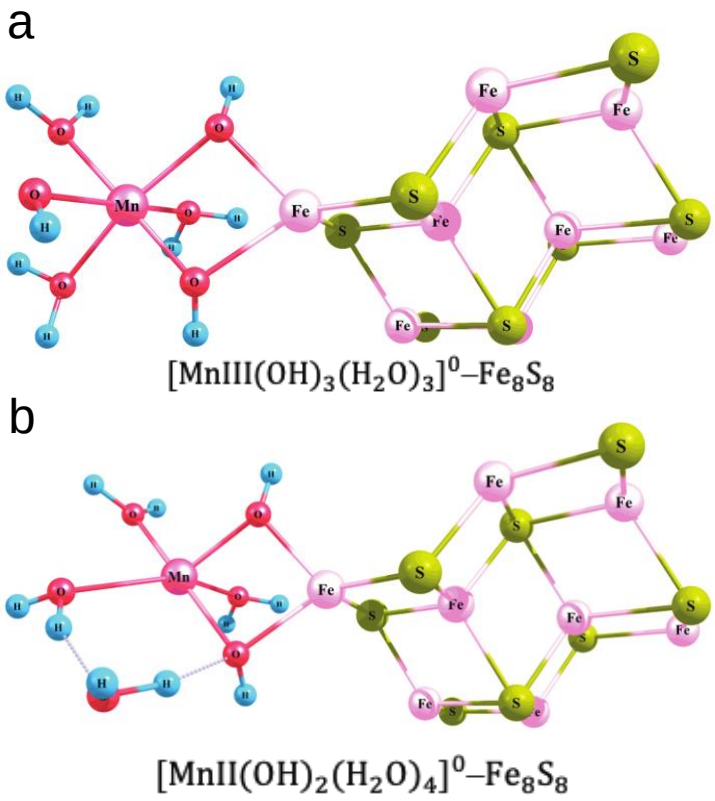

Figure 4.5a Adsorption of $[MnIII(OH)_3(H_2O)_3]^0$ on a mackinawite cluster. **b.** Adsorption of $[MnII(OH)_2(H_2O)_2]^0$ on a mackinawite cluster.

4.4.2.2. Adsorption of quinone species of different oxidation states to a Fe_8S_8 cluster

The optimized structures of (hydro-/semi-) quinone on a Fe_8S_8 nanoparticle are shown in Figure 4.6. One O atom from a hydroxyl group is bonded to a Fe atom in the mackinawite cluster.

The adsorption Gibbs free energies of hydroquinone, semiquinone, and quinone on the mackinawite cluster are -28, -85, and -63 kJ/mol, respectively. Since both iron sulfide and hydroquinone are electron donors, there is barely any electron transfer between the two species. Because semiquinone and quinone are oxidants, their charges when adsorbed are -0.76 for semiquinone and -0.81 for quinone, indicating having received an electron. The spin density changes lead to the same conclusion about electron transfer. The spin of semiquinone decreases from 1 to 0.21, and the spin of quinone changes from 0 to -0.81. Both charge and spin increased by approximately 0.8 for the mackinawite cluster when the organic adsorbate is semiquinone or quinone, indicating oxidation of the mackinawite.

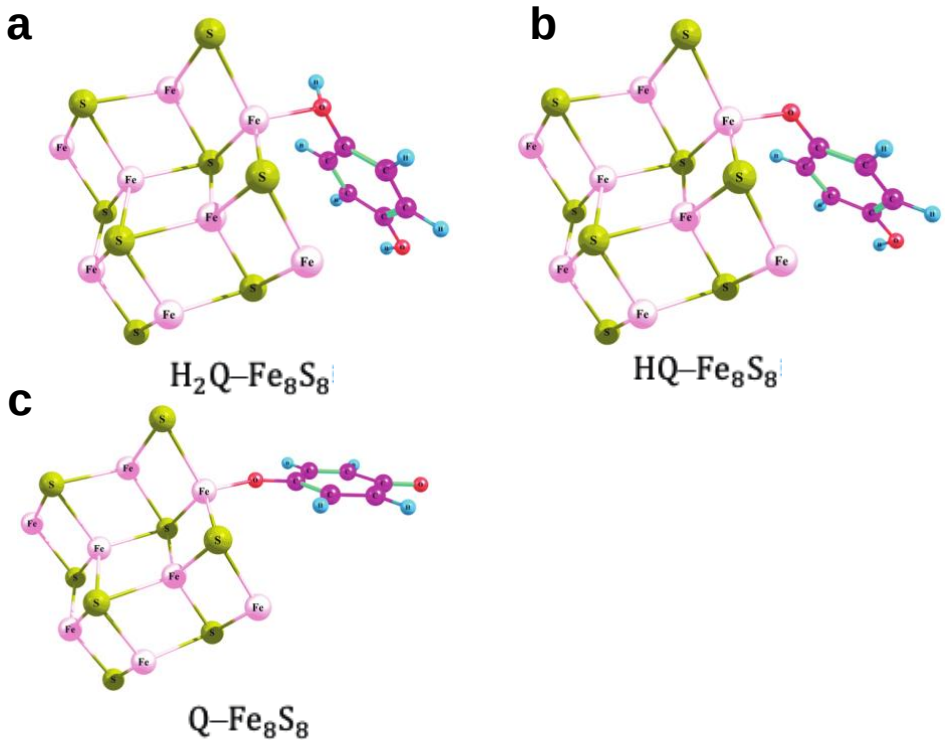

Figure 4.6 Optimized quinone species with all three oxidation states adsorbed on the mackinawite cluster.

4.4.2.3. Co-adsorption of metal-aqua and quinone species to mackinawite cluster

After adsorbing metal-aqua and quinone species separately, we co-adsorb the oxidant

Fe(III)/Mn(III) aqueous complex and reductant hydroquinone on the same mackinawite cluster to examine the potential role of mackinawite in the redox reaction. For both Fe(III)/Mn(III)-aqua, we use the acidic species $[M(H_2O)_6]^{3+}$ and neutral species $[M(OH)_3(H_2O)_3]^0$, where *M* represents Fe/Mn. The optimized structures of co-adsorption are shown in Figure 4.7. The co-adsorption processes are all energetically favorable, with the adsorption energy variation from -87 to -313 kJ/mol (Equations 4.24 – 4.26). Without co-adsorption, $[Fe(H_2O)_6]^{3+}$ oxidizes mackinawite (Equations 4.17 - 4.19) and hydroquinone (Equation 4.11). Co-adsorption leads to electron transfer from the mackinawite to $[Fe(OH)_3(H_2O)_3]^0$ while the hydroquinone remains unaffected (Equation 4.24), in contrast to no electron transfer happening at single adsorption (Equation 4.20). This result indicates that the adsorption of hydroquinone on a mackinawite cluster makes it a stronger reductant to reduce neutral $[Fe(OH)_3(H_2O)_3]^0$. The same phenomenon, however, is not observed in $[Mn(OH)_3(H_2O)_3]^0$ where no electrons are transferred even during co-adsorption.

Table 4.3 Electron transfer between the M-aqua, quinone, and mackinawite cluster.

complex	Electron transfer?			
	Fe		Mn	
M-aqua with quinone				
H_2Q–$[M(OH)_3(H_2O)_3]^0$	No		No	
HQ–$[M(OH)_2(H_2O)_4]^0$	From Fe(II)-aqua to HQ	~ 0.5	From Mn(II) to HQ	~ 1
H_2Q–$[M(H_2O)_6]^{3+}$	From H_2Q to Fe(III)	~ 1	From H_2Q to Mn(III)	~ 1
HQ–$[M(H_2O)_6]^{2+}$	No		No	
M-aqua with mackinawite cluster				
$[M(OH)_3(H_2O)_3]^0$–Fe_8S_8	No		No	
$[M(OH)_2(H_2O)_4]^0$–Fe_8S_8	No		No	
$[M(H_2O)_6]^{3+}$–Fe_8S_8	From Fe_8S_8 to Fe(III)-aqua	~ 1	From Fe_8S_8 to Mn(III)-aqua	~ 1
$[M(H_2O)_6]^{2+}$–Fe_8S_8	No		No	
Quinone with mackinawite cluster				
H_2Q–Fe_8S_8	No		No	
HQ–Fe_8S_8	From Fe_8S_8 to HQ	~ 0.75		
Q–Fe_8S_8	From Fe_8S_8 to Q	~ 0.85		
Three species				
$[M(OH)_3(H_2O)_3]^0$–Fe_8S_8 –H_2Q	From Fe_8S_8 to Fe(III)-aqua	~ 0.67	No	
$M(H_2O)_6^{3+}$–Fe_8S_8–H_2Q	From Fe_8S_8 to Fe(III)-aqua	~ 1		

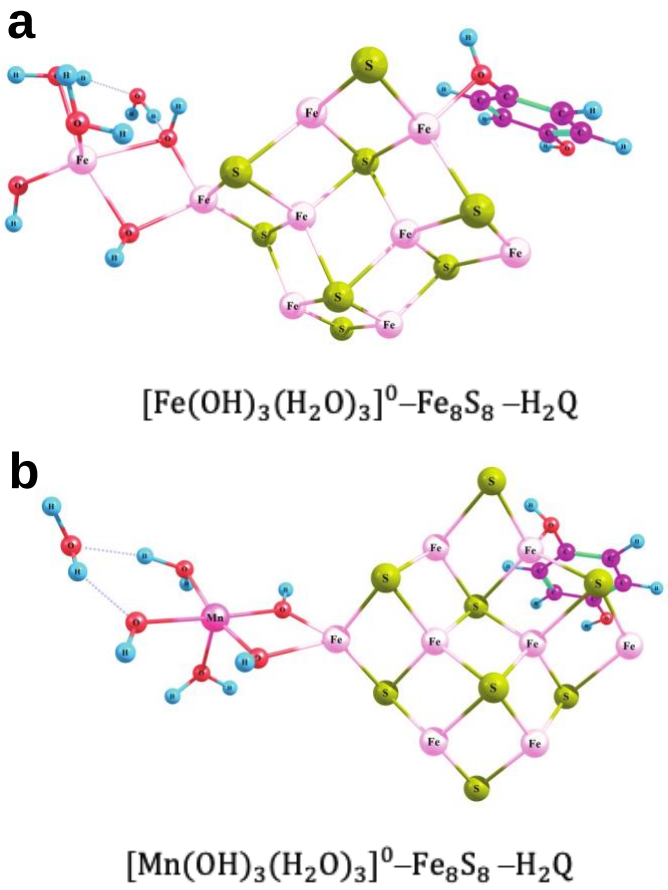

Figure 4.7 Optimized structures of co-adsorption.

4.4.3 Derivation of Pourbaix diagrams for adsorbed species

After we have derived the free energies for the geochemical reactions above, we can evaluate how complexation or (co-)adsorption affects the redox potentials of Fe and Mn. We also made an attempt to derive Pourbaix diagrams for dissolved Fe species that adsorb on a mackinawite cluster. This methodology can be important for a wide range of geochemical applications because many redox processes take place in the adsorbed state, and the mineral surface can aid in the reaction either by helping to dehydrate the species or in the actual electron

shuttling process. Since it is challenging to derive absolute values of standard reduction potentials of dissolved, complexed, or adsorbed species, we calculate the differences between the reactions in adsorbed/complex state and the dissolved one and add this difference to the experimental standard reduction potential of dissolved species.

We start from the derivation of dissolved species of Fe without adsorption using experimental literature data shown in Table 4.4. The half-equations and their pH or reduction potentials are presented in Table 4.5. The pH is calculated by using the equation $\Delta G = -RTlnK$, where *K* is the equilibrium constant. The concentration of dissolved species on the lines separating Eh/pH regions with certain species are predominant are assumed to be equal at room temperature. The SRP is then calculated by $\Delta G = -nFE^o$ and using the Nernst's equation $E = E^o - \frac{nF}{RT}lnK$ where E^o is the standard reduction potential, F is the Faraday constant, R and T are the gas constant in temperature, and K is the equilibrium constant of the reaction.

The Pourbaix diagram construction for Fe-adsorbed is based on the energy difference from dissolved species that are not adsorbed using experimental data. Details can be found in Methods Section 4.3.2. One example is given here for a better explanation. The experimentally determined SRP of Fe^{3+}/Fe^{2+} is 0.77 V. Using the $\Delta\Delta G$ (ΔG_2 - ΔG_1) of the two half-equations $[Fe(H_2O)_6]^{3+}$–$Fe_8S_8 \rightarrow [Fe(H_2O)_6]^{2+}$–$Fe_8S_8$ (ΔG_2) and $[Fe(H_2O)_6]^{3+} \rightarrow [Fe(H_2O)_6]^{2+}$ (ΔG_1), we obtain the SRP of the Fe^{3+}-Fe_8S_8/Fe^{2+}-Fe_8S_8 using $E^\circ = \frac{\Delta\Delta G}{-nF} + 0.77\,V$ (Equation 4.3). The same protocol was used for other half-reactions. One difficulty in this example is that, as mentioned above, this process includes both adsorption of aqueous ferric iron to mackinawite and electron transfer. The Pourbaix diagram for both adsorbed or free is shown in Figure 4.8. When adsorbed to a mackinawite cluster, the whole *E*-pH panel has only two species left, $[FeIII(OH)(H_2O)_5]^{2+}$–Fe_8S_8 and $[FeIII(OH)_2(H_2O)_4]^{+}$–$Fe_8S_8$. Others are beyond the stability

of water. However, they are actually $[FeII(OH)]^{+}$–$Fe_8S_8{}^{+}$ and $[FeII(OH)_2]^{0}$–$Fe_8S_8{}^{+}$ (coordinated water omitted), when taking the spontaneous electron transfer into account.

Table 4.4 Thermodynamic data from the literature for dissolved Fe species.

Species	state	$\Delta_f G$ (kJ/mol)	reference
Fe^{2+}	aq	-91.88	(Beverskog and Puigdomenech, 1996)
$FeOH^{+}$	aq	-270.8	(Beverskog and Puigdomenech, 1996)
$Fe(OH)_2$	aq	-447.43	(Beverskog and Puigdomenech, 1996)
$Fe(OH)_3^{-}$	aq	-612.65	(Beverskog and Puigdomenech, 1996)
$Fe(OH)_4^{2-}$	aq	-775.87	(Beverskog and Puigdomenech, 1996)
Fe^{3+}	aq	-17.59	(Beverskog and Puigdomenech, 1996)
$FeOH^{2+}$	aq	-242.23	(Beverskog and Puigdomenech, 1996)
$Fe(OH)_2^{+}$	aq	-459.5	(Beverskog and Puigdomenech, 1996)
$Fe(OH)_3$	aq	-660.51	(Beverskog and Puigdomenech, 1996)
$Fe(OH)_4^{-}$	aq	-842.85	(Beverskog and Puigdomenech, 1996)
$Fe(OH)_4^{2-}$	aq	-322	(Beverskog and Puigdomenech, 1996)
H_2O	aq	-237.1	(Robie and Hemingway, 1995)
OH^{-}	aq	-157.3	(Robie and Hemingway, 1995)

Table 4.5 Pourbaix diagram construction for Fe in solution from literature thermodynamic data in Table 4.4.

Eqn.	Half reactions	ΔG^0 (kJ/mol)	pH	E^o(V)	Eh (V)
	acid-base reactions				
(30)	$Fe^{2+} + H_2O \rightarrow Fe(OH)^{+} + H^{+}$	58.18	10.2		
(31)	$Fe(OH)^{+} + H_2O \rightarrow Fe(OH)_2(aq) + H^{+}$	60.47	10.6		
(32)	$Fe(OH)_2(aq) + H_2O \rightarrow Fe(OH)_3^{-} + H^{+}$	71.88	12.6		
(33)	$Fe(OH)_3^{-} + H_2O \rightarrow Fe(OH)_4^{2-} + H^{+}$	73.88	12.9		
(34)	$Fe^{3+} + H_2O \rightarrow Fe(OH)^{2+} + H^{+}$	12.46	2.2		
(35)	$Fe(OH)^{2+} + H_2O \rightarrow Fe(OH)_2^{+} + H^{+}$	19.83	3.5		
(36)	$Fe(OH)_2^{+} + H_2O \rightarrow Fe(OH)_3(aq) + H^{+}$	36.09	6.3		
(37)	$Fe(OH)_3(aq) + H_2O \rightarrow Fe(OH)_4^{-} + H^{+}$	54.76	9.6		
	redox reactions				
(38)	$Fe^{3+} + e^{-} \rightarrow Fe^{2+}$	-74.29		0.77	0.77
(39)	$Fe(OH)^{2+} + H^{+} + e^{-} \rightarrow Fe^{2+} + H_2O$	-86.75		0.90	0.90 - 0.0591 pH
(40)	$Fe(OH)_2^{+} + 2H^{+} + e^{-} \rightarrow Fe^{2+} + 2H_2O$	-106.6		1.10	1.10 - 0.118 pH
(41)	$Fe(OH)_3(aq) + 3H^{+} + e^{-} \rightarrow Fe^{2+} + 3H_2O$	-142.7		1.48	1.48 - 0.177 pH
(42)	$Fe(OH)_4^{-} + 4H^{+} + e^{-} \rightarrow Fe^{2+} + 4H_2O$	-197.4		2.05	2.05 - 0.237 pH
(43)	$Fe(OH)_4^{-} + 3H^{+} + e^{-} \rightarrow Fe(OH)^{+} + 3H_2O$	-139.3		1.44	1.44 - 0.177 pH
(44)	$Fe(OH)_4^{-} + 2H^{+} + e^{-} \rightarrow Fe(OH)_2(aq) + 2H_2O$	-78.8		0.82	0.82- 0.118 pH
(45)	$Fe(OH)_4^{-} + H^{+} + e^{-} \rightarrow Fe(OH)_3^{-} + H_2O$	-6.9		0.072	0.072 - 0.059 pH
(46)	$Fe(OH)_4^{-} + e^{-} \rightarrow Fe(OH)_4^{2-}$	67.0		-0.69	-0.69

Table 4.6 Pourbaix diagram construction for Fe adsorbed on a mackinawite cluster. The unit for Gibbs free energy: kJ/mol. The unit for potentials: V.

Eqn.	Half reaction	pKa_{exp}	$\Delta\Delta G^o$	ΔpKa	pKa_{cal}	
	Acid-base reactions					
(47)	$[FeII(H_2O)_6]^{2+}–Fe_8S_8 \rightarrow [FeII(OH)(H_2O)_5]^{+}–Fe_8S_8 + H^+$		-109	-19.1	-8.9	
(48)	$[FeII(OH)(H_2O)_5]^{+}–Fe_8S_8 \rightarrow [FeII(OH)_2(H_2O)_4]^{0}–Fe_8S_8 + H^+$		-71	-12.5	-1.9	
(49)	$[FeIII(H_2O)_6]^{3+}–Fe_8S_8 \rightarrow [FeIII(OH)(H_2O)_5]^{2+}–Fe_8S_8 + H^+$		325	57	59	
(50)	$[FeIII(OH)(H_2O)_5]^{2+}–Fe_8S_8 \rightarrow [FeIII(OH)_2(H_2O)_4]^{+}–Fe_8S_8 + H^+$	3.5	20	3.4	6.9	
(51)	$[FeIII(OH)_2(H_2O)_4]^{+}–Fe_8S_8 \rightarrow [FeIII(OH)_3(H_2O)_3]^{0}–Fe_8S_8 + H^+$		96	16.9	23	
	Oxidation-reduction	ΔE^o_{exp}	$\Delta\Delta G^o$	ΔE^o	E^o_{cal}	Eh
(52)	$[FeIII(H_2O)_6]^{3+}–Fe_8S_8 + e^- \rightarrow [FeII(H_2O)_6]^{2+}–Fe_8S_8$	0.77	564	-5.8	-5.1	
(53)	$[FeIII(H_2O)_6]^{3+}–Fe_8S_8 + e^- \rightarrow [FeII(OH)(H_2O)_5]^{+}–Fe_8S_8 + H^+$		455	-4.7	-4.6	-4.6+0.059 pH
(54)	$[FeIII(OH)(H_2O)_5]^{+}–Fe_8S_8 + e^- \rightarrow [FeII(OH)(H_2O)_5]^{+}–Fe_8S_8$		130	-1.3	-1.0	
(55)	$[FeIII(OH)_2(H_2O)_4]^{+}–Fe_8S_8 + H^+ + e^- \rightarrow [FeII(OH)(H_2O)_5]^{+}–Fe_8S_8$		110	-1.1	-0.6	-0.6-0.059pH

Table 4.6b. Calculated reduction potentials for Mn(III)/Mn(II) when they adsorb on mackinawite or complex with hydroquinone. The unit for Gibbs free energy: kJ/mol. The unit for potentials: V.

Eqn.	Half reaction	E^o_{exp} [a]	$\Delta\Delta G^o$	ΔE^c	E^o_{calc}
(56)	$MnIII(H_2O)_6^{3+} + e^- \rightarrow MnII(H_2O)_6^{2+}$	~1.56	0	0	1.56
(57)	$MnIII(H_2O)_6^{3+}–Fe_8S_8 + e^- \rightarrow MnII(H_2O)_6^{2+}–Fe_8S_8$	N/A	38	-0.4	1.17
(58)	$MnIII(H_2O)_6^{3+}–H_2Q + e^- \rightarrow MnII(H_2O)_6^{2+}–H_2Q$	N/A	238	-2.5	-1.7

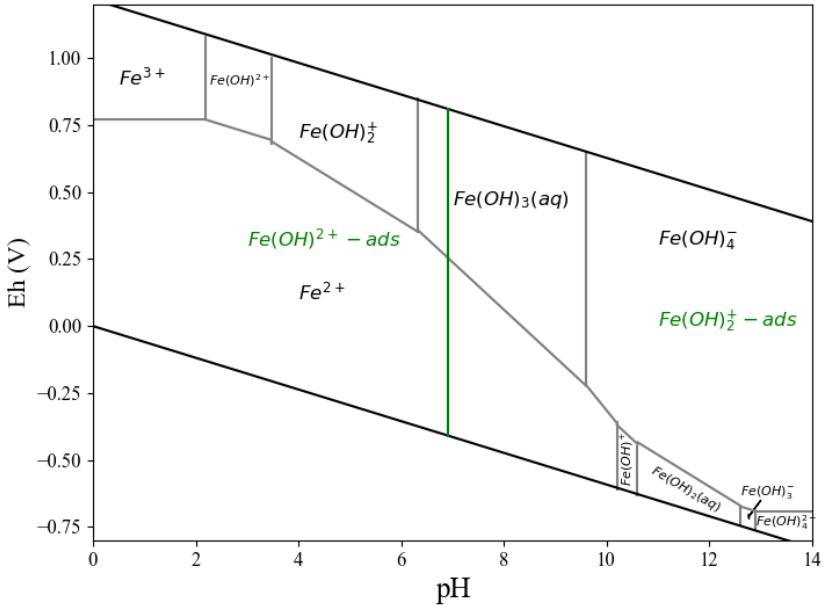

Figure 4.8 Grey lines represent the Pourbaix diagram of Fe with all dissolved species. The green line illustrates the Pourbaix diagram when dissolved Fe species are adsorbed on a mackinawite cluster. It is constructed manually using data in Tables 4.5 and 4.6.

4.5 Discussions and implications

Aqueous Fe and Mn, natural organic matter, and FeS nanoparticles are all present in natural waters, such as low-oxygen environments along terrestrial to aquatic interfaces, where they likely interact and thus influence many geochemical/biochemical processes. Knowledge of the thermodynamics and electron distribution provides new information on the interaction between these constituents. One is how the complexation and adsorption affect the oxidation ability (reduction potential) of Fe(III) and Mn(III), which greatly affects the cycling of the metal. FeS nanoparticles lately have shown great potential in environmental remediation (Renock et al., 2009; Jeong et al., 2010; Gong et al., 2012; Bi et al., 2013; Niazi and Burton, 2016; Chen et al., 2019). The oxidation of FeS is an important topic that has received much attention because it may release toxic metal incorporated in the iron sulfide structure (Holmes, 1999; Liu et al., 2008). Our results show that the adsorption of redox-active dissolved metal species may oxidize the FeS nanoparticle depending on pH and on the reducing capacity of NOM (i.e., the abundance of hydroquinone), which also has environmental implications.

4.5.1 Implications on Fe and Mn cycle for natural systems

Micro-nutrient iron plays a crucial role in many essential life processes (Hänsch and Mendel, 2009; Butler, 2018). In highly acidic waters, ferric iron oxides can be dissolved, resulting in a relatively high concentration of both Fe^{2+} and Fe^{3+}. The Fe^{3+} can be reduced by various organic and inorganic reductants such as hydroquinone and mackinawite nanoparticles, as indicated by partial electron transfer in this study. Dissolved organic matter is also reported to reduce part of Fe^{3+} to Fe^{2+} in acidic solutions (pH 3 – 5) in Jiang et al. (2015) and therefore affect the iron removal or bioavailability of Fe (Rose and Waite, 2003).

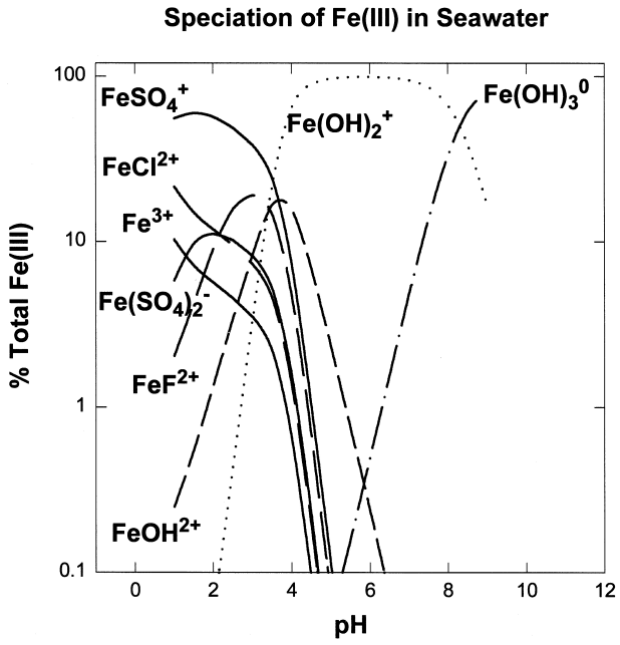

Figure 4.9 Speciation of Fe(III) in seawater (Millero et al., 1995; Millero, 1998).

In circumneutral or basic solutions such as surface water, iron particles tend to precipitate out due to the high pH (~8.1) in the oxic water column (Goldberg, 1954), leaving the dissolved iron in the ocean usually below 4 nmol/kg ('GEOTRACES', https://www.bodc.ac.uk/geotraces/data/dp/). The low concentration greatly limits oceanic primary productivity (Moore et al., 2001, 2013). For that reason, Fe speciation and its biochemical cycling have been intensely investigated for the past decades (Millero et al., 1995; Boyd and Ellwood, 2010; Caprara et al., 2016; Tagliabue et al., 2017; Lohan and Tagliabue, 2018). Some studies suggested that dissolved Fe(II) has been prevented from oxidation and stabilized in the presence of both dissolved organic ligands and particulate organic carbon in deep-sea hydrothermal venting (Bennett et al., 2008; Toner et al., 2009). More than 99% of dissolved Fe in the ocean is complex with organic ligands (Gledhill and Buck, 2012). Our results suggest that dissolved Fe/Mn-aqua species adsorbing on mackinawite or complex with hydroquinone is thermodynamically favorable. Although the electron transfer does not happen spontaneously between dissolved $Fe(OH)_3$ and hydroquinone or mackinawite alone, when they are both present, dissolved $Fe(OH)_3$ can be

reduced to $Fe(OH)_2$, and Fe(II) may be more bioavailable than Fe(III) (Bury et al., 2001). This process will promote the non-reductive dissolution of ferrihydrite according to Le Chatelier's principle and may yield elevated concentrations of Fe^{2+}/Mn^{2+} in natural waters. Toner et al., 2009 mentioned that the stability constants for Fe(II)-complexing organic ligands are approximately equal to Fe(III), at least for organo-sulfur compound $C_3H_8S_2$. Given this information, organic ligands may not reduce Fe(III) to Fe(II) but keep their original oxidation state when complexation happens. With mackinawite nanoparticles, Fe(III) and organic particles are more favorably adsorbed on the particle surface. The adsorption of $Fe(OH)_3 \cdot 3H_2O$ on mackinawite cluster may also prevent scavenging of Fe(III) and affect the biogeochemical cycle of iron.

Mn(II) is initially released into the environment from hydrothermal fluids. Dissolved Mn (III) is a strong oxidant. Mn(III) is also stable as a soluble species in the oxygenated water column when stabilized by organic ligands as Mn(III)–L complexes.

4.5.2 Mackinawite oxidation

Pollutant metals such as Cr, Hg, and As can be incorporated into mineral mackinawite (Renock et al., 2009; Jeong et al., 2010; Gong et al., 2012; Niazi and Burton, 2016; Chen et al., 2019). The oxidation of mackinawite will result in releasing those elements into the water. In basic pH solutions, neutral iron hydroxide $M(OH)_3^0 \cdot 3H_2O$ does not seem to oxidize mackinawite when there is no organic matter co-adsorbed. However, in acidic solutions, mackinawite will be oxidized by Fe^{3+}. In basic pH conditions, although there is no electron transfer between neutral Fe(III) and a mackinawite cluster, the electron transfer can be promoted in the presence of small organic molecules such as hydroquinone.

4.6 Conclusions

In summary, we used DFT to compute the thermodynamics and electron distribution for

the interaction of dissolved Fe/Mn at different pH with quinone species and their (co-)adsorption on a mackinawite cluster. All these species are common in various environments, and they likely interact. The results show that Fe^{3+}/Mn^{3+} can be reduced by hydroquinone or mackinawite particles to become their reduced state in acidic or neutral solution, but not at basic pH when the dissolved oxidant species are $Fe(OH)_3^0 \cdot 3H_2O$ or $Mn(OH)_3^0 \cdot 3H_2O$. However, when the oxidant metal-aqua and hydroquinone are co-adsorbed on a mackinawite nanoparticle, the presence of organic matter facilitates the electron transfer between $Fe(OH)_3^0 \cdot 3H_2O$ / $Mn(OH)_3^0 \cdot 3H_2O$ and mackinawite. The complexation of dissolved Fe/Mn with organic matters and the adsorption of Fe/Mn on nanoparticles are mostly thermodynamically favorable, indicating the complexation and adsorption processes may help stabilize the species and keeps Fe^{3+} from sinking out of the ocean or Mn^{3+} from disproportionation. Dissolved Fe concentration in the ocean is low and limits the ocean's primary production. Binding to organic ligands or adsorbing on FeS nanoparticles helps increase the dissolved Fe/Mn concentration in solution, especially more bioavailable Fe(II). On the other hand, the oxidation of organic matters or mackinawite nanoparticles may also have great environmental implications. Mackinawite oxidation may release contaminated elements incorporated in the crystal. Using the Gibbs free energy data computed for each species, we attempted to calculate the reduction-potential shift of Fe^{3+}/Fe^{2+} and Mn^{3+}/Mn^{2+} when adsorbed on mackinawite or complexed to hydroquinone. However, some of the processes are significantly affected by the electron transfer processes.

4.7 References

Bai Y., Sun T., Angenent L. T., Haderlein S. B. and Kappler A. (2020) Electron hopping enables rapid electron transfer between quinone-/hydroquinone-containing organic molecules in microbial iron(III) mineral reduction. *Environ. Sci. Technol.* **54**, 10646–10653.

Bennett S. A., Achterberg E. P., Connelly D. P., Statham P. J., Fones G. R. and German C. R. (2008) The distribution and stabilisation of dissolved Fe in deep-sea hydrothermal plumes. *Earth and Planetary Science Letters* **270**, 157–167.

Beverskog B. and Puigdomenech I. (1996) Revised pourbaix diagrams for iron at 25–300 °C. *Corrosion Science* **38**, 2121–2135.

Bi Y., Hyun S. P., Kukkadapu R. K. and Hayes K. F. (2013) Oxidative dissolution of UO_2 in a simulated groundwater containing synthetic nanocrystalline mackinawite. *Geochimica et Cosmochimica Acta* **102**, 175–190.

Boyd P. W. and Ellwood M. J. (2010) The biogeochemical cycle of iron in the ocean. *Nature Geosci* **3**, 675–682.

Buchachenko A. L. (1995) MIE versus CIE: Comparative analysis of magnetic and classical isotope effects. *Chem. Rev.* **95**, 2507–2528.

Buchachenko A. L. and Berdinsky V. L. (2002) Electron spin catalysis. *Chem. Rev.* **102**, 603–612.

Bury N. R., Grosell M., Wood C. M., Hogstrand C., Wilson R. W., Rankin J. C., Busk M., Lecklin T. and Jensen F. B. (2001) Intestinal iron uptake in the European flounder (Platichthys flesus). *Journal of Experimental Biology* **204**, 3779–3787.

Butler D. (2018) Researchers have finally created a tool to spot duplicated images across thousands of papers. *Nature*.

Caprara S., Buck K. N., Gerringa L. J. A., Rijkenberg M. J. A. and Monticelli D. (2016) A compilation of iron speciation data for open oceanic waters. *Frontiers in Marine Science* **3**.

Chen Yaoning, Liang W., Li Y., Wu Y., Chen Yanrong, Xiao W., Zhao L., Zhang J. and Li H. (2019) Modification, application and reaction mechanisms of nano-sized iron sulfide particles for pollutant removal from soil and water: A review. *Chemical Engineering Journal* **362**, 144–159.

Daugherty E. E., Gilbert B., Nico P. S. and Borch T. (2017) Complexation and redox buffering of iron(II) by dissolved organic matter. *Environ. Sci. Technol.* **51**, 11096–11104.

De Abreu H. A., Guimarães L. and Duarte H. A. (2006) Density-functional theory study of iron(III) hydrolysis in aqueous solution. *J. Phys. Chem. A* **110**, 7713–7718.

Devey A. J., Grau-Crespo R. and de Leeuw N. H. (2008) Combined density functional theory and interatomic potential study of the bulk and surface structures and properties of the iron sulfide mackinawite (FeS). *J. Phys. Chem. C* **112**, 10960–10967.

Gledhill M. and Buck K. (2012) The organic complexation of iron in the marine environment: A review. *Frontiers in Microbiology* **3**.

Goldberg E. D. (1954) Marine geochemistry 1. Chemical scavengers of the sea. *The Journal of Geology* **62**, 249–265.

Gong Y., Liu Y., Xiong Z., Kaback D. and Zhao D. (2012) Immobilization of mercury in field soil and sediment using carboxymethyl cellulose stabilized iron sulfide nanoparticles. *Nanotechnology* **23**, 294007.

Hammes-Schiffer S. (2010) Introduction: Proton-coupled electron transfer. *Chem. Rev.* **110**, 6937–6938.

Hänsch R. and Mendel R. R. (2009) Physiological functions of mineral micronutrients (Cu, Zn, Mn, Fe, Ni, Mo, B, Cl). *Current Opinion in Plant Biology* **12**, 259–266.

Holmes J. (1999) Fate of incorporated metals during mackinawite oxidation in sea water. *Applied Geochemistry* **14**, 277–281.

Huynh M. H. V. and Meyer T. J. (2007) Proton-coupled electron transfer. *Chem. Rev.* **107**, 5004–5064.

Hyun S. P., Davis J. A., Sun K. and Hayes K. F. (2012) Uranium(VI) reduction by iron(II) monosulfide mackinawite. *Environ. Sci. Technol.* **46**, 3369–3376.

Jeong H. Y., Han Y.-S., Park S. W. and Hayes K. F. (2010) Aerobic oxidation of mackinawite (FeS) and its environmental implication for arsenic mobilization. *Geochimica et Cosmochimica Acta* **74**, 3182–3198.

Jiang C., Garg S. and Waite T. D. (2015) Hydroquinone-mediated redox cycling of iron and concomitant oxidation of hydroquinone in oxic waters under acidic conditions: comparison with iron–natural organic matter interactions. *Environ. Sci. Technol.* **49**, 14076–14084.

Kelly C. P., Cramer C. J. and Truhlar D. G. (2006) Aqueous solvation free energies of ions and ion−water clusters based on an accurate value for the absolute aqueous solvation free energy of the proton. *J. Phys. Chem. B* **110**, 16066–16081.

Klüpfel L., Piepenbrock A., Kappler A. and Sander M. (2014) Humic substances as fully regenerable electron acceptors in recurrently anoxic environments. *Nature Geosci* **7**, 195–200.

Kwon K. D., Refson K., Bone S., Qiao R., Yang W., Liu Z. and Sposito G. (2011) Magnetic ordering in tetragonal FeS: Evidence for strong itinerant spin fluctuations. *Phys. Rev. B* **83**, 064402.

Levar C. E., Hoffman C. L., Dunshee A. J., Toner B. M. and Bond D. R. (2017) Redox potential as a master variable controlling pathways of metal reduction by Geobacter sulfurreducens. *ISME J* **11**, 741–752.

Liu J., Valsaraj K. T., Devai I. and DeLaune R. D. (2008) Immobilization of aqueous Hg(II) by mackinawite (FeS). *Journal of Hazardous Materials* **157**, 432–440.

Lohan M. C. and Tagliabue A. (2018) Oceanic micronutrients: Trace metals that are essential for marine life. *Elements* **14**, 385–390.

Luu Y.-S. and Ramsay J. A. (2003) Review: microbial mechanisms of accessing insoluble Fe(III) as an energy source. *World Journal of Microbiology and Biotechnology* **19**, 215–225.

Ma B., Tong X., Guo C., Guo Xiaoning, Guo Xiangyun and Keil F. J. (2016) Pyrite nanoparticles: an Earth-abundant mineral catalyst for activation of molecular hydrogen and hydrogenation of nitroaromatics. *RSC Adv.* **6**, 55220–55224.

Madison A. S., Tebo B. M., Mucci A., Sundby B. and George W. Luther I. I. I. (2013) Abundant porewater Mn(III) is a major component of the sedimentary redox system. *Science*.

Mayer J. M. (2004) Proton-coupled electron transfer: A reaction chemist's view. *Annual Review of Physical Chemistry* **55**, 363–90.

Meyer T. E., Przysiecki C. T., Watkins J. A., Bhattacharyya A., Simondsen R. P., Cusanovich M. A. and Tollin G. (1983) Correlation between rate constant for reduction and redox potential as a basis for systematic investigation of reaction mechanisms of electron transfer proteins. *Proceedings of the National Academy of Sciences* **80**, 6740–6744.

Millero F. J. (1998) Solubility of Fe(III) in seawater. *Earth and Planetary Science Letters* **154**, 323–329.

Millero F. J., Yao W. and Aicher J. (1995) The speciation of Fe(II) and Fe(III) in natural waters. *Marine Chemistry* **50**, 21–39.

Moore C. M., Mills M. M., Arrigo K. R., Berman-Frank I., Bopp L., Boyd P. W., Galbraith E. D., Geider R. J., Guieu C., Jaccard S. L., Jickells T. D., La Roche J., Lenton T. M., Mahowald N. M., Marañón E., Marinov I., Moore J. K., Nakatsuka T., Oschlies A., Saito M. A., Thingstad T. F., Tsuda A. and Ulloa O. (2013) Processes and patterns of oceanic nutrient limitation. *Nature Geosci* **6**, 701–710.

Moore J. K., Doney S. C., Glover D. M. and Fung I. Y. (2001) Iron cycling and nutrient-limitation patterns in surface waters of the World Ocean. *Deep Sea Research Part II: Topical Studies in Oceanography* **49**, 463–507.

Mullet M., Boursiquot S., Abdelmoula M., Génin J.-M. and Ehrhardt J.-J. (2002) Surface chemistry and structural properties of mackinawite prepared by reaction of sulfide ions with metallic iron. *Geochimica et Cosmochimica Acta* **66**, 829–836.

Niazi N. K. and Burton E. D. (2016) Arsenic sorption to nanoparticulate mackinawite (FeS): An examination of phosphate competition. *Environmental Pollution* **218**, 111–117.

Palascak M. W. and Shields G. C. (2004) Accurate Experimental Values for the free energies of hydration of H^+, OH^-, and H_3O^+. *J. Phys. Chem. A* **108**, 3692–3694.

Poggenburg C., Mikutta R., Sander M., Schippers A., Marchanka A., Dohrmann R. and Guggenberger G. (2016) Microbial reduction of ferrihydrite-organic matter coprecipitates by Shewanella putrefaciens and Geobacter metallireducens in comparison to mediated electrochemical reduction. *Chemical Geology* **447**, 133–147.

Renock D., Gallegos T., Utsunomiya S., Hayes K., Ewing R. C. and Becker U. (2009) Chemical and structural characterization of As immobilization by nanoparticles of mackinawite (FeSm). *Chemical Geology* **268**, 116–125.

Robie R. A. and Hemingway B. S. (1995) *Thermodynamic properties of minerals and related substances at 298.15 K and 1 bar (10^5 pascals) pressure and at higher temperatures*., U.S. G.P.O. ; For sale by U.S. Geological Survey, Information Services,.

Rose A. L. and Waite T. D. (2003) Kinetics of iron complexation by dissolved natural organic matter in coastal waters. *Marine Chemistry* **84**, 85–103.

Sander M., Hofstetter T. B. and Gorski C. A. (2015) Electrochemical analyses of redox-active Iron minerals: A review of nonmediated and mediated approaches. *Environ. Sci. Technol.* **49**, 5862–5878.

Sanden S. A., K. Szilagyi R., Li Y., Kitadai N., M. Webb S., Yano T., Nakamura R., Hara M. and E. McGlynn S. (2021) Electrochemically induced metal- vs. ligand-based redox changes in mackinawite: identification of a Fe^{3+} - and polysulfide-containing intermediate. *Dalton Transactions* **50**, 11763–11774.

Santana-Casiano J. M., González-Dávila M., González A. G. and Millero F. J. (2010) Fe(III) reduction in the presence of catechol in seawater. *Aquat Geochem* **16**, 467–482.

Schröder C., Wan M., Butler I. B., Tait A., Peiffer S. and McCammon C. A. (2020) Identification of mackinawite and constraints on its electronic configuration using Mössbauer spectroscopy. *Minerals* **10**, 1090.

Strathmann T. J. and Stone A. T. (2002) Reduction of oxamyl and related pesticides by FeII: Influence of organic ligands and natural organic matter. *Environ. Sci. Technol.* **36**, 5172–5183.

Strathmann T. J. (2011) Redox reactivity of organically complexed iron(II) species with aquatic contaminants. In *Aquatic Redox Chemistry* ACS Symposium Series. American Chemical Society. pp. 283–313.

Sundararajan M., S. Assary R., H. Hillier I. and J. Vaughan D. (2011) The mechanism of the reduction of $[AnO_2]^{2+}$ (An = U, Np, Pu) in aqueous solution, and by Fe(II) containing proteins and mineral surfaces, probed by DFT calculations. *Dalton Transactions* **40**, 11156–11163.

Swart M. and Costas M. (2015) *Spin States in Biochemistry and Inorganic Chemistry: Influence on Structure and Reactivity*., John Wiley & Sons.

Tagliabue A., Bowie A. R., Boyd P. W., Buck K. N., Johnson K. S. and Saito M. A. (2017) The integral role of iron in ocean biogeochemistry. *Nature* **543**, 51–59.

Toner B. M., Fakra S. C., Manganini S. J., Santelli C. M., Marcus M. A., Moffett J. W., Rouxel O., German C. R. and Edwards K. J. (2009) Preservation of iron(II) by carbon-rich matrices in a hydrothermal plume. *Nature Geosci* **2**, 197–201.

Uudsemaa M. and Tamm T. (2003) Density-functional theory calculations of aqueous redox potentials of fourth-period transition metals. *J. Phys. Chem. A* **107**, 9997–10003.

Vaughan D. J. and Ridout M. S. (1971) Mössbauer studies of some sulphide minerals. *Journal of Inorganic and Nuclear Chemistry* **33**, 741–746.

Wallace G., Sander M., Chin Y.-P. and A. Arnold W. (2017) Quantifying the electron donating capacities of sulfide and dissolved organic matter in sediment pore waters of wetlands. *Environmental Science: Processes & Impacts* **19**, 758–767.

Webb S. M., Dick G. J., Bargar J. R. and Tebo B. M. (2005) Evidence for the presence of Mn(III) intermediates in the bacterial oxidation of Mn(II). *PNAS* **102**, 5558–5563.

Wegh R. T. and Meijerink A. (1999) Spin-allowed and spin-forbidden $4f^n \leftrightarrow 4f^{n-1}5d$ transitions for heavy lanthanides in fluoride hosts. *Phys. Rev. B* **60**, 10820–10830.

Weinberg D. R., Gagliardi C. J., Hull J. F., Murphy C. F., Kent C. A., Westlake B. C., Paul A., Ess D. H., McCafferty D. G. and Meyer T. J. (2012) Proton-coupled electron transfer. *Chem. Rev.* **112**, 4016–4093.

Wiertz J. V., Mateo M. and Escobar B. (2006) Mechanism of pyrite catalysis of As(III) oxidation in bioleaching solutions at 30 °C and 70 °C. *Hydrometallurgy* **83**, 35–39.

Yang Z., Kappler A. and Jiang J. (2016) Reducing capacities and distribution of redox-active functional groups in low molecular weight fractions of humic acids. *Environ. Sci. Technol.* **50**, 12105–12113.

CHAPTER 5

Conclusions

Both experimental and computational approaches are used in this dissertation to address problems regarding mineral properties and chemical reactions. The projects in this dissertation cover a broad range of topics, from high-temperature properties of minerals and their applications in planetary science to low-temperature surface environmental problems. I present this chapter as the concluding remarks for each chapter, including the achievements and limitations of each study and potential future work.

Chapter 2 experimentally deals with the element distribution between olivine and melt for natural lunar samples. Highly accurate data for natural olivine grains and their host melt were obtained. By pushing the limit of analytical instruments, we report partition coefficients of 21 elements. Some of them are very low in concentration in natural samples and were rarely reported in the literature. Given that the formation of the Moon is closely connected to the Earth, data are further compared with those reported under terrestrial conditions to understand better the similarities and differences in chemical compositions between the two planetary bodies.

Most of the partitioning data measured for lunar samples agree well with those in terrestrial basalts, except for V and Cr. Lunar basalts show higher V partition coefficients and lower Cr partition coefficients for olivine and melt. Although both V and Cr exhibit various valence states, the oxygen fugacity difference between the Moon and Earth is the dominant reason for the V partition coefficient difference; however, it does not explain the difference in Cr partitioning. The smaller

partition coefficients of Cr in lunar basalts than in terrestrial basalts seem to be due to compositional effects. The difference in V and Cr partition coefficients on the Moon can explain the much higher Cr concentration and lower V concentration in evolved lunar basalts than in evolved terrestrial basalts. By analyzing the chemical composition of lunar samples from the literature, we found a constant V/Cr ratio of approximately 0.039 in lunar basalts. Constant ratios are useful in geochemistry to help derive the concentration of a larger reservoir, such as the primitive mantle or the whole Moon. The partition coefficients determined during this study can be applied to model lunar magma evolution, infer melt composition from olivine composition, and model partial melting of the lunar mantle.

The factors controlling Cr partitioning in olivine and melt are still unclear. The work in Chapter 2 attempts to build a model using all published data found to give an explicit equation. Yet, it is not ideal. In the future, it is worth trying computational methods to investigate partitioning by changing one factor at a time. Related computational work has already started (e.g., Allan et al., 2003, simulating mineral–melt trace-element partitioning), although experimental geochemistry is still the dominant approach. One strong competitive advantage of computational methods is that they can model an actual equilibrium, which is often difficult to reach experimentally. On the other hand, computational results may be highly dependent on computation parameters and model setup. Combining the experimental and computational approaches should give us a more accurate and better understanding. Another thing to try is to use better algorithms in machine learning. Machine learning has been used widely in a variety of scientific disciplines for the last decades. Its application in geology started in the last decade (Rodriguez-Galiano et al., 2015; Karpatne et al., 2019; Dumakor-Dupey et al., 2021). One can believe it will provide more new ideas, especially for complicated models.

Chapter 3 also deals with minerals under elevated pressure and temperature conditions. Computational methods (DFT with QHA) are used to model olivine's structural and vibrational properties. Absorption infrared and Raman spectroscopy are widely used, especially in exploring mineral phases and compositions for planetary materials and the associated geological processes. We primarily evaluate the temperature and pressure effect on the vibrational modes and briefly explore the impact of other factors, such as composition, configuration, and isotope composition. This is the first time, to our knowledge, that vibrational frequencies under simultaneous high-temperature and high-pressure conditions are reported for olivine. Temperature and pressure affect the frequency of each mode roughly linearly; however, different modes react differently to elevated pressures and temperatures, depending on if they are associated with translation, rotation, or internal movement of SiO_4. With the knowledge of the slopes of frequencies as a function of pressure or temperature for a given mode, we can parameterize frequency changes for each mode with T and P. We also demonstrate that although isotopes may have a limited effect on vibrational frequencies, other factors (temperature, pressure, configuration, composition, e.g., within a solid solution series) can affect peak positions of modes remarkably. The vibrational modes are a combined effect of all factors. Therefore, one should fully evaluate all factors before using IR and Raman spectroscopy to indicate compositions or T, P conditions.

In Chapter 3, the quasi-harmonic approximation (QHA), combined with a quantum-mechanical approach, is used to evaluate the temperature effect on vibrational modes. In this way, temperature and pressure affect the vibrational frequencies merely by changing cell parameters/volume. However, this is a simplification. A volume independent contribution arising from anharmonic interactions can be significant when the temperature is very high. Therefore, one must take caution when applying QHA to mantle-core conditions or even deep mantle ones.

Although we provide a methodology to evaluate simultaneous high-temperature and high-pressure effects, it is limited in the temperature range. For higher temperature conditions, molecular dynamics may have to be used to include anharmonicity. Future studies may also work on modeling vibrational frequencies that consider all critical factors (*T*, *P*, cation distribution, composition, etc.).

In the Appendix of Chapter 3, we present the preliminary results on the thermodynamics of the forsterite-fayalite solid solution for different Fe-Mg ordering in the unit cell with temperature. The results show that Fe prefers M1 octahedral sites, and Mg prefers M2 sites thermodynamically. There is no reversal in the temperature range from 273 K to 1273 K. This part is related to the vibrational spectroscopy section of Chapter 3 but stands as a separate project. At this point, it is only presented in the Appendix because more interpretational work has to be done, for example, to develop a three-dimensional phase diagram with the mole fraction of Fe in the M1 and M2 sites as independent variables, and phase separation is calculated as a function of temperature.

Chapter 4 uses density functional theory (DFT) to examine the complexation and redox reaction of dissolved metal species (Fe and Mn) with small organic redox-active molecules and their co-adsorption on a mackinawite nanoparticle that can potentially act as a dehydration host, as an inert mineral surface, or it can take part in the reaction or act as a redox catalyst. The thermodynamics and electron distribution (charge and spin density) were computed. Considering the ubiquity of natural organic matter and nanoparticles, it is essential to understand their interactions. Results show that the complexation and adsorption for most species are thermodynamically favorable, but occasionally with slight positive Gibbs free energies of reaction. The reactivities of Fe(III) or Mn(III) change significantly with pH (it has to be noted that these

types of calculations cannot explicitly calculate pH values directly but allow for the modeling of pH ranges depending on the protonation state of the species). There is spontaneous electron transfer from the reductants hydroquinone or the mackinawite cluster to dissolved Fe(III) or Mn(III) at acidic or neutral solutions, but not to neutral species $[Fe(OH)_3(H_2O)_3]^0$ or $[Mn(OH)_3(H_2O)_3]^0$, which are expected at basic pH values. When hydroquinone is co-adsorbed on the mackinawite particle, however, an electron transfers from the mackinawite cluster to $[Fe(OH)_3(H_2O)_3]^0$. In short, the complexation and adsorption may induce remarkable changes in the reactivity of the metal and affect Fe and Mn cycling in various water bodies. We also attempted to construct the Pourbaix (potential-pH) diagram of Fe when adsorbed on an iron sulfide nanoparticle. Since there are multiple ways to adsorb the Fe/Mn-aqua on a molecule, we started the initial structures with similar configurations for different species. Modeling all possible adsorbing structures is computationally expensive and beyond the scope of this study. We give a flavor of how adsorption affects the reactivity and cycling of metals. The development of Pourbaix diagrams for adsorbed, complexed, or co-adsorbed species using a combination of experimentally derived solution data and quantum-mechanically derived adsorption and complexation data is new and could have a considerable impact on environmental geochemistry. Given that a significant portion of environmentally relevant reactions takes place on surfaces, this could open up an avenue for developing reaction models at different pH, Eh, the concentration of organic matter, and prevalent mineral surfaces in a much more detailed way.

We also examine the spin status of Fe in mackinawite in the form of a Fe_8S_8 cluster. Even though it was put in the Appendix, the work can be developed into a separate project because mineral spin ordering is essential. Using different computational programs, we show that high spin is much lower in energy than low spin. Among all the high-spin possibilities, one

antiferromagnetic setting is the energetically most favorable ground state, at least under static conditions.

References

Allan N. L., Du Z., Lavrentiev M. Yu., Blundy J. D., Purton J. A. and van Westrenen W. (2003) Atomistic simulation of mineral–melt trace-element partitioning. *Physics of the Earth and Planetary Interiors* **139**, 93–111.

Dumakor-Dupey N. K., Arya S. and Jha A. (2021) Advances in blast-induced impact prediction—A review of machine learning applications. *Minerals* **11**, 601.

Karpatne A., Ebert-Uphoff I., Ravela S., Babaie H. A. and Kumar V. (2019) Machine learning for the geosciences: challenges and opportunities. *IEEE Transactions on Knowledge and Data Engineering* **31**, 1544–1554.

Rodriguez-Galiano V., Sanchez-Castillo M., Chica-Olmo M. and Chica-Rivas M. (2015) Machine learning predictive models for mineral prospectivity: An evaluation of neural networks, random forest, regression trees and support vector machines. *Ore Geology Reviews* **71**, 804–818.

Appendix A

Supplemental Figures for Chapter 2

Title

Sha Chen, Peng Ni, Youxue Zhang, and Joel Gagnon

This file of research data and supplementary materials include the following:

(1) Calibration curves for measurement of trace element concentrations in olivine in lunar samples by LA-ICP-MS with various laser spot sizes, 65, 85 and 110 μm, respectively (Figs. A0.1-A0.3).

(2) Comparison of trace element concentrations in standards in this work by LA-ICP-MS with reference values (Table A0.1 in the data file, Figure A0.4). The reference values are from GeoRem (Jochum et al. 2005, 2006, 2011).

(3) Calibration curves for measurement of trace element concentrations in olivine-hosted melt inclusions in lunar sample 12009 (Figure A0.5).

(4) Comparison of trace element concentrations in standards in this work by SIMS with reference values (Table A0.2 in the data file, Figure A0.6). The reference values are from GeoRem (Jochum et al. 2005, 2006, 2011).

(5) Trace element composition in San Carlos olivine (Table A0.3 in the data file) measured to assess LA-ICP-MS data quality. The measurement was on the same grain that has been measured

by Spandler et al. (2010), and comparison was shown. Note that Spandler et al. (2010) used NIST standards 610 and 612, which contain trace element concentrations of ~500 ppm and ~50 ppm, whereas we used many more standards, especially including those with trace element concentrations as low as 0.02 ppm (NIST 616). Therefore, our data are expected to be more accurate for elements with lower concentrations (< 5 ppm) in olivine, such as Ti, V, Y, and Zr. The comparison is excellent except for lower Al concentration by a factor of about 2 in our work. This is likely because we specifically used a standard (SRM 1830 glass, containing 635 ppm Al) that contains fairly low Al concentration because Al concentration in San Carlos olivine is low.

In addition, all data behind the figures, plus raw SIMS data are in the data file in spreadsheet format.

Supplemental File Figures

Figure A0.1. Calibration curves for LA-ICP-MS analyses with 65-μm spot size. Lunar samples measured in this batch include: 74235-4, 12040-36, and 12040-41. All the standards in the plot are used for calibration.

Figure A0.2. Calibration curves for LA-ICP-MS analyses with 85-μm spot size. Lunar samples measured in this batch include: 12009-6, 12009-11, 15647-6, 15016-10. All the calibrations are shown here, however, the data reported are from ^{7}Li, ^{27}Al, ^{45}Sc, ^{49}Ti, ^{51}V, ^{53}Cr, ^{55}Mn, ^{59}Co, ^{60}Ni, ^{66}Zn, ^{89}Y, ^{90}Zr, ^{118}Sn, ^{157}Gd, ^{159}Tb, ^{163}Dy, ^{165}Ho, ^{166}Er, ^{169}Tm, ^{172}Yb, ^{175}Lu. For 15647-6, a very short time integration was used due to the bad spectrum shape.

Figure A0.3. Calibration curves for LA-ICP-MS analyses of San Carlos olivine with spot size of 110 μm. San Carlos olivine was measured in a different batch from the samples reported in this study. Therefore, a separate calibration was shown here.

Figure A0.4. Comparison of measured concentrations in 8 reference materials (five NIST standards NIST610, NIST612, NIST614, NIST616, and SRM1830; and three MPI-DING standards GOR-132G, GOR-128G, and St-Hs-G) for measurement of elements in olivine by LA-ICP-MS with reference values (GeoRem website, Jochum et al. 2005, 2006, 2011) or certified values. SRM 1830 is used for the calibration of low Al concentration in olivine, and only a few certified values are known. The error bars are about the size of or smaller than the symbols. The line in each panel is 1:1 line.

Figure A0.5. SIMS calibration for transition elements for sample 12009-6 and 12009-11. Data reported are from ^{51}V, ^{52}Cr, ^{55}Mn, ^{59}Co, and ^{60}Ni. Data for Ni, Cu and Zn are not used because the calibration curves are deemed unsatisfactory.

Figure A0.6. Comparison of measured concentration in 6 reference materials (NIST standards NIST610, NIST612, and three MPI-DING standards GOR-132G, GOR-128G, T1-G and ATHO-G) for measurement of concentrations in melt inclusions in 12009-6 and 12009-11 by SIMS with reference values (GeoRem website, Jochum et al. 2005, 2006, 2011).

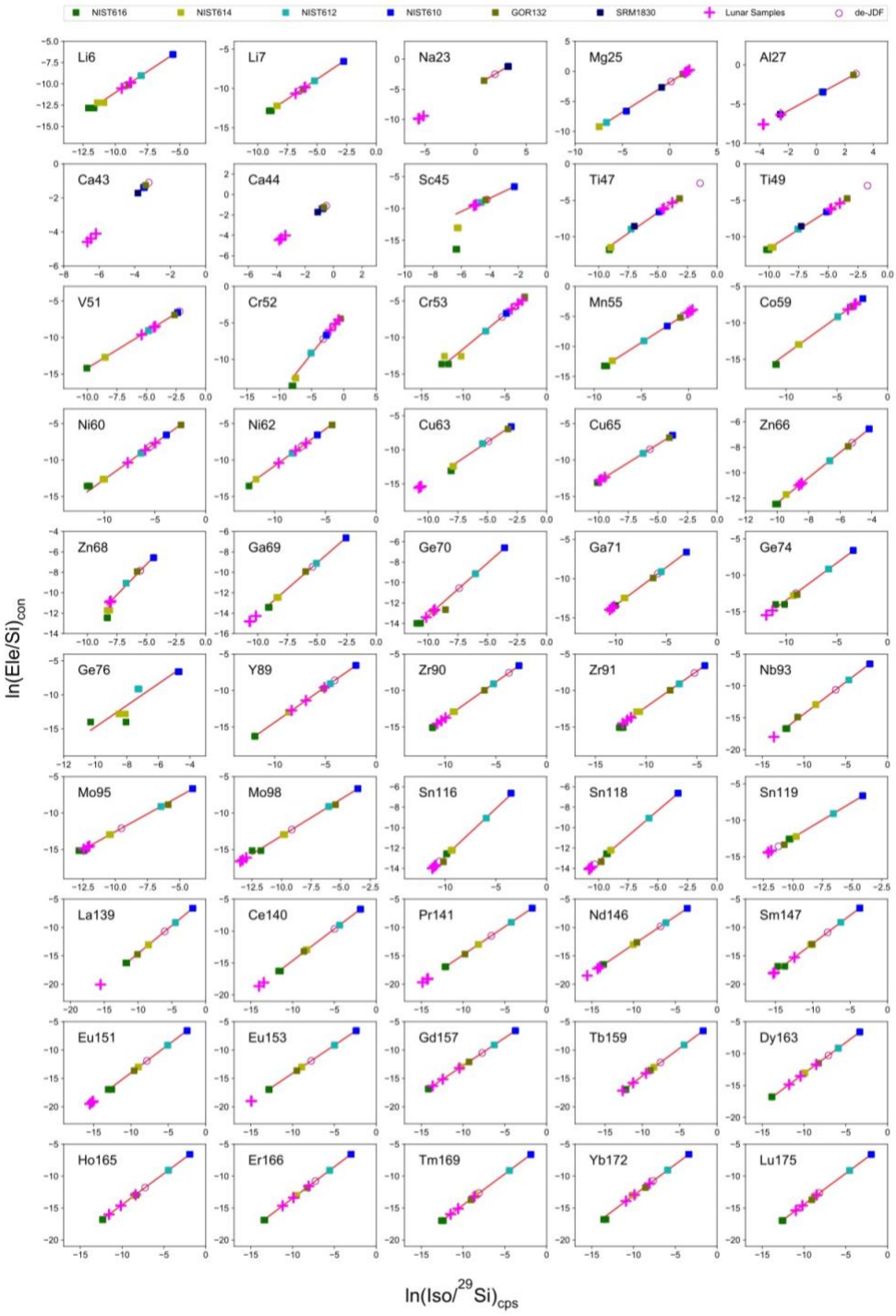

Figure A.0.1 Calibration curves for LA-ICP-MS analyses with 65-μm spot size. Lunar samples measured in this batch include: 74235-4, 12040-36, and 12040-41. All the standards in the plot are used for calibration.

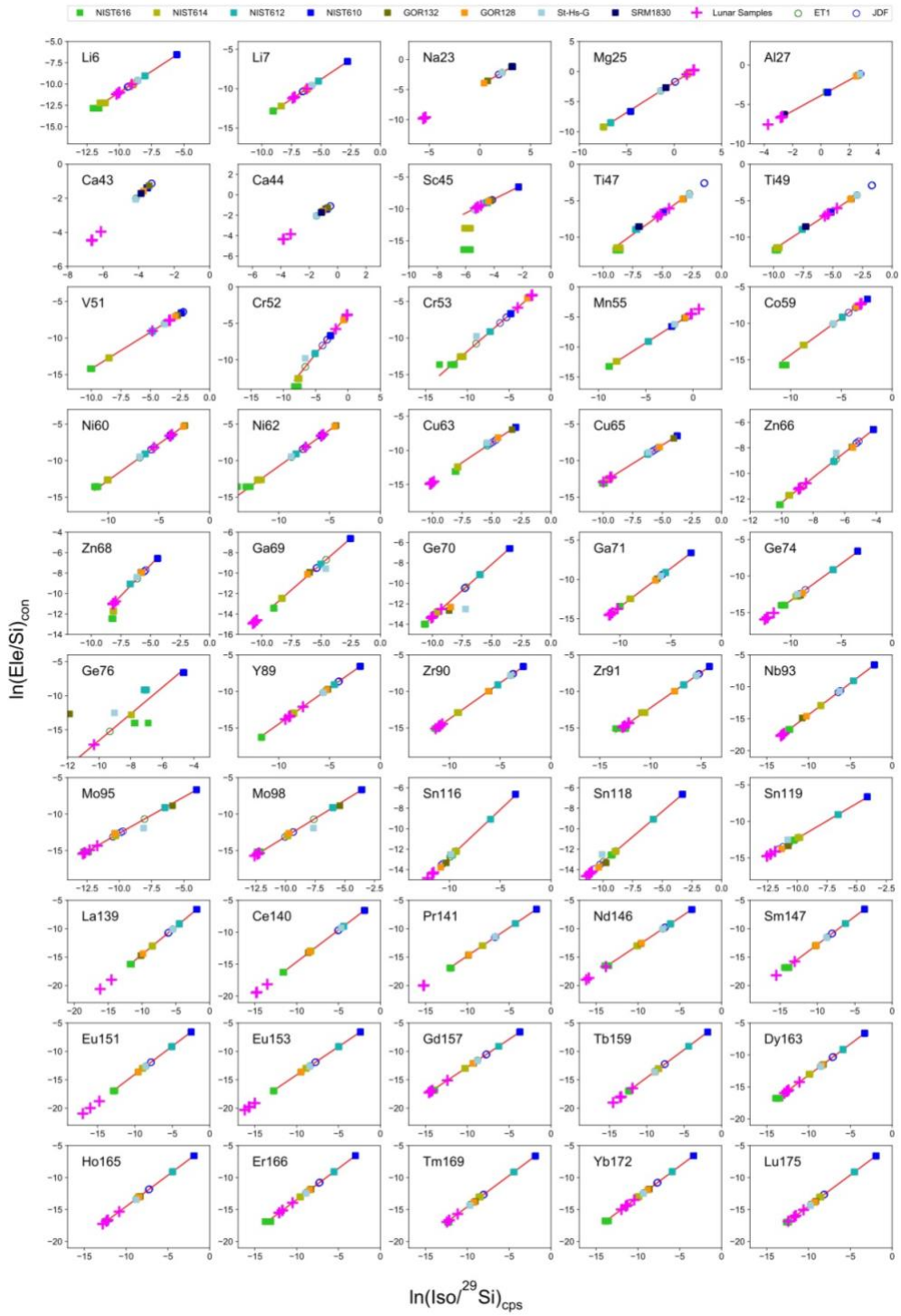

Figure A.0.2 Calibration curves for LA-ICP-MS analyses with 85-μm spot size. Lunar samples measured in this batch include: 12009-6, 12009-11, 15647-6, 15016-10. All the calibrations are shown here, however, the data reported are from ^{7}Li, ^{27}Al, ^{45}Sc, ^{49}Ti, ^{51}V, ^{53}Cr, ^{55}Mn, ^{59}Co, ^{60}Ni, ^{66}Zn, ^{89}Y, ^{90}Zr, ^{118}Sn, ^{157}Gd, ^{159}Tb, ^{163}Dy, ^{165}Ho, ^{166}Er, ^{169}Tm, ^{172}Yb, ^{175}Lu. For 15647-6, a very short time integration was used due to the bad spectrum shape.

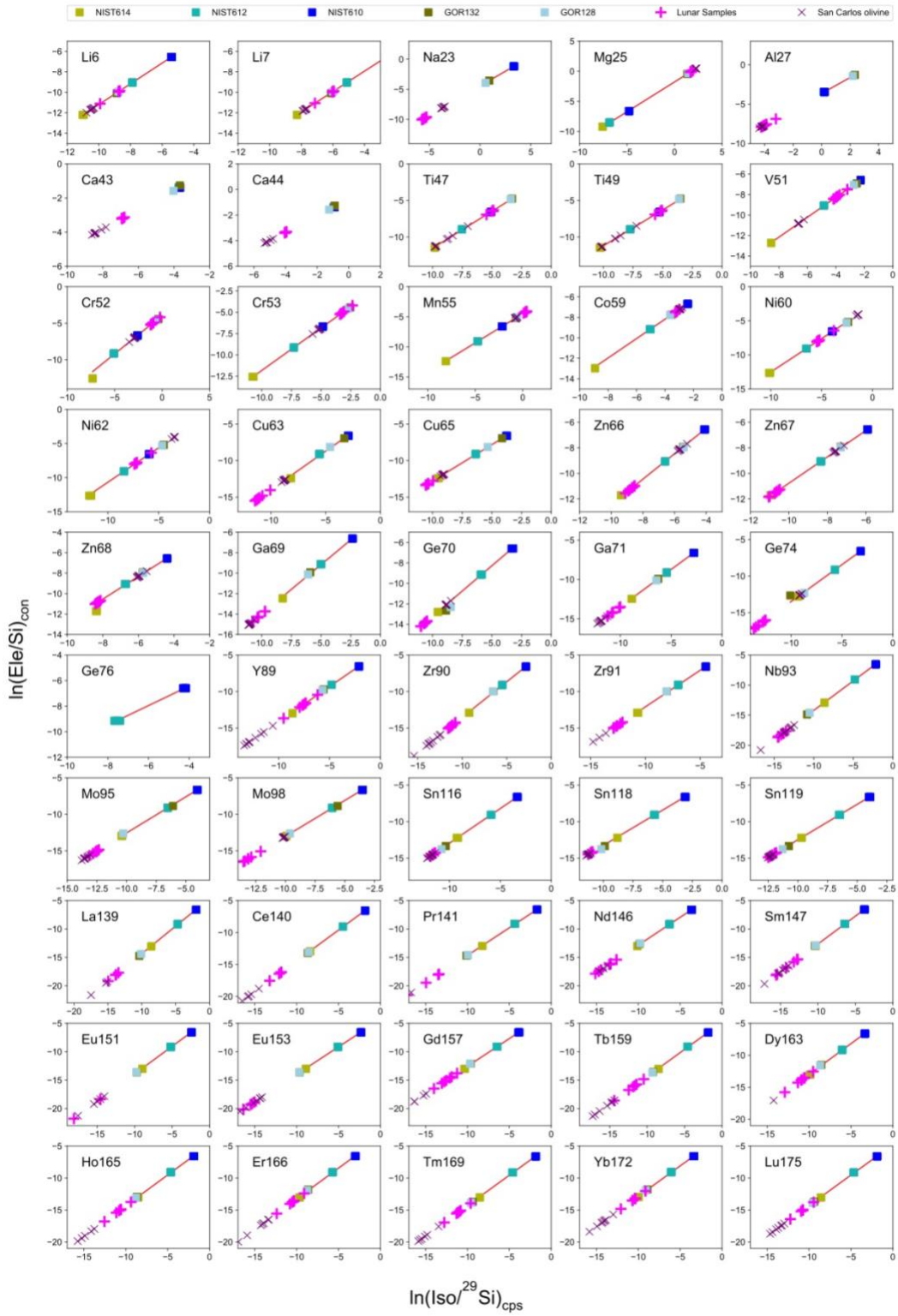

Figure A.0.3 Calibration curves for LA-ICP-MS analyses of San Carlos olivine with spot size of 110 μm. San Carlos olivine was measured in a different batch from the samples reported in this study. Therefore, a separate calibration was shown here.

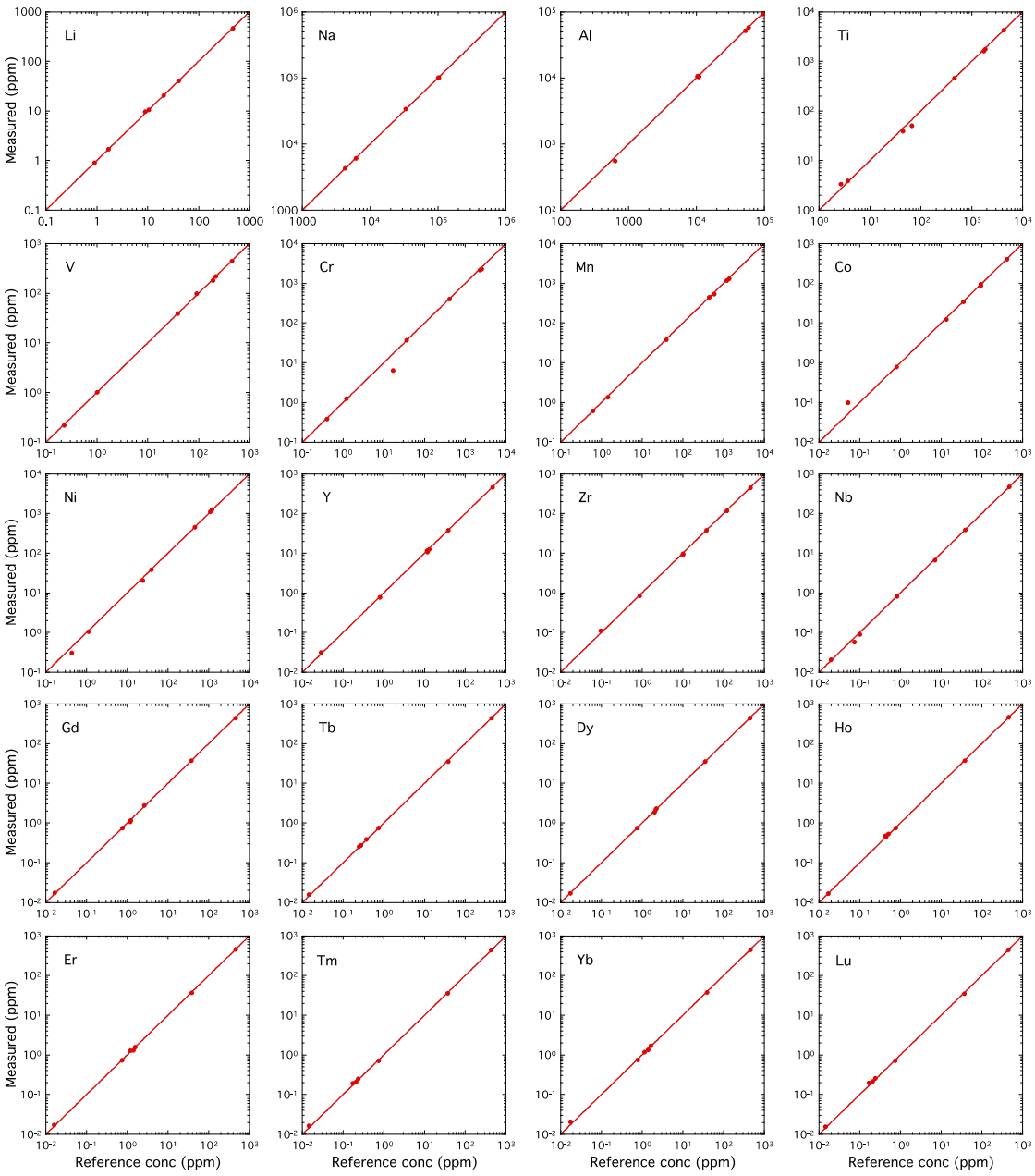

Figure A.0.4 Comparison of measured concentrations in 8 reference materials (five NIST standards NIST610, NIST612, NIST614, NIST616, and SRM1830; and three MPI-DING standards GOR-132G, GOR-128G, and St-Hs-G) for measurement of elements in olivine by LA-ICP-MS with reference values (GeoRem website, Jochum et al. 2005, 2006, 2011) or certified values. SRM 1830 is used for the calibration of low Al concentration in olivine, and only a few certified values are known. The error bars are about the size of or smaller than the symbols. The line in each panel is 1:1 line.

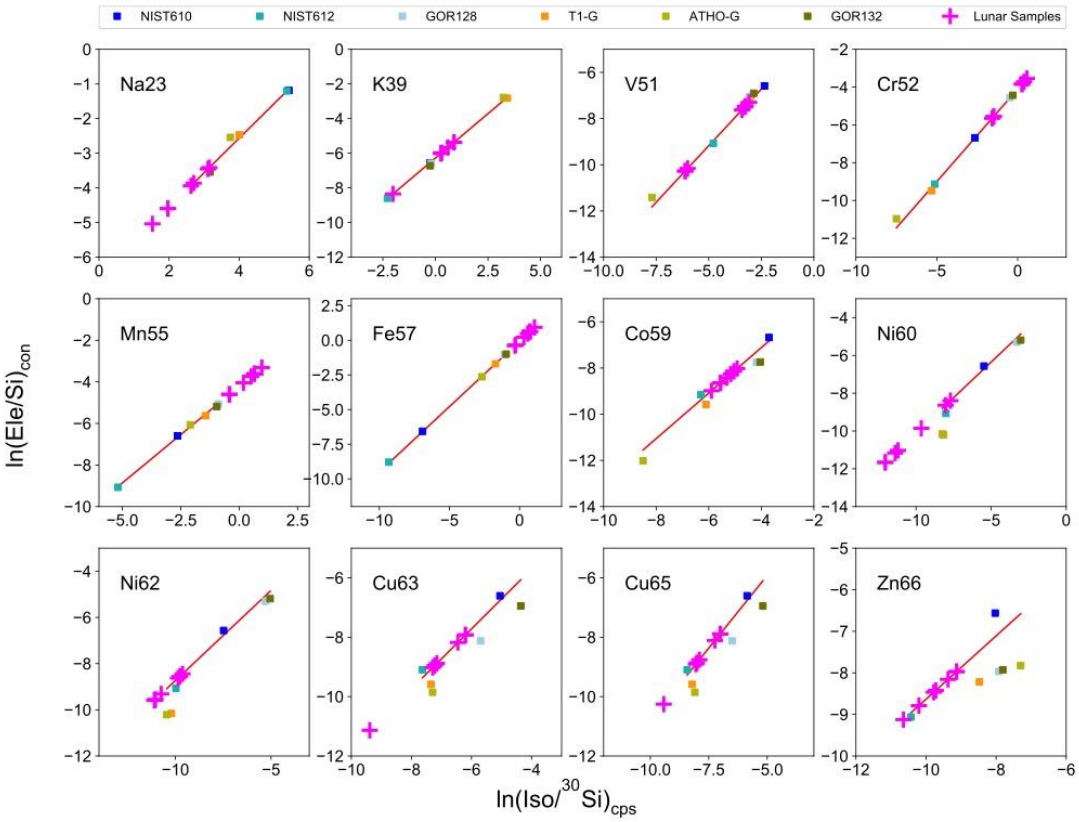

Figure A.0.5 SIMS calibration for transition elements for sample 12009-6 and 12009-11. Data reported are from ^{51}V, ^{52}Cr, ^{55}Mn, ^{59}Co, and ^{60}Ni. Data for Ni, Cu and Zn are not used because the calibration curves are deemed unsatisfactory.

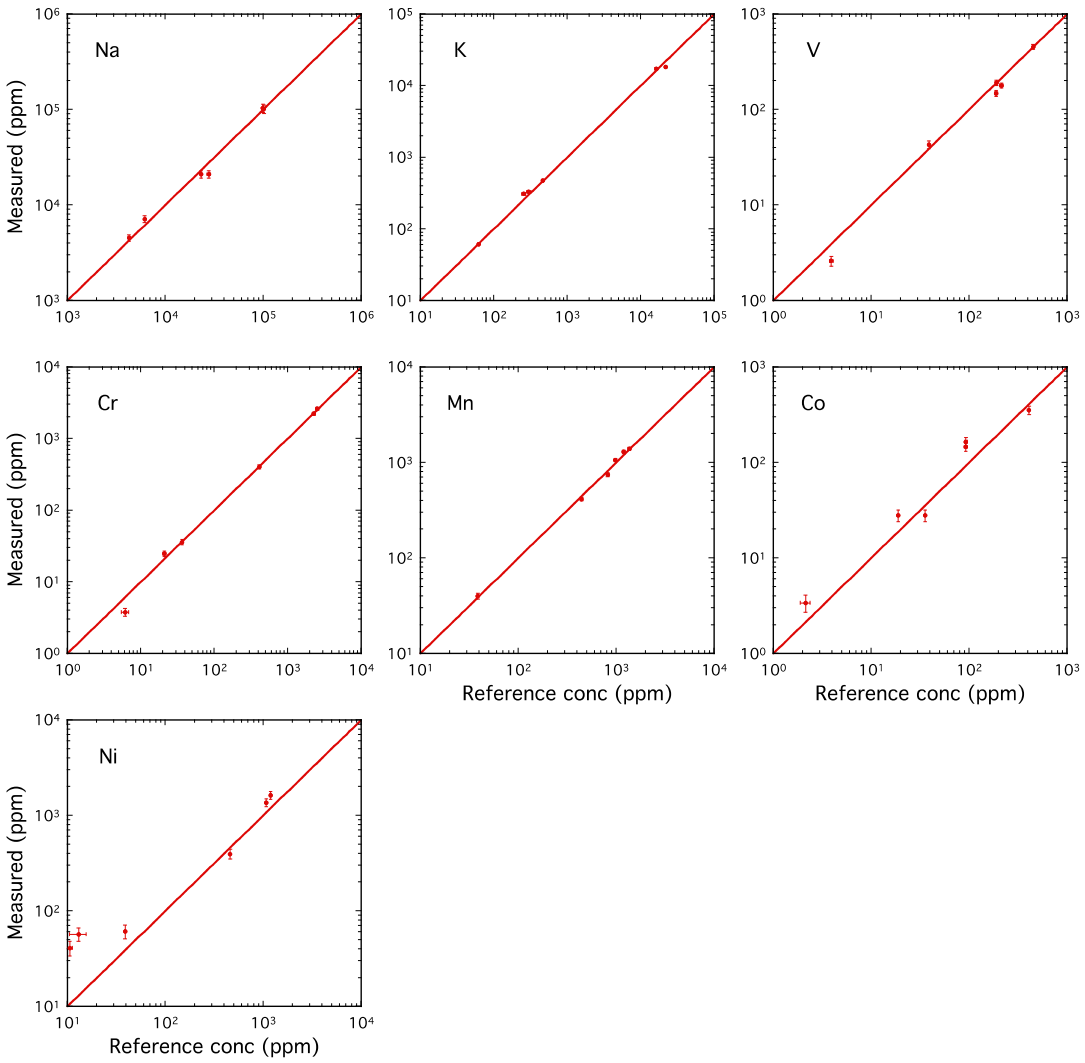

Figure A.0.6 Comparison of measured concentration in 6 reference materials (NIST standards NIST610, NIST612, and three MPI-DING standards GOR-132G, GOR-128G, T1-G and ATHO-G) for measurement of concentrations in melt inclusions in 12009-6 and 12009-11 by SIMS with reference values (GeoRem website, Jochum et al. 2005, 2006, 2011).

Appendix B

Supplemental Tables for Chapter 3

Table B0.1 Adsorption IR vibrational frequencies at different temperature and pressure by CRYSTAL17.

T (K)	static	300	500	700	900	0	0	0	1000	1500	1500	2000	2000
P (GPa)	static	0	0	0	0	1	5	10	5	10	5	10	20
B1*u*													
1	209.7	205.1	204.7	203.8	202.7	206.2	214.0	207.5	205.5	201.9	205.9	205.7	215.1
2	279.4	267.6	264.1	260.3	259.4	278.8	294.7	300.0	276.2	281.9	265.7	276.3	302.1
3	293.3	276.2	272.7	269.6	269.3	291.0	313.1	321.7	285.6	294.8	274.8	286.3	323.3
4	309.5	290.7	287.7	285.4	286.5	302.1	337.9	346.2	299.6	305.8	290.0	298.5	357.7
5	415.6	394.6	390.5	387.8	390.6	409.9	444.2	456.0	404.5	415.5	393.6	404.7	457.2
6	423.6	408.6	405.7	402.5	401.9	421.4	446.9	463.6	417.0	426.9	406.4	417.4	467.1
7	488.8	476.2	473.5	472.5	475.2	483.9	503.4	507.0	482.3	486.7	474.6	481.0	514.8
8	512.3	501.8	499.9	499.0	496.5	507.8	534.3	537.1	506.0	506.1	502.9	505.0	549.8
9	885.5	866.6	865.3	862.8	873.2	875.8	904.1	905.5	873.8	875.7	866.3	872.3	916.6
B2*u*													
1	205.9	192.3	189.3	187.7	186.8	201.5	218.7	226.9	200.3	205.0	190.9	199.6	226.2
2	271.1	264.8	261.9	260.0	253.9	274.3	289.7	293.1	275.6	282.5	265.3	271.7	298.4
3	296.2	281.4	277.2	274.3	273.0	295.4	316.6	319.2	294.1	299.5	277.8	291.1	325.9
4	321.7	317.1	315.3	313.8	314.4	322.9	340.9	347.2	320.7	328.9	317.4	320.3	356.4
5	388.5	367.2	363.5	360.4	361.5	383.2	418.5	430.1	377.1	387.3	364.4	378.5	438.5
6	409.8	398.2	395.6	392.9	392.7	409.4	430.9	441.9	403.9	412.9	397.1	405.9	451.5
7	475.8	460.1	457.8	453.7	456.2	473.3	501.8	514.9	467.7	475.6	459.0	468.7	520.9
8	509.0	496.3	493.5	490.3	489.0	507.8	533.0	540.2	504.3	512.4	495.7	503.5	551.6
9	538.8	526.9	525.4	523.0	526.7	534.9	554.8	566.1	536.2	539.7	528.2	531.3	571.4
10	615.1	604.6	602.2	601.7	600.1	611.7	635.5	632.3	615.9	620.8	606.9	609.5	648.7
11	849.7	828.8	826.3	824.2	835.8	838.9	871.9	869.7	844.7	848.4	828.6	835.0	889.0
12	965.6	950.0	945.8	943.2	945.7	962.7	988.9	999.7	958.3	962.3	943.2	959.7	1000.5
13	988.1	972.7	969.4	967.4	970.2	983.8	1011.6	1021.3	981.8	985.9	971.5	979.9	1029.2
B3*u*													
1	141.4	135.3	132.9	131.2	129.5	142.0	154.0	159.6	141.4	144.7	135.1	140.2	161.2
2	278.9	265.2	261.5	259.3	255.9	277.3	304.4	304.1	281.1	280.4	265.6	273.6	319.8
3	294.4	278.4	275.1	273.0	272.8	289.0	313.8	318.9	286.2	295.8	277.8	285.9	325.9
4	349.5	332.7	327.9	324.6	317.8	349.4	384.6	397.6	345.6	358.9	330.9	345.2	406.5
5	402.8	392.2	390.2	386.5	383.0	403.2	425.0	430.6	403.2	406.0	391.0	399.8	442.2
6	428.4	414.0	411.3	409.3	410.7	425.4	456.1	462.7	422.3	424.5	413.0	420.9	478.8
7	463.9	447.7	445.9	441.9	444.1	460.2	484.7	496.7	454.3	465.4	445.2	455.8	502.0
8	515.0	501.1	498.1	495.1	496.1	511.8	532.9	533.3	510.5	514.7	499.6	507.9	541.6
9	533.7	522.9	522.3	520.4	521.0	529.8	559.4	566.8	533.2	535.4	523.0	526.8	579.8
10	638.9	626.0	623.0	621.8	622.4	634.9	658.4	661.2	632.6	642.0	626.3	631.9	671.7
11	849.1	827.8	825.4	822.9	833.3	837.9	871.7	869.0	843.2	847.0	829.1	833.6	888.3
12	888.6	865.0	862.0	861.1	870.5	874.6	907.3	902.9	878.0	874.5	862.5	870.7	923.7
13	991.1	971.6	967.9	965.8	969.4	986.1	1022.4	1030.7	982.1	991.8	966.5	981.9	1041.0

Table B0.2. Raman vibrational frequencies at different temperature and pressure by CRYSTAL17. For some low frequency data (Ag), it is replaced by — because of inaccurate data.

T (K)	static	300	500	700	900	0	0	0	1000	1500	1500	2000	2000
P (GPa)	static	0	0	0	0	1	5	10	5	10	5	10	20
Ag													
1	65.8	109.2	—	—	—	—	—	146.4	—	—	—	88.9	—
2	211.1	258.8	231.5	225.1	223.8	279.6	216.0	212.6	—	—	159.9	248.5	221.8
3	305.7	296.3	292.2	284.3	279.5	307.5	332.5	336.2	228	273.7	272.3	302.5	351.2
4	326.9	314.1	309.3	305.2	303.1	329.9	355.3	348.3	313	313.2	306.3	321.5	377.2
5	344.9	332.9	330.9	331.6	328.8	351.7	375.4	377.5	325	374.1	330.2	335.8	402.2
6	440.4	410.9	436.5	465.9	462.5	429.9	450.3	464.3	431	417.9	483.9	447.8	466.1
7	567.0	510.1	494.6	481.2	490.6	499.9	519.4	592.2	444	670.3	588.9	519.7	536.3
8	605.5	611.2	704.9	684.2	630.2	613.5	758.6	639.5	680	695.2	654.8	597.1	867.8
9	837.8	812.3	826.1	814.3	825.7	849.3	858.8	834.5	909	822.5	861.4	811.2	887.8
10	855.8	857.8	926.5	899.7	900.4	905.3	884.0	874.4	915	946.7	923.4	831.8	915.2
11	969.3	948.4	1196.4	957.4	968.6	1004.5	1137.5	1017.6	1056	1010.5	955.6	947.0	1153.2
B1g													
1	222.2	215.6	211.8	211.5	209.2	221.8	237.7	238.9	226	212.3	214.3	220.2	248.6
2	259.4	248.9	245.1	244.0	240.0	257.8	276.2	276.6	261	256.8	248.7	254.3	287.4
3	313.3	301.2	297.1	294.2	292.1	314.6	338.6	352.7	314	319.6	297.9	310.8	359.4
4	361.0	347.3	343.8	342.1	345.4	358.1	379.7	388.9	352	358.6	349.4	354.2	395.2
5	390.1	382.9	381.6	380.4	378.6	389.4	403.2	408.1	383	368.8	381.3	387.3	413.6
6	439.6	425.6	421.9	420.1	420.2	438.3	466.9	476.4	428	440.8	421.3	433.6	482.2
7	608.4	584.2	582.2	578.8	588.5	590.7	629.2	620.0	606	599.4	584.7	588.5	655.0
8	641.4	629.4	628.1	624.7	625.5	638.6	664.7	669.6	643	652.1	630.3	634.7	688.3
9	854.4	830.2	829.0	825.1	837.3	841.4	878.3	872.7	842	862.7	831.6	837.1	890.1
10	874.1	856.5	854.0	852.2	858.8	866.3	898.5	896.6	878	872.1	856.2	862.9	932.1
11	980.6	962.9	958.4	956.6	960.8	977.5	1013.8	1020.2	973	981.9	965.9	972.2	1031.2
B2g													
1	188.1	171.0	168.6	164.4	163.8	183.2	209.3	219.3	172	189.6	169.3	178.9	222.1
2	297.8	287.7	288.2	285.4	287.4	291.5	309.0	307.7	288	298.0	288.0	289.6	317.4
3	322.7	310.1	306.4	304.9	302.6	320.6	341.7	353.8	315	327.0	307.7	317.0	354.8
4	377.4	363.6	359.2	356.6	355.2	378.1	405.1	422.3	369	385.0	362.7	373.2	422.0
5	418.7	406.4	403.4	402.8	403.5	414.4	440.2	451.2	427	421.1	415.6	411.5	455.9
6	615.5	596.0	593.4	593.5	600.9	603.4	629.2	623.1	613	604.7	597.2	600.6	642.6
7	939.6	919.8	916.5	916.1	924.8	927.1	957.9	955.8	928	929.8	919.4	925.9	966.6
B3g													
1	183.2	177.4	176.6	175.5	174.9	180.6	189.3	187.3	179	180.9	176.3	179.2	194.4
2	250.3	232.3	231.2	227.3	228.2	241.7	266.7	267.8	240	248.1	230.8	239.3	276.8
3	324.9	308.6	304.7	300.4	300.2	323.5	349.0	362.8	319	331.3	306.0	318.8	362.1
4	374.8	360.4	358.1	356.8	358.9	369.5	392.5	394.1	366	377.7	356.9	366.7	403.0
5	447.0	429.6	425.5	424.5	427.4	441.4	473.1	489.3	438	449.4	437.3	437.3	489.8
6	615.2	593.6	591.3	591.0	598.8	599.6	627.8	615.8	616	608.0	597.5	597.8	642.8
7	896.7	876.3	873.1	872.2	880.7	884.6	913.9	914.3	877	883.0	874.7	881.2	926.0

Appendix C

Thermodynamics of Forsterite-Fayalite Solid Solution

Co-authors: Sha Chen and Udo Becker

C.1 Abstract

The thermodynamics of mixing and its dependence on cation distribution in forsterite-fayalite solid solution were studied using density functional theory (DFT) at different temperatures from 273 K to 1273 K. The Gibbs free energy of mixing, including the vibrational part and configurational part, were computed for all 58 different configurations in a unit cell. Results show that Fe prefers M1 site of olivine, and this stands the whole temperature range we computed (273 – 1273 K). For each composition, there may be various ways for Fe-Mg distribution. The Boltzmann factor ($e^{-\frac{\Delta G}{RT}}$) was used as the weighting factor to calculate a weighted mixing energy for each composition X_{Fo} because lower-energy configuration is preferred and should weights more than high-energy configuration. The energies of mixing are more complicated than one-parameter or two-parameter models. More complex function need to be used to fit the mixing energy using the composition with temperature.

C.2 Introduction

The Fe-Mg distribution in the octahedral sites of olivine and the thermodynamics of the forsterite-fayalite solid solution have received considerable attention because of their importance

in the thermodynamics, transport, and other physical properties. In addition, partially filled 3d shell electrons in Fe lead to spin and magnetic properties.

Considerable research has been done on the preference of Fe in the Fe-Mg olivine M1 and M2 sites. However, the results have been conflicting and puzzling. XRD and Mössbauer resonance spectroscopy analysis shows that most natural olivine crystals are slightly enriched in Fe^{2+} in the smaller M1 (Smyth and Hazen, 1973). Exceptions are some terrestrial Mg-rich olivines. They have a slight preference for Fe^{2+} for the M2 site (Ghose and Ganguly, 1982). Besides, some studies concluded that the site preference is temperature-related, and there is a reverse with increasing temperature. Artioli et al. (1995), Rinaldi and Wilson (1996), and Rinaldi et al. (2000) did single crystal neutron diffraction studies on natural olivine Fa10 and Fa12 at temperatures up to 1300 °C. They found Fe^{2+} to be initially enriched in the M1 site. Beyond a certain critical temperature of about 900 °C, the site preference was reversed. Similarly, Redfern et al. (2000) found a slight preference for M1 at temperatures below ~ 600 °C. Above 630 °C, the Fe preference switches to M2. Other studies found no reverse with temperature (Morozov et al., 2005; Abdu et al., 2009; Chatterjee et al., 2011). The cation distribution (site preference) in olivine has been summarized as being controlled by three factors: the smaller of the two cations goes to the smaller M1 (size effect), the more electronegative element goes into the "less ionic" M1 site, transition metal prefers the site the has larger crystal field stabilization energy (CFSE). The CFSE at M1 exceeds that in M2.

The mixing of different cations often results in differences in thermodynamic properties, such as the Gibbs free energy G, enthalpy H, the entropy S, and volume V of mixing. These properties are important in mineralogy and petrology. There can be direct measurements of these entities, such as using calorimetry to measure the enthalpy and heat capacity and X-ray diffraction

to obtain the volume and cation distribution of the unit cell. Indirect measurements, for example, to extract data from the phase diagram. Considering the large compositional ranges that need to be investigated and different temperatures and pressures, experiments are complicated and time-consuming, with difficulties in the experiments to probe the entire temperature and composition of the range, with the added challenge of obtaining equilibrium for each data point. Many phase equilibrium experiments on silicates need to be carried out at high temperatures for equilibria to be reached and to get measurable thermodynamic entities; therefore, there is a lack of data at low temperatures. Furthermore, the free energy changes associated with cation mixing in solid solutions are small.

We aim to study the thermodynamics of the mixing of the cation (Fe-Mg) distribution in olivine. The beauty of quantum mechanical calculations also allows for determining the spin status of Fe in olivine. About the spin status of Fe in olivine, Fe is expected to be high-spin rather than a low-spin state because of energy and cell parameter reasons. A detailed discussion can be found in Section 3.5.6 of Chapter 3. The energies of the ferromagnetic (FM) and antiferromagnetic (AFM) Fe in fayalite are close to each other, with the AFM case being slightly lower in energy at very low temperatures, i.e., below the Neel temperature of ~65 K (below which there is ~noncollinear antiferromagnetic ordering and above which there is a paramagnetic spin state). Therefore, we use the FM case in all calculations, which is also easier to handle computationally.

C.3 Computational methods

Crystal17 was used for the quantum-mechanical calculations that are used for the derivation of thermodynamic. The generalized gradient approximation using the Purdue Becke Ernzerhof (PBE) density functional PBE (Perdew et al., 1996) was used. The initial forsterite structure used the cell parameters from Bostroem (1987), 4.749, 10.1985, and 5.9792 Å for the

three cell parameters. Atom substitution was used to partially or fully replace Mg with Fe on the M1 and M2 positions to study the thermodynamics of the solid solution. Geometry optimization was first conducted to obtain the optimized structure. The optimized structures were then used for frequency calculations in a separate run to obtain thermodynamic data (the CpT term for the derivation of the enthalpy and an additional $-T\Delta S_{vib}$ term to obtain the Gibbs free energy of vibration) from 273 K to 1273 K with the data of every 100 K.

The substitution is set to occur in a unit cell, instead of supercell. There are four formula units containing 28 atoms in the olivine unit cell. Despite the spin, the total number of configurations was calculated to be 58 different configurations (Table C0.2). Chapter 3 presented the energies of fayalite for different spin status, high spin are much thermodynamically favorable than low spin, and antiferromagnetic shows the lowest energy at static conditions. Given that energies of FM and AFM are close, the order may reverse with temperature. Therefore, for each Fe-Mg ordering, we computed both FM and ATM. There may be multiple ways to achieve a total spin of 0 for AFM in the eight cation positions in the olivine unit cell. To simply the calculations, we only considered Fe in M1 or M2 sites have opposite direction spins. All Fe atoms in M1 sites spin up, and all Fe in M2 sites spin down. The lower free energy between FM and AFM was used to calculate the mixing energy.

Table C0.1 The number of configurations for each solid solution composition in the olivine unit cell. Symmetry is considered. For each composition, the multiplicity may be more than 1. The total multiplicity of all configurations gives 2^8=256.

Composition	# of Mg atoms	# of configurations
fo	8	1
$fo_{12.5}fa_{87.5}$	7	2
$fo_{25}fa_{75}$	6	8
$fo_{37.5}fa_{62.5}$	5	10
$fo_{50}fa_{50}$	4	16
$fo_{62.5}fa_{37.5}$	3	10
$fo_{75}fa_{25}$	2	8
$fo_{87.5}fa_{12.5}$	1	2

fa	0	1

C.4 Thermodynamics

The entropy of mixing, ΔS^{mix}, can be broken down into two parts, a vibrational part (ΔS^{mix}_{vib}) and a configurational part (ΔS^{mix}_{conf}). The general expression of the configurational part is $\Delta S^{mix}_{conf} = -R \sum X_i ln X_i$ where R is the gas constant, and X_i is the molar fraction of component *i* in a mixture or solid solution. For olivine with M1 and M2, two different sites, it can be written as:

$$\Delta S^{mix}_{conf} = -R\left(X^{M1}_{Fe}\ln X^{M1}_{Fe} + X^{M1}_{Mg}\ln X^{M1}_{Mg} + X^{M2}_{Fe} ln X^{M2}_{Fe} + X^{M2}_{Mg} ln X^{M2}_{Mg}\right) \quad \text{(B-1)}$$

Where X^{M1}_{Fe} and $X^{M1}_{Mg}$are the molar percentage of Fe and Mg in site M1, with the additional constraint that $X^{M1}_{Fe}+X^{M1}_{Mg} = 1$becase M1 sites are either occupied by Mg or Fe ions. The same works for $X^{M2}_{Fe}$and X^{M2}_{Mg} (Kroll et al., 2006). It can also be derived from Boltzmann's equation $S = k_B ln\ \Omega$. Here is the derivation:

For one molar olivine $(Mg,Fe)_2SiO_4$ with two sites, the Boltzmann's equation becomes

$$S = k_B ln\Omega = k_B ln \frac{N_A! \cdot N_A!}{(X^{M1}_{Fe}N_A)! \cdot (X^{M1}_{Mg}N_A)! \cdot (X^{M2}_{Fe}N_A)! \cdot (X^{M2}_{Mg}N_A)!}$$

Where N_A is the Avogadro's constant. The "!" is the factorial calculation.

When N is very large, Stirling's approximation gives us

$$ln\ N! = N\ ln\ N - N$$

Then,

$$ln\Omega = ln \frac{N_A! \cdot N_A!}{(X^{M1}_{Fe}N_A)! \cdot (X^{M1}_{Mg}N_A)! \cdot (X^{M2}_{Fe}N_A)! \cdot (X^{M2}_{Mg}N_A)!}$$

$$= 2 \cdot ln(N_A!) - ln\,(X^{M1}_{Fe}N_A)! - ln\,(X^{M1}_{Mg}N_A)! - ln\,(X^{M2}_{Fe}N_A)! - ln\,(X^{M2}_{Mg}N_A)!$$

$$= 2N_A \cdot ln(N_A) - 2N_A - [(X^{M1}_{Fe}N_A\ ln\,(X^{M1}_{Fe}N_A) - X^{M1}_{Fe}N_A] - [(X^{M1}_{Mg}N_A\ ln\,(X^{M1}_{Mg}N_A) - X^{M1}_{Mg}N_A]$$

$$- [(X^{M2}_{Fe}N_A\ ln\,(X^{M2}_{Fe}N_A) - X^{M2}_{Fe}N_A] - [(X^{M2}_{Mg}N_A\ ln\,(X^{M2}_{Mg}N_A) - X^{M2}_{Mg}N_A]$$

$$= -N_A \cdot [X^{M1}_{Fe}\ln X^{M1}_{Fe} + X^{M1}_{Mg}\ln X^{M1}_{Mg} + X^{M2}_{Fe} ln X^{M2}_{Fe} + X^{M2}_{Mg} ln X^{M2}_{Mg}]$$

Therefore,

$$S = k_B ln\Omega$$

$$= -k_B N_A \left[X_{Fe}^{M1} \ln X_{Fe}^{M1} + X_{Mg}^{M1} \ln X_{Mg}^{M1} + X_{Fe}^{M2} ln X_{Fe}^{M2} + X_{Mg}^{M2} ln X_{Mg}^{M2}\right]$$

$$= -R \cdot \left[X_{Fe}^{M1} \ln X_{Fe}^{M1} + X_{Mg}^{M1} \ln X_{Mg}^{M1} + X_{Fe}^{M2} ln X_{Fe}^{M2} + X_{Mg}^{M2} ln X_{Mg}^{M2}\right]$$

The Gibbs free energy of mixing

$$\Delta G^{mix} = \Delta H^{mix} - \mathrm{T}\Delta S^{mix} = \Delta H^{mix} - \mathrm{T}\Delta S_{vib}^{mix} - \mathrm{T}\Delta S_{conf}^{mix} = \Delta G_{vib}^{mix} - \mathrm{T}\Delta S_{conf}^{mix}$$

$$\Delta G^{mix} = G_{vib}^{\mathrm{SS}} - \mathrm{X}G_{vib}^{\mathrm{fa}} - (1-X)G_{vib}^{\mathrm{fo}} - \mathrm{T}\Delta \mathrm{S}_{conf}^{mix} \qquad \text{(B-2)}$$

Where G_{vib}^{SS} is the Gibbs free energy of a solid solution with *X* molar Fa and 1-*X* molar Fo.

For ideal solutions, the mixing energy ΔG^{mix} is 0. For non-ideal regular solutions, the excess free energy of mixing, is a measure of the deviation from ideal thermodynamic mixing. ΔG^{mix} is the Gibbs free energy of mixing, that determines the stability at a given pressure and temperature. Several models have been suggested to connect the molar excess Gibbs free energy of solid solutions. Guggenheim (1937) suggested that the molar excess Gibbs energy of a binary solution may be represented by a polynomial expression:

$$\Delta G_m^{mix} = X_1 X_2 [A_0 + A_1(X_1 - X_2)] + A_2(X_1 - X_2)^2 + \cdots]$$

The simplest form of deviation from ideality is a Simple Mixture, with only A_0 non-zero. Conventionally, A_0 is replaced by the symbol W or $\mathrm{W^G}$. So that

$$\Delta \mathrm{G_m^{mix}} = \mathrm{W^G X_1 X_2} \qquad \text{(B-3)}$$

For asymmetric solutions, one parameter is not enough to describe the energy excel. A two-parameter model as

$$\Delta \mathrm{G^{xs}} = \left(\mathrm{W_{21}^G X_1} + \mathrm{W_{12}^G X_2}\right)\mathrm{X_1 X_2} \qquad \text{(B-4)}$$

The interaction parameters $\mathrm{W_{ij}}$ may be treated like normal thermodynamic state function. For instance, $\mathrm{W^G = W^H - TW^S + PW^V}$ is valid. It can also be extended to ternary or quaternary solid solutions.

C.5 Results

Vibrational part of mechanical energy (ME), enthalpy (H), and free energy (G) data were obtained for each configuration (58 in total) from 273 K to 1273 K. The data for 273 K is shown in Table B0.2 as an example. For each composition Xfo, more Fe in M1 site (lower X_{Mg}^{M1}) has lower mixing energy (Table B0.2). For the whole compositional range, mixing energy of each configuration increases with X_{Mg}^{M1} and decreases with X_{Mg}^{M2} (Figure B0.1). Considering that $X_{Mg}^{M1} + X_{Fe}^{M1} = 1$, mixing energy will be lower with more Fe in M1 site and less Fe in M2 site. We did a simple model as

$$\Delta G^{mix} = a + b \cdot X_{Fe}^{M1} + c \cdot X_{Fe}^{M2} \quad \text{(B-5)}$$

For each configuration at each temperature. The fitting for 273 K gives

$$\Delta G^{mix} = 2.17 - 7.54 \cdot X_{Fe}^{M1} + 6.83 \cdot X_{Fe}^{M2} \quad \text{(B-6)}$$

With the R^2 of 0.78. The coefficients sign also show that Fe prefers M1 and Mg prefers M2. Although the fitting gets worse with higher temperature (R^2 from 0.78 for 273 K gradually change to 0.38 for 1273 K), the parameter b is also positive and increases with temperature, and the parameter c gets more negative with temperature.

Table C0.2 The Gibbs free energy of mixing for each configuration at 273 K. X_{Fa}: the mole fraction of fayalite in olivine. It has nine possible values: 0, 0.125, 0.25, 0.375, 0.5, 0.625, 0.75, 0.875, and 1. $\mathbf{X_{Fe}^{M1}}$: mole fraction of Fe in M1 site. It has five possible values: 0, 0.25, 0.5, 0.75, and 1. $\mathbf{X_{Mg}^{M1} + X_{Fe}^{M1} = 1}$. $\mathbf{X_{Fe}^{M2}}$: mole fraction of Fe in M2 site. It has five possible values: 0, 0.25, 0.5, 0.75, and 1. $\mathbf{X_{Mg}^{M2} + X_{Fe}^{M2} = 1}$.

N	XFa	X_{Fe}^{M1}	X_{Fe}^{M2}	Mul.	ΔG^{mix}	N	XFa	X_{Fe}^{M1}	X_{Fe}^{M2}	Mul.	ΔG^{mix}
1	0	0	0	1	0	30	0.5	0.5	0.5	4	4.09
2	0.125	0.25	0	4	0.07	31	0.5	0.5	0.5	4	2.38
3	0.125	0	0.25	4	2.80	32	0.5	0.5	0.5	4	2.70
4	0.25	0.5	0	2	-3.36	33	0.5	0.5	0.5	4	3.83
5	0.25	0.5	0	2	0.99	34	0.5	0.5	0.5	4	2.62
6	0.25	0.5	0	2	1.47	35	0.5	0.5	0.5	4	3.19
7	0.25	0.25	0.25	8	1.39	36	0.5	0.25	0.75	8	5.82
8	0.25	0.25	0.25	8	1.06	37	0.5	0.25	0.75	8	5.43
9	0.25	0	0.5	2	5.19	38	0.625	1	0.25	4	-4.55
10	0.25	0	0.5	2	4.20	39	0.625	0.75	0.5	4	2.02
11	0.25	0	0.5	2	4.76	40	0.625	0.75	0.5	8	-0.25
12	0.365	0.5	0.25	8	1.88	41	0.625	0.75	0.5	8	-0.09
13	0.375	0.75	0	4	-1.82	42	0.625	0.75	0.5	4	-0.31
14	0.375	0.5	0.25	4	-1.53	43	0.625	0.5	0.75	4	2.67
15	0.375	0.5	0.25	4	-1.73	44	0.625	0.5	0.75	4	1.32
16	0.375	0.5	0.25	8	1.59	45	0.625	0.5	0.75	8	4.46
17	0.375	0.25	0.5	4	4.30	46	0.625	0.5	0.75	8	4.89
18	0.375	0.25	0.5	8	2.71	47	0.625	0.25	1	4	8.66
19	0.375	0.25	0.5	8	3.26	48	0.75	0.75	0.75	8	2.27
20	0.375	0.25	0.5	4	3.25	49	0.75	1	0.5	2	-3.45
21	0.375	0	0.75	4	7.69	50	0.75	1	0.5	2	-4.23
22	0.5	0	1	1	11.38	51	0.75	1	0.5	2	-3.03
23	0.5	0.75	0.25	8	-0.43	52	0.75	0.75	0.75	8	0.76
24	0.5	1	0	1	-3.34	53	0.75	0.5	1	2	4.43
25	0.5	0.75	0.25	8	-0.08	54	0.75	0.5	1	2	7.08
26	0.5	0.5	0.5	2	0.75	55	0.75	0.5	1	2	7.32
27	0.5	0.5	0.5	4	-0.55	56	0.875	1	0.75	4	-1.78
28	0.5	0.5	0.5	4	-0.52	57	0.875	0.75	1	4	3.48
29	0.5	0.5	0.5	2	-1.75	58	1	1	1	1	0

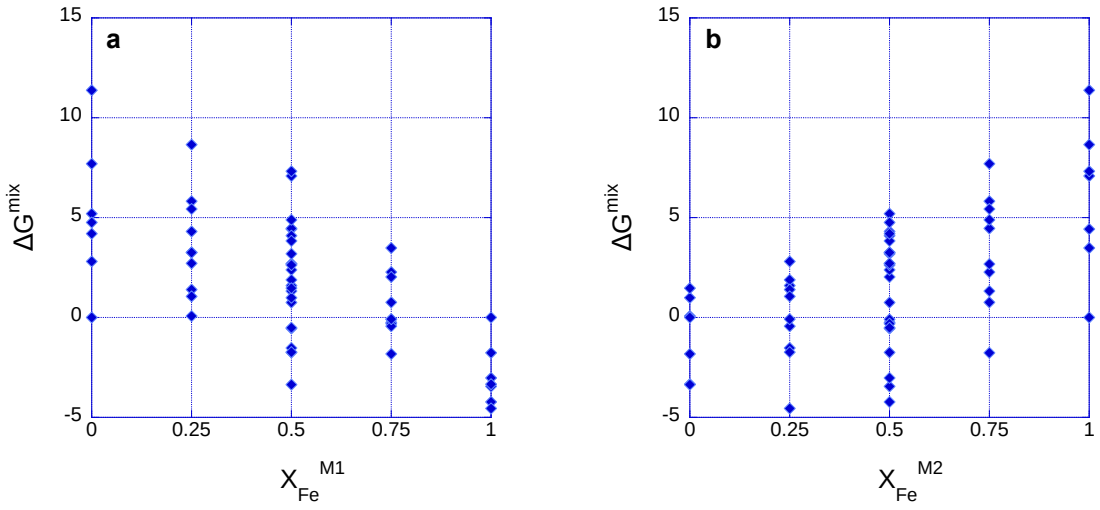

Figure C0.1 The Gibbs free energy of mixing for each configuration with the mole fraction of Fe in M1/M2 site at 273 K.

For different configurations with the same X_{Fo} composition, we used Boltzmann factor to obtain a weighted mixing energy. The data is in Table B0.3. The figure in Figure B0.2.

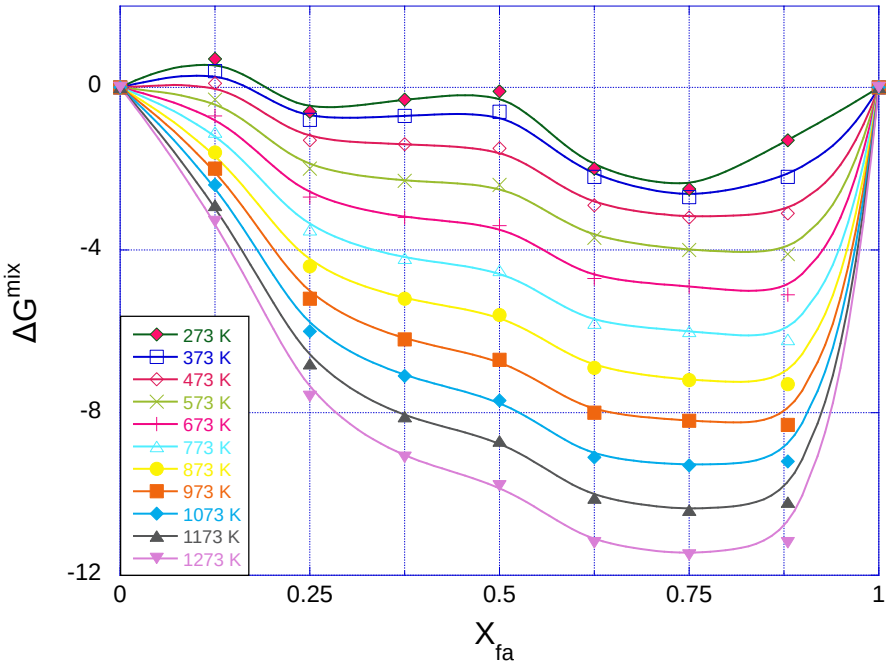

Figure C0.2 The weighted Gibbs free energy of mixing with X_{Fa} for temperatures from 273 K to 1273 K.

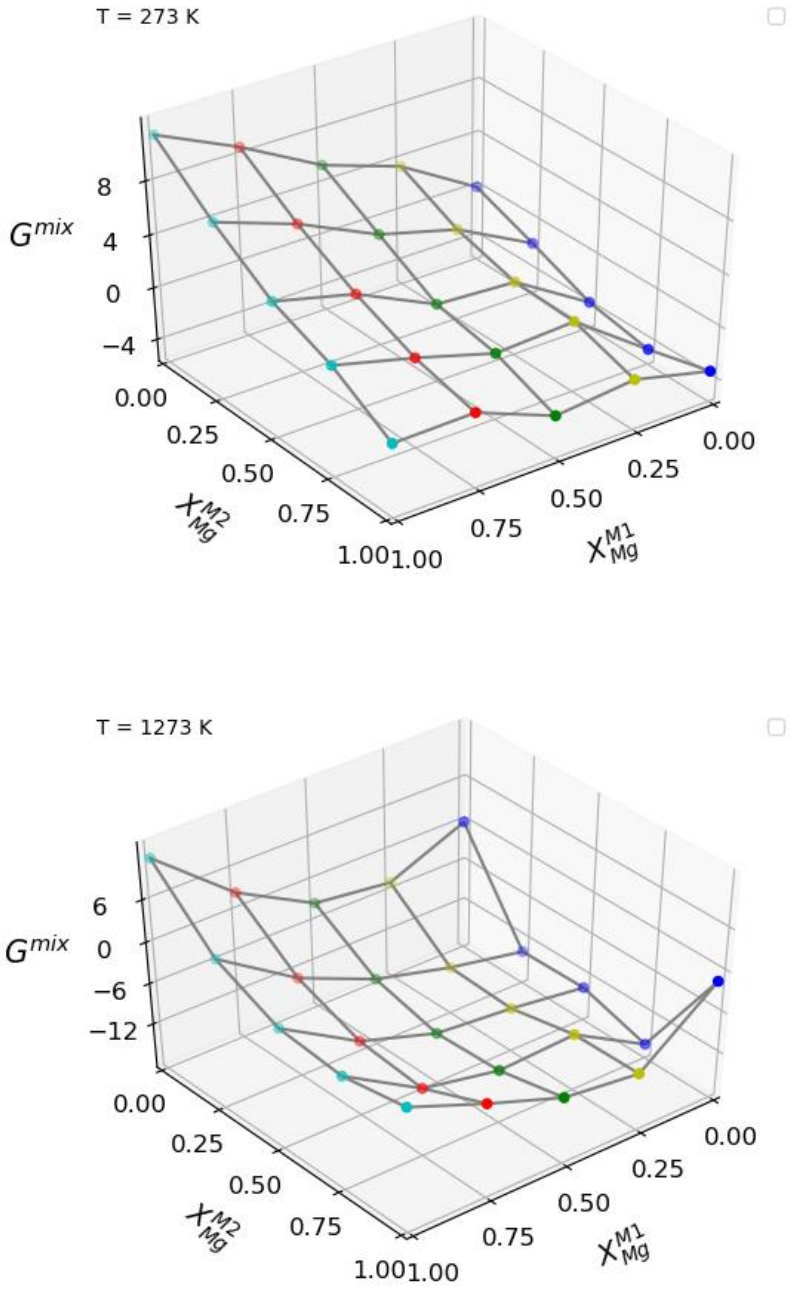

Figure C0.3 The weighted Gibbs free energy of mixing with X_{Mg}^{M1} and X_{Mg}^{M2} (3D plot) at temperature 273 K and 1273 K. Different configurations with the same X_{Fo}, $\boldsymbol{X_{Mg}^{M1}}$ and $\boldsymbol{X_{Mg}^{M2}}$ are grouped together and computed a weighted mixing energy. There are 25 groups in total. Five different colors are used to differentiate different $\boldsymbol{X_{Mg}^{M1}}$ sets for better visualization. Faded dots are further away (smaller $\boldsymbol{X_{Mg}^{M2}}$ in this plot). Clear dots are closer (higher $\boldsymbol{X_{Mg}^{M2}}$ here).

Table C0.3 The weighted Gibbs free energy of mixing with X_{Fo} and X_{Fa} at various temperatures, including both vibrational and configurational parts. X_{Fo}: the mole fraction of forsterite in the forsterite-fayalite solid solution. . f.u.: formula unit. The energy calculated for a unit cell is divided by four to obtain the mixing energy for one formula unit.

		ΔG^{mix} (kJ/mol/f.u.)										
X_{Fo}	X_{Fa}	273 K	373 K	473 K	573 K	673 K	773 K	873 K	973 K	1073 K	1173 K	1273 K
0	1	0	0	0	0	0	0	0	0	0	0	0
0.125	0.88	-1.3	-2.2	-3.1	-4.1	-5.1	-6.2	-7.3	-8.3	-9.2	-10.2	-11.2
0.25	0.75	-2.5	-2.7	-3.2	-4.0	-4.9	-6.0	-7.2	-8.2	-9.3	-10.4	-11.5
0.375	0.625	-2.0	-2.2	-2.9	-3.7	-4.7	-5.8	-6.9	-8.0	-9.1	-10.1	-11.2
0.5	0.5	-0.1	-0.6	-1.5	-2.4	-3.4	-4.5	-5.6	-6.7	-7.7	-8.7	-9.8
0.625	0.375	-0.3	-0.7	-1.4	-2.3	-3.2	-4.2	-5.2	-6.2	-7.1	-8.1	-9.1
0.75	0.25	-0.6	-0.8	-1.3	-2.0	-2.7	-3.5	-4.4	-5.2	-6.0	-6.8	-7.6
0.875	0.125	0.7	0.4	0.1	-0.3	-0.7	-1.1	-1.6	-2.0	-2.4	-2.9	-3.3
1	0	0	0	0	0	0	0	0	0	0	0	0

Table C0.4 The weighted Gibbs free energy of mixing with X_{Mg}^{M1} and X_{Mg}^{M2} at various temperatures, including both vibrational and configurational parts. X_{Fo}: the mole fraction of forsterite in the forsterite-fayalite solid solution. $\boldsymbol{X_{Mg}^{M1}}$: the mole fraction of Mg in M1 site of the unit cell. The possible values are 0, 0.25, 0.5, 0.75, and 1 given four positions in M1. The same for M2. $\boldsymbol{X_{Mg}^{M2}}$: the mole fraction of Mg in M2 site of the unit cell. f.u.: formula unit. The energy calculated for a unit cell is divided by four to obtain the mixing energy for one formula unit.

Com.	Fe-Mg distri.		ΔG^{mix} (kJ/mol/f.u.)										
X_{Fo}	X_{Mg}^{M1}	X_{Mg}^{M2}	273 K	373 K	473 K	573 K	673 K	773 K	873 K	973 K	1073 K	1173 K	1273 K
0	0	0	0	0	0	0	0	0	0	0	0	0	0
0.125	0	0.25	-1.78	-2.93	-4.14	-5.38	-6.66	-7.97	-9.30	-10.4	-11.6	-12.7	-13.9
0.25	0	0.5	-3.68	-4.59	-5.51	-6.49	-7.48	-8.58	-9.73	-10.7	-11.7	-12.7	-13.7
0.375	0	0.75	-4.55	-5.70	-6.88	-8.11	-9.35	-10.63	-11.9	-13.1	-14.2	-15.4	-16.6
0.5	0	1	-3.34	-3.26	-3.16	-3.05	-2.92	-2.77	-2.61	-2.33	-2.02	-1.69	-1.36
0.125	0.25	0	3.48	2.85	2.17	1.44	0.52	-0.43	-1.40	-2.19	-2.96	-3.75	-4.55
0.25	0.25	0.25	1.27	0.03	-1.26	-2.59	-3.95	-5.33	-6.74	-7.99	-9.22	-10.5	-11.7
0.375	0.25	0.5	-0.05	-1.20	-2.39	-3.62	-4.88	-6.17	-7.47	-8.65	-9.82	-11.0	-12.2
0.5	0.25	0.75	-0.27	-1.26	-2.27	-3.29	-4.33	-5.38	-6.44	-7.40	-8.34	-9.30	-10.3
0.625	0.25	1	-1.82	-2.62	-3.44	-4.28	-5.14	-6.01	-6.90	-7.70	-8.50	-9.31	-10.1
0.25	0.5	0	5.45	4.69	3.84	2.95	2.03	1.08	0.10	-0.73	-1.54	-2.36	-3.20
0.375	0.5	0.25	2.86	1.85	0.74	-0.44	-1.67	-2.92	-4.20	-5.36	-6.51	-7.67	-8.85
0.5	0.5	0.5	0.30	-0.57	-1.59	-2.73	-3.94	-5.18	-6.45	-7.62	-8.79	-9.97	-11.2
0.625	0.5	0.75	-0.58	-1.34	-2.25	-3.25	-4.31	-5.40	-6.51	-7.56	-8.62	-9.68	-10.8
0.75	0.5	1	-2.40	-2.83	-3.36	-3.96	-4.61	-5.29	-6.00	-6.66	-7.33	-8.01	-8.70
0.375	0.75	0	8.66	8.09	7.50	6.88	6.24	5.58	4.90	4.36	3.82	3.28	2.72
0.5	0.75	0.25	5.61	4.67	3.71	2.73	1.72	0.70	-0.33	-1.26	-2.18	-3.11	-4.05
0.625	0.75	0.5	3.14	2.13	1.07	0.00	-1.10	-2.21	-3.33	-4.37	-5.41	-6.46	-7.51
0.75	0.75	0.75	1.21	0.27	-0.69	-1.67	-2.65	-3.65	-4.65	-5.60	-6.55	-7.50	-8.46
0.875	0.75	1	0.07	-0.38	-0.84	-1.30	-1.77	-2.25	-2.73	-3.18	-3.63	-4.08	-4.54
0.5	1	0	11.4	11.4	11.5	11.5	11.5	11.5	11.5	11.6	11.7	11.8	11.8
0.625	1	0.25	7.69	7.26	6.82	6.36	5.90	5.42	4.93	4.52	4.12	3.71	3.29
0.75	1	0.5	4.64	4.12	3.58	3.02	2.46	1.89	1.31	0.78	0.25	-0.27	-0.81
0.875	1	0.75	2.80	2.36	1.92	1.47	1.01	0.55	0.08	-0.35	-0.79	-1.23	-1.67
1	1	1	0	0	0	0	0	0	0	0	0	0	0

C.6 References

Abdu Y. A., Annersten H., Ericsson T. and Hawthorne F. C. (2009) High-temperature cation ordering in olivine: an in situ Mössbauer study of synthetic $(Mg_{0.55}Fe_{0.45})_2 SiO_4$. In *ICAME 2007* (eds. N. S. Gajbhiye and S. K. Date). Springer, Berlin, Heidelberg. pp. 981–985.

Artioli G., Rinaldi R., Wilson C. C. and Zanazzi P. F. (1995) High-temperature Fe-Mg cation partitioning in olivine: In-situ single-crystal neutron diffraction study. *American Mineralogist* **80**, 197–200.

Bostroem D. (1987) Single-crystal X-ray diffraction studies of synthetic Ni-Mg olivine solid solutions. *American Mineralogist* **72**, 965–972.

Chatterjee S., Bhattacharyya S., Sengupta S. and Saha-Dasgupta T. (2011) Crossover of cation partitioning in olivines: a combination of ab initio and Monte Carlo study. *Phys Chem Minerals* **38**, 259–265.

Ghose S. and Ganguly J. (1982) Mg-Fe Order-Disorder in Ferromagnesian Silicates. In *Advances in Physical Geochemistry* (ed. S. K. Saxena). Advances in Physical Geochemistry. Springer, New York, NY. pp. 3–99.

Guggenheim E. A. (1937) The theoretical basis of Raoult's law. *Trans. Faraday Soc.* **33**, 151–156.

Kroll H., Kirfel A. and Heinemann R. (2006) Order and anti-order in olivine II: Thermodynamic analysis and crystal-chemical modelling. *European Journal of Mineralogy* **18**, 691–704.

Morozov M., Brinkmann C., Grodzicki M., Lottermoser W., Tippelt G., Amthauer G. and Kroll H. (2005) Octahedral cation partitioning in Mg,Fe^{2+}-olivine. Mössbauer spectroscopic study of synthetic $(Mg_{0.5}\ Fe^{2+}{}_{0.5})_2SiO_4$ (Fa50). *Hyperfine Interact* **166**, 573–578.

Perdew J. P., Burke K. and Ernzerhof M. (1996) Generalized Gradient Approximation Made Simple. *Phys. Rev. Lett.* **77**, 3865–3868.

Rinaldi R., Artioli G., Wilson C. C. and McIntyre G. (2000) Octahedral cation ordering in olivine at high temperature. I: in situ neutron single-crystal diffraction studies on natural mantle olivines (Fa12 and Fa10). *Phys Chem Min* **27**, 623–629.

Rinaldi R. and Wilson C. C. (1996) Crystal dynamics by neutron time-of-flight Laue diffraction in olivine up to 1573K using single frame methods. *Solid State Communications* **97**, 395–400.

Redfern S. A. T., Artioli G., Rinaldi R., Henderson C. M. B., Knight K. S. and Wood B. J. (2000) Octahedral cation ordering in olivine at high temperature. II: an in situ neutron powder diffraction study on synthetic $MgFeSiO_4$ (Fa50). *Phys Chem Min* **27**, 630–637.

Smyth J. R. and Hazen R. M. (1973) The crystal structures of forsterite and hortonolite at several temperatures up to 900°C. *American Mineralogist* **58**, 588–593.

Appendix D

Spin State of Iron in Mackinawite

Spin Status of Mackinawite

Co-authors: Sha Chen and Udo Becker

D.1 Introduction

Literature has conflicting conclusions over the electron configuration of Fe in the iron sulfide mineral mackinawite. For example, Mossbauer spectroscopy studies from Vaughan and Ridout (1971) and Mullet et al. (2002) concluded the presence of low spin Fe. Devey et al. (2008) had the same conclusion by using DFT calculations. Other studies, however, seem to show otherwise. Kwon et al. (2011) used DFT calculations and demonstrated the ground state of antiferromagnetic for mackinawite. Schröder et al. (2020) conducted Mossbauer study on different synthesized mackinawite. They supported non-zero magnetic moments, and suggested spin fluctuations with the stoichiometry of the mineral.

Here, spin configuration of mackinawite is examined thermodynamically using different computation programs in this Supplementary. We studied the mineral unit cell, mineral slab, and the mackinawite cluster (Fe_8S_8) used in the Chapter 4. The Gibbs free energies are computed and compared using multiple computational tools, Gaussian, Crystal 17, and CASTEP. Single-point calculations (no geometry optimization) were conducted for different spin configurations, low spin and different high spin configurations. We will present in detail the results of the mackinawite

cluster using different programs. Although we also have the results of the mineral and the mineral slab, the data and details of calculation are not stated here. They are mentioned briefly in the Conclusion.

D.2 Spin configuration of mackinawite cluster Fe_8S_8

Three programs, Gaussian, CASTEP, and Crystal 17 have been used for the single point computation of mackinawite cluster. For the same total spin, there may be various settings. Therefore, each atom is labelled from 1 to 16 in Figure D0.1 to better differentiate different configurations.

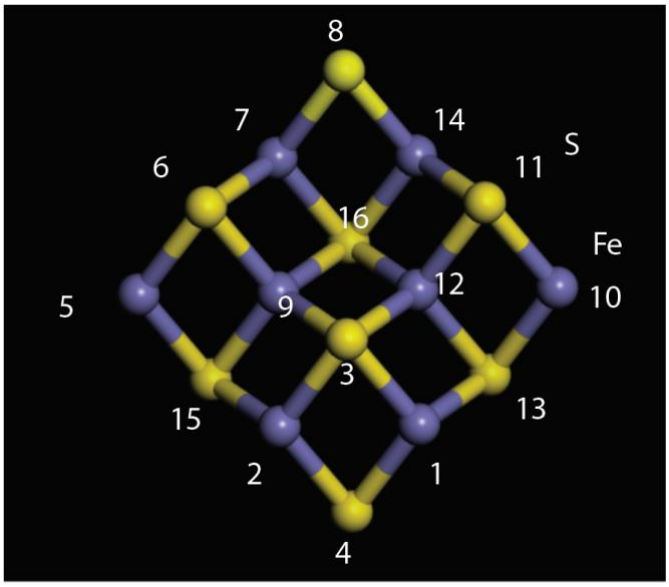

Figure D0.1 Structure of the mackinawite cluster. The Fe and S atoms are labelled from 1 to 16 in the cluster. Yellow balls represent S. Blue balls are Fe.

For Gaussian calculations, the total energies are shown in Table D0.1. The low spin configurations are approximately 2000 kJ/mol higher in energy than high spin. For high spin, we calculated anti-ferromagnetic (AFM), ferro-magnetic (FM), and a setting with the total spin (1/2) of 16. The AFM calculation gave lower energy than FM by 75 kJ/mol. The spin of 16 calculation (six Fe atoms spin up and two spin down) is slightly lower than the AFM configuration calculated. We have to stress that no conclusion can be drawn that spin of 16 is more energetically favorable

than AFM because only one AFM was calculated here. The same direction Fe atoms are close to each other. Therefore, this AFM configuration should have higher energy than other AFM settings.

Table D0.1 Gaussian calculation results for the mackinawite cluster. E: the calculated total energy. E_rela: the total energy relative to FM. Low spin: all eight Fe atoms have no unpaired electrons; AFM: four Fe atoms spin up and the rest four Fe atoms spin down to a total spin of 0. S=16: six Fe atoms spin up and two Fe atoms spin down. FM: all 8 Fe atoms spin up with a total spin of 32. The atom number position can be found in Figure D0.1.

	Spin up atoms	Spin down atoms	E_rela (kJ/mol)
Low spin, restricted	None	None	2044
Low spin, open shell	None	None	1974
High spin, AFM	1, 2, 7, 14	5, 9, 10, 12	-75
high spin, S=16	1, 2, 5, 7, 10, 14	9, 12	-110
FM, S=32	All Fe	None	0

In Crystal 17 calculations, the mackinawite cluster is considered a molecule with the symmetry of P1. Because it is easier to assign the spin of each Fe atom, more configurations were computed than using Gaussian. The energies for all runs are summarized in Table D0.2. The restricted low spin calculation has significantly higher energy than all high spin configurations by more than 1557 kJ/mol. For the high spin calculations, the energies vary even for the same total spin. The lowest energy is one of the antiferromagnetic settings with the same spin Fe atoms far away from each other.

Table D0.2 Crystal17 computational results for the spin of mackinawite cluster. The atom number position can be found in Figure D0.1.

S (1/2)	#S corner	#S edge	#S center	Spin up atoms	Spin down atoms	E_rela (kJ/mol)
32	8	16	8	All Fe	None	0
24	8	8	8	1, 2, 5, 7, 9, 10, 12	14	-123
24	0	16	8	1, 2, 5, 7, 9, 12, 14	10	-154
24	8	16	8	1, 2, 5, 9, 10, 12, 14	7	-168
16	0	8	8	1, 2, 9, 10, 12, 14	5, 7	-200
16	8	16	-8	1, 2, 5, 7, 10, 14	9, 12	-190
16	-8	16	8	1, 2, 7, 9, 12, 14	5, 10	-203
16	8	0	8	2, 5, 9, 10, 12, 14	1, 7	-243
8	0	8	0	1, 5, 7, 12, 14	2, 9, 10	-255
8	0	0	8	7, 9, 10, 12, 14	1, 2, 5	-200
0, AFM	0	0	0	2, 7, 9, 10	1, 5, 12, 14	-312
0, AFM	-8	16	-8	1, 2, 7, 14	5, 9, 10 12	-102
0, AFM	0	0	0	1, 10, 12, 14	2, 5, 7, 9	-185
0, AFM	0	0	0	1, 9, 10, 14	2, 5, 7, 12	-273
0, LS	0	0	0	None	None	1557

Since CASTEP can only work on periodic crystals, we placed the cluster first into a larger unit cell to make it periodic. The symmetry of the lattice is primitive of C-centered monoclinic with a and b parameters of 14.694 Å and c parameters of 12.619069 Å. With the symmetry, the same position (all corner sites, edge sites, or center sites) would share the same spin. Assuming for each position, there could be a high spin up or down (+4/-4) or intermediate up spin(+2). There would be 27 possibilities in total. One calculation failed and the rest 26 calculation results are shown in Table D0.3. Among all the high spin/intermediate spin calculations, the antiferromagnetic setting with spin up for the four edge Fe atoms and spin down for the two center and two corner Fe atoms gives the lowest energy among all the calculations.

Table D0.3 CASTEP computational results for the spin of mackinawite cluster.

	Energy_rela	Formal spin			
	(kJ/mol)	Fe center	Fe edge	Fe corner	spin
1	0.0	4	4	4	32
2	-408.4	4	4	-4	16
3	-167.6	4	4	2	28
4	-466.4	4	-4	4	0
5	-408.4	4	-4	-4	-16
6	-461.3	4	-4	2	-4
7	-266.7	4	2	4	24
8	-409.6	4	2	-4	8
9	-344.0	4	2	2	20
10	-408.4	-4	4	4	16
11	-466.4	-4	4	-4	0
12	-464.7	-4	4	2	12
13	-408.3	-4	-4	4	-16
14	0.0	-4	-4	-4	-32
15	-343.6	-4	-4	2	-20
16	-428.9	-4	2	4	8
17	-299.7	-4	2	2	4
18	-167.6	2	4	4	28
19	-280.7	2	4	-4	12
20	-266.7	2	4	2	24
21	-461.3	2	-4	4	-4
22	-344.1	2	-4	-4	-20
23	-409.5	2	-4	2	-8
24	-344.1	2	2	4	20
25	-461.3	2	2	-4	4
26	-408.4	2	2	2	16

D.3 Conclusion

In conclusion, all the three programs used, Gaussian 09, CASTEP, and Crystal 17, demonstrate that high spin is much more thermodynamically favorable than low spin. Since none of the three programs considered all possible configurations, we cannot use the result of one program to find the ground state. However, we can have a better understanding by combining all the computations. If the symmetry of C2h of the cluster is considered, we can conclude from the CASTEP results that antiferromagnetic setting with the edge Fe atoms spin up and both corner and center Fe atoms spin down (atom number 5, 9, 10, and 12 in the Figure D0.1), or the opposite has the lowest energy. This setting is also computed by both Gaussian and Crystal. The results show that the above mentioned AFM configuration is not the ground state if no symmetry is considered in the spin assignment. Although the spin of $16\cdot\frac{\hbar}{2}$ is the lowest in the five calculations in Gaussian, it is only 25 kJ/mol lower than that AFM configuration. Other AFM configurations calculated by Crystal 17 can have up to 210 kJ/mol even lower than that. We can safely conclude that the ground state of the mackinawite cluster is an antiferromagnetic configuration.

The calculation for periodic 2D cluster and 3D crystal were also calculated, but since they were not used in the calculation of Chapter 4. The details are not discussed here. But the results are the same: high spin is more thermodynamically favorable than low spin for mackinawite, and antiferromagnetic has the lowest energy.

Another thing worth noting is that CASTEP results of the 2D slab and 3D indicate that the surface is more stable than the bulk. It can be explained by the mackinawite structure. The interaction between sheets is weak. It can also explain why mackinawite minerals do not grow into large crystals and it often occurs as nanoparticles.

D.4 References

Devey A. J., Grau-Crespo R. and de Leeuw N. H. (2008) Combined Density Functional Theory and Interatomic Potential Study of the Bulk and Surface Structures and Properties of the Iron Sulfide Mackinawite (FeS). *J. Phys. Chem. C* **112**, 10960–10967.

Kwon K. D., Refson K., Bone S., Qiao R., Yang W., Liu Z. and Sposito G. (2011) Magnetic ordering in tetragonal FeS: Evidence for strong itinerant spin fluctuations. *Phys. Rev. B* **83**, 064402.

Mullet M., Boursiquot S., Abdelmoula M., Génin J.-M. and Ehrhardt J.-J. (2002) Surface chemistry and structural properties of mackinawite prepared by reaction of sulfide ions with metallic iron. *Geochimica et Cosmochimica Acta* **66**, 829–836.

Schröder C., Wan M., Butler I. B., Tait A., Peiffer S. and McCammon C. A. (2020) Identification of Mackinawite and Constraints on Its Electronic Configuration Using Mössbauer Spectroscopy. *Minerals* **10**, 1090.

Vaughan D. J. and Ridout M. S. (1971) Mössbauer studies of some sulphide minerals. *Journal of Inorganic and Nuclear Chemistry* **33**, 741–746.